AGH UNIVERSITY OF KRAKOW

FIELD OF SCIENCE ENGINEERING AND TECHNOLOGY

SCIENTIFIC DISCIPLINE MECHANICAL ENGINEERING

DOCTORAL THESIS

The Study of Interaction of Shear Horizontal Guided Waves with Distributed and Local Nonlinearities

Author: Mariusz Osika

First supervisor: Prof. Wiesław Jerzy Staszewski, PhD, DSc
Assisting supervisor: Aleksandra Ziaja–Sujdak, PhD

Completed in: Faculty of Mechanical Engineering and Robotics

Kraków, 2024

AKADEMIA GÓRNICZO-HUTNICZA IM. STANISŁAWA STASZICA W KRAKOWIE

DZIEDZINA NAUK INŻYNIERYJNO–TECHNICZNYCH

DYSCYPLINA INŻYNIERIA MECHANICZNA

ROZPRAWA DOKTORSKA

Analiza Interakcji Prowadzonych Fal Poprzecznie Spolaryzowanych z Rozproszoną oraz Lokalną Nieliniowością

Autor: Mariusz Osika

Promotor rozprawy: prof. dr hab. inż. Wiesław Jerzy Staszewski
Promotor pomocniczy: dr inż. Aleksandra Ziaja–Sujdak

Praca wykonana: Wydział Inżynierii Mechanicznej i Robotyki

Kraków, 2024

I dedicate this work to my wife Kasia

and son Franio.

Dedykuję tę pracę mojej żonie Kasi

i synowi Franiowi.

Acknowledgements

I sincerely thank my Supervisors for our successful collaboration and continuous motivation. My special thanks go to Prof. Wiesław Staszewski, PhD, DSc for the numerous academic discussions, inspiration and time dedicated to working with me, which have contributed significantly to the final form of this thesis. I would also like to express my gratitude to Aleksandra Ziaja–Sujdak, PhD for introducing me to the academic approach to conducting research. Her guidance enabled me to perform independent research, which has impacted the preparation of this work. I am very grateful for the opportunity to participate in a fascinating and challenging adventure involving participating in a research project UMO–2018/30/Q/ST8/00571 financed by the Polish National Science Centre, conducting research and writing this dissertation.

I want to thank my close family for their support throughout my research and preparation of this dissertation. My heartfelt thanks go to my parents, Bernadeta and Roman, for their constant and unwavering belief in me. I am grateful for their example of a life filled with hard work and an upbringing that has shaped me as a person and led to my involvement in research. I would also like to express my gratitude to my siblings Marcin, Piotr, Paweł and Karolina for their tremendous support.

I would also like to thank my wife's parents, Alfreda and Wiesław, whom I treat as my own parents, for their enormous help and kindness during my work on this thesis. I am incredibly grateful to my father–in–law Wiesław – who unfortunately could not see the finalisation of this dissertation – for convincing me to accept the challenge of the research work presented in this thesis.

Special thanks go to my beloved wife Kasia for her love, patience, unwavering faith in me and constant support. I also appreciate her understanding and patience when I was frustrated by my mistakes and tedious work. I also value the fact that I could celebrate my successes with her and when I overcame any difficulties. Her indirect contribution to this dissertation, resulting from her constant trust in me, is invaluable. Finally, I would like to thank my son, Franio, for also supporting me in my work in his own way and for his ability to take me away from it and make me aware of what and who is the most important part of my life.

Podziękowania

Pragnę serdecznie podziękować moim Promotorom za owocną współpracę oraz nieustającą motywację. Szczególne wyrazy uznania kieruję do Pana prof. dr hab. inż. Wiesława Staszewskiego za liczne merytoryczne dyskusje naukowe, inspirację i poświęcony czas, które w istotny sposób przyczyniły się do nadania tej pracy ostatecznego kształtu. Ponadto, dziękuję Pani dr inż. Aleksandrze Ziaji–Sujdak za wprowadzenie mnie w akademickie podejście do prowadzenia badań naukowych. Jej wskazówki umożliwiły mi samodzielne prowadzenie prac badawczych, co niewątpliwie wpłynęło na powstanie tej rozprawy. Jestem ogromnie wdzięczny za możliwość uczestniczenia w niezwykle kształcącej, pasjonującej i pełnej wyzwań przygodzie, obejmującej udział w projekcie badawczym UMO–2018/30/Q/ST8/00571 finansowanym przez Narodowe Centrum Nauki, prowadzenie badań naukowych oraz przygotowanie tej rozprawy doktorskiej.

Dziękuję mojej najbliższej rodzinie za wsparcie w czasie, gdy prowadziłem badania naukowe i opracowywałem tę rozprawę doktorską. Dziękuję moim rodzicom, Bernadecie i Romanowi, za nieustanną i niezachwianą wiarę we mnie. Pragnę wyrazić wdzięczność dla Nich za przykład życia wypełnionego ciężką pracą oraz wychowanie, które ukształtowało mnie jako człowieka i zaowocowało moim zaangażowaniem w pracach badawczych. Pragnę również podziękować mojemu rodzeństwu Marcinowi, Piotrowi, Pawłowi oraz Karolinie za ich wsparcie.

Chciałbym również podziękować rodzicom mojej żony, Alfredzie oraz Wiesławowi, których traktuję jak własnych rodziców, za ogrom okazanej mi pomocy oraz życzliwości w trakcie pracy naukowej. Jestem ogromnie wdzięczny mojemu teściowi Wiesławowi, który niestety nie doczekał zakończenia prac nad tą rozprawą doktorską, za to, że przekonał mnie do podjęcia wyzwania, którymi były przedstawione w tej rozprawie prace badawcze.

Szczególne podziękowania kieruję do mojej ukochanej żony Kasi, za jej miłość, cierpliwość, niezachwianą wiarę we mnie i nieustanne wsparcie. Dziękuję jej również za to, że niejednokrotnie z wyrozumiałością znosiła moje zachowania wynikające z frustracji związanych z moimi pomyłkami i żmudną pracą. Doceniam także to, że mogłem cieszyć się razem z nią z moich sukcesów oraz gdy udawało mi się przezwyciężać wszelkie przeciwności. Jej pośredni wkład w opracowanie tej rozprawy doktorskiej, który wynikał z nieustannej wiary we mnie, jest nieoceniony. Ostatnie podziękowania kieruję do mojego synusia Franciszka za to, że również na swój sposób wspierał mnie w pracy oraz za to, że potrafił niejednokrotnie oderwać mnie od niej i uświadamiał, co i kto jest najważniejsze w moim życiu.

Abstract

The thesis presents an investigation of two nonlinear phenomena associated with shear horizontal guided wave propagation. This group of waves propagate in thin–walled structures. The first effect studied is the classical phenomenon of wave interaction with a distributed nonlinearity i.e., nonlinear material. The second phenomenon investigated is the nonclassical wave interaction – induced by combined monochromatic and amplitude–modulated excitation – with a local nonlinearity that could be considered as fatigue damage. This phenomenon is analogous to the original effect observed for radio waves and called the Luxembourg–Gorky (L–G) effect.

The research described in this thesis starts with a literature review on the nonlinear phenomena investigated. Following this critical review, the objectives and aims of the research work conducted are defined. The analytical calculations – based on the perturbation approach – form the theoretical background of the problems investigated. The results of the theoretical work are verified using numerical simulations. This work is based on the Local Interaction Simulation Approach (LISA), implemented for the nonlinear shear horizontal wavefield and focused on problems investigated. Since the L–G effect – retooled for elastic waves – has never been fully explained so far, experimental research work in this area is undertaken to accomplish the analytical and numerical research effort.

For the sake of completeness, the analytical work starts with the relevant theoretical background related to the adopted Lagrange description for a continuous medium, tensor measures of stresses, strains tensor fields and the general simplifying assumptions for the calculations undertaken. Furthermore, derivations of the solid dynamics equations are provided, leading to the linear propagation problem of the considered multimodal and dispersive wave group. For small wave propagation amplitudes assumed, the first classical wave propagation nonlinear problem is analysed, using the multiplescale perturbation method. The Landau–Lifshitz model is employed to describe the nonlinear material. A series of recursive calculations is performed to obtain successive approximations of the exact solution. The multiplescale perturbation method allowed elimination of the secular terms in the approximation solution describing the distortions of the analysed wavefield and dispersion curves. Following this analysis, a new concept of nonlinear shear horizontal guided wave modes is proposed.

The nonclassical nonlinear problem – i.e., the elastic equivalent of the L–G effect – is then investigated. To ensure a comprehensive understanding, the analysis starts with the theoretical background of the original L–G effect initially observed for electromagnetic waves. Following this introduction, a new nonlinear viscoelastic crack model with Kelvin–Voigt structure is proposed. Shear wave interaction with the proposed crack nonlinearity is investigated analytically using the classical perturbation approach. The modulation transfer was observed in the approximate solution obtained and represents the L–G effect. This indicates that the proposed model allows the modelling of this phenomenon. The frequency and wavenumber pairs characterising the additional waves generated by the interaction between the propagating waves and the local nonlinear region have also been determined. Furthermore, the calculations show that all modes of shear horizontal guided waves are generated as a result of the interaction of waves with the local crack nonlinearity. It was concluded from the results that the index of transferred modulation is higher when modulations are transferred from higher to lower frequencies i.e., when the carrier frequency of the amplitude–modulated wave is higher than the carrier frequency of the monochromatic wave in the combined excitation. The dependence between the carrier frequencies of the monochromatic and amplitude–modulated waves and the index of transferred modulation is also investigated. In summary, the proposed physical model explains the elastic equivalent of the L–G effect. This model corresponds well with previously observed experimental results and theoretical assumptions. The proposed model is also compatible with the physical explanation of the original L–G effect for electromagnetic waves.

Simulation studies – based on the LISA method – are performed for both nonlinear problems investigated. The dissertation presents a general derivation of the iterative equations for this simulation technique, based on the finite difference method. The relevant equations are implemented for the nonlinear wavefield and problems investigated. Time domain responses and spatial coordinates are used to obtain amplitude spectra in the frequency and wavenumber domain. In addition, the analysed wavefield is decomposed using the orthogonal base of functions, corresponding to individual shear horizontal guided wave modes. The results confirm the predictions from the analytical calculations for both nonlinear problems investigated.

Since experimental work related to the first problem investigated is relatively well reported in the literature, the experimental studies presented in the thesis focus only on the analysis of the L–G effect. The specimens used in these investigations are aluminium beams. Two different specimens – i.e., intact and cracked – are investigated. Ultrasonic waves are excited in these beams using dedicated low–profile, surface–bonded piezoceramic actuators. The responses of investigated beams are gathered using noncontact 3–D laser vibrometry. The experimental results obtained confirm the findings from analytical analysis and numerical simulations, showing that the nonlinear modulation transfer is more effective from higher to lower frequencies than in the

opposite direction. The effect of carrier frequencies of exciting waves on modulation transfer is also investigated, confirming previously obtain analytical and simulated results.

Finally, the research work undertaken is summarised and the major conclusions are provided. The research presented gives a deeper physical understanding of the two nonlinear shear wave phenomena investigated. More scientific questions are risen and possible future research directions identified at the end of the thesis.

Streszczenie

W opracowanej rozprawie doktorskiej przedstawiono analizę dwóch nieliniowych zjawisk związanych z ultradźwiękowymi prowadzonymi falami poprzecznie spolaryzowanymi. Propagacja tej grupy fal jest możliwa w strukturach cienkościennych. Pierwszym z rozważanych efektów było klasyczne zjawisko interakcji fal z nieliniowością rozproszoną, czyli nieliniowym materiałem. Drugim zjawiskiem było nieklasyczne wzajemne oddziaływanie dwóch fal – wzbudzanych jednocześnie przez monochromatyczne oraz modulowane amplitudowo wymuszenie – oraz lokalnej nieliniowości (np. uszkodzenia zmęczeniowego). Jest ono analogicznym efektem do tego, które zaobserwowano dla fal radiowych, czyli tzw. zjawiska Luksemburg – Gorki (L–G).

Prace przedstawiane w niniejszej rozprawie obejmowały opracowanie przeglądu literatury dotyczącej rozważanych zjawisk nieliniowych. Na jego podstawie zdefiniowano cele oraz zakres podjętych prac badawczych. Wśród nich można wskazać obliczenia analityczne bazujące na metodzie perturbacji, które pozwoliły na teoretyczną analizę fizycznych podstaw badanych zjawisk oraz umożliwiły dalsze rozważania. Wyniki otrzymane na podstawie prac analitycznych zweryfikowano z wykorzystaniem symulacji numerycznych bazujących na opracowanej implementacji metody Local Interaction Simulation Approach (LISA) dla fal poprzecznie spolaryzowanych. Opracowane narzędzie numeryczne było dedykowane do modelowania wyżej wymieniowych zjawisk nieliniowych. Ponadto ze względu na fakt, że efekt L–G nie został jak dotąd w pełni zbadany, podjęto prace eksperymentalne, aby dopełnić podjęte badania analityczne oraz symulacyjne.

Dla pełnego obrazu przeprowadzone prace analityczne zostały poprzedzone wstępem teoretycznym, który przedstawiał analizę: przyjętego opisu Lagrange'a medium ciągłego, miar tensorowych pól naprężeń oraz odkształceń, oraz ogólnych założeń upraszczających obliczenia. Ponadto przedstawiono wyprowadzenie równań opisujących dynamikę ciała odkształcalnego. Na ich podstawie sformułowano matematyczny model opisujący zjawisko propagacji wielomodowej i dyspersyjnej grupy fal rozważanej w tej pracy. Pierwsze nieliniowe klasyczne zjawisko propagacji fal zbadano analitycznie w oparciu o metodę perturbacji w jej wariancie wielkoskalowym, przy założeniu małych amplitud modelowanych fal. W celu opisu materiału nieliniowego wykorzystano model Landau–Lifszyca. W ramach przyjętej techniki obliczeniowej

przeprowadzono obliczenia rekurencyjne w celu wyznaczenia kolejnych przybliżeń dokładnego rozwiązania. Wykorzystana wieloskalowa metoda perturbacji umożliwiła wyeliminowanie składników sekularnych w wyznaczonym przybliżonym rozwiązaniu, z których wynikał opis zniekształceń pola falowego oraz krzywych dyspersji. Na podstawie przeprowadzonych obliczeń sformułowano koncepcję nieliniowych modów dla prowadzonych fal poprzecznie spolaryzowanych.

Kolejne przeprowadzone badania teoretyczne dotyczyły nieklasycznego nieliniowego zjawiska, mianowicie efektu L–G. Dla zapewnienia kompletnego zrozumienia badanego zjawiska opracowane obliczenia analityczne przeprowadzone w celu analizy efektu L–G dla prowadzonych fal poprzecznie spolaryzowanych poprzedzono rozważaniami nad tym efektem, który zaobserwowano dla fal radiowych. Bazując na analizie teoretycznej z zakresu elektrodynamiki, opracowano model lokalnego uszkodzenia, jako nieliniowego materiału wiskoelastycznego o strukturze odpowiadającej modelowi Kelvina–Voigta. Interakcja pomiędzy falami ścinającymi oraz nieliniowym obszarem opisanym przez zaproponowany model nieliniowy, który stanowił model lokalnego uszkodzenia, przeprowadzono z wykorzystaniem metody perturbacji w jej klasycznym wariancie. W przybliżonych rozwiązaniach wynikających z przeprowadzonych rozważań analitycznych zaobserwowano przeniesienie modulacji, które reprezentowało zjawisko L–G. Oznaczało to, że zaproponowany model umożliwia modelowanie tego nieliniowego efektu fizycznego. Wyznaczone wyniki analityczne pozwoliły na zidentyfikowanie par częstotliwości i liczb falowych charakteryzujących dodatkowe fale wzbudzone w wyniku wzajemnego oddziaływania fal oraz uszkodzenia. Ponadto, przeprowadzone obliczenia wskazały na wzbudzanie wszystkich modów na skutek interakcji fal z lokalną nieliniowością. Na podstawie uzyskanych wyników stwierdzono również, że współczynnik głębokości przenoszonej modulacji jest wyższy, gdy modulacje są przenoszone z wyższych do niższych częstotliwości, tj. gdy częstotliwość nośna fali modulowanej amplitudowo jest wyższa niż częstotliwość nośna fali monochromatycznej w wykorzystanym wzbudzeniu. Zbadano również zależność między częstotliwościami nośnymi fali monochromatycznej i fali modulowanej amplitudowo a współczynnikiem głębokości przenoszonej modulacji. Podsumowując, zaproponowany model pozwala na wyjaśnienie zjawiska L–G dla rozważanej grupy fal. Ponadto, dobrze koresponduje on z wcześniej zaobserwowanymi wynikami eksperymentalnymi i założeniami teoretycznymi. Jest on również zgodny z fizycznym wyjaśnieniem oryginalnego efektu L–G dla fal elektromagnetycznych.

Badania symulacyjne, oparte na metodzie LISA, przeprowadzono dla badanych zjawisk nieliniowych. W rozprawie przedstawiono ogólne wyprowadzenie równań iteracyjnych dla tej techniki symulacyjnej, która opiera się na metodzie różnic skończonych. Wyprowadzone ogólne równania zostały zaimplementowane dla nieliniowego pola falowego fal poprzecznie spolaryzowanych i badanych zjawisk nieliniowych. Wyniki symulacyjne w dziedzinie czasu i

współrzędnych przestrzennych wykorzystano do wyznaczanie widm amplitudowych w dziedzinie częstotliwości i liczby falowej. Ponadto przeprowadzono dekompozycję pola falowego względem ortogonalnej bazy funkcyjnej, odpowiadającej prowadzonym falom poprzecznie spolaryzowanym. Wyniki symulacji numerycznych dla opracowanych modeli potwierdzają przewidywania wynikające z obliczeń analitycznych dla obu badanych problemów nieliniowych.

Ponieważ prace eksperymentalne związane z pierwszym badanym problemem są stosunkowo dobrze opisane w literaturze, badania eksperymentalne przedstawione w rozprawie koncentrują się tylko na analizie efektu L–G. Próbkami wykorzystanymi w tych badaniach były belki aluminiowe. Rozważane były dwie różne próbki, bez pęknięcia zmęczeniowego i z uszkodzeniem zmęczeniowym. Fale ultradźwiękowe wzbudzano w tych komponentach z wykorzystaniem dedykowanych przetworników piezoceramicznych. Odpowiedzi badanych belek rejestrowano za pomocą bezkontaktowej metody pomiarowej tj. wibrometrii laserowej 3–D. Otrzymane wyniki eksperymentalne potwierdziły wnioski wynikające z przeprowadzonych analiz analitycznych i symulacji numerycznych. Na podstawie pomiarów laboratoryjnych pokazano, że nieliniowy transfer modulacji jest bardziej efektywny z wyższych do niższych częstotliwości niż w przypadku odwrotnym. Zbadano również wpływ częstotliwości nośnych fal wzbudzanych na transfer modulacji, potwierdzając wcześniej uzyskane wyniki analityczne i symulacyjne.

Opracowana rozprawa została zakończona podsumowaniem podjętych prac badawczych i przedstawieniem głównych wniosków. Przeprowadzone badania pozwalają na głębsze zrozumienia fizycznych podstaw dwóch badanych zjawisk nieliniowych związanych z falami prowadzonymi poprzecznie spolaryzowanymi. Na końcu rozprawy sformułowano kolejne pytania badawcze i określono możliwe przyszłe kierunki badań.

Contents

List of Figures

List of Tables

Chapter 1

Introduction

This chapter introduces research area of interest, explains major topics within this area and justifies their importance. Previous research work in the field – related to the problems investigated – is reviewed. This review concludes by identifying knowledge gaps, which motivate the conducted study. Finally, the main hypotheses, aims and objectives of the research work undertaken are formulated.

1.1 Problem statement and motivation

Engineering structures require monitoring to detect potential material defects, degradation and structural damage, to ensure safe operation and to minimise operating costs. This requires reliable Non–Destructive Testing (NDT) for material evaluation and early detection of structural manufacturing and operational defects. Various NDT techniques have been developed for the last few decades. These include vision techniques, X–ray inspection, magnetic testing, thermal imaging, ultrasonic wave–based methods, and many other approaches based on different physical phenomena. Ultrasonic testing is particularly attractive due to damage sensitivity, use convenience, versatility and tremendous amount of gathered experience. Previous research and field experience shows that ultrasonic methods – used to inspect surface and in–depth material defects – can be automated. Research and field applications – that relate to on–line monitoring based on permanently attached transducers – demonstrate the potential of ultrasonic methods for Structural Health Monitoring (SHM) systems Boller et al. (2009).

Damage sensitivity of ultrasonic methods depend on excitation parameters such as amplitude and frequency/wavelength. The wavelength of propagating waves and structural dimensions allow one to excite bulk or guided waves in tested components. Ultrasonic bulk wave propagation refers to waves that do not interact with boundaries. This usually refers to waves propagating in infinite media. In contrast, guided waves require boundaries for propagation. Thus, guided waves propagate in plates, rods, tubes and other structural elements. Bulk wave propagation for damage

detection requires wavelengths that are significantly smaller than geometric dimensions of tested components. In contrast, the wavelengths of guided waves are comparable to dimensions of investigated components and defects Rose (2014). The latter is particularly important for good damage sensitivity.

The volume of material in which guided waves propagate is significantly larger than a local region sonified by bulk waves. Guided waves (e.g., Lamb waves propagating in plates) are capable to cover the entire thickness of monitored structures and propagate over relatively long distances, allowing monitoring with one probe position. Bulk waves cover a local zone just below a transducer that needs to be moved to collect data. Hence, inspection based on guided waves is more suitable for SHM applications. All these practical aspects are discussed in Staszewski et al. (2003).

Ultrasonic waves propagating in solids can be either longitudinal (compressional or P waves) or transverse (shear or S waves). The particle motion of the former waves is in the direction of propagation. The latter waves exhibit the particles motion that is perpendicular to this direction and can be in either vertical (SV waves) or horizontal (SH wave) directions. Ultrasonic longitudinal and shear waves have been investigated for several decades for damage detection. A number of damage detection methods based on linear and nonlinear phenomena related to bulk and guided wave propagation have been proposed and implemented in NDT and SHM, as reviewed in Staszewski et al. (2003); Boller et al. (2009); Stepinski et al. (2013); Jhang et al. (2020a). Nonlinear ultrasonic wave propagation is particularly attractive for detection of small defects at an early stage of formation and growth Rose (2014). However, practical implementations of these approaches face challenges related to excitation and interpretation of results. Low excitation amplitudes usually do not trigger nonlinearities in wave propagation, whereas large excitation amplitudes often produce intrinsic material and measurement chain nonlinearities. The problem is that damage–related nonlinearities are not easy to separate from intrinsic nonlinearities. In addition, these nonlinearities lead to various classical phenomena (e.g., higher harmonic generation) and nonclassical phenomena (e.g., slow dynamics or modulations). The latter phenomena are remarkably sensitive to micro–structural damage, as reviewed in Pieczonka et al. (2015).

There is enough experimental evidence showing that nonlinear phenomena are significantly enhanced in the presence of small material defects Broda et al. (2014); Pieczonka et al. (2015); Kundu (2019); Jhang et al. (2020b). However, these studies are mainly related to longitudinal ultrasonic waves. Although linear field of ultrasonic shear waves has been investigated for damage detection for several decades, nonlinear propagation of these waves has yet to be fully explored for material evaluation. This is particularly related to shear horizontal waves that in the linear regime have already demonstrated good sensitivity to small cracks (e.g., Rose (2014); Jhang et al. (2020a)) and in the nonlinear regime show some potential for even micro–structural damage detection Liu

et al. (2013b,a); Shengbo & Cheng (2019); Fuzhen Wen (2021); Lissenden (2021). The latter development relates to higher harmonic generation.

Hence, the integration of shear horizontal guided wave propagation and methods based on classical or nonclassical nonlinear phenomena provides significant potential for the development of efficient NDT methods. Guided waves are generally dispersive and multimodal. Therefore, their mathematical models of wave propagation become difficult when combined with nonlinear phenomena. Thus, comprehensive study of nonlinear shear horizontal guided wave propagation is essential for the development of dedicated, reliable damage detection applications. However, modelling and full understanding of physical mechanisms involved in wave interaction with distributed and local nonlinearities is not only attractive but also challenging. This is the major motivation behind the research study undertaken.

1.2 Literature review

This section reviews previous research work related to the field investigated. Nonlinear ultrasonic wave propagation is initially discussed. Then more detailed developments are overviewed. Since the research work undertaken relates to higher harmonic generation (classical nonlinear effect) and modulation transfer (nonclassical nonlinear effect), the review focuses on these two aspects.

1.2.1 Overview of developments related to nonlinear ultrasonic waves

Local and distributed material defects (e.g., fatigue cracks, microcracks, delamination) can affect ultrasonic waves propagating in a solid medium. These interactions – linear or nonlinear in nature – result in a distortion of wavefields. Nonlinear effects have been the subject of extensive study in the NDT area since the pioneering work in the 1960s Breazeale & Ford (1965); Hikata et al. (1965). Various methods – based on nonlinear effects – have been developed and applied to detect and identify material defects for the last few decades, as reviewed in Staszewski et al. (2003); Boller et al. (2009); Stepinski et al. (2013); Pieczonka et al. (2015); Jhang et al. (2020b). All these methods fall into the category of classical or nonclassical approaches. This classification results from the types of nonlinearities observed in responses of investigated systems.

The aforementioned classical approaches include methods based on higher harmonic generation, wave mixing of harmonic waves and acoustoelastic effect. These phenomena can be observed in homogeneous materials, which can be described by hyperelastic material models. Damage detection research work on higher harmonic generation relies on the analysis of amplitudes of higher harmonics employed for crack detection and localisation Nagy (1998); Cantrell & Yost (2001); Broda et al. (2016). Different methods that utilise nonlinear wave mixing have been developed for detecting and identifying defects in material and structural damage.

These techniques comprise both i.e., collinear Korneev & Demčenko (2014) and noncollinear Croxford et al. (2009) approaches. In addition, some investigations have been conducted in this field to explore the acoustoelastic effect that can be used either to estimate higher–order elastic constants in solid media Herzer et al. (2019). The fundamental theory of nonlinear elasticity can be utilised in order to describe and explain higher–order harmonic generation, wave mixing of ultrasonic waves acoustoelastic effect, as discussed in Auld (1973); Rose (2014); Jhang et al. (2020b). A theoretical summary of the three discussed nonlinear effects resulting from interactions of propagating ultrasonic waves with defects – which form the basis of many monitoring methods – can be found in Korneev et al. (1998). Nonlinear ultrasonic guided waves have been utilised to develop classical approaches for damage detection. These include methods based on the higher harmonic generation of Rayleigh waves de Lima & Hamilton (2003); Herrmann et al. (2006), Lamb waves de Lima & Hamilton (2003); Srivastava & Lanza di Scalea (2009); Müller et al. (2010), shear waves de Lima & Hamilton (2003); Chillara & Lissenden (2014), and their combinations Liu et al. (2013a); Shengbo & Cheng (2019). The primary focus of theoretical research in this field is the investigation of internal resonances, which play a fundamental role in generation of higher–order harmonics and mixing of guided waves. Practical aspects of these classical nonlinear effects related to damage detection are discussed in Matlack et al. (2014); Lissenden et al. (2015); Lissenden (2021).

The nonclassical nonlinear approaches in this field originate from the observation of various ultrasonic wave propagation phenomena in mesoscopic materials (e.g., rocks, polycrystals) Johnson & Shankland (1989); Johnson et al. (1996); Guyer & Johnson (1999). These work have been extended to nonclassical, contact–type interactions between ultrasonic waves and defects in various materials (e.g., cracks in metals or delamination in composites) Meo & Zumpano (2005); Aymerich & Staszewski (2010b,a). The studies on the nonclassical nonlinear phenomena in mesoscopic materials comprise sub–harmonic Moussatov et al. (2003) generation and slow dynamics effects Johnson & Shankland (1989); Johnson et al. (1996); Guyer & Johnson (1999); Gusev et al. (2009). In contrast, investigations of nonclassical nonlinear contact–type phenomena in damage detection applications concentrate mainly on nonlinear vibro–acoustic modulations Donskoy & Sutin (1998); Van Den Abeele et al. (2000); Solodov et al. (2002); Meo & Zumpano (2005); Klepka et al. (2011). In all these applications structural damage (e.g., fatigue cracks, micro–cracks, delamination, loose joints) is perturbed by relatively strong, Low–Frequency (LF) vibration and probed by weak High–Frequency (HF) ultrasonic excitation. Wave–damage interactions lead then to modulation of the HF wave by the LF wave. Extensive research conducted for the last 2–3 decades relates to theoretical modelling, numerical simulations, monitoring strategies and signal processing, as reviewed in Jhang (2009); Broda et al. (2014); Pieczonka et al. (2015). One of the most interesting developments in this field relates to the nonclassical modulation transfer phenomenon observed in Zaitsev et al. (2002a,b,

2006) and utilised for damage detection in Aymerich & Staszewski (2010a), as further discussed in Section 1.2.3.

In summary, there are still knowledge gaps concerning nonlinear phenomena related to shear horizontal guided waves. This includes the classical effect of third harmonic generation, for which in–depth investigation is still required to understand two important aspects i.e., how nonlinear material distorts excited shear horizontal guided waves and how the relevant dispersion relations are affected. Furthermore, it appears that the nonclassical, nonlinear modulation transfer effect has not been researched for shear horizontal wavefield. The research work undertaken and reported in this thesis is motivated by these gaps. In order to set up research objectives, more detailed reviews of the previous work related to the above mentioned two nonlinear classical and nonclassical effects is presented in the following sections.

1.2.2 Studies on higher harmonics generation for shear horizontal guided waves

Recent years have shown increased research attention to ultrasonic detection methods based on nonlinear physical phenomena. It is widely understood that these methods, while offering significant implementation challenges, exhibit enhanced sensitivity to early–stage, micro–structural defects Solodov (1998); Lissenden et al. (2015); Lissenden (2021). There are four fundamental primary sources of nonlinearities that can be observed in ultrasonic responses. These are:

- material properties – e.g., grain structure, inclusions leading to elastic and/or damping inherent nonlinearities;
- material defects – e.g., cracks in metals or delaminations in composites;
- structural assemblies leading to contact-type nonlinearities (e.g., due to friction);
- intrinsic effects resulting for example from the measurement chain (e.g., actuation, amplification).

The second source is of major interest to the NDT and SHM research communities. Nonlinear propagation of ultrasonic waves and the effect of higher harmonic generation have been the topic of theoretical investigations and practical implementations for material defect evaluation since the first research work in the early 1960s Breazeale & Thompson (1963); Breazeale & Ford (1965). Most research activities in this field have been concentrated on nonlinear bulk and surface waves Zarembo & Krasil'nikov (1971); Solodov (1998); Stepinski et al. (2013); Lissenden et al. (2015); Jhang et al. (2020a). More recently, research attention has focused on the study of nonlinear guided waves in plate–like structures. The impact of material nonlinearity on Lamb

wave propagation has been studied in–depth theoretically Deng (1999); Srivastava & Lanza di Scalea (2009); Sun et al. (2023), numerically Chillara & Lissenden (2014); Ong et al. (2017); Yang et al. (2019), and experimentally Herrmann et al. (2006); Deng et al. (2005); Matlack et al. (2011). All these investigations have provided insight into the physical mechanisms governing higher harmonic generation in propagating in hyperelastic media and demonstrated the potential of these waves for early damage detection. The theoretical description of physical process underlying the cumulative generation of second harmonics in nonlinear Lamb wave propagation has been provided in Deng (1999). In this work, the fundamental perturbation analysis – known as the straightforward expansion method Nayfeh (2011) – and the reciprocity relation Auld (1973) have been employed to establish synchronism conditions between the primary and secondary Lamb wave modes.

The interaction between Lamb waves and shear horizontal waves has also been studied using the analytical approach based on the fundamental perturbation technique in de Lima & Hamilton (2003); Liu et al. (2013b). These research investigations have revealed that the Lamb wave primary wavefield cannot lead to the generation of higher harmonics of shear horizontal guided waves in a semi–infinite hyperelastic medium. However, the research in Liu et al. (2013a); Shengbo & Cheng (2019) have demonstrated that the generation of the Lamb wave secondary wavefield by shear horizontal primary waves can be observed in a nonlinear elastic material. These studies have revealed how Lamb and shear horizontal waves can excite each other due to mutual interaction.

The theoretical investigations of nonlinear guided wave propagation given in the above publications show that approximated solutions (i.e., solutions based on the straightforward expansion perturbation technique Nayfeh (2011)) exhibit infinitely increasing amplitudes with wave propagation distance (due to secular terms in solution) for the synchronism condition between modes. This effect restricts the validity of approximated solutions to small values of time and distance of wave propagation. The approximated solutions for nonlinear wave propagation problems and selected variants of the perturbation method have been studied in Nayfeh & Mook (1979); Whitham (1999). Other variants of the perturbation technique, which eliminate secular terms in approximated solutions, have recently been applied to the study nonlinear guided wave propagation. The Lindstedt–Poincare technique has been used in Packo et al. (2016) to investigate the effect of nonlinear material parameters, excitation amplitude and frequency on the dispersion characteristics of nonlinear Lamb waves. The multiplescale method was used in Kanda & Sugiura (2021) to analyse the interaction between two Lamb wave modes propagating in nonlinear material in the presence of linear damping. The cyclic energy transfer between primary and secondary modes – observed with propagation distance – have been analytically predicted by the introduction of detuning parameter Nayfeh & Mook (1979).

In contrast to nonlinear Lamb waves, corresponding research on nonlinear shear horizontal wave propagation is limited. The cumulative second harmonic generation condition for nonlinear

shear horizontal modes have been studied in Mingxi (1998); Li et al. (2015); Lissenden (2021). These studies adopted the straightforward expansion perturbation technique for nonlinear elastodynamic governing equations and the traction boundary conditions. The mathematical problems from applying this perturbation have been solved using the partial wave technique, modal decomposition, and reciprocity relation Auld (1973). The potential of nonlinear shear horizontal wave propagation for early detection of material degradation has been discussed in Lissenden (2021). It appears that distortion of the primary wavefield due to material nonlinearity has not been investigated and is the major missing element in all previous work in the field.

1.2.3 Studies on the Luxembourg–Gorky effect for shear horizontal guided waves

The nonlinear interaction of electromagnetic waves was the source of the first observation of the nonclassical transfer of modulation between waves. In this interaction, modulations of powerful low–frequency radio waves were transferred to weaker high–frequency radio waves. This effect was observed in the cities of Luxembourg and Gorky (today Nizhny Novgorod) in the 1930s and reported in Tellegen (1933). The nonlinear cross modulation – now known as the Luxembourg–Gorky (L–G) effect – is of a nonlinear dissipative nature and was explained by fluctuations in the attenuation of ionospheric plasma Graffi (1936); Ginzburg & Gurevich (1960); Bailey (1965); Gurevich (1978); Layzer et al. (1965). Since many equivalent nonlinear phenomena exist in different fields of physics, an analogous effect was observed in optics, fluid mechanics and plasma physics, where electromagnetic (or elastic) waves propagating in plasma (or liquids with micro–bubbles) showed not only dissipation and scattering but also modulation transfer Ginzburg & Gurevich (1960); Bassanini (1974); Renaud et al. (2010); de Boer & Vester (2018). Interestingly, these modulation transfers have often not been called the L–G effect but have also been attributed to the nonlinear dissipation mechanism.

The nonkinetic and kinetic theories of plasma physics have provided explanations for the L–G effect for radio waves. This includes the first physical explanation based on the theory of radio waves in the ionosphere and discharges in gases Bailey & Martyn (1934). Nonkinetic theories do not consider probability distributions for the velocities of the particles forming the plasma. The amplitude–modulated high–power radio waves lead to heating of plasma and the modulation of its temperature. This results in modulation of the effective collision frequency between electrons and molecules and provides attenuation and modulation of weak radio waves. The elementary nonlinear theory of propagation of radio waves in the plasma is sufficient to explain the modulation transfer. An overview of developments in the theory of ionospheric radio waves is given in Huxley & Ratcliffe (1949).

In contrast to the nonkinetic approach, the electron–molecule collision is described by the Boltzmann collision integral in the kinetic approach used for the L–G effect explanation. The amplitude–modulated strong radio waves induce modulation of electron velocity distribution, leading to the modulation transfer to weak radio waves. These two theories rely on nonlinear dissipation to explain the original L–G effect for radio waves.

The nonclassical nonlinear modulation transfer phenomenon was also observed for ultrasonic waves propagating in glass Zaitsev et al. (2002a), and claimed as the elastic equivalent of the original L–G effect. In this work, a cracked glass rod was subjected to two ultrasonic wave excitations i.e., the low–frequency amplitude–modulated wave (named as the "pumping" wave) and the high–frequency wave of constant amplitude (named as the "probing" wave. Remarkably, for very small strain levels – that were insufficient to perturb the entire crack – the amplitude modulation of the first wave was transferred to the second wave. This effect was later adapted for crack detection in glass Zaitsev et al. (2002a,b), fatigue crack detection in aluminium Gusev et al. (2009) and delamination detection in composites Aymerich & Staszewski (2010a).

It is important to underline that the classical nonlinear wave mixing approach Jones & Kobett (1963); Akgün & Demiray (2001) – used for instance in Non–Destructive Evaluation (NDE) Croxford et al. (2009); Ju et al. (2019); Shan et al. (2024) – differs in nature from the nonlinear nonclassical modulation transfer effect observed for electromagnetic and elastic waves. The former is inherently based on the classical theory of nonlinear wave mixing developed in the 1960s and 1970s and relates to nonlinear elastic properties of media. In contrast, the L–G effect relates to nonclassical nonlinear dissipation, as explained in Graffi (1936); Ginzburg (1948); Bailey (1965) for electromagnetic waves and in Layzer et al. (1965); Renaud et al. (2010) for fluid–bubble interactions. In plasma, an external alternating electric field generates a flow of charged particles. These moving particles are responsible for the attenuation of electromagnetic waves. In fluids, bubbles are coupled to the flow and act as soft oscillators that attenuate propagating waves. In both cases, the nonlinear dissipation modulates the propagating waves and is a distributed or local nonlinearity.

The acoustic equivalent of the L–G effect observed in Zaitsev et al. (2002b) has not been yet fully explained. However, theoretical considerations in Zaitsev et al. (2002a, 2005); Gusev et al. (2009); Aymerich & Staszewski (2010b) indicate that this effect could be explained by local nonlinearity associated with crack–wave interaction. Most local crack–wave interaction models rely on nonlinear elastic behaviour, as reviewed in Broda et al. (2014). The well–known vibroacoustic modulation technique employed for damage detection adopts nonlinear contact–type elastic crack–wave interaction models (e.g., classical nonlinear elasticity, bilinear stiffness, breathing cracks and clapping contacts, hysteresis, Hertzian contact, rough–surfaces contact, nonlinear dissipation, thermoelasticity) to explain the modulation mechanism, as reviewed in Pieczonka et al. (2015). However, the L–G effect resulting from the crack–wave

interaction exhibits nonclassical behaviour. With the increasing amplitude of the low–frequency wave, the amplitude of the high–frequency is attenuated but its frequency is not shifted, as demonstrated in Zaitsev et al. (2002a). Therefore, dissipation involved cannot be explained using classical frictional and hysteretic models. Internal contacts of crack asperities – caused by the ultrasonic "pumping" wave, lead to dissipation of the ultrasonic "probing" wave. Some simplified asymptotic formulas for the local nonlinear thermoelastic losses have been provided in Zaitsev et al. (2002a) to explain this nonclassical behaviour.

Research work of Savage (1966); Landau & Lifshitz (1989); Mayer (1990); Guyer & Johnson (1999) discusses various models used in seismology to explain elastic wave dissipation i.e., wave–induced temperature gradient and dissipation in polycrystalline materials. These models support the explanation given in Zaitsev et al. (2002a,b, 2005). Moreover, damping in polycrystalline materials often utilises complex models commonly used in viscoelastic materials. For example, the Kelvin–Voigt model has been previously used for crack modelling in seismology Min & Vo-Dai (2008). However, the nonlinearity in these models can only be attributed to elastic behaviour and therefore can not be used to explain the acoustic equivalent of the L–G phenomenon.

To conclude, the significant enhancement of nonlinear damping of ultrasonic waves has been postulated to explain the acoustic equivalent of the L–G effect observed in a cracked solid. The experimental evidence confirms the proposed hypothesis and shows that nonlinear dissipation rather than nonlinear elasticity, is behind this effect. In addition, experimental investigations in Klepka et al. (2011) demonstrate a unique link between nonlinear modulations and dissipation. Therefore, if nonlinear dissipation is behind this nonlinear crack–wave effect, the question arises as to what attenuation mechanism is involved. Relatively limited research work in this field indicates that better physical understanding and theoretical explanation of the acoustic equivalent of the L–G effect is needed.

1.3 Dissertation aims and objectives

The presented literature review discusses and identifies two enthralling nonlinear phenomena associated with ultrasonic wave propagation that require further research investigations. These are the classical higher harmonic generation and the nonclassical modulation transfer known as the acoustic equivalent of the L–G effect. The former relates to wave interaction with nonlinear material (distributed nonlinearity) and has been previously investigated to some extend for shear horizontal waves. The latter is associated with crack–wave interaction (local nonlinearity), has not been fully explained and never investigated for shear horizontal waves. Research investigations presented in the thesis aims to extend the work on these nonlinear phenomena. The major focus is on theoretical modelling and numerical simulations that can provide not only better physical

explanation but also lay down fundamental understanding that will underpin damage detection applications. In order to fulfil this objective two main research hypotheses are formulated. These are:

- The concept of nonlinear modes – previously formulated for vibration of nonlinear discrete and continuous mechanical systems – may be extended to encompass propagation of multi–modal and dispersive shear horizontal guided waves in solids that can be described by a hyperelastic material model.

- A local nonclassical, nonlinear dissipation model can be formulated for material damage to explain the L–G effect – i.e., the nonclassical, nonlinear modulation transfer – for shear horizontal waves.

The scope of work required to support the formulated hypotheses can be outlined as follows.

Theoretical and numerical analyses of the aforementioned nonlinear phenomena will be provided. As a result, the nonlinear shear wave propagation theory will be extended to offer a relevant wave propagation distributed model and damage–wave interaction local model of nonlinearity. In addition, powerful numerical simulation tools for nonlinear shear wave propagation will be developed.

The major focus will be on analytical and numerical modelling techniques. However, experimental validation will be also provided. The objective is to gain a deeper understanding of fundamental physics and to explore the potential feasibility of using nonlinear shear horizontal guided waves for practical applications.

Thus, the research programme aims to achieve the following objectives:

- Provide a fundamental understanding based on analytical calculations of the propagation phenomenon of nonlinear shear horizontal guided waves, including the generation of higer–order harmonics and the L–G effect.

- Use the perturbation method to analyse nonlinear models with both local and distributed nonlinearities.

- Use the multiplescale variant of the perturbation method to obtain approximations to exact solutions, allowing broader observations and conclusions.

- Development of a numerical tool based on the Local Interaction Simulation Approach (LISA) method to model the propagation of shear horizontal guided waves in a nonlinear material and their interaction with a local nonlinear region.

- Demonstrate the occurrence of phenomena not yet described in the literature for shear horizontal guided waves through experimental work.

1.4 Structure of the thesis

This dissertation consists of seven chapters. The overview of the remaining chapters is provided below.

Chapter 2 provides a comprehensive theoretical overview of the wave propagation phenomenon in solid media. It begins by defining the fundamental assumptions for the conducted calculations and describing utilised in this work Lagrange's description of deformable media. The chapter presents the selected measures of stress and strain fields and the derivation of the equations that govern the dynamics of continuous solid media. Furthermore, the investigation includes a detailed analysis of linear shear horizontal guided waves within elastic media.

Chapter 3 presents the analytical analysis of the interaction between small–amplitude shear horizontal guided waves and a nonlinear elastic material described using the Landau–Lifshitz hyperelasticity model. The study employs the multiplescale perturbation method to investigate interresonance between particular modes of the shear horizontal guided wave. Moreover, it demonstrates how the definition of nonlinear modes can be extended to the shear horizontal guided wave propagation.

Chapter 4 investigates analytically the acoustic equivalent of the L–G effect for shear horizontal guided waves. For the sake of completeness, it briefly describes the original L–G effect observed in radio waves and the theory developed to explain this phenomenon in the framework of electrodynamics. It is followed by the introduction of a nonlinear viscoelastic model characterising local defects in the solid medium. This model allows for the extension of the L–G effect to shear horizontal guided wave propagation and is consistent with established theories for the L–G effect for radio waves. Moreover, this chapter demonstrates the applicability of the introduced model for modelling nonlinear interactions in wave propagation and structural defects such as fatigue cracks.

Chapter 5 is divided into three main parts. The first part outlines the implementation of the LISA method for modelling nonlinear phenomena for shear horizontal guided waves. The second part validates the developed theory for the nonlinear interaction of shear horizontal guided waves and hyperelastic material through numerical simulations. The obtained numerical results confirm analytical results and exhibit the generation of higher harmonics and distortion of the shear horizontal guided wavefield. The third part presents the numerical simulations conducted for the L–G phenomenon for shear horizontal guided waves using the introduced nonlinear defect model. The obtained results confirm effective modulation transfer in the presence of local nonlinearity, thus validating the analytical findings.

Chapter 6 presents laboratory experiments on the L–G effect for shear horizontal waves. Laser vibrometry was used to measure the velocity response of the investigated specimens with shear horizontal waves generated using piezoelectric transducers. The amplitude spectra in the

frequency domain revealed the presence of the acoustic equivalent of the L-G effect. The analytical calculation and simulation results were confirmed by demonstrating efficient modulation transfer from higher to lower frequencies. In addition, the experimental determination of the dependence of the modulation index on the carrier frequencies was in agreement with analytical and numerical results.

Chapter 7 summarises research investigations presented in this dissertation. Conclusions are drawn and main contributions are highlighted. Furthermore, possible directions for future research are outlined.

Chapter 2

Elastic wave propagation – theoretical background

This chapter is an introduction to the fundamental theory of shear horizontal guided wave propagation in solid media. Basic kinematic relations used in the finite deformation solid mechanics are described. Furthermore, governing equations and boundary conditions for elastodynamics are discussed. Stress measures used in solid mechanics are also outlined. This includes formulas adopted in analytical and numerical investigations. The concepts presented are utilised to analyse elastic wave propagation in an unbounded linear solid. The definition of guided waves in mechanical systems is also given, with particular focus on shear horizontal guided waves. The chapter concludes with the theoretical analysis of linear shear horizontal guided waves propagation.

2.1 The basics and assumptions

This dissertation presents analytical calculations for physical systems observed in a three–dimensional (3–D) Euclidean space. The observation time is defined using a set of real numbers. Furthermore, the Cartesian coordinate systems are used to describe and analyse investigated wave propagation phenomena. Therefore, no distinction is made in this work between covariant and contravariant coordinates.

Mechanical systems considered in this work were assumed to consist of deformable solids. A model of a continuous medium – 3–D differential manifold – was used to describe such systems. Thus, deformable bodies studied can be associated with a subset of 3–D Euclidean space for which a continuous and differentiable function can be defined at each point.

In this work, the concept of “particle” will only be used as a convenient expression to provide physical interpretation of abstract mathematical object such as a point. In the context of the adopted model of 3–D deformable body, the assumption is that a set of particles forming an elastic body

is uncountably infinite. Moreover, infinite particles always fill this volume in the space between any two close particles. Therefore, a continuous medium (also called a continuum) is investigated. These properties arise from the assumption that the assumed size of particle is infinitesimal i.e., infinitely small.

In continuum mechanics, two fundamental approaches can be used to describe motion of deformable solids. These are the Lagrangian (or material) and Eulerian (or spatial) methods. The Lagrangian description uses coordinates of material point or particle in its reference (undeformed) configuration. In contrast, the Eulerian description adopts coordinates of particles using its current (deformed) position, as independent variables. In both approaches, time is an independent variable Achenbach (1973); Miklowitz (1978); Ogden (1997); Truesdell & Noll (2004).

The mathematical descriptions of physical systems based on the Lagrangian and Eulerian approaches – which enable modelling deformable continuous media such as fluids and solids – are equivalent Ogden (1997); Truesdell & Noll (2004). The choice of a particular description depends on the nature of physical phenomena investigated. It is convenient to use the Lagrange description to analyse phenomena associated with vibration of individual particles of solids, such as vibration of continuous systems or wave propagation in solids. This approach involves identifying a reference configuration corresponding to a static equilibrium state, at the beginning of analytical modelling. Then, the position of each particle of the body resulting from the action of external forces and the dynamic of the system is determined for a selected time value i.e., in the present configuration. Material properties of the continuum and other quantities characterising the mechanical system are expressed as functions of coordinates of particles in the reference state. Furthermore, all physical fields resulting from these calculations – such as position field of particles of the analysed medium (current configuration of the body), relevant displacements, velocities, accelerations, strain fields, strain rates and stresses – are also functions of these coordinates. Moreover, it is worth noting that boundary conditions for systems described in such a way are defined on boundaries explicitly described by reference coordinates Morse & Ingard (1986); Truesdell & Noll (2004); Lai et al. (2010).The above discussion justifies using the Lagrange description in the work presented, to analyse shear horizontal guided wave propagation in a solid.

In contrast, the Eulerian approach is suitable for studying fluid motion phenomena. It is because physical fields that characterise fluid are investigated with respect to their current positions i.e., the region the analysed medium occupies as a consequence of its motion. Therefore, it is natural to take coordinates of the current configuration as independent variables. Furthermore, using these coordinates enables one defining boundary conditions on a boundary explicitly described by the current coordinates. Further reading in this area can utilise vast literature on the subject e.g., Morse & Ingard (1986); Truesdell & Noll (2004); Lai et al. (2010); Rao (2011).

2.2 Fundamentals of deformation kinematics

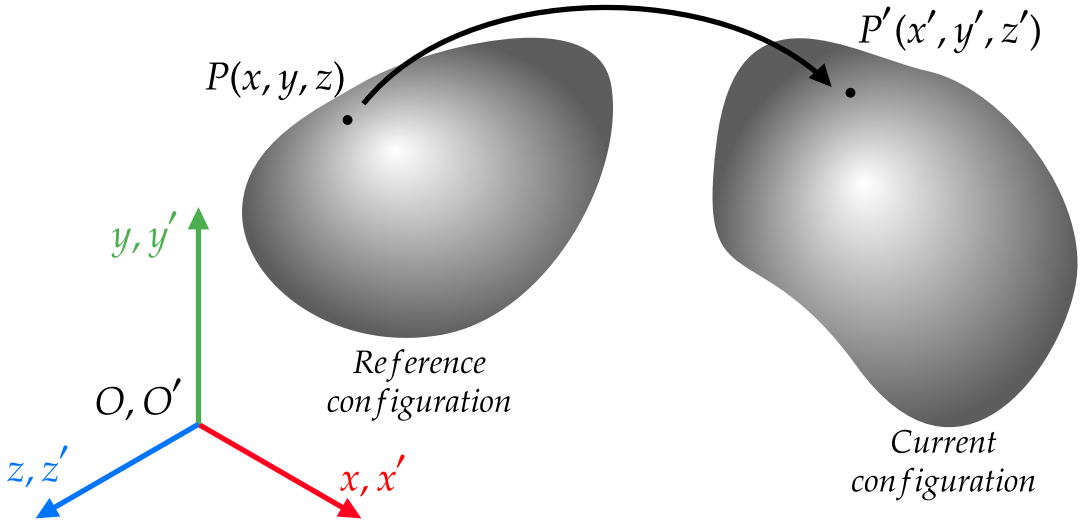

Figure 2.1: Reference and current configurations for a finite deformation problem. Aligned origins and unit vectors are assumed in calculations.

Figure 2.1 illustrates two body configurations and coordinate frames used to describe them. Generally, the origins and unit vectors for such Cartesian coordinate system introduced do not have to coincide. However, in this work the origin and axes of both material coordinate systems are aligned to facilitate calculations. It is important to note that despite this assumption, the referenced and current systems analysed are different and should be distinguished.

The Cartesian coordinates x, y, and z correspond to the points of the analysed body before deformation i.e., in the reference configuration. The coordinates of the points of the deformed solid – i.e., in the current configuration – are denoted by x', y' and z'. Thus, it is possible to define the position vectors for each particle in both – i.e., the reference and current – configurations as follows

$$\boldsymbol{r} = \boldsymbol{i}x + \boldsymbol{j}y + \boldsymbol{k}z, \tag{2.1}$$

$$\boldsymbol{r'} = \boldsymbol{i'}x' + \boldsymbol{j'}y' + \boldsymbol{k'}z', \tag{2.2}$$

where $\boldsymbol{i}$, $\boldsymbol{j}$, $\boldsymbol{k}$, $\boldsymbol{i'}$, $\boldsymbol{j'}$ and $\boldsymbol{k'}$ are unit base vectors. In the work presented, vectors and tensors of higher orders are described using bold fonts. Vectors are first–order tensors and can be represented as column matrices with elements that correspond to the components of vectors in the adopted coordinate system. Thus, one can write $\boldsymbol{r} = [x, y, z]^T$ and $\boldsymbol{r'} = [x', y', z']^T$ for the coordinate frames corresponding to the reference and current configurations, respectively.

In general, it is essential to distinguish between the two orthogonal vector bases introduced. The transformation of components of any vector between the adopted Cartesian coordinate systems is

defined by the $\boldsymbol{R}$ second–order two–point tensors known as a shifter in literature Eringen (1974); Narasimhan (1993); Zienkiewicz & Taylor (2013). The components of the $\boldsymbol{R}$ tensor are equal to the scalar products of individual versors that form the orthonormal bases of the introduced rectangular coordinate systems.

In this work, coinciding principal directions of Cartesian coordinate frames are assumed. If the versors of the adopted coordinate systems align, the transformation of the components of any vector from one coordinate system to the other system is trivial. Namely, the $\boldsymbol{R}$ shifter is equal to the second–order identity tensor $\boldsymbol{I}$. This results from the values of the scalar products i.e., $\boldsymbol{i} \cdot \boldsymbol{i'} = 1$, $\boldsymbol{j} \cdot \boldsymbol{j'} = 1$ and $\boldsymbol{k} \cdot \boldsymbol{k'} = 1$.

Determining mapping – or in other words transformation between the $\boldsymbol{r}$ and $\boldsymbol{r'}$ position vectors – is a fundamental problem in elastodynamics. In general, this mapping can be expressed as

$$\boldsymbol{r'} = \boldsymbol{\chi}(\boldsymbol{r}, t). \tag{2.3}$$

In this notation, the components of the $\boldsymbol{\chi}(\boldsymbol{r})$ vector–valued function can be written as

$$x' = \chi_{x'}(x, y, z, t), \tag{2.4}$$

$$y' = \chi_{y'}(x, y, z, t), \tag{2.5}$$

$$z' = \chi_{z'}(x, y, z, t). \tag{2.6}$$

To ensure that the $\boldsymbol{\chi}(\boldsymbol{r}, t)$ mapping between the reference and current configurations remains continuous and bijective, the J Jacobian of this transformation must be nonzero and strictly positive. This quantity is equal to the $\det[\boldsymbol{F}]$ determinant of the deformation gradient tensor that is a second–order tensor and represents the fundamental measure of deformation. It is defined as

$$\boldsymbol{F} = \nabla \boldsymbol{r'}(\boldsymbol{r}), \tag{2.7}$$

where ∇ is the nabla differential operator with respect to the x, y and z Lagrangian coordinates. By assuming that the Jacobian fulfils inequality $J > 0$, it is possible to determine the $\boldsymbol{\chi}^{-1}(\boldsymbol{r'})$ inverse mapping uniquely.

It is a well–known that any tensor of second–order can be represented by a quadratic matrix composed of its components Ogden (1997); Zienkiewicz & Taylor (2013). Therefore, the $\boldsymbol{F}$ tensor can be represented in a matrix form as

$$\boldsymbol{F} = \begin{bmatrix} \frac{\partial x'}{\partial x} & \frac{\partial x'}{\partial y} & \frac{\partial x'}{\partial z} \\ \frac{\partial y'}{\partial x} & \frac{\partial y'}{\partial y} & \frac{\partial y'}{\partial z} \\ \frac{\partial z'}{\partial x} & \frac{\partial z'}{\partial y} & \frac{\partial z'}{\partial z}. \end{bmatrix} \tag{2.8}$$

The $\boldsymbol{F}$ deformation gradient is a nonsymmetric second–order tensor; more precisely it is a two–point tensor since it refers simultaneously to the reference and current configurations Eringen (1974); Truesdell & Noll (2004).

A change in geometry of solid occurs as a consequence of displacement of its particles. The $\boldsymbol{F}$ deformation gradient allows one determining the relation between the differential line element in the reference and current configurations. This relationship can be expressed as

$$d\boldsymbol{r} = \boldsymbol{F} d\boldsymbol{r}'. \tag{2.9}$$

The individual components of differential line elements can be written as

$$dx' = \frac{\partial x'}{\partial x}dx + \frac{\partial x'}{\partial y}dy + \frac{\partial x'}{\partial z}dz, \tag{2.10}$$

$$dy' = \frac{\partial x'}{\partial x}dx + \frac{\partial x'}{\partial y}dy + \frac{\partial x'}{\partial z}dz, \tag{2.11}$$

$$dz' = \frac{\partial x'}{\partial x}dx + \frac{\partial x'}{\partial y}dy + \frac{\partial x'}{\partial z}dz. \tag{2.12}$$

Moreover, the relationships between the differential surfaces for the considered configurations are also based on the definition of the $\boldsymbol{F}$ tensor. This formula is known in the literature as the Nanson's relation Ogden (1997); Truesdell & Noll (2004) and can be written as

$$\boldsymbol{n}' dA' = J \left(\boldsymbol{F}^{-1}\right)^T \boldsymbol{n} dA, \tag{2.13}$$

where $\boldsymbol{n}'$ and $\boldsymbol{n}$ are normal vectors to differential surfaces in the current and reference configurations, respectively.

Furthermore, it is possible to determine the relation between the differential volume based on the $\boldsymbol{F}$ tensor in the reference and the current configurations, according to the following relation

$$dV' = JdV. \tag{2.14}$$

Only positions of particles of the continuous medium in both the reference and current configurations have been discussed until now. Based on the definitions introduced, the vector displacement field can be defined as $\boldsymbol{u} = \boldsymbol{i}u + \boldsymbol{j}v + \boldsymbol{k}w$ (or in a matrix form as $\boldsymbol{u} = [u, v, w]^T$). The vector displacement is a crucial quantity in mechanics of deformable solids and can defined as

$$\boldsymbol{u}(\boldsymbol{r}, t) = \boldsymbol{r'}(\boldsymbol{r}, t) - \boldsymbol{r}. \tag{2.15}$$

The governing partial differential equations and boundary conditions for elastodynamics will be defined for this field. Based on it, other physical fields will be defined i.e., strain, strain rated and stress tensors. Upon substitution of Eq. (2.15) into Eq. (2.7), the $\boldsymbol{F}$ deformation gradient can be rewritten as

$$\boldsymbol{F} = \boldsymbol{R} + \nabla \boldsymbol{u} = \boldsymbol{I} + \nabla \boldsymbol{u}, \tag{2.16}$$

where the use of the R tensor in notation is purely formal from a mathematical viewpoint but reveals the general theory. The $\boldsymbol{F}$ deformation gradient can be also written in a matrix form as

$$\boldsymbol{F} = \begin{bmatrix} 1+\frac{\partial u}{\partial x} & \frac{\partial u}{\partial y} & \frac{\partial u}{\partial z} \\ \frac{\partial v}{\partial x} & 1+\frac{\partial v}{\partial y} & \frac{\partial v}{\partial z} \\ \frac{\partial w}{\partial x} & \frac{\partial w}{\partial y} & 1+\frac{\partial w}{\partial z}. \end{bmatrix} \tag{2.17}$$

Following the above description, governing partial differential equations and relevant boundary conditions for elastodynamics can be defined for the analysed field. Then other physical fields can be introduced i.e., strain, strain rates and stress tensors. The following section presents selected measures of stress and strain.

2.3 Measures of the strain field in the reference configuration

As previously discussed, the $\boldsymbol{F}$ deformation gradient tensor is a fundamental measure of deformation of solid medium. However, its direct use in equations leads to complications in calculations. Therefore, it is more suitable to introduce measures of deformation that refer only to coordinates corresponding to the reference or current configurations. For the assumed Lagrangian description, the right Cauchy–Green deformation tensor can be introduced as Eringen (1974); Zienkiewicz & Taylor (2013); Hackett (2016)

$$\boldsymbol{C} = \boldsymbol{F}^T \boldsymbol{F}. \tag{2.18}$$

It follows from the definition that this tensor is symmetric and its order is equal to two. The right Cauchy–Green tensor relates to the square of length of differential line elements in the current and reference configurations. Multiplication of the left and right sides of Eq. (2.9) by the relevant transpose vectors yields

$$d\boldsymbol{r'}^T d\boldsymbol{r'} = d\boldsymbol{r}^T \boldsymbol{C} d\boldsymbol{r}. \tag{2.19}$$

Another measure of strain is the Lagrange strain tensor. This second–order tensor defines the relationship between the change of the square of length of differential line elements in the reference and current configurations with differential line elements in the reference configuration. Following the definition of the squares of lengths of differential line elements in both configurations and Eq. (2.19), one can obtain

$$d\boldsymbol{r'}^T d\boldsymbol{r'} - d\boldsymbol{r}^T d\boldsymbol{r} = d\boldsymbol{r}^T \boldsymbol{C} d\boldsymbol{r} - d\boldsymbol{r}^T \boldsymbol{C} d\boldsymbol{r} = d\boldsymbol{r}^T (\boldsymbol{C} - \boldsymbol{I}) d\boldsymbol{r} = 2 d\boldsymbol{r}^T \boldsymbol{\varepsilon_{GL}} d\boldsymbol{r} \tag{2.20}$$

This equation defines the Green–Lagrange tensor, which is a symmetric second–order tensor. The Green–Lagrange tensor is commonly known as the finite strain tensor in the literature and can be given as Miklowitz (1978); Lai et al. (2010); Zienkiewicz & Taylor (2013); Żur et al. (2023)

$$\boldsymbol{\varepsilon_{GL}} = \frac{1}{2}(\boldsymbol{C} - \boldsymbol{I}) = \frac{1}{2}\left(\nabla \boldsymbol{u} + (\nabla \boldsymbol{u})^T + (\nabla \boldsymbol{u})^T \nabla \boldsymbol{u}\right) \tag{2.21}$$

The exclusion of nonlinear terms in the above expression leads to the definition of the Cauchy strain tensor – also known as the infinitesimal strain tensor – used in linear analyses Achenbach (1973); Miklowitz (1978)

$$\boldsymbol{\varepsilon}_C = \frac{1}{2}\left(\nabla \boldsymbol{u} + (\nabla \boldsymbol{u})^T\right). \tag{2.22}$$

2.4 Measures of the stress field

In the previous subsections, the kinematic description of motion of a continuous solid has been considered. Forces that cause the relevant motion and deformation have not been investigated. Forces that act at any point of deformable body can be introduced through the concepts of body and surface forces. The body forces – such as those associated with gravity and electric, magnetic fields – act throughout a volume. In contrast, surface forces act on any surface of solid, including boundaries. These forces result from interactions between adjacent particles Miklowitz (1978); Nowacki (1986); Skalmierski (1991); Perzyna (1998); Lai et al. (2010).

The surface forces can be defined at each body point with respect to the Euler or Lagrangian coordinates. Therefore, differential forces acting on the differential surface of the body in the reference and current configurations can be defined. Differential forces depend on the orientation of the differential surface i.e., the normal vector associated with it. For the current configuration, the $d\boldsymbol{f'}$ differential force acting on the dA' differential surface with the $\boldsymbol{n'}$ normal vector can be defined as

$$d\boldsymbol{f'} = \boldsymbol{t'} dA', \tag{2.23}$$

where $\boldsymbol{t'}$ denotes the traction. Following the Cauchy's theorem – described and analysed in Miklowitz (1978); Ogden (1997); Lai et al. (2010) – the traction is equal to the linear transformation of the normal vector and can be expressed as

$$\boldsymbol{t'} = \boldsymbol{\sigma}_C \boldsymbol{n'}, \tag{2.24}$$

where $\boldsymbol{\sigma}_C$ is the Cauchy stress tensor. This tensor fully defines this transformation and is commonly referred to as the "true" stress tensor Ogden (1997); Lai et al. (2010); Hackett (2016).

For the analysis performed, it is necessary to consider a measure of traction and stress fields corresponding to the reference configuration of the body. This measure results from the adopted mathematical description of physical phenomena with respect to the Lagrangian coordinates. As result, the definition of the $d\boldsymbol{f'}$ differential force can be rewritten as

$$d\boldsymbol{f'} = \boldsymbol{t} dA, \tag{2.25}$$

where $\boldsymbol{t}$ denotes traction acting on the dA differential surface with the $\boldsymbol{n}$ normal vector for reference configuration of solid. The $\boldsymbol{t}$ traction measure according to Cauchy theory is a linear

transformation of the $\boldsymbol{n}$ normal vector and can be expressed as

$$\boldsymbol{t} = \boldsymbol{\sigma}_{\boldsymbol{PK}}^{\boldsymbol{I}} \boldsymbol{n}. \tag{2.26}$$

This transformation is fully defined by the two–point second order tensor $\boldsymbol{\sigma}_{\boldsymbol{PK}}^{\boldsymbol{I}}$ known in the literature as the first Piola–Kirchhoff stress tensor Perzyna (1998); Lai et al. (2010); Hackett (2016); Packo et al. (2019). This tensor allows one calculation of forces acting with respect to the current configuration of solid, based on the reference configuration. Therefore, the traction based on the first Piola–Kirchhoff stress tensor has the same direction as the traction based on the Cauchy stress tensor. The relationship between the $\boldsymbol{\sigma}_{\boldsymbol{C}}$ and $\boldsymbol{\sigma}_{\boldsymbol{PK}}^{\boldsymbol{I}}$ tensors can be obtained by using Eqs. (2.23) – (2.26) and the Nanson's formula (Eq. (2.13)) to give

$$\boldsymbol{\sigma}_{\boldsymbol{C}} = \frac{1}{J} \boldsymbol{\sigma}_{\boldsymbol{PK}}^{\boldsymbol{I}} \boldsymbol{F}^{T}. \tag{2.27}$$

Another important measure of stress, as a function of Lagrangian coordinates, is the $\boldsymbol{\sigma}_{\boldsymbol{PK}}^{\boldsymbol{II}}$ second Piola–Kirchhoff stress tensor. This tensor defines the linear transformation of the $\boldsymbol{n}$ normal vector to the differential surface in the reference state. The distinction from previously described stress measures results from the fact that the $\tilde{\boldsymbol{t}}$ traction corresponding to this stress tensor is associated with the reference configuration of the considered medium. This transformation yields

$$\tilde{\boldsymbol{t}} = \boldsymbol{\sigma}_{\boldsymbol{PK}}^{\boldsymbol{II}} \boldsymbol{n}. \tag{2.28}$$

Based on the above relationship, the differential force acting on a differential surface of the solid can be defined using the Cauchy principle, but this time in the reference state i.e.,

$$d\boldsymbol{f} = \tilde{\boldsymbol{t}} dA. \tag{2.29}$$

Utilising Eqs. (2.25) – (2.29) – and knowing from Eq. (2.9) how differentials of vector–valued functions transform between reference and current reference frames – the $\boldsymbol{\sigma}_{\boldsymbol{PK}}^{\boldsymbol{I}}$ and $\boldsymbol{\sigma}_{\boldsymbol{PK}}^{\boldsymbol{II}}$ stress tensors are related i.e.,

$$\boldsymbol{\sigma}_{\boldsymbol{PK}}^{\boldsymbol{I}} = \boldsymbol{F} \boldsymbol{\sigma}_{\boldsymbol{PK}}^{\boldsymbol{II}}. \tag{2.30}$$

There are different tensor measures of strain and stress field, as described in the previous subsections. Following these measures, the strain energy and power per volume of the deformed body can be determined. In order to achieve this, an appropriate strain and stress tensor pair – known as the conjugate pair in the literature Ogden (1997); Perzyna (1998); Lai et al. (2010); Hackett (2016) – has to be selected. For the $\boldsymbol{F}$ deformation tensor and the $\boldsymbol{\varepsilon}_{\boldsymbol{GL}}$ Green–Lagrange strain tensor – that are functions of Lagrangian coordinates – the $\boldsymbol{\sigma}_{\boldsymbol{PK}}^{\boldsymbol{I}}$ first and $\boldsymbol{\sigma}_{\boldsymbol{PK}}^{\boldsymbol{II}}$ second Piola–Kirchhoff tensors are the conjugate stress tensors, respectively. Following the definitions of these strain, stress and strain energy density one obtains Achenbach (1973); Landau & Lifshitz (1989); Miklowitz (1978); Hackett (2016)

$$dU = \boldsymbol{\sigma}_{\boldsymbol{PK}}^{\boldsymbol{I}} : d\boldsymbol{F} = \boldsymbol{\sigma}_{\boldsymbol{PK}}^{\boldsymbol{II}} : d\boldsymbol{\varepsilon}_{\boldsymbol{GL}}, \tag{2.31}$$

where the ":" symbol denotes the inner tensor product. The particular role in the theory of hyperelastic material models pays the conjugate pair consisting of the $\boldsymbol{\varepsilon_{GL}}$ Green–Lagrange strain tensor and the $\boldsymbol{\sigma_{PK}^{II}}$ second Piola–Kirchhoff stress tensor Ogden (1997); Lai et al. (2010).

2.5 Governing equations and boundary conditions in elastodynamics in Lagrangian description

Derivation of the governing dynamic equations for continuous mechanical systems in the Lagrangian description requires the application of the principle of conservation of the linear momentum and the rotational momentum for the arbitrarily selected V volume and the corresponding ∂V boundary surface in the assumed reference state. Following the definitions and relationships presented in the previous subsections, the linear momentum balance equation for the reference configuration can be written as

$$\frac{\partial}{\partial t}\int_V \rho \frac{\partial \boldsymbol{u}}{\partial t} dV = \int_{\partial V} \boldsymbol{\sigma_{PK}^{I}} \boldsymbol{n} dA + \int_V \tilde{\boldsymbol{F}} dV, \tag{2.32}$$

where ρ and $\tilde{\boldsymbol{F}}$ denote the density of the solid medium in the undeformed state and the body force field, respectively. All physical fields incorporated in this equation depend on t time and x, y, z Lagrangian coordinates. Therefore, this relationship is referred to as the Lagrangian equation of motion, although forces involved correspond to the current state of the continuous system Ogden (1997). For abbreviation, the mentioned independent variables are omitted in the mathematical notation.

Upon application of the divergence theorem (i.e., the Gauss–Ostrogradsky theorem) for the surface integral in Eq. (2.32), one can rewrite Eq. (2.32) as Miklowitz (1978); Nowacki (1986); Skalmierski (1991); Ogden (1997); Chadwick (1999)

$$\int_V \left(\rho \frac{\partial^2 \boldsymbol{u}}{\partial t^2} - \nabla \boldsymbol{\sigma_{PK}^{I}} - \tilde{\boldsymbol{F}} \right) dV = \boldsymbol{0}. \tag{2.33}$$

Thus, the elastodynamics field equation can be formulated as

$$\rho \frac{\partial^2 \boldsymbol{u}}{\partial t^2} = \nabla \boldsymbol{\sigma_{PK}^{I}} + \tilde{\boldsymbol{F}}. \tag{2.34}$$

This equation is known in the literature as the Navier equation or the Cauchy's first law of motion Skalmierski (1991); Ogden (1997); Perzyna (1998); Chadwick (1999); Giurgiutiu (2008); Żak (2024).

The rotational momentum balance principle needs to be considered in the entire analysis, as mentioned earlier. This principle can be written as

$$\frac{\partial}{\partial t}\int_V \rho(\boldsymbol{u}+\boldsymbol{r}-\boldsymbol{r_0}) \times \frac{\partial \boldsymbol{u}}{\partial t} dV = \int_{\partial V} (\boldsymbol{u}+\boldsymbol{r}-\boldsymbol{r_0}) \times (\boldsymbol{\sigma_{PK}^{I}} \boldsymbol{n}) dA + \int_V (\boldsymbol{u}+\boldsymbol{r}-\boldsymbol{r_0}) \times \tilde{\boldsymbol{F}} dV, \tag{2.35}$$

with respect to a arbitrarily selected point, defined by the $\boldsymbol{r_0}$ position vector in the reference state. Grouping the terms in Eq. (2.35) and substituting Eq. (2.34) gives the balance of rotational momentum in the form

$$\int_V (\boldsymbol{u} + \boldsymbol{r} - \boldsymbol{r_0}) \times \nabla \boldsymbol{\sigma^I_{PK}} dV = \int_{\partial V} (\boldsymbol{u} + \boldsymbol{r} - \boldsymbol{r_0}) \times (\boldsymbol{\sigma^I_{PK}} \boldsymbol{n}) dA. \tag{2.36}$$

Eq. (2.36) can be expressed in an equivalent tensor form by replacing the vector products with the skew–symmetric tensors Ogden (1997); Chadwick (1999). This approach leads to the simplification of calculation and gives

$$\begin{aligned} &\int_V \left((\boldsymbol{u} + \boldsymbol{r} - \boldsymbol{r_0}) \otimes \nabla \boldsymbol{\sigma^I_{PK}} - \nabla \boldsymbol{\sigma^I_{PK}} \otimes (\boldsymbol{u} + \boldsymbol{r} - \boldsymbol{r_0}) \right) dV = \\ &\int_{\partial V} \left((\boldsymbol{u} + \boldsymbol{r} - \boldsymbol{r_0}) \otimes (\boldsymbol{\sigma^I_{PK}} \boldsymbol{n}) - (\boldsymbol{\sigma^I_{PK}} \boldsymbol{n}) \otimes (\boldsymbol{u} + \boldsymbol{r} - \boldsymbol{r_0}) \right) dA, \end{aligned} \tag{2.37}$$

where "$\otimes$" represents the tensor product. One can deduce that the vectors resulting from the vector products in Eq. (2.36) are the axial vectors of the skew–symmetric tensors in Eq. (2.37) Ogden (1997); Chadwick (1999). The application of the divergence theorem for surface integrals Ogden (1997) yields

$$\int_{\partial V} \left(\boldsymbol{F} \boldsymbol{\sigma^I_{PK}} - \left(\boldsymbol{F} \boldsymbol{\sigma^I_{PK}} \right)^T \right) dV = 0. \tag{2.38}$$

It follows from the above equation that

$$\boldsymbol{F} \boldsymbol{\sigma^I_{PK}} = (\boldsymbol{F} \boldsymbol{\sigma^I_{PK}})^T. \tag{2.39}$$

The above relationship is named in the literature as the second Cauchy's law of motion Ogden (1997); Chadwick (1999). Eq. (2.39) shows that the $\boldsymbol{\sigma^I_{PK}}$ first Piola–Kirchhoff stress tensor is a nonsymmetric tensor.

The Eqs. (2.34) and (2.39) can be rewritten upon substitution of Eq. (2.30) and incorporating the $\boldsymbol{\sigma^{II}_{PK}}$ second Piola–Kirchhoff stress tensor as

$$\rho \frac{\partial^2 \boldsymbol{u}}{\partial t^2} = \nabla \left(\boldsymbol{F} \boldsymbol{\sigma^{II}_{PK}} \right) + \tilde{\boldsymbol{F}}. \tag{2.40}$$

$$\boldsymbol{\sigma^{II}_{PK}} = (\boldsymbol{\sigma^{II}_{PK}})^T \tag{2.41}$$

This time the symmetric property of the $\boldsymbol{\sigma^{II}_{PK}}$ second Piola–Kirchhoff tensor can be deduced from Eq. (2.41).

The derived governing equations are sufficient to investigate the dynamics of infinite continuous mechanical systems. However, analytical analysis of bounded media requires the formulation of boundary conditions. The fundamental boundary conditions for a continuum body comprise of two types i.e., displacement boundary conditions and traction boundary conditions Zienkiewicz & Taylor (2013); Żak (2024). Mixed boundary conditions result from the

combination of the two previously mentioned types. Displacement boundary condition can be express as a requirement at each point on the $\partial\Gamma_u$ displacement boundary

$$\boldsymbol{u} = \bar{\boldsymbol{u}}, \tag{2.42}$$

where $\bar{\boldsymbol{u}}$ is arbitrarily assumed vector–valued function. The second type of boundary condition is a traction boundary condition that can be expressed as a requirement at each point on the $\partial\Gamma_t$ traction boundary i.e.,

$$\boldsymbol{\sigma}^{\boldsymbol{I}}_{\boldsymbol{PK}}\boldsymbol{n} = \boldsymbol{F}\boldsymbol{\sigma}^{\boldsymbol{II}}_{\boldsymbol{PK}}\boldsymbol{n} = \bar{\boldsymbol{t}}, \tag{2.43}$$

where $\bar{\boldsymbol{t}}$ is arbitrarily assumed vector–valued function. In general the assumed boundary condition may be nonlinear.

For the analysis of linear solid media under infinitesimal deformation, the Lagrangian and Eulerian descriptions coalesce Sokolnikoff (1956). Furthermore, all stress measures are equal, and the Cauchy strain tensor is used as a measure of the strain field Miklowitz (1978); Zienkiewicz & Taylor (2013). However, it is necessary to distinguish between the reference and current configurations to study wave propagation in nonlinear solid media. Therefore, an adequate mathematical description – based on the Lagrangian or Eulerian description – must be adapted even for small but finite displacements of solid particles. Nevertheless, the stress measures used in this dissertation, which are functions of Lagrange coordinates, are approximately equal Packo et al. (2019). This conclusion can be expressed as

$$\boldsymbol{\sigma}^{\boldsymbol{I}}_{\boldsymbol{PK}} = (\boldsymbol{I} + \nabla\boldsymbol{u})\boldsymbol{\sigma}^{\boldsymbol{II}}_{\boldsymbol{PK}} \simeq \boldsymbol{\sigma}^{\boldsymbol{II}}_{\boldsymbol{PK}}. \tag{2.44}$$

The symmetry of the second Piola–Kirchhoff tensor facilitates analytical and numerical calculations. Therefore, in this work, this tensor is adopted as a measure of the stress field in the solid material, keeping in mind that such simplification is valid only for small displacement amplitude of the particles forming the continuous medium i.e., for the micrometre scale. Nevertheless, for formal reasons, nonlinear components must be retained in the definition of strains, to be consistent with the higher–order terms in the constitutive equation in the definition of stresses. A detailed analysis of this type of simplification can be found in Packo et al. (2019). Based on this assumption, the simplified governing dynamic equation for a continuous mechanical system can eventually be written as

$$\rho\frac{\partial^2\boldsymbol{u}}{\partial t^2} = \nabla\boldsymbol{\sigma}^{\boldsymbol{II}}_{\boldsymbol{PK}} + \tilde{\boldsymbol{F}}. \tag{2.45}$$

Furthermore, the traction boundary conditions from Eq. (2.43) may be reduced as follows

$$\boldsymbol{\sigma}^{\boldsymbol{II}}_{\boldsymbol{PK}}\boldsymbol{n} = \bar{\boldsymbol{t}}, \tag{2.46}$$

The second Piola–Kirchhoff stress tensor in the nonlinear analyses presented in this work herein will be denoted by $\boldsymbol{\sigma}$ for brevity.

The presented equations, which describe continuous mechanical systems, need to be supplemented by constitutive equations between deformations and stresses. Together with the partial differential equations and boundary conditions described above and the geometrical definition of strains, they form a complete mathematical problem in which the displacement field is unknown, and all other fields result from it, except body forces. In the case of inelastic phenomena, this dependence is expressed as integral or differential equations (see Appendix B). In contrast, hyperelastic phenomena can be expressed as polynomial functions of many variables that are components of the strain tensor.

The investigation of transient solutions requires initial conditions. These conditions describe the state of a body at the t_0 initial time of an analysis at each point in the body. The kinematic initial conditions are specified as

$$\boldsymbol{u} = \boldsymbol{v}_{t_0}, \text{ for } t = t_0, \tag{2.47}$$

$$\frac{\partial \boldsymbol{u}}{\partial t} = \Upsilon_{t_0}, \text{ for } t = t_0, \tag{2.48}$$

and initial conditions for stresses are given by

$$\boldsymbol{\sigma} = \boldsymbol{\Sigma}_{t_0}, \text{ for } t = t_0. \tag{2.49}$$

It is not necessary to define the initial conditions for analyses of steady–state time–space harmonic solutions.

2.6 Linear bulk elastic waves

This section provides the fundamentals of the linear elastic wave propagation theory. For such analysis, stress measures and traction coalesce Sokolnikoff (1956); Miklowitz (1978). Moreover, the Cauchy strain tensor is used to measure the strain field.

For continuous linear deformable solid medium, the general relationship between the $\boldsymbol{\sigma}$ stress tensor and the $\boldsymbol{\varepsilon_C}$ Cauchy strain tensor is given by

$$\boldsymbol{\sigma}(t) = \int_{-\infty}^{t} \boldsymbol{G}(t-\tau) : \frac{\partial \boldsymbol{\varepsilon_C}(\tau)}{\partial \tau} d\tau, \tag{2.50}$$

where $\boldsymbol{G}$ denotes the fourth order tensor, whose components are relaxations functions. The works in Christensen (2012); Findley et al. (1989); Carcione (2022) provide a detailed analysis of the relaxation functions, their definitions and mathematical properties. Mathematical form of relaxation function depends on assumed viscoelastic material models. The relationship analysed is a convolution integral. The upper limit of integration is determined by the fact that the relaxation functions are zero for negative arguments. The lower limit of integration is assumed generally and can be adapted depending on the particular problem under investigation Findley

et al. (1989); Carcione (2022). It is important to note that all quantities in Eq. (2.50) are functions of the x, y and z spatial coordinates and are omitted for brevity of the mathematical notation.

In the considered 3–D space, this tensor has 81 components that depend on 21 independent relaxation functions that fully define the anisotropic body Achenbach (1973, 2003); Carcione (2022); Christensen (2012); Findley et al. (1989). The presented relationship allows one to model inelastic effects for solid materials. In the case of ideal elastic bodies for which inelastic effects do not appear, Eq. (2.50) reduces to the relation

$$\boldsymbol{\sigma} = \boldsymbol{C} : \boldsymbol{\varepsilon_C}, \tag{2.51}$$

where $\boldsymbol{C}$ is the elastic tensor. The components of this fourth–order tensor depend on independent 21 elastic coefficients that fully describe an anisotropic elastic body.

The relationship between the stress and the Cauchy strain tensors for an isotropic linear deformable body is fully defined by two relaxation functions i.e., the $G_s(t)$ shear relaxation function and the $G_p(t)$ volumetric relaxation function. These two functions fully define isotropic material with inelastic effects. The $(\boldsymbol{\sigma})_{dev}$, $(\boldsymbol{\varepsilon_C})_{dev}$ deviatoric and the $(\sigma)_{vol}$, $(\varepsilon_C)_{vol}$ volumetric stress and strain can be used to derive the relationships between the individual components of the stress and strain tensors. The definitions of these quantities result from Carcione (2022); Osika & Kijanka (2024)

$$\boldsymbol{\sigma} = (\boldsymbol{\sigma})_{dev} + \frac{1}{3}(\sigma)_{vol}\boldsymbol{I} = (\boldsymbol{\sigma})_{dev} + \frac{1}{3}\,\mathrm{tr}(\boldsymbol{\sigma})\boldsymbol{I}, \tag{2.52}$$

$$\boldsymbol{\varepsilon_C} = (\boldsymbol{\varepsilon_C})_{dev} + \frac{1}{3}(\varepsilon_C)_{vol}\boldsymbol{I} = (\boldsymbol{\varepsilon_C})_{dev} + \frac{1}{3}\,\mathrm{tr}(\boldsymbol{\varepsilon_C})\boldsymbol{I}, \tag{2.53}$$

where “tr” operator denotes the trace of the second–order tensor. The equation below defines the deviatoric stress tensor associated with the change of shape of viscoelastic material

$$(\boldsymbol{\sigma})_{dev} = 2\int_{-\infty}^{t} G_s(t-\tau)\frac{\partial(\boldsymbol{\varepsilon_C})_{dev}(\tau)}{\partial\tau}d\tau. \tag{2.54}$$

On the other hand, the volumetric stress resulting from volume changes of the body is given by the scalar equation

$$(\sigma)_{vol} = 3\int_{-\infty}^{t} G_p(t-\tau)\frac{\partial(\varepsilon_C)_{vol}(\tau)}{\partial\tau}d\tau, \tag{2.55}$$

For ideal elastic material Eqs. (2.54) – (2.55) reduce to

$$\boldsymbol{\sigma}_{dev} = 2\mu(\boldsymbol{\varepsilon_C})_{dev}, \tag{2.56}$$

$$\sigma_{vol} = 3K(\varepsilon_C)_{vol}, \tag{2.57}$$

where μ and K are shear and bulk modulus, respectively. Other elastic constants may be introduced according to the nature of the problems and the interpretation of mathematical quantities. The mathematical conditions that these constants must fulfilled are described in the works Landau

& Lifshitz (1989); Christensen (2012); Findley et al. (1989); Carcione (2022). The μ material constant together with the $\lambda = K - \frac{2}{3}\mu$ constant form a pair of Lamé elastic moduli. This pair will be used to describe linear isotropic media in the current work.

By substituting the geometric definition of the Cauchy strain tensor from Eq. (2.22) into the constitutive relation between strain and stress – that results from Eqs. (2.52) – (2.56) – the relation between the displacement and stress fields can be obtained. Based on it, the differential governing Eq. (2.45) – in the absence of body forces – can be rewritten as Miklowitz (1978); Skalmierski (1991); Graff (2012); Carcione (2022)

$$\rho \frac{\partial^2 \boldsymbol{u}}{\partial t^2} = (\lambda + \mu)\nabla(\nabla \cdot \boldsymbol{u}) + \mu \nabla^2 \boldsymbol{u}. \tag{2.58}$$

Eq. (2.58) provides a description of linear wave propagation in an elastic solid without boundaries. In such medium waves can propagate in all directions freely. The Helmholtz decomposition can be used to investigate this problem. According to the theory Morse & Feshbach (1953); Achenbach (1973, 2003); Miklowitz (1978); Graff (2012) it is possible to represent the $\boldsymbol{u}$ displacement field in terms of the φ scalar and the $\boldsymbol{\psi} = i\psi_x + j\psi_y + k\psi_z$ (or in the matrix form $\boldsymbol{\psi} = [\psi_x, \psi_y, \psi_y]^T$) vector potential fields as

$$\boldsymbol{u} = \nabla\varphi + \nabla \times \boldsymbol{\psi}. \tag{2.59}$$

Eq. (2.59) shows that three components of the displacement field are given in terms of four scalar functions. Therefore, to ensure uniqueness of decomposition, an additional condition i.e., a gauge condition, must be defined. In general, the gauge condition is given by

$$\nabla \cdot \boldsymbol{\psi} = g, \tag{2.60}$$

where g is the scalar function that depends on spatial coordinates. The gauge selection depends on the nature of the considered problem. The simplest gauge condition, which is used in the calculations in this chapter, corresponds to the assumption that $g = 0$ Morse & Feshbach (1953); Miklowitz (1978).

Upon substituting Eq. (2.59) into Eq. (2.58) and rearranging terms, the uncoupled scalar and vector wave equations can be obtained as

$$\frac{1}{c_p^2}\frac{\partial^2 \varphi}{\partial t^2} = \nabla^2 \varphi, \tag{2.61}$$

$$\frac{1}{c_s^2}\frac{\partial^2 \boldsymbol{\psi}}{\partial t^2} = \nabla^2 \boldsymbol{\psi}, \tag{2.62}$$

where $c_p = \sqrt{\frac{\lambda+2\mu}{\rho}}$ and $c_s = \sqrt{\frac{\mu}{\rho}}$ are the phase velocities. This relationship and the assumed gauge condition indicate that three independent waves can propagate in an elastic solid. These are namely, the longitudinal wave with the phase velocity equal to c_p and the two shear waves with the phase

velocity equal to c_s. Applying the divergence and curl operators gives the physical interpretation of the two terms on the right–hand side of Eq. (2.59) depending on the Helmholtz potentials. More precisely, one can write that $\nabla \cdot \boldsymbol{u} = \nabla^2 \varphi$ and $\nabla \times \boldsymbol{u} = \nabla \times \nabla \times \boldsymbol{\psi}$. These relations show that the scalar potential φ describes the longitudinal wave, while the vector potential $\boldsymbol{\psi}$ describes the shear waves.

This problem can be solved by the method of separation of variables Meirovitch (1980); Rao (2006), which leads to the possible steady–state space–time harmonic solution in the forms

$$\varphi = \frac{1}{2}\hat{\varphi} e^{i(\boldsymbol{\gamma_p} \cdot \boldsymbol{r} - \omega t)} + c.c. = \frac{1}{2}\hat{\varphi} e^{i(\xi_p x + \eta_p x + \zeta_p z - \omega t)} + c.c., \tag{2.63}$$

$$\boldsymbol{\psi} = \frac{1}{2}\hat{\boldsymbol{\psi}} e^{i(\boldsymbol{\gamma_s} \cdot \boldsymbol{r} - \omega t)} + c.c. = \frac{1}{2}\hat{\boldsymbol{\psi}} e^{i(\xi_s x + \eta_s x + \zeta_s z - \omega t)} + c.c., \tag{2.64}$$

where $\hat{\varphi}$, $\hat{\boldsymbol{\psi}} = [\hat{\psi}_x, \hat{\psi}_y, \hat{\psi}_z]^T$, $\boldsymbol{\gamma_p} = [\xi_p, \eta_p, \zeta_p]^T$, and $\boldsymbol{\gamma_s} = [\xi_s, \eta_s, \zeta_s]^T$ are the complex scalar amplitude, the complex vector amplitude, the longitudinal and shear wavenumber vectors, respectively. Moreover, c.c. stands for the complex conjugate. Upon substitution of Eqs.(2.63) – (2.64) into Eqs.(2.61) – (2.62), longitudinal and shear waves phase velocities are equal to

$$c_p = \frac{\omega}{\sqrt{\xi_p^2 + \eta_p^2 + \zeta_p^2}} = \frac{\omega \lambda_p}{2\pi}, \tag{2.65}$$

$$c_s = \frac{\omega}{\sqrt{\xi_s^2 + \eta_s^2 + \zeta_s^2}} = \frac{\omega \lambda_s}{2\pi}, \tag{2.66}$$

where λ_p and λ_s represent the wavelengths of the longitudinal and shear waves, respectively. These relationships show that the modulus of the longitudinal and shear wavenumber vectors are linear functions of the angular frequency in an infinite elastic solid medium. The dependence between the angular frequency and the modulus of the wavenumber vector is the dispersion relation. From the relationships presented, it follows that propagating bulk waves in an ideal elastic solid are nondispersive.

For deformable solids with the parameters depending on the angular frequency, as in the case of viscoelastic materials Rose (2014); Carcione (2022); Osika & Kijanka (2024), this relationship may not be linear and the relevant bulk waves are dispersive. Another source of dispersion of waves propagating in solids results from geometry of the analysed system and boundary conditions imposed. Nonlinear properties of medium can also influence the dispersion relation, as demonstrated in Packo et al. (2016); Osika et al. (2022).

An alternative approach that can be used to determine and analyse dispersion relations and phase velocities in a deformable solid medium is based on the Kelvin–Christoffel equation, as discussed in Achenbach (1973); Carcione (2022). This approach is particularly valuable for the analysis of bulk wave propagation in elastic and viscoelastic anisotropic materials.

2.7 Linear elastic guided waves in plate–like structures

Elastic guided waves can only exist in bounded media. Plate–like structures are an illustrative example of systems in which they can be observed. Multiple reflections of propagating bulk waves from boundaries of the system and their conversions lead to the generation of an infinite number of modes with the corresponding dispersion relations. The current work focuses on an infinite 2h–thick plate bounded by two parallel traction–free surfaces. Fig. 2.2 presents a schematic geometrical representation of the investigated system with marked global Cartesian coordinates and indicates the components of the displacements of the individual particles. The invariance along the z–axis direction is assumed, thus reducing the entire analysis to the selected cross–section of the plate.

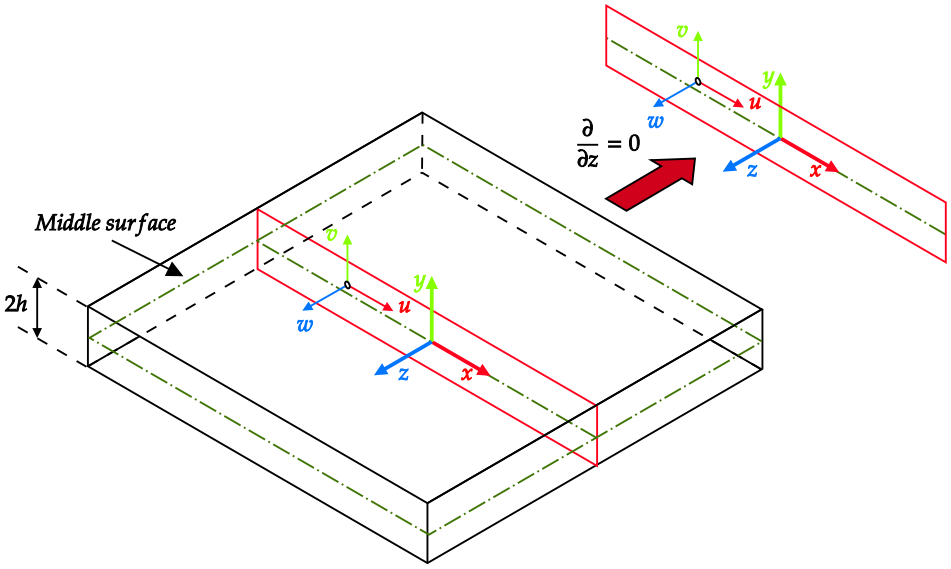

Figure 2.2: The geometrical model of the studied system with the adopted coordinate system.

For the mechanical system under consideration, the governing partial differential equation given by Eq. (2.58) is supplemented by the traction boundary conditions expressed as

$$\boldsymbol{t} = \boldsymbol{\sigma}\boldsymbol{n} = 0, \text{ for } y = \pm h, \tag{2.67}$$

where the normal vector can be represented in a matrix form as $\boldsymbol{n} = \pm[0, 1, 0]^T$ at $y = \pm 0$. Due to the assumed invariance along the z–axis direction, the partial differential equations – resulting from Eq. (2.58) and the boundary conditions defined in Eq. (2.67) that govern the u and v displacement components – are coupled. The scalar equation corresponding to the w displacement and the associated boundary conditions are independent.

The first two equations and their associated boundary conditions form a mathematical model of guided waves investigated analytically for the first time in Lamb (1917). Therefore, these waves are known as Lamb waves, after the author of the cited original work. Lamb waves arise due to the simultaneous interaction of longitudinal waves and shear vertical waves with the boundary of the medium. Only the φ and ψ_z potentials are required to describe the particle motion corresponding to Lamb waves. The governing partial differential equations

$$\frac{1}{c_p^2}\frac{\partial^2\varphi}{\partial t^2} = \frac{\partial^2\varphi}{\partial x^2} + \frac{\partial^2\varphi}{\partial y^2}, \tag{2.68}$$

$$\frac{1}{c_s^2}\frac{\partial^2\psi_z}{\partial t^2} = \frac{\partial^2\psi_z}{\partial x^2} + \frac{\partial^2\psi_z}{\partial y^2}, \tag{2.69}$$

and the coupled associated boundary conditions

$$t_x = \pm\sigma_{yx} = \mu\left(2\frac{\partial^2\varphi}{\partial x\partial y} - \frac{\partial^2\psi_z}{\partial x^2} + \frac{\partial^2\psi_z}{\partial y^2}\right) = 0, \text{ for } y = \pm h, \tag{2.70}$$

$$t_y = \pm\sigma_{yy} = \lambda\frac{\partial^2\varphi}{\partial x^2} + (\lambda+2\mu)\frac{\partial^2\varphi}{\partial y^2} - 2\mu\frac{\partial^2\psi_z}{\partial x\partial y} = 0, \text{ for } y = \pm h \tag{2.71}$$

give the complete mathematical model for this group of waves. This problem can be solved by the method of separation of variables Meirovitch (1980); Rao (2006), which leads to the possible complex solution in the form

$$\varphi = \frac{1}{2}\hat{\varphi}(y)e^{i(\xi x-\omega t)} + c.c., \tag{2.72}$$

$$\psi_z = \frac{1}{2}\hat{\psi}_z(y)e^{i(\xi x-\omega t)} + c.c., \tag{2.73}$$

where $\hat{\varphi}(y)$ and $\hat{\psi}_z(y)$ are the complex–value functions that define how the potentials φ and ψ_z are distributed along the thickness of the plate under consideration. Substituting the derived form of the solution to the Eqs. (2.68) – (2.71) and grouping terms, lead to the self–adjoint boundary value problem for functions depending on the y variable Viktorov (1967); Packo et al. (2016). Its solution leads to the Rayleigh–Lamb equation, which results in infinite dispersion relations and associated eigenfunctions. The considered problem was analysed in detail in Viktorov (1967); Miklowitz (1978); Achenbach (1973, 2003); Mindlin & Yang (2006); Graff (2012); Packo et al. (2016).

The scalar governing equation and boundary conditions corresponding to the w displacement component – that describe the linear shear horizontal guided waves propagation phenomenon – are as follows

$$\frac{1}{c_s^2}\frac{\partial^2 w}{\partial t^2} = \frac{\partial^2 w}{\partial x^2} + \frac{\partial^2 w}{\partial y^2}, \tag{2.74}$$

$$t_z = \pm\sigma_{yz} = \mu\frac{\partial w}{\partial y} = 0, \text{ for } y = \pm h. \tag{2.75}$$

A detailed analysis of this mathematical problem is provided in the following section.

2.8 Theoretical analysis of shear horizontal guided waves

The homogeneous governing Eq. (2.74), in combination with the associated boundary conditions specified in Eq. (2.75), describes the linear shear horizontal guided wave propagation phenomenon. This problem can be solved by applying the separation of variables technique. In this approach, the solution of the problem under consideration can be represented as the product of two scalar functions with independent arguments i.e.,

$$w(x,y,t) = Y(y)A(x,t). \tag{2.76}$$

The $Y(y)$ function must satisfy the boundary conditions and the $A(x,t)$ function represents the time and space distribution of the shear horizontal guided wave in an elastic plate. This assumption leads to the eigenvalue problem that can be defined as

$$Y''(y) + \eta^2 Y(y) = 0, \tag{2.77}$$

$$\pm\frac{\partial Y(y)}{\partial y} = 0, \text{ for } y = \pm h, \tag{2.78}$$

for the first introduced function, where η is arbitrarily assumed constant that result from application of the separation of variables method. The partial differential equation for the $A(x,t)$ second introduced function can be written as

$$\frac{\partial^2 A}{\partial x^2} - \eta^2 A - \frac{1}{c_s^2}\frac{\partial^2 A}{\partial t^2} = 0. \tag{2.79}$$

The solution of the ordinary differential equation from Eq. (2.77) is given by

$$Y(y) = C_1 \sin(\eta y) + C_2 \cos(\eta y), \tag{2.80}$$

where C_1 and C_2 are real constants. These constants result from the system of homogenous linear equations obtained by substituting Eq. (2.80) into the boundary conditions defined in Eq. (2.78) and can be written in a matrix form as follows

$$\begin{bmatrix} \cos(\eta h) & -\sin(\eta h) \\ \cos(\eta h) & \sin(\eta h) \end{bmatrix} \begin{bmatrix} C_1 \\ C_2 \end{bmatrix} = \begin{bmatrix} 0 \\ 0 \end{bmatrix}. \tag{2.81}$$

The above system of linear equations has a trivial solution. It has non–zero solutions if and only if the determinant of the coefficient matrix equals to zero. Thus, a characteristic equation can be formulated in the form

$$\sin(\eta h)\cos(\eta h) = 0 \tag{2.82}$$

which yields an infinite set of eigenvalues.

The provided considerations for the investigated boundary value problem defined by Eqs. (2.77) and (2.78) lead to an infinite series of distinct η_m^2 eigenvalues and $Y^{(m)}(y)$ associated

eigenfunctionswith $m \in \{0, 1, 2, \ldots\}$. The eigenvalues can be expressed as $\eta_m^2 = \left(m\frac{\pi}{2h}\right)^2$. The eigenfunctions describe physically natural modes that can be normalised to determine unique amplitudes and, in turn obtain normal modes Reismann (1968); Meirovitch (2003). The modes of the considered guided wave group can be denoted as SH0, SH1, SH2, ... Giurgiutiu (2008). Moreover, the $\{Y^{(m)}(y)\}$ eigenfunction set can be dived into two subsets i.e., the symmetric $\{Y_S^{(i)}(y)\}$ and the antisymmetric $\{Y_A^{(i)}(y)\}$ modes for shear horizontal guided waves given as

$$Y_S^{(i)}(y) = \cos(\eta_{2i} y), \tag{2.83}$$

$$Y_A^{(i)}(y) = \sin(\eta_{2i+1} y), \tag{2.84}$$

where $i \in \{0,\ 1,\ 2,\ \ldots\}$. The symmetric and asymmetric modes correspond to the even and odd values of the m index, respectively. Selected eigenfunctions are presented graphically in Fig. 2.3.

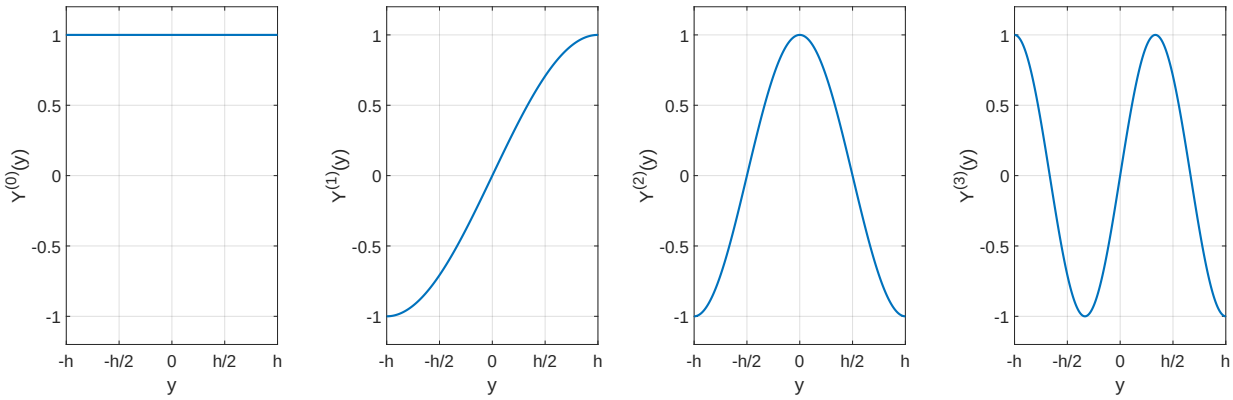

(a) (b) (c) (d)

Figure 2.3: Selected eigenfunctions for shear horizontal guided waves: (a) SH0 mode–shape (b) SH1 mode–shape (c) SH2 mode–shape (d) SH3 mode–shape.

The analysed eigenvalue problem is self–adjoint. Therefore, there is a guarantee that the eigenvalues are real and non–negative Reismann (1968); Rao (2006); Meirovitch (1980, 2003); Haberman (2013). According to Meirovitch (2003); Rao (2006), the proof of the self–adjoint of the operator in Eq. (2.77) – which is the second derivative – is trivial. It consists of the application of the integration by parts twice and the use of the defined boundary conditions.

It is crucial to highlight that the eigenfunctions are orthogonal and form a complete set of functions. In order to demonstrate the orthogonality of modes, it is necessary to consider the equations for two arbitrarily chosen modes, denoted by r and s. The equation corresponding to mode r is multiplied by the eigenfunction $Y^{(s)}(y)$ and the equation corresponding to mode s is multiplied by the eigenfunction $Y^{(r)}(y)$. After that, these equations are subtracted from each other and integrated over the range from $-h$ to h. These operations lead to the following relationship

$$\int_{-h}^{h} \left(\left(Y^{(r)}(y)'' + \eta_r^2 Y^{(r)}(y)\right) Y^{(s)}(y) - \left(Y^{(s)}(y)'' + \eta_s^2 Y^{(s)}(y)\right) Y^{(r)}(y)\right) dy = 0. \tag{2.85}$$

After performing successive integrations by parts and grouping the terms, one obtains

$$\left(\eta_r^2 - \eta_s^2\right) \int_{-h}^{h} Y^{(r)}(y) Y^{(s)}(y) dy = 0. \tag{2.86}$$

This relationship clearly shows that any two $Y^{(r)}(y)$ and $Y^{(s)}(y)$ distinct eigenfunctions ($r \neq s$) are orthogonal.

For each $Y^{(m)}(y)$ function with $\eta = \eta_m$, an associated solution of Eq. (2.79) can be identified and denoted as $A^{(m)}(x,t)$. Therefore, the general solution for the problem defined by Eqs. (4.32) and (4.33) can be given by

$$\begin{aligned} w(x,y,t) &= \sum_{m=0}^{\infty} Y^{(m)}(y) A^{(m)}(x,t) \\ &= \sum_{i=0}^{\infty} \left(Y_S^{(i)}(y) A^{(2i)}(x,t) + Y_A^{(i)}(y) A^{(2i+1)}(x,t) \right). \end{aligned} \tag{2.87}$$

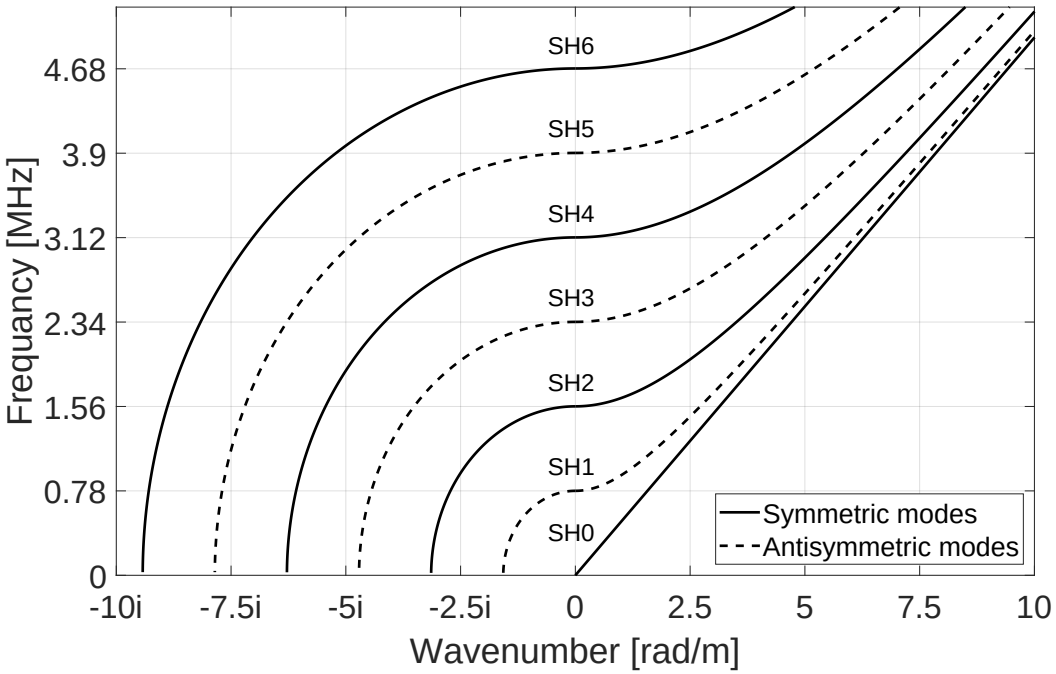

Figure 2.4: The analytical dispersion curves in a 2 mm thick aluminium plate.

The equation that governs the evolution of the amplitude for the m–th mode is commonly known as the Klein–Gordon equation Whitham (1999); Osika et al. (2022). This equation can be solved using the integral transform method, as presented in Duffy (2004). The analysis of the complex steady–state harmonic solutions of this partial differential equation in time and space results in the dispersion relation that can be written as

$$\frac{\omega^2}{c_s^2} = \eta_m^2 + \xi^2, \tag{2.88}$$

where ω is an angular frequency and ξ is a wavenumber. The ω angular frequency and the η_m^2 eigenvalue are real numbers. Therefore, the ξ wavenumber is purely real for $\frac{\omega^2}{c_s^2} \geq \eta_m^2$ or purely imaginary for $\frac{\omega^2}{c_s^2} < \eta_m^2$. The angular frequencies below which wavenumbers are purely imaginary are named in the literature as critical angular frequencies or cut–off angular frequencies Achenbach (1973); Miklowitz (1978); Giurgiutiu (2008). The complex values of the wave number correspond to evanescent waves. The dispersion curves for an aluminium plate with a thickness of 2 mm and the given parameters $\rho = 2700\ \frac{kg}{m^3}$ and $\mu = 26.32$ GPa are shown in the Fig. 2.4, as an example.

Chapter 3

Analytical investigation of nonlinear modes for shear horizontal guided waves

This chapter presents analytical analysis of nonlinear shear horizontal guided wave propagation in a hyperelastic plate. The main focus is on the influence of nonlinear material parameters, excitation frequency, wavenumber, and wave amplitude on the generation of nonlinear modes. A new concept of nonlinear modes for shear horizontal guided waves is introduced, following the analytical work based on the multiplescale variant of the perturbation analysis.

3.1 Definition of hyperelastic material and problem formulation

Nonlinear shear horizontal wave propagation in plate–like structures is analysed. Distributed nonlinearity associated with hyperelastic effects is investigated. As a result, the relationship between components of the displacement vector and the stress tensor is nonlinear. The mathematical formula for this nonlinear relationship results from the geometric definition of strain tensor and the constitutive equation that describes the relationship between stress and strain tensors components. Small but finite amplitude waves are considered. Therefore, the Green–Lagrange strain tensor definition is assumed. The second Piola–Kirchhoff stress tensor is used as a measure of the stress field, as discussed in Section 2.4. This tensor has previously been used in analytical calculations and numerical simulations in Packo et al. (2012, 2016); Osika et al. (2021, 2022). Individual components of this stress tensor result from Eq. (2.31) and are given as Landau & Lifshitz (1989); Liu et al. (2013a); Hackett (2016)

$$\sigma_{ij} = \frac{\partial U(\boldsymbol{\varepsilon_{GL}})}{\partial (\varepsilon_{GL})_{ij}}, \tag{3.1}$$

where $U(\boldsymbol{\varepsilon_{GL}})$ is the strain energy density and subscripts $i, j \in \{x,\ y,\ z\}$. The Landau–Lifshitz nonlinear model of hyperelasticity is adopted to characterise properties of a hyperelastic material. The fourth order expansion of the strain energy density $U(\boldsymbol{\varepsilon_{GL}})$ is defined as Landau & Lifshitz (1989); Hamilton et al. (2004)

$$U(\boldsymbol{\varepsilon_{GL}}) = \frac{\lambda}{2}I_1^2 + \mu I_2 + \frac{\mathcal{A}}{3}I_3 + \mathcal{B}I_1I_2 + \frac{\mathcal{C}}{3}I_1^3 + \mathcal{E}I_1I_3 + \mathcal{F}I_1^2I_2 + \mathcal{G}I_2^2 + \mathcal{H}I_1^4, \tag{3.2}$$

where $\lambda,\ \mu$ represent the Lamé elastic constants, $\mathcal{A},\ \mathcal{B},\ \mathcal{C}$ are the Third Order Elastic Constants (TOEC) and $\mathcal{E},\ \mathcal{F},\ \mathcal{G},\ \mathcal{H}$ are the Fourth Order Elastic Constants (FOEC) Hamilton et al. (2004); Liu et al. (2013a); Lissenden (2021). The three scalars in the above equation – namely I_1, I_2 and I_3 – denote the first, second and third invariants of the $\boldsymbol{\varepsilon_{GL}}$ Green–Lagrange strain tensor, respectively. These scalars are defined as

$$\begin{aligned} I_1 &= \mathrm{tr}(\boldsymbol{\varepsilon_{GL}}), \\ I_2 &= \mathrm{tr}(\boldsymbol{\varepsilon_{GL}^2}), \\ I_3 &= \mathrm{tr}(\boldsymbol{\varepsilon_{GL}^3}). \end{aligned} \tag{3.3}$$

The invariance along the z–axis, denoted as $\frac{\partial}{\partial z} = 0$, is assumed, as discussed in Section 2.7. For a linear solid medium, this assumption leads to decoupling of the partial differential equations for a linear medium i.e., one equation governs shear horizontal guided wave propagation and the other two equation describe Lamb wave propagation. However, this decoupling does not hold for the hyperelastic material model considered. Definitions of stress components include nonlinear terms that couple equations involved, as demonstrated in Liu et al. (2013a); Shengbo & Cheng (2019). Therefore, for the problem of shear horizontal wave propagation investigated, additional assumptions are introduced. Negligible contributions of displacements and mass force components associated with the x and y directions are assumed i.e., $\mathbf{u} = [0,\ 0,\ w]^T$ and $\tilde{\mathbf{F}} = [0,\ 0,\ \tilde{F}_z]^T$. As a result, the mathematical model – initially formulated in Eq. (2.45) – reduces from a vector equation to a scalar partial differential equation as

$$\tilde{F}_z + \frac{\partial \sigma_{xz}}{\partial x} + \frac{\partial \sigma_{yz}}{\partial y} = \rho \frac{\partial^2 w}{\partial t^2}. \tag{3.4}$$

The components of the second Piola–Kirchhoff stress tensor given in Eq. (3.4) for the Landau–Lifshitz strain energy density defined in Eq. (3.2) can be expressed as

$$\begin{aligned} \sigma_{xz} = {} & 2\mu\varepsilon_{xz} + \mathcal{A}(\varepsilon_{xx}\varepsilon_{xz} + \varepsilon_{xy}\varepsilon_{yz} + \varepsilon_{xz}\varepsilon_{zz}) + 2\mathcal{B}\varepsilon_{xz}(\varepsilon_{xx} + \varepsilon_{yy} + \varepsilon_{zz}) \\ & + 3\mathcal{E}(\varepsilon_{xx} + \varepsilon_{yy} + \varepsilon_{zz})(\varepsilon_{xx}\varepsilon_{xz} + \varepsilon_{xy}\varepsilon_{yz} + \varepsilon_{xz}\varepsilon_{zz}) + 2\mathcal{F}\varepsilon_{xz}(\varepsilon_{xx} \\ & + \varepsilon_{yy} + \varepsilon_{zz})^2 + 4\mathcal{G}\varepsilon_{xz}(\varepsilon_{xx}^2 + 2\varepsilon_{xy}^2 + 2\varepsilon_{xz}^2 + \varepsilon_{yy}^2 + 2\varepsilon_{yz}^2 + \varepsilon_{zz}^2), \end{aligned} \tag{3.5}$$

$$\begin{aligned} \sigma_{yz} = {} & 2\mu\varepsilon_{yz} + \mathcal{A}(\varepsilon_{xy}\varepsilon_{xz} + \varepsilon_{yy}\varepsilon_{yz} + \varepsilon_{yz}\varepsilon_{zz}) + 2\mathcal{B}\varepsilon_{yz}(\varepsilon_{xx} + \varepsilon_{yy} + \varepsilon_{zz}) \\ & + 3\mathcal{E}(\varepsilon_{xx} + \varepsilon_{yy} + \varepsilon_{zz})(\varepsilon_{xy}\varepsilon_{xz} + \varepsilon_{yy}\varepsilon_{yz} + \varepsilon_{yz}\varepsilon_{zz}) + 2\mathcal{F}\varepsilon_{yz}(\varepsilon_{xx} \\ & + \varepsilon_{yy} + \varepsilon_{zz})^2 + 4\mathcal{G}\varepsilon_{yz}(\varepsilon_{xx}^2 + 2\varepsilon_{xy}^2 + 2\varepsilon_{xz}^2 + \varepsilon_{yy}^2 + 2\varepsilon_{yz}^2 + \varepsilon_{zz}^2). \end{aligned} \tag{3.6}$$

Combining the Green–Lagrange strain tensor definition from Eq. (2.21) with Eqs. (3.5) – (3.6) yields the constitutive relations for σ_{xz}, σ_{yz} stress components and w displacement. The resulting relations can be written for the analysed stress components as

$$\begin{aligned}\sigma_{xz} = \mu\frac{\partial w}{\partial x} + \left(\frac{\mathcal{A}}{4} + \frac{\mathcal{B}}{2}\right)\frac{\partial w}{\partial x}\left(\left(\frac{\partial w}{\partial x}\right)^2 + \left(\frac{\partial w}{\partial y}\right)^2\right) + \left(\frac{3\mathcal{E}}{8} + \frac{\mathcal{F}}{2}\right)\frac{\partial w}{\partial x}\left(\left(\frac{\partial w}{\partial x}\right)^2\right.\\ \left. + \left(\frac{\partial w}{\partial y}\right)^2\right)^2 + \frac{\mathcal{G}}{2}\frac{\partial w}{\partial x}\left(2\left(\frac{\partial w}{\partial x}\right)^2 + 2\left(\frac{\partial w}{\partial y}\right)^2 + 2\left(\frac{\partial w}{\partial x}\right)^2\left(\frac{\partial w}{\partial y}\right)^2\right.\\ \left. + \left(\frac{\partial w}{\partial x}\right)^4 + \left(\frac{\partial w}{\partial y}\right)^4\right),\end{aligned} \tag{3.7}$$

$$\begin{aligned}\sigma_{yz} = \mu\frac{\partial w}{\partial y} + \left(\frac{\mathcal{A}}{4} + \frac{\mathcal{B}}{2}\right)\frac{\partial w}{\partial y}\left(\left(\frac{\partial w}{\partial x}\right)^2 + \left(\frac{\partial w}{\partial y}\right)^2\right) + \left(\frac{3\mathcal{E}}{8} + \frac{\mathcal{F}}{2}\right)\frac{\partial w}{\partial y}\left(\left(\frac{\partial w}{\partial x}\right)^2\right.\\ \left. + \left(\frac{\partial w}{\partial y}\right)^2\right)^2 + \frac{\mathcal{G}}{2}\frac{\partial w}{\partial y}\left(2\left(\frac{\partial w}{\partial x}\right)^2 + 2\left(\frac{\partial w}{\partial y}\right)^2 + 2\left(\frac{\partial w}{\partial x}\right)^2\left(\frac{\partial w}{\partial y}\right)^2\right.\\ \left. + \left(\frac{\partial w}{\partial x}\right)^4 + \left(\frac{\partial w}{\partial y}\right)^4\right).\end{aligned} \tag{3.8}$$

The components of the stress tensor – i.e., σ_{xz} and σ_{xz} – can be decomposed into linear (denoted by the superscript L) and nonlinear (denoted by the superscript NL) terms i.e., $\sigma_{xz} = \sigma_{xz}^{L} + \sigma_{xz}^{NL}$ and $\sigma_{yz} = \sigma_{yz}^{L} + \sigma_{yz}^{NL}$. In this work, geometric nonlinearities proportional to linear material parameters are negligible due to the adopted measure of the stress field. However, previous research work in Zabolotskaya et al. (2004); Wochner et al. (2008) shows that a different stress measure – known as the first Piola–Kirchhoff stress tensor – can be used to account for geometric nonlinearities.

Without external body forces, Eq. (3.4) and the nonlinear stress definitions from Eqs. (3.7) – (3.8) yield the nonlinear homogeneous displacement equation of motion that can be given as

$$\frac{\partial^2 w}{\partial x^2} + \frac{\partial^2 w}{\partial y^2} - \frac{1}{c_s^2}\frac{\partial^2 w}{\partial t^2} = -\frac{1}{\mu}\left(\frac{\partial \sigma_{xz}^{NL}}{\partial x} + \frac{\partial \sigma_{yz}^{NL}}{\partial y}\right), \tag{3.9}$$

where $c_s = \sqrt{\frac{\mu}{\rho}}$ and σ_{xz}^{NL}, σ_{xz}^{NL} are the shear wave velocity and nonlinear terms of stress components in Eqs. (3.7) and (3.8), respectively. The linear and nonlinear terms are written intentionally on different sides of the above equation, to facilitate further calculations. Eqs. (3.7) – (3.9) constitute the analytical model of shear horizontal wave propagation in the unbounded nonlinear Landau–Lifshitz solid medium that is described by two Lagrangian coordinates x, y and one displacement component w. Here only the t_z component of the traction is considered due to the assumption introduced in Section 2.7. The traction–free boundary conditions for the propagation of shear horizontal guided waves require that

$$t_z = \pm\sigma_{yz} = 0, \text{ for } y = \pm h, \tag{3.10}$$

where σ_{yz} is defined by Eq (3.8). The adopted boundary conditions are nonlinear and homogeneous. When the linear and nonlinear terms in Eq. (3.10) are grouped, this equation can be rewritten as

$$\pm\frac{\partial w}{\partial y} = \mp\frac{1}{\mu}\sigma_{yz}^{NL}, \text{ for } y = \pm h. \tag{3.11}$$

The governing Eq. (3.9) with the boundary conditions defined in Eq. (3.11) form a complete mathematical model of shear horizontal guided waves propagation problem in the Landau–Lifshitz hyperelastic solid medium.

3.2 Perturbation analysis of nonlinear shear horizontal guided waves

It is evident that the problem formulated in Section 3.1 by Eqs. (3.9) and (3.11) is nonlinear. Analytical solution of this problem is generally tedious, if not possible. Therefore, an asymptotic approximation of the exact solutions can be derived using perturbation analysis Nayfeh & Mook (1979). In this work, the multiplescale perturbation technique is used in combination with the modal decomposition technique. This particular approach has been applied to various nonlinear mechanical systems, as shown in Nayfeh & Nayfeh (1994); Nayfeh (1995); Nayfeh & Nayfeh (1995). The major objective of the adopted approach is to eliminate the presence of secular terms in the approximate solution. These terms tend to be infinite and cannot be eliminated by the classical perturbation analysis. The secular terms are inconsistent with physical properties of the conservative system under consideration.

A small parameter ε – which does not appear explicitly in the Eqs. (3.9) and (3.11) – is introduced, to perform an asymptotic expansion of the solution using the multiplescale perturbation method. This parameter acts as a bookkeeping parameter, to facilitate the asymptotic analysis. In addition, to eliminate the presence of secular terms – that can increase infinitely – additional time scales are introduced to the problem, as described in the literature Nayfeh (2011); Holmes (2012); Kevorkian & Cole (2013). The t_n additional time scales are defined as

$$t_n = \varepsilon^n t, \tag{3.12}$$

where $n \in \{0, 1, 2, \ldots\}$. With the introduction of these new time scales, the relevant derivatives, with respect to the time variable t, can be calculate using a chain rule. Thus, the first derivative with respect to t can be given as

$$\frac{\partial}{\partial t} = \frac{\partial}{\partial t_0} + \varepsilon\frac{\partial}{\partial t_1} + \varepsilon^2\frac{\partial}{\partial t_2} + \cdots . \tag{3.13}$$

whereas the second derivative with respect to t can be expanded as

$$\frac{\partial^2}{\partial t^2} = \frac{\partial^2}{\partial t_0^2} + 2\varepsilon\frac{\partial}{\partial t_0, t_1} + \varepsilon^2\left(\frac{\partial^2}{\partial t_1^2} + 2\frac{\partial}{\partial t_0, t_2}\right) + \cdots . \tag{3.14}$$

By using these new variables, the asymptotic expansion without secular terms can be obtained. As a result, the solution of the nonlinear problem investigated – i.e., propagation of shear horizontal waves in a hyperelastic medium – can be more accurately approximated.

One can see that the required number of introduced time scales depends on the order of the expansion. Therefore, the approximate solution for the nonlinear shear horizontal wave propagation problem can be expressed as

$$w(x,y,t_0,t_2,\ldots) = \varepsilon w_1(x,y,t_0,t_2,\ldots) + \varepsilon^3 w_3(x,y,t_0,t_2,\ldots) + \cdots , \tag{3.15}$$

where the subscripts attached to w denote the order of approximation. The small dimensionless parameter ε acts as a measure of amplitude of the solution, as shown in Nayfeh (2011). When the amplitude is considered small, one can set it to unity. The variable t_0 corresponds to the fast time scale, while t_2 represents the slow time scale, which characterises the modulation of amplitude and phase, resulting from the material nonlinearity Nayfeh & Pai (2004).

Without the loss of generality, the t_1 slow time variable and the w_2 term are neglected in Eq. (3.15). Then, the analysed nonlinearity is an odd function of spatial derivatives of the w wavefield. The introduction of t_1 and the incorporation of w_2 into the expansion of w would yield equations indicating that w is independent of t_1 and that w_2 satisfies the same equations as w_1. Consequently, omitting w_2 does not affect the solution Nayfeh & Mook (1979).

By substituting Eqs. (3.14) and (3.15) in Eqs. (3.9) and (3.11) and setting the terms proportional to powers of the parameter ε to zero – the governing equations and associated boundary conditions for the first and third order approximations can be defined by

$$O(\varepsilon) : \frac{\partial^2 w_1}{\partial x^2} + \frac{\partial^2 w_1}{\partial y^2} - \frac{1}{c_s^2}\frac{\partial^2 w_1}{\partial t_0^2} = 0, \tag{3.16}$$

$$O(\varepsilon) : \pm\frac{\partial w_1}{\partial y} = 0, \text{ for } y = \pm h, \tag{3.17}$$

$$\begin{aligned} O(\varepsilon^3) :& \frac{\partial^2 w_3}{\partial x^2} + \frac{\partial^2 w_3}{\partial y^2} - \frac{1}{c_s^2}\frac{\partial^2 w_3}{\partial t_0^2} = \frac{2}{c_s^2}\frac{\partial w_1}{\partial t_0, t_2} - \frac{1}{\mu}\left(\frac{\partial (\sigma_{xz}^{NL})_1}{\partial x} + \frac{\partial (\sigma_{yz}^{NL})_1}{\partial y}\right) = \\ &= \frac{2}{c_s^2}\frac{\partial w_1}{\partial t_0, t_2} - \frac{1}{\mu}\left(\frac{\mathcal{A}}{4} + \frac{\mathcal{B}}{2} + \mathcal{G}\right)\left[\frac{\partial}{\partial x}\left(\frac{\partial w_1}{\partial x}\left(\frac{\partial w_1}{\partial x}^2 + \frac{\partial w_1}{\partial y}^2\right)\right)\right. \\ &\left. + \frac{\partial}{\partial y}\left(\frac{\partial w_1}{\partial y}\left(\frac{\partial w_1}{\partial x}^2 + \frac{\partial w_1}{\partial y}^2\right)\right)\right], \end{aligned} \tag{3.18}$$

$$\begin{aligned} O(\varepsilon^3) :& \pm\frac{\partial w_3}{\partial y} = \mp\frac{1}{\mu}(\sigma_{yz}^{NL})_1 = \mp\frac{1}{\mu}\left(\frac{\mathcal{A}}{4} + \frac{\mathcal{B}}{2} + \mathcal{G}\right)\frac{\partial w_1}{\partial y} \\ &\times \left(\frac{\partial w_1}{\partial x}^2 + \frac{\partial w_1}{\partial y}^2\right), \text{ for } y = \pm h. \end{aligned} \tag{3.19}$$

The terms $(\sigma_{xz}^{NL})_1$ and $(\sigma_{yz}^{NL})_1$ that occur in the Eqs. (3.18) – (3.19) represent the nonlinear components σ_{xz} and σ_{yz} of the stress tensor for the first–order approximation solution w_1 as defined by Eqs. (3.7) – (3.8).

At this point it is important to emphasise that the nonlinear homogeneous problem of shear horizontal guided wave propagation in a hyperelastic material – defined by Eqs. (3.9) – (3.11) – has been reduced to a system of linear partial differential equations with corresponding linear boundary conditions. The linear differential operators acting on w_1 and w_3 on the left–hand side of Eqs. (3.16) – (3.19) are identical. This also holds for higher order approximations. The nonlinear forcing terms on the right hand side of the analysed equations can be interpreted as excitation of the higher order approximation by the lower order approximation of the shear horizontal wavefield. This excitation depends on the definition of nonlinearity. Consequently, the problems described by Eqs. (3.16) to (3.19) have to be solved recursively. The multiplescale perturbation method – in combination with the normal mode decomposition Nayfeh & Nayfeh (1994, 1995) – is used in the next subsections to determine the approximate solution in terms of the nonlinear normal modes.

3.2.1 First order approximation

The first–order shear horizontal guided wave problem described by Eqs. (3.16) and (3.17) corresponds to the classical linear plate problem of shear horizontal guided wave propagation. The solution for the first–order homogeneous problem in steady–state harmonic form is obtained by summing up harmonic waves with angular frequency–wavenumber pairs (ω, ξ), derived individually from the dispersion relations of each mode. The through–thickness profiles of these waves correspond to the shear horizontal mode shapes. These mode shapes – being the eigenfunctions of the shear horizontal guided wave problem – are orthogonal and form a complete set of functions and can be used to solve the inhomogeneous problem defined by Eqs. (3.18) and (3.19).

One can analytically investigates how the assumed material nonlinearity affects the dispersion characteristics and the higher–order displacement field of shear horizontal guided waves in a 2h–thick plate. In other words, the question is how the displacement field is distorted. A steady–state harmonic solution is assumed for the system under consideration. This field corresponds to the dominant m_0–th mode propagating in the positive direction of the x–axis Holmes (2012); Nayfeh (2008); Nayfeh & Pai (2004). The problem investigated involves resonances between an infinite number of linear shear horizontal modes, as noted in Liu et al. (2013a). In order to accurately derive the w_1 first–order approximation, it is crucial to incorporate all shear horizontal modes involved in the internal resonances and propagating in the positive direction of the x–axis. The solution to the first–order approximation problem – which restores the linear shear horizontal guided wave propagation model presented and analysed in detail in Section 2.8 – in the presence of the dispersive dominant m_0–th shear horizontal mode, takes the form as

$$w_1(x, y, t_0, t_2) = \sum_r \vartheta^r Y^{(rm_0)}(y) \alpha_1^{(rm_0)}(t_2) e^{ir(\xi_0 x - \omega_0 t_0)} + c.c., \tag{3.20}$$

where c.c. stands for the complex conjugate of all preceding terms and $r \in \{1,\ 3,\ \ldots\}$ belongs to a set of odd numbers, according to the form of the assumed nonlinearity. The m_0–th shear horizontal mode serves as the primary driving mode, which can be directly excited in a mechanical system with the ω_0 angular frequency and the ξ_0 wavenumber satisfying the dispersion relation given by Eq. (2.88). The higher order modes (i.e., odd multiples of m_0) can be considered as companion modes that exist because of internal resonances.

The $\alpha_1^{(rm_0)}(t_2)$ coefficient in Eq. (3.20) corresponds to the complex amplitude of the rm_0–th shear horizontal mode. The determination of this coefficient is essential to prevent the presence of secular terms in the approximate solutions. The dimensionless parameter $\vartheta \ll 1$ in Eq. (3.20) is introduced to indicate the amplitude range for all propagating modes. This parameter arranges the forcing terms in descending order and therefore indicates the amplitude range of higher–order modes. When m_0 is equal to 0 – indicating the nondispersive SH0 mode as the driving mode – the distribution of the displacement field along the y–direction reduces to the linear mode shape of SH0 in the first–order approximation. This is because the SH0 mode interacts only with itself through internal resonance within the material nonlinearity considered. In this specific scenario, the first approximate solution can be formulated as

$$w_1(x, y, t_0, t_2) = Y^{(0)}(y) \sum_r \vartheta^r \alpha_1^{(r)}(t_2) e^{ir(\xi_0 x - \omega_0 t_0)} + c.c. \tag{3.21}$$

In this notation, the symbol m_0 is intentionally omitted since it is equal to zero. Therefore, it is possible to distinguish between the $\alpha^{(r)}$ coefficients, which correspond to the amplitudes of the individual harmonic waves. An analogous approach was followed for all calculations corresponding to the case where mode SH0 is the dominant mode.

3.2.2 Third order approximation

The mathematical model defined by the Eqs. (3.18) and (3.19) describes the linear inhomogeneous shear horizontal guided wave problem. The forcing conditions – which depend on the first–order solution defined by the Eq. (3.20) or (3.21) – cannot be arbitrary. Therefore, the dependence of the first–order solution on the slow time scale t_2 is determined in order to eliminate the secular forcing terms that lead to a nonphysical solution. This section investigates two specific cases of first–order solutions and their impact on higher–order solutions. In the first case investigated, only the dispersive mode is analysed only. In the second case, the SH0 mode is considered separately due to its nondispersive properties.

3.2.2.1 Third order approximation for dispersive modes

The problem defined by the Eqs. (3.18) and (3.19) is linear and inhomogeneous. The forcing terms in the boundary conditions represent external forces acting on the system boundaries. The

boundary conditions must be homogenous in order to use the eigenfunction expansion method to find the solution Reismann (1968); Rao (2006); Meirovitch (1980). This can be achieved by using the properties of the Dirac delta function, as shown in Meirovitch (2003). In effect, Eq. (3.18) with the associated homogeneous boundary conditions can be rewritten as

$$\begin{aligned}\frac{\partial^2 w_3}{\partial x^2}+\frac{\partial^2 w_3}{\partial y^2}-\frac{1}{c_s^2}\frac{\partial^2 w_3}{\partial t_0^2} =&\frac{2}{c_s^2}\frac{\partial^2 w_1}{\partial t_0 \partial t_2}-\frac{1}{\mu}\Bigg(\frac{\partial(\sigma_{xz}^{NL})_1}{\partial x}+\frac{\partial(\sigma_{yz}^{NL})_1}{\partial y}\\ &-\delta(y-h)(\sigma_{yz}^{NL})_1+\delta(y+h)(\sigma_{yz}^{NL})_1\Bigg),\end{aligned} \tag{3.22}$$

$$\pm\frac{\partial w_3}{\partial y}=0, \text{ for } y=\pm h. \tag{3.23}$$

The solution of the governing Eq. (3.22) and the associated boundary condition defined in Eq. (3.23) can be expressed as

$$w_3(x,y,t_0,t_2)=\sum_{m=0}^{\infty} Y^{(m)}(y)A_3^{(m)}(x,t_0,t_2), \tag{3.24}$$

where the $Y^{(m)}(y)$ eigenfunctions – satisfying homogeneous boundary conditions – are known, whereas the $A^{(m)}(x,t_0,t_2)$ amplitudes need to be determined. To shorten the notation, the f_1^{NL} term is introduced, which corresponds to the space–distributed forcing term and is defined as follows

$$f_1^{NL}=\frac{\partial(\sigma_{xz}^{NL})_1}{\partial x}+\frac{\partial(\sigma_{yz}^{NL})_1}{\partial y}. \tag{3.25}$$

Substituting Eqs. (3.24) and (3.20) into Eq. (3.22) yields the governing equation as

$$\begin{aligned}&\sum_{m=0}^{\infty} Y^{(m)}\frac{\partial^2 A_3^{(m)}}{\partial x^2}+\sum_{m=0}^{\infty} Y^{(m)\prime\prime}A_3^{(m)}-\frac{1}{c_s^2}\sum_{m=0}^{\infty} Y^{(m)}\frac{\partial^2 A_3^{(m)}}{\partial t_0^2}=\frac{2}{c_s^2}\frac{\partial^2 w_1}{\partial t_0\partial t_2}\\ &-\frac{1}{\mu}\left(f_1^{NL}-\delta(y-h)(\sigma_{yz}^{NL})_1+\delta(y+h)(\sigma_{yz}^{NL})_1\right).\end{aligned} \tag{3.26}$$

When Eq. (2.77) is used and the $Y^{(m)\prime\prime}(y)$ second derivative of m–th eigenfunction is removed, the considered problem can be rewritten as

$$\begin{aligned}&\sum_{m=0}^{\infty} Y^{(m)}\left(\frac{\partial^2 A_3^{(m)}}{\partial x^2}-\eta_m^2 A_3^{(m)}-\frac{1}{c_s^2}\frac{\partial^2 A_3^{(m)}}{\partial t_0^2}\right)=\frac{2}{c_s^2}\frac{\partial^2 w_1}{\partial t_0\partial t_2}\\ &-\frac{1}{\mu}\left(f_1^{NL}-\delta(y-h)(\sigma_{yz}^{NL})_1+\delta(y+h)(\sigma_{yz}^{NL})_1\right).\end{aligned} \tag{3.27}$$

Prior to further analysis, one can expand the f_1^{NL} inhomogeneous term using the functional base defined by the $\{Y^{(m)}(y)\}$ set of eigenfunctions

$$\begin{aligned}f_1^{NL}=&\vartheta^3\sum_{r=1,3}Y^{(rm_0)}\sum_{k=1,3}C_{(1,\vartheta^3)}^{(rm_0,k)}e^{ik(\xi_0 x-\omega_0 t_0)}+\\ &\vartheta^5\sum_{r=1,3,5}Y^{(rm_0)}\sum_{k=1,3,5}C_{(1,\vartheta^5)}^{(rm_0,k)}e^{ik(\xi_0 x-\omega_0 t_0)}+\ldots+c.c.\end{aligned} \tag{3.28}$$

Here, the $C^{(r,k)}_{(1,\vartheta^3)}, C^{(r,k)}_{(1,\vartheta^5)}, \ldots$ coefficients depend on the $\{\alpha_1^{(rm_0)}(t_2)\}$ set of complex amplitudes. Multiplying Eq. (3.27) by $Y^{(m)}(y)$ and then integrating over the variable y in the interval $\langle -h, h\rangle$, together with the application of orthogonality conditions, gives an infinite number of uncoupled partial differential equations governing each of the $A_3^{(m)}(x, y, t_0, t_2)$ amplitudes

$$\frac{\partial^2 A_3^{(m)}}{\partial x^2} - \eta_m^2 A_3^{(m)} - \frac{1}{c_s^2}\frac{\partial^2 A_3^{(m)}}{\partial t_0^2} = \frac{\int_{-h}^{h}(\frac{2}{c_s^2}\frac{\partial^2 w_1}{\partial t_0 \partial t_2} - \frac{1}{\mu} f_1^{NL}) Y^{(m)}(y) dy}{\int_{-h}^{h}(Y^{(m)}(y))^2 dy}. \tag{3.29}$$

For this particular case, the absence of external forces resulting from the boundary conditions for each mode amplitude is observed due to the application of the Dirac delta function property and the boundary conditions associated with the solution of the first order approximation (Eq. (3.17)). However, it is necessary to note that in general, these boundary forcing excitation terms are not negligible.

Upon substituting the series from the Eqs. (3.20) and (3.28) into the Eq. (3.29) it becomes apparent that only the equations corresponding to the amplitudes for the modes m_0, $3m_0$, $5m_0$, etc. are inhomogeneous. Therefore, the expansion of the $w_3(x, t_1, t_2)$ third–order approximation from equation (3.24) contains only terms with numbers that are odd multiples of m_0, analogous to the first–order solution $w_1(x, t_1, t_2)$ given in Eq. (3.20). The first three inhomogeneous equations derived from Eq. (3.29) are as follows

$$\begin{aligned}\frac{\partial^2 A_3^{(m_0)}}{\partial x^2} - \eta_{m_0}^2 A_3^{(m_0)} - \frac{1}{c_s^2}\frac{\partial^2 A_3^{(m_0)}}{\partial t_0^2} &= -i\omega_0\vartheta\frac{2}{c_s^2}\frac{\partial \alpha_1^{(m_0)}}{\partial t_2} e^{i(\xi_0 x - \omega_0 t_0)} \\ &- \frac{1}{\mu}\left(\vartheta^3 \sum_{k=1,3} C^{(m_0,k)}_{(1,\vartheta^3)} e^{ik(\xi_0 x - \omega_0 t_0)} + \ldots\right) + c.c.,\end{aligned} \tag{3.30}$$

$$\begin{aligned}\frac{\partial^2 A_3^{(3m_0)}}{\partial x^2} - \eta_{3m_0}^2 A_3^{(3m_0)} - \frac{1}{c_s^2}\frac{\partial^2 A_3^{(3m_0)}}{\partial t_0^2} &= -i3\omega_0\vartheta^3\frac{2}{c_s^2}\frac{\partial \alpha_1^{(3m_0)}}{\partial t_2} e^{i3(\xi_0 x - \omega_0 t_0)} \\ &- \frac{1}{\mu}\left(\vartheta^3 \sum_{k=1,3} C^{(3m_0,k)}_{(1,\vartheta^3)} e^{ik(\xi_0 x - \omega_0 t_0)} + \ldots\right) + c.c.,\end{aligned} \tag{3.31}$$

$$\begin{aligned}\frac{\partial^2 A_3^{(5m_0)}}{\partial x^2} - \eta_{5m_0}^2 A_3^{(5m_0)} - \frac{1}{c_s^2}\frac{\partial^2 A_3^{(5m_0)}}{\partial t_0^2} &= -i5\omega_0\vartheta^5\frac{2}{c_s^2}\frac{\partial \alpha_1^{(5m_0)}}{\partial t_2} e^{i5(\xi_0 x - \omega_0 t_0)} \\ &- \frac{1}{\mu}\left(\vartheta^5 \sum_{k=1,3,5} C^{(5m_0,k)}_{(1,\vartheta^5)} e^{ik(\xi_0 x - \omega_0 t_0)} + \ldots\right) + c.c.\end{aligned} \tag{3.32}$$

All forcing terms are ranked in descending order as defined by the ϑ parameter on the right–hand side of the above equations. In addition, these equations contain terms that produce nonphysical results. These terms are proportional to $e^{ir(\xi_0 x - \omega_0 t_0)}$ for each $A_3^{(rm_0)}$ amplitude and should be removed. In general, for each analysed equation there are an infinite number of these terms proportional to successive odd powers of ϑ. To remove all these components, it is necessary to solve an infinite number of coupled differential equations and to determine a set of functions of

the slow time variable $\{\alpha_1^{(rm_0)}(t_2)\}$. This process is tedious or even impossible to do analytically. Therefore, only the most important components have been considered to simplify the calculation. The larger number of forcing components – proportional to successive powers of the ϑ parameter – is included in the calculation, the more accurate solution will be, but the number of calculations will increase significantly.

The multiplescale perturbation technique was used to eliminate the secular terms in the higher–order approximate solutions. Therefore, the set of amplitudes $\{\alpha_1^{(rm_0)}(t_2)\}$ represents a solution of the coupled partial differential equations defined by

$$-i\omega_0\vartheta\frac{2}{c_s^2}\frac{\partial\alpha_1^{(m_0)}}{\partial t_2}-\frac{1}{\mu}\vartheta^3C_{(1,\vartheta^3)}^{(m_0,1)}+\ldots=0, \tag{3.33}$$

$$-i3\omega_0\vartheta^3\frac{2}{c_s^2}\frac{\partial\alpha_1^{(3m_0)}}{\partial t_2}-\frac{1}{\mu}\vartheta^3C_{(1,\vartheta^3)}^{(3m_0,3)}+\ldots=0, \tag{3.34}$$

$$-i5\omega_0\vartheta^5\frac{2}{c_s^2}\frac{\partial\alpha_1^{(5m_0)}}{\partial t_2}-\frac{1}{\mu}\vartheta^5C_{(1,\vartheta^5)}^{(5m_0,5)}+\ldots=0. \tag{3.35}$$

The analysis presented is restricted to the solution of the Eq. (3.33) with omitted terms proportional to ϑ^5 and higher powers of this parameter. The definitions of the $C_{(1,\vartheta^3)}^{(r,k)}, C_{(1,\vartheta^5)}^{(r,k)},\ldots$ coefficients result from the substitution of Eq. (3.20) into Eq. (3.25) and the expansion using the $\{Y^{(m)}(y)\}$ functional base given in Eq. (3.28). The complex solution of Eq. (3.33) where

$$C_{(1,\vartheta^3)}^{(m_0,1)}=-\frac{1}{4}\left(\frac{\mathcal{A}}{4}+\frac{\mathcal{B}}{2}+\mathcal{G}\right)\left(9\eta_{m_0}^4+2\eta_{m_0}^2\xi_0^2+9\xi_0^4\right)\left(\alpha_1^{(m_0)}\right)^2\overline{\alpha_1^{(m_0)}}, \tag{3.36}$$

can be represented in the form given by

$$\alpha_1^{(m_0)}(t_2)=\frac{1}{2}\beta^{(m_0)}(t_2)e^{i\gamma^{(m_0)}(t_2)}. \tag{3.37}$$

The over–line in Eq. (3.36) represents the complex conjugate. The $\beta^{(m_0)}(t_2)$ and $\gamma^{(m_0)}(t_2)$ functions of the t_2 slow time re real–valued. Upon the separation of the real and imaginary components and the removal of insignificant terms, the resulting expressions are obtained from Eq. (3.33) as

$$\frac{\partial\beta^{(m_0)}}{\partial t_2}\simeq 0, \tag{3.38}$$

$$\frac{\partial\gamma^{(m_0)}}{\partial t_2}\simeq-\frac{\vartheta^2c_s^2}{32\mu\omega_0}\left(\frac{\mathcal{A}}{4}+\frac{\mathcal{B}}{2}+\mathcal{G}\right)\left(9\eta_{m_0}^4+2\eta_{m_0}^2\xi_0^2+9\xi_0^4\right)\left(\beta^{(m_0)}\right)^2. \tag{3.39}$$

It follows from Eq. (3.38) that $\beta^{(m_0)}$ is equal to an arbitrary constant and this leads to the final solution in the form

$$\beta^{(m_0)}\simeq\beta_0^{(m_0)}, \tag{3.40}$$

$$\gamma^{(m_0)}\simeq-\frac{\vartheta^2c_s^2}{32\mu\omega_0}\left(\frac{\mathcal{A}}{4}+\frac{\mathcal{B}}{2}+\mathcal{G}\right)\left(9\eta_{m_0}^4+2\eta_{m_0}^2\xi_0^2+9\xi_0^4\right)\left(\beta_0^{(m_0)}\right)^2t_2+\gamma_0^{(m_0)}, \tag{3.41}$$

where $\beta_0^{(m_0)}$ and $\gamma_0^{(m_0)}$ are the integration constants. It yields from Eqs. (3.40) and (3.41) that

$$\alpha_1^{(m_0)}(t_2) \simeq \beta_0^{(m_0)} e^{i\left(-\frac{\vartheta^2 c_s^2}{32\mu\omega_0}\left(\frac{\mathcal{A}}{4}+\frac{\mathcal{B}}{2}+\mathcal{G}\right)(9\eta_{m_0}^4+2\eta_{m_0}^2\xi_0^2+9\xi_0^4)(\beta_0^{(m_0)})^2 t_2+\gamma_0^{(m_0)}\right)}. \tag{3.42}$$

Eq. (3.42) shows that the amplitude of the dominant m_0–th shear horizontal mode is periodic in the first–order approximate solution. Therefore, steady–state time–space solutions for this shear horizontal mode are possible in the nonlinear system under consideration.

Eqs. (3.21) and (3.42) yield the following dispersion relation for the dominant m_0–th shear horizontal mode

$$\begin{aligned}\omega_{m_0}(\xi_0, \beta_0^{(m_0)}) =& \omega_0 + \varepsilon\omega_1 + \varepsilon^2\omega_2 + \ldots = \\ =& \omega_0 + \varepsilon^2 \frac{\vartheta^2 c_s}{32\mu\sqrt{\xi_0^2+\eta_{m_0}^2}}\left(\frac{\mathcal{A}}{4}+\frac{\mathcal{B}}{2}+\mathcal{G}\right)(9\eta_{m_0}^4+2\eta_{m_0}^2\xi_0^2 \\ &+ 9\xi_0^4)\left(\beta_0^{(m_0)}\right)^2 + \ldots,\end{aligned} \tag{3.43}$$

where $\omega_0 = c_s\sqrt{\xi_0^2+\eta_{m_0}^2}$. The wavenumber–dependent nature of the nonlinear frequency shift is demonstrated by Eq. (3.43). For wavenumbers smaller than the η_{m_0} corresponding to the considered dominant mode, the distortion of the dispersion relation is nearly constant. A cubic function can be used to approximate the frequency shift for wavenumbers larger than this eigenvalue.

One should note that the change in angular frequency of the dispersion curve, specifically for the dominant m_0–th shear horizontal mode, is affected by the $\beta_0^{(m_0)}$ amplitude as well as the elastic constants $\mathcal{A}$, $\mathcal{B}$ and $\mathcal{G}$. By taking into account the most significant forcing terms, further calculations will then allow one to determine higher mode dispersion curve shifts, due to the presence of material nonlinearity.

The $C_{(1,\vartheta^3)}^{(rm_0,k)}$, $C_{(1,\vartheta^5)}^{(rm_0,k)}$, ...coefficients in Eqs. (3.33) – (3.34) tend to zero as the nonlinear material parameters vanish. In this scenario, the integration constants can be chosen such that the amplitudes $\alpha^{(rm_0)}(t_2)$ of all modes – except the m_0–th shear horizontal mode – are equal to zero. Hence, only the m_0–th shear horizontal mode exists in the system under investigation for material nonlinear constants equal to zero.

The double series represents the solution of the third order problem given by Eqs. (3.18) – (3.19) and can be defined as

$$w_3(x, y, t_0, t_2) = \sum_r Y^{(rm_0)} \sum_k \alpha_2^{(rm_0,k)}(t_2) e^{ik(\xi_0 x - \omega_0 t_0)}, \tag{3.44}$$

where indexes r, k $\in \{1,\ 3, \ldots\}$ are odd natural numbers and for $r = k$ the $\alpha_2^{(rm_0,k)}$ amplitudes are equal to zero. This result is obtained by eliminating the nonphysical secular terms. The derived mathematical representation implies that the w_3 third–order displacement field can be expressed

as the sum of an infinite number of space–time harmonic waves. The distribution of the wavefield along the y axis is given by the sum of an infinite number of the $Y^{(rm_0)}(y)$ eigenfunctions, multiplied by their corresponding amplitudes. The derivation of the amplitudes $\alpha_2^{(rm_0,k)}(t_2)$ requires calculations for the fifth–order approximation and the removal of secular components.

3.2.2.2 Third order approximation for the nondispersive SH0 mode

This subsection presents calculations for the first–order approximation, which contains only the linear SH0 mode (Eq. (3.21)). These calculations were carried out using the multiplescale perturbation method to find the fifth–order solution. The results show that the amplitudes of individual time–space harmonic waves in the first–order solution depend on the t_2 slow time scale.

Inserting Eq. (3.21) into the governing equation and associated boundary conditions – defined by Eq. (3.17) and (3.19) – yields the same expressions as before i.e., Eqs. (3.22) and (3.23). The $(\sigma_{yz}^{NL})_1$ term in Eq. (3.22) vanishes due to the definition of σ_{yz} in Eq. (3.8) and the form of the $Y^{(0)}(y)$ eigenfunction. The solution of this equation has the form given by Eq. (3.24). The right side of Eq. (3.27) is nonorthogonal only with the $Y^{(0)}(y)$ eigenfunction for the first order approximation defined in Eq. (3.20). This implies that all equations that correspond to $A_1^{(m)}(x,t_0,t_2)$ amplitudes are homogeneous and have trivial solutions, except for $m=0$. The only inhomogeneous equation can be written as

$$\frac{\partial^2 A_3^{(0)}}{\partial x^2} - \frac{1}{c_s^2}\frac{\partial^2 A_3^{(0)}}{\partial t_0^2} = \frac{\int_{-h}^{h}\left(\frac{2}{c_s^2}\frac{\partial^2 w_1}{\partial t_0 \partial t_2} - \frac{1}{\mu} f_1^{NL}\right) Y^{(0)}(y)dy}{\int_{-h}^{h}\left(Y^{(0)}(y)\right)^2 dy}. \tag{3.45}$$

The term f_1^{NL} is defined in Eq. (3.28). After the substitution of Eq. (3.21) into Eq. (3.45), the considered expression can be rewritten as

$$\begin{aligned}\frac{\partial^2 A_3^{(0)}}{\partial x^2} - \frac{1}{c_s^2}\frac{\partial^2 A_3^{(0)}}{\partial t_0^2} &= -i\frac{2\omega_0}{c_s^2}\sum_r r\vartheta^r \frac{\partial \alpha_1^{(r)}}{\partial t_2} e^{ir(\xi_0 x - \omega_0 t_0)} \\ &- \frac{1}{\mu}\left(\vartheta^3 \sum_k C_{(1,\vartheta^3)}^{(0,k)} e^{ik(\xi_0 x - \omega_0 t_0)} + \dots\right) + c.c.\end{aligned} \tag{3.46}$$

It is clear that any forcing term proportional to successive powers of $e^{i(\xi_0 x - \omega_0 t_0)}$ contributes to the generation of nonphysical secular terms. Therefore, these terms need to be eliminated to ensure that the third–order approximation remains bounded Nayfeh (2011). To avoid the presence of secular terms, the set of amplitudes $\alpha_1^{(r)}(t_2)$ must satisfy the set of an infinite number of ordinary differential equations. This system of differential equations can be organised in the same way as the system of equations for the dispersive modes. The first three equations are identical to Eqs. (3.33) – (3.35), where $m_0 = 0$. By performing further calculations, the $\alpha_1^{(r)}(t_2)$ individual amplitudes can be determined. Thus the third–order approximation becomes a solution of a

homogeneous differential equation. This solution is analogous to Eq. (3.21) i.e., the solution incorporate only the SH0 mode. In this case, the solution of Eq. (3.33) – with the $C^{(0,1)}_{(1,\vartheta^3)}$ coefficient denoted by

$$C^{(0,1)}_{(1,\vartheta^3)} = -3\left(\frac{\mathcal{A}}{4}+\frac{\mathcal{B}}{2}+\mathcal{G}\right)\xi_0^4\left(\alpha_1^{(1)}\right)^2\overline{\alpha_1^{(1)}}, \tag{3.47}$$

– can be written in the form

$$\alpha_1^{(1)}(t_2) \simeq \beta_0^{(1)} e^{i\left(-\frac{3\vartheta^2 c_s^2}{8\mu\omega_0}\left(\frac{\mathcal{A}}{4}+\frac{\mathcal{B}}{2}+\mathcal{G}\right)\xi_0^4\left(\beta_0^{(1)}\right)^2 t_2+\gamma_0^{(1)}\right)}. \tag{3.48}$$

Therefore, the amplitude of the primary SH0 mode exhibits periodic behaviour in the first–order approximate solution for the investigated nonlinear problem. The dispersion relation for the first harmonic of the SH0 mode – obtained from the Eqs. (3.21) and (3.48) – depends on its amplitude and can be expressed as

$$\begin{aligned}\omega_{SH0}(\xi_0,\beta_0^{(1)}) =&\omega_0+\varepsilon\omega_1+\varepsilon^2\omega_2+\ldots= \\ =&\omega_0+\varepsilon^2\frac{3\vartheta^2 c_s}{8\mu}\left(\frac{\mathcal{A}}{4}+\frac{\mathcal{B}}{2}+\mathcal{G}\right)\xi_0^3\left(\beta_0^{(1)}\right)^2+\ldots,\end{aligned} \tag{3.49}$$

where $\omega_0 = c_s\xi_0$. Eq. (3.49) shows that the frequency shift of the nondispersive SH0 mode is a cubic function of wavenumber.

It is interesting to note that the approach used in this section to obtain an approximate solution for the SH0 mode can also be used to analyse shear bulk waves.

3.3 Discussion for the analytical analysis of nonlinear shear horizontal guided waves modes

This section takes a broader view of nonlinear modes and discusses the approximate solutions obtained in sections 3.2.1 and 3.2.2. The general solution, formulated by Eq. (3.15), describes the propagation of shear horizontal guided waves in nonlinear materials, specifically for the case where the dominant dispersive mode is m_0. Eqs. (3.20) and (3.44) are the first– and third–order approximations, respectively. For the m_0 driving mode, the general solution can be rewritten as

$$\begin{aligned}w(x,y,t_0,t_2) =&\varepsilon\sum_{r=1,3,5,\ldots}\vartheta^r Y^{(rm_0)}\alpha_1^{(rm_0)}(t_2)e^{ir(\xi_0 x-\omega_0 t_0)} \\ &+\varepsilon^3\sum_{r=1,3,5,\ldots}Y^{(rm_0)}\sum_{k=1,3,5,\ldots}\alpha_2^{(rm_0,k)}(t_2)e^{ik(\xi_0 x-\omega_0 t_0)}+c.c.,\end{aligned} \tag{3.50}$$

where for $r = k$ the $\alpha_2^{(rm_0,k)}$ amplitudes are equal to zero. Therefore, the steady–state harmonic solution for the first–order homogeneous problem can be represented as the sum of infinite harmonic waves characterised by angular frequencies and wavenumber pairs $(\omega,\xi) = (r\omega_0, r\xi_0)$

resulting from the dispersion relations associated with each mode. The spatial profiles across the thickness of the structure for these waves correspond to the linear shear horizontal mode shapes. Notably, the first–order approximation is a sum of modes coupled by internal resonances. Consequently, the approximate solution can be reformulated as

$$\begin{aligned} w(x,y,t_0,t_2) =& \varepsilon Y^{(m_0)} \vartheta \alpha_1^{(m_0)}(t_2) e^{i(\xi_0 x - \omega_0 t_0)} \\ &+ \varepsilon \sum_{r=3,5,\ldots} \vartheta^r Y^{(rm_0)} \alpha_1^{(rm_0)}(t_2) e^{ir(\xi_0 x - \omega_0 t_0)} \\ &+ \varepsilon^3 \sum_{r=1,3,5,\ldots} Y^{(rm_0)} \sum_{k=1,3,5,\ldots} \alpha_2^{(rm_0,k)}(t_2) e^{ik(\xi_0 x - \omega_0 t_0)} + c.c. \end{aligned} \tag{3.51}$$

The modal decomposition method was used to determine the first– and third–order approximations and to identify the contributions of specific mode shapes and higher harmonics to the resulting displacement field. The solution described by Eq. (3.51), which includes the first and third–order approximations, can be interpreted as a nonlinear m_0–th mode, analogously to the nonlinear vibration analysis presented in Nayfeh (1995). In this context, the first term in Eq. (3.50) represents the wavefield corresponding to the driving m_0 SH mode, while the additional terms can be treated as the nonlinear distortion. As the analysed nonlinear material parameters approach zero, the terms resulting from hyperlasticity vanish. The concept of nonlinear modes in mechanical systems was initially introduced in the mid–1960s Rosenberg (1966) and subsequently explored in a series of articles on nonlinear discrete and continuous vibration systems Vakakis & Rand (1992a,b); Nayfeh & Nayfeh (1994, 1995); Nayfeh (1995); Kerschen (2014).

The approximate solution for the problem of nonlinear shear horizontal wave propagation, with the dominant nondispersive mode corresponding to $m_0 = 0$, can be expressed as

$$\begin{aligned} w(x,y,t_0,t_2) =& \varepsilon Y^{(0)} \sum_{r=1,3,5,\ldots} \vartheta^r \alpha_1^{(r)}(t_2) e^{ir(\xi_0 x - \omega_0 t_0)} \\ &+ \varepsilon^3 Y^{(0)} \sum_{r=1,3,5,\ldots} \alpha_2^{(r)}(t_2) e^{ir(\xi_0 x - \omega_0 t_0)} + c.c. \end{aligned} \tag{3.52}$$

As mentioned above, the steady–state harmonic solution for the first–order homogeneous problem can be expressed as the sum of harmonic waves with angular frequency wave number pairs arising from the $m_0 = 0$ shear horizontal mode dispersion relations. The SH0 mode shapes correspond to the through–thickness profiles for each of these waves. This first–order approximation involves only the SH0 mode, which for the problem under consideration, is in internal resonance only with itself. Furthermore, the solution obtained for this case can be interpreted as a nonlinear SH0 mode following Nayfeh & Nayfeh (1994); Nayfeh (1995); Nayfeh & Nayfeh (1995). It is noteworthy that the wavefield is distorted in this case only along the x–axis, due to the generation of odd higher

harmonics. The resulting approximate solution for this case can be rewritten as

$$\begin{aligned} w(x,y,t_0,t_2) =& \varepsilon Y^{(0)} \vartheta \alpha_1^{(1)}(t_2) e^{i(\xi_0 x - \omega_0 t_0)} \\ &+ \varepsilon Y^{(0)} \sum_{r=3,5,\ldots} \vartheta^r \alpha_1^{(r)}(t_2) e^{ir(\xi_0 x - \omega_0 t_0)} \\ &+ \varepsilon^3 Y^{(0)} \sum_{r=1,3,5,\ldots} \alpha_2^{(r)}(t_2) e^{ir(\xi_0 x - \omega_0 t_0)} + c.c. \end{aligned} \tag{3.53}$$

The first term in the equation represents the wavefield for the dominant SH0 mode in a linear material. The other terms can be interpreted as the nonlinear distortion of the wavefield, which becomes negligible as the nonlinear parameters approach zero.

In Nayfeh & Nayfeh (1994, 1995); Nayfeh (1995), a nonlinear mode vibration analysis is introduced, which gives the third–order contribution of all modes except the n–th linear mode to the n–th nonlinear mode in a nonlinear system. In the current work, the contribution of each rm_0–th shear horizontal mode shape to the nonlinear shear horizontal modes is determined using Eqs. (3.51) and (3.53), in both cases investigated. The first term in these equations represents the linear wavefield. The remaining terms can be treated as mode distortion or the residual part of the total wavefield. The amplitudes α, which depend on the slow time t_2, measure the contribution of each shear horizontal linear mode shape and the generated higher harmonics to the approximate solution.

The first and third approximate solutions of the considered nonlinear medium pass through their static equilibrium and simultaneously reach maximum displacements for the assumed value of the x coordinate (refer to Eqs. (3.51) and (3.53)). Thus, these solutions can be interpreted as nonlinear modes, according to the theory presented in Rosenberg (1966); Vakakis & Rand (1992a,b); Nayfeh & Nayfeh (1994); Nayfeh (1995); Nayfeh & Nayfeh (1995); Kerschen (2014).

The amplitude of the dispersive and nondispersive shear horizontal modes in the approximate solution depends on the third–order elastic constants $\mathcal{A}$ and $\mathcal{B}$ and the fourth–order elastic constant $\mathcal{G}$. The effect of other nonlinear material parameters is negligible. This conclusion follows from the definitions of the nonlinear stress tensor components given in Eqs. (3.7) and (3.8).

The approximate solution reveals the distortion of the dispersion curves for the dominant shear horizontal modes due to the presence of material nonlinearity. This distortion is directly related to a linear combination of specific nonlinear material constants, namely $\frac{\mathcal{A}}{4} + \frac{\mathcal{B}}{2} + \mathcal{G}$ and the square of the amplitude of the dominant m_0–th shear horizontal mode, as described in Eqs. (3.43) and (3.49). The analytical linear and nonlinear dispersion relations for selected dominant shear horizontal modes with amplitudes equal to 1, 5 and 10 μm are shown in Figure 3.1 to illustrate the dependence considered. A 2 mm thick aluminium plate is analysed as an example. The linear and nonlinear elastic material parameters are given in Table 3.1. The material density ρ = 2700 kg/m^3 is assumed. A scaling factor equal to 10 is applied to the component ω_2 in the derived dispersion relationships (Eqs. (3.43) and (3.49)) to visualise the

distortion of the dispersion curves. Analogous nonlinear distortions of the dispersion curves have been observed for Lamb wave propagation in a hyperelastic material Packo et al. (2016).

Table 3.1: Material properties (in GPa) of aluminium used in analytical calculations for nonlinear dispersion curves for dominant modes of shear horizontal guided waves.

λ	μ	$\mathcal{A}$	$\mathcal{B}$	$\mathcal{C}$	$\mathcal{E}$	$\mathcal{F}$	$\mathcal{G}$	$\mathcal{H}$
51.08	26.32	-195.90	-118.31	-3.46	81.74	165.23	228.40	-25.12

In the low frequency and wavenumber range, the distortion of the dispersion curves is marginal for different assumed amplitudes of the dominant mode. Nevertheless, as the frequency, wavenumber and amplitude increase, the differences between the linear and nonlinear curves become apparent.

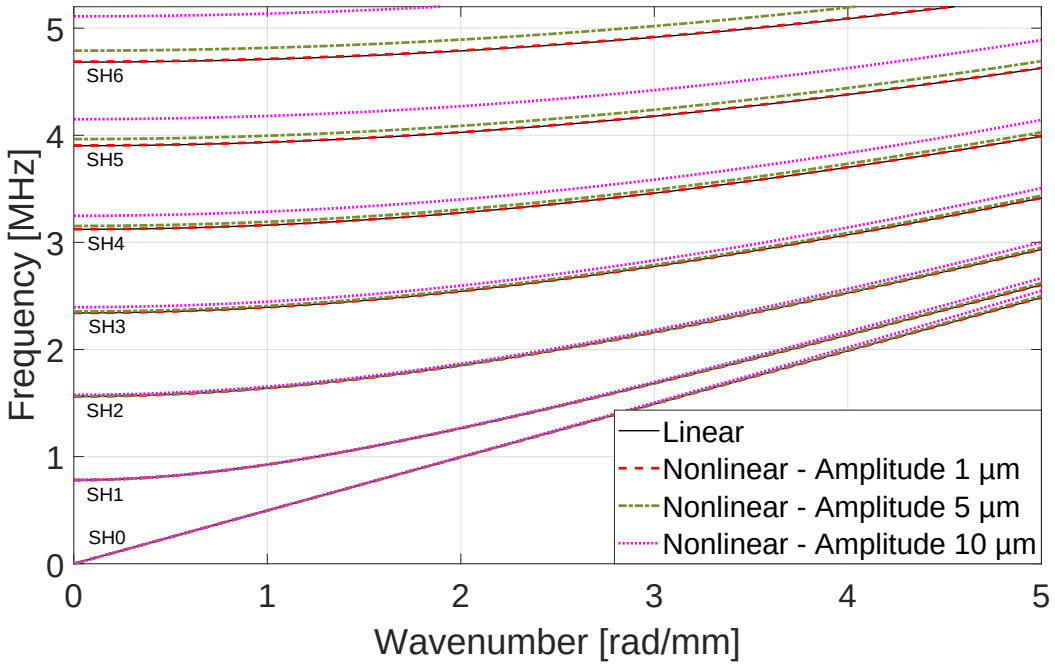

Figure 3.1: Linear and nonlinear analytical dispersion curves for dominant shear horizontal modes (Eqs. (3.43) and (3.49)) in a 2 mm thick aluminium plate for selected amplitudes. The scale factor for component ω_2 is equal to 10.

Figure 3.2 illustrates the nonlinear frequency shift (without scaling factor) as a function of wavenumber. For dispersive modes, one can see that this function is constant for wavenumbers much smaller than the η_m^2 eigenvalue corresponding to the selected mode. This conclusion follows from Eq. (3.43). However, for wavenumbers much greater than the eigenvalue associated with the analysed shear horizontal mode, the nonlinear frequency correction can be approximated as a cubic function of the wavenumber. For the nondispersive mode SH0, the frequency correction is a cubic

function of the wavenumber (see Eq. (3.49)). For clarity, the frequency correction for the SH0 mode is plotted as a solid line.

It is essential to state that the stress values in the material, limit the applicability of the theory presented on the distortion of dispersion curves. Plastic deformation could arise for the state of material, for which the component related to the material nonlinearity in the dispersion relation is significant.

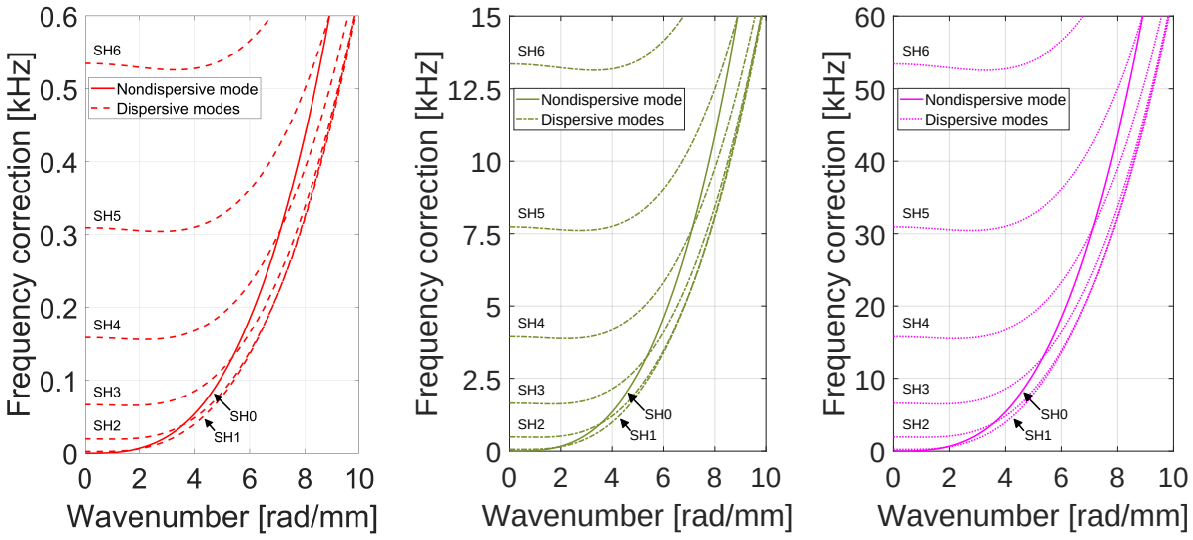

Figure 3.2: The analytical nonlinear frequency correction for 2 mm thick aluminium plate, for selected values of amplitude of the dominant mode: (a) 1 μm, (b) 5 μm and (c) 10 μm.

Chapter 4

Analytical investigation of the Luxembourg–Gorky effect for shear horizontal guided waves

This chapter investigates the Luxembourg–Gorky (L–G) effect for shear horizontal guided waves. This nonclassical effect was originally observed for electromagnetic waves in the early 1930s, and explained theoretically in the following few decades. Similar effect was also observed in the early 2000s for ultrasonic waves, but up to date not fully explained. This chapter presents the theoretical work that aims to fulfil this gap. Firstly, the theoretical background behind the original L–G effect is provided, for the sake of completeness. Then the retooled nonlinear L–G effect for shear horizontal waves is investigated analytically.

4.1 The Luxembourg–Gorky effect for electromagnetic waves

4.1.1 Background

The L–G effect is one of many nonlinear effects observed for electromagnetic waves. This nonlinear and nonclassical phenomenon was first observed and reported for radio waves in the early 1930s, when the powerful broadcasting radio station in Luxembourg (251.9 kHz) could be heard in Eindhoven in the background of a number of other weaker radio transmitters located in Beromünster (651.7 kHz), Budapest (545 kHz) or Milan (902.9 kHz) Tellegen (1933). A similar phenomenon was observed in the city of Gorky (today Nizhny Novgorod), where a signal generated by a high–power Moscow transmission facility could be detected while other local radio stations were being received. According to the first observation and investigation of the L–G effect, the wave to which the modulation is transferred is called the “wanted” wave, and the wave from which the modulation is transferred is called the “interacting”, “unwanted” or “disturbing”

wave. This terminology is used throughout the current study on the elastic equivalent of the L–G effect. The L–G effect for electromagnetic waves, with the individual waves denoted, is schematically illustrated in Figure 4.1.

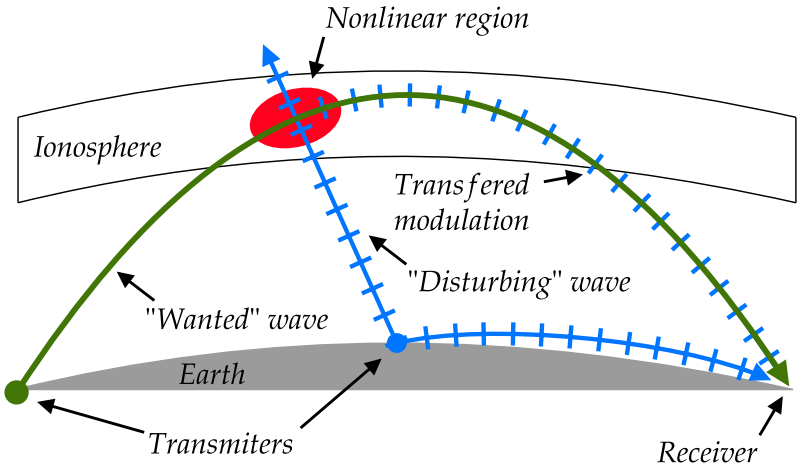

Figure 4.1: A schematic visualization of the nonlinear mechanism of the Luxembourg–Gorky effect.

Following initial reports Bailey & Martyn (1934), it has been proposed that the observed L–G effect originates from nonlinear absorption of transmitted radio waves. These authors ground their theoretical explanation on concepts associated with electrical discharges in gases Huxley & Ratcliffe (1949). The first theoretical explanation of the L–G effect initiated a series of researches based on the theory of ionospheric physics Bailey (1965); Ginzburg (1970); Bassanini (1974); Gurevich (1978). These analytical studies demonstrate that the interacting radio wave emitted by a powerful radio station can significantly disturb the lower ionosphere and affect the upper ionosphere. Therefore, heating of electrons that form plasma in the lower ionosphere leads to an increase in their effective temperature. As a result, the frequency of electron collisions increases, thus enhancing nonlinear absorption of radio waves. The simultaneous interaction of the "wanted" wave and the "interacting" wave in the nonlinear region of the locally heated plasma generates combined wave components, leading to modulation transfer.

Another independent theoretical explanation for the L–G effect is given in Graffi (1936). This research also focuses on nonlinear radio wave attenuation. However, the entire theoretical investigation focuses on systems with memory effects. Consequently, a new nonlinear hereditary model for a current density in plasma has been formulated Fabrizio & Morro (2003). This model is consistent with the ideas introduced by Volterra and Boltzmann for systems with memory, which in mechanics correspond to viscoelastic materials. The study in Graffi (1936) emphasises that the L–G effect occurs due to the simultaneous action of hereditary and nonlinear effects.

Different approaches have been adopted to describe the state of the nonlinear ionospheric plasma. These include: the elementary nonkinetic theory, the kinetic theory and the

magnetohydrodynamic approach Baranov (2006). In the elementary theory, the velocity distributions of electrons and ions are ignored and the concept of the "average" electron (or ion) is adopted. Hence, the state of plasma is characterised by velocities of these "average" particles. Their effective temperature can be calculated on the basis of their kinetic energy for the considered medium, because the temperature is a measure of the average kinetic energy. On the other hand, kinetic theory takes into account the probability distribution of electron and ion velocities, which is governed by the Boltzmann kinetic equation. This theory was introduced in Ginzburg (1948, 1970); Ginzburg & Gurevich (1960) to provide a theoretical explanation of the L–G effect. In the hydrodynamic theory, the plasma is treated as a fluid and averaged properties are used for its hydrodynamic description. The hydrodynamic approach is attractive because the hydrodynamic equations are easier to solve than the Boltzmann equation.

The research work described in this dissertation investigates the L–G effect retooled for elastic shear horizontal guided waves. Although, the work presented relies on the fundamentals of elastic wave theory and nonlinear dissipation, it is inspired by the previous work on electromagnetic waves in ionosphere. Therefore, a brief overview of the elementary nonkinetic ionospheric plasma theory is given in the next section, for the sake of completeness.

4.1.2 Electromagnetic waves in weak nonlinear plasma

The four coupled Maxwell equations provide a complete description of the electromagnetic field in an arbitrary medium. These equations are given as

$$\nabla \cdot \mathbf{D} = \varrho, \tag{4.1}$$

$$\nabla \times \mathbf{E} = -\frac{\partial \mathbf{B}}{\partial t}, \tag{4.2}$$

$$\nabla \cdot \mathbf{B} = 0, \tag{4.3}$$

$$\nabla \times \mathbf{H} = \mathbf{J} + \frac{\partial \mathbf{D}}{\partial t}. \tag{4.4}$$

Here $\mathbf{E}$, $\mathbf{D}$, $\mathbf{B}$, $\mathbf{H}$, $\mathbf{J}$ and ϱ represent the electric field strength, electric induction, magnetic induction, magnetic field strength, current density and charge density, respectively. The relationships between the electric strength field and the electric induction field, and between the magnetic strength field and the magnetic induction field, in the Maxwell equations are defined as

$$\mathbf{D} = \hat{\varepsilon}\mathbf{E}, \tag{4.5}$$

$$\mathbf{B} = \hat{\mu}\mathbf{H}, \tag{4.6}$$

where $\hat{\mu}$ represents the magnetic permeability, while $\hat{\varepsilon}$ denotes the electric permittivity. In general, these physical quantities are second–order tensors. Since isotropic ionospheric plasma is investigated, both $\hat{\mu}$ and $\hat{\varepsilon}$ can be considered as scalars.

When the curl operation is applied to Eqs. (4.2) and (4.4) (i.e., the Faraday and the Ampere laws), and Eqs. (4.1) and (4.3) (i.e., the Gauss laws for electric and magnetic fields) are incorporated – together with the constitutive relations (4.5) and (4.6) – the partial differential equations governing propagation of electromagnetic waves can be obtained. The first governing equation represents the electric field and the remaining equation corresponds to the magnetic field.

In the elementary nonkinetic theory, the analytical description of the L–G effect based on the interaction of electromagnetic waves requires only the wave equation related to the **E** electric field strength Ginzburg & Gurevich (1960); Ginzburg (1970); Gurevich (1978). Nevertheless, additional nonlinear relationships are essential to accurately describe the state of the medium under investigation i.e., the ionospheric plasma. Consequently, in this approach the state of the plasma is defined by two variables: the mean velocity of the directed motion of electrons and the effective electron temperature Ginzburg & Gurevich (1960); Ginzburg (1970); Gurevich (1978). By definition, the flow of charged particles through a specified surface in a plasma is a current density which is directly proportional to the mean velocity of motion of electrons.

4.1.3 Physical mechanism of the L–G effect for electromagnetic waves

As explained in the previous section, the analysis of radio wave propagation allows one to use the wave equation for the electric field as

$$\nabla^2\mathbf{E} - \nabla(\nabla\cdot\mathbf{E}) - \hat{\mu}\frac{\partial\mathbf{J}}{\partial t} - \hat{\mu}\hat{\varepsilon}\frac{\partial^2\mathbf{E}}{\partial t^2} = 0. \tag{4.7}$$

The state of the ionospheric plasma is completely defined by the current density and the temperature. The equations that govern these quantities can be expressed as Ginzburg & Gurevich (1960); Gurevich (1978)

$$\frac{\partial\mathbf{J}}{\partial t} + \nu(T_e)\mathbf{J} = \frac{e^2N}{m_e}\mathbf{E}, \tag{4.8}$$

$$\frac{\partial T_e}{\partial t} + \delta_c(T_e)\nu(T_e)(T_e - T) = \frac{2}{3\kappa N}\mathbf{J}\cdot\mathbf{E}. \tag{4.9}$$

In these relationships e, m_e, N, κ, ν, and δ_c represent the charge and the mass of the electron, the concentration of electrons, the Boltzmann constant, the effective collisional frequency of electrons, and the mean effective energy transfer fraction in collisions between electrons and heavy particles, respectively. Furthermore, T_e denotes the effective temperature of the electrons, while T represents the absolute temperature of the plasma in the absence of an electric field. Eqs. (4.7) – (4.9) form a system of nonlinear differential equations that are coupled.

The model illustrated here finds applications in the study of various nonlinear phenomena associated with propagation and interaction of radio waves in ionospheric plasma. Eqs. (4.7) – (4.9) indicate that the propagation of electromagnetic waves in considered medium leads to the

generation of a flow of charged particles. As a result, the mean velocity of plasma molecules increases, leading to a rise in their effective temperature. This is because temperature is a measure of the average kinetic energy of particles in the given medium that consists of partly or completely ionised gases. For electromagnetic fields that cause a small temperature increase of ionospheric plasma, Eqs. (4.7) – (4.9) describe the linear attenuation mechanism. For this linear dissipation phenomenon, the energy of the electromagnetic waves is converted into the kinetic energy of the particles forming the plasma, which ultimately leads to a growth in their effective temperature.

The interaction of high–power radio waves with plasma can lead to a significant rise in the local effective electron temperature by a factor of 20 to 40 Gurevich (1976). This increase in temperature causes a corresponding increase in the effective collision frequency of the electrons, which can result in an amplification of the nonlinear absorption of radio waves. As a result, local nonlinear inhomogeneities are formed in the plasma, which may provide opportunities to observe nonlinear phenomena associated with the interaction of radio waves. The approximate solution to the problem defined by Eqs. (4.7) – (4.9) – which predicts the physical phenomena described – is based on the perturbation technique and can be found in the relevant literature e.g., Ginzburg (1970); Plotkin (1977); Gurevich (1978).

This analytical method yields a set of linear partial differential equations that must be solved recursively. Analytical solutions of these linear equations are successive approximations to the exact solution of the original nonlinear problem. The nonlinear forcing terms in these equations can be interpreted as the excitation of higher order approximations by the lower order approximations. The nature of these terms depends on the assumed definition of nonlinearity in the system under consideration. For the mathematical model resulting from the application of the perturbation technique, it is evident that the nonlinear forcing terms for these successive approximation solutions include components related to a variety of phenomena, including cross–modulation, generation of higher harmonics and modulation transfer. The latter effect is of particular interest in the work presented in this dissertation.

An alternative mathematical description of the nonlinear attenuation described above is the Graffi model Graffi (1936); Fabrizio & Morro (2003), which was mentioned in Section 4.1. This model is also grounded in the elementary plasma theory and adopts the concept of an “average” electron. However, it does not address the relationships between temperature, electric field strength and current density in the plasma. Instead, it defines a nonlinear hereditary relation for the current density and the electric field strength as Graffi (1936); Fabrizio & Morro (2003)

$$\mathbf{J}(t) = \int_0^t \hat{\boldsymbol{\sigma}}\mathbf{E}(\tau)d\tau + \int_0^t \int_0^t \int_0^t \hat{\boldsymbol{\gamma}}\mathbf{E}(\tau_1)\mathbf{E}(\tau_2)\mathbf{E}(\tau_3)d\tau_1 d\tau_2 d\tau_3 + \cdots , \tag{4.10}$$

where the kernels functions $\hat{\boldsymbol{\sigma}}$ and $\hat{\boldsymbol{\gamma}}$ – which govern the conductivity phenomenon in plasma – are functions of the $(t-\tau)$ and $(t-\tau_1, t-\tau_2, t-\tau_3)$ arguments, respectively. The Graffi model

indicates that the L–G effect results from the simultaneous action of hereditary and nonlinear effects. The terms incorporated in the considered equation describe the broad context of nonlinear conduction observed in plasma. The primary and secondary components are associated with the linear and nonlinear contributions to the $\mathbf{J}(t)$ current density, respectively. More detailed discussion of Eqs. (4.7) and (4.10) can be found in Graffi (1936); Fabrizio & Morro (2003). It is important to emphasise that the definition of $\mathbf{J}(t)$ presented here is inherently related to the group of materials with memory effects. In mechanical systems, such properties characterise viscoelastic materials, which arise directly from the definition of elastic materials Christensen (2012); Findley et al. (1989); Carcione (2022). These materials are closely related to dissipation phenomenon.

In conclusion, the nonclassical modulation transfer phenomenon underlying the original L–G effect is attributed to nonlinear damping. Consequently, it is proposed that an equivalent nonlinear damping model can be formulated to explain the L–G effect retooled for elastic shear horizontal waves. This is the main motivation for the research presented in the next section.

4.2 The L–G effect retooled for shear horizontal guided waves

4.2.1 Background

The mechanism of wave modulation transfer – similar to the original L–G effect for electromagnetic waves – is reported in Zaitsev et al. (2002b,a). The effect described in this work is associated with the nonclassical (i.e., nonfrictional and nonhysteretic) and nonlinear damping of waves, resulting from the crack–wave interaction. This mechanism can be briefly outlined as follows. Experimental investigations have demonstrated that as the amplitude of a strong ("disturbing") wave increases, the amplitude of a weaker ("wanted") wave decreases without a simultaneous frequency shift. Consequently, classical theories – involving adhesive–friction or hysteretic damping – are not sufficient to explain the observed wave attenuation. Interestingly, this phenomenon has been observed even for very low strain levels, insufficient to initiate crack opening but sufficient to perturb contacting crack asperities. This perturbation of asperities results in a local temperature gradient. In Zaitsev et al. (2002a), the wave attenuation is explained by the thermoelastic phenomenon in the vicinity of the crack.

For aluminium, empirical evidence presented in Klepka et al. (2011) firmly establishes a direct relationship between the temperature field in the vicinity of the crack and the transfered modulation sideband amplitude. Furthermore, empirical investigations in Moussatov et al. (2003) and theoretical analyses in Fillinger et al. (2006) suggest the existence of nonhysteretic dissipative nonlinearity attributed to crack behaviour, when the L–G retooled effect for elastic waves is investigated. The presence of a strong wave significantly influences dissipation of the weak wave,

as it propagates through a crack. This dissipation is attributed to significant thermoelastic losses that do not affect local elastic properties of the system. Previous research studies suggest that under low strain conditions – for which crack–induced dissipation by adhesion or friction is not possible – small cracks (or distributed micro–cracks) can effectively dissipate elastic wave energy due to the thermoelastic phenomenon, especially at inner crack interfaces. Mathematical formulae describing thermoelastic losses in the vicinity of these strip–like inner contacts are given in Zaitsev et al. (2002a) but a full physical and analytical explanation is not provided.

These formulae are based on the well–established approximation used in the study of polycrystalline materials Landau & Lifshitz (1989). It is important to note that the experimental research cited above suggests a similar level of dissipation for larger cracks as well as for a large number of very small cracks. However, physical explanation of the experimentally demonstrated in Zaitsev et al. (2002b, 2005) nonlinear modulation transfer effect which is still challenging. In summary, this study acknowledges previous research work in the field demonstrating the connection between weaker wave attenuation and dissipative behaviour of cracks, which is analogous to attenuation in polycrystalline materials. However, all this work show that a comprehensive explanation of the modulation transfer mechanism remains incomplete.

In recent studies, a nonlinear modulation transfer phenomenon for shear horizontal guided waves has been observed in a locally cracked glass plate and reported in Osika et al. (2023a). However, physical explanation given in Zaitsev et al. (2005) – which relies on thermoelastic coupling – is insufficient to explain this phenomenon. This is mainly due to the inherent decoupling of displacement components associated with propagating shear waves and the temperature field. Hence, there is a need for another model of nonlinear mechanical wave dissipation.

4.2.2 Nonlinear dissipation in wave propagation

In this work, only shear horizontal waves are investigated. The propagation of these waves leads to generation of shear stresses within damaged area. This observation is consistent with the assumption made in Osika et al. (2022). In addition, this study assumes the presence of a closed crack, thereby representing scenarios in which propagating waves are unable to activate adhesive–frictional and hysteretic damping mechanisms. This assumption is in line with the work presented in Zaitsev et al. (2002a, 2005), where nonlinear damping that explains the L–G effect in mechanical systems results mainly from a strong locally enhanced thermoelastic phenomenon. This physical effect can be used to model the behaviour of polycrystalline materials, as shown in Landau & Lifshitz (1989). The theory behind this modelling originates from the pioneering research work in seismology Zener (1938); Zener et al. (1938). However, the model proposed in the current work, to explained the L–G effect retooled for shear horizontal elastic waves, utilises a

different physical mechanism of damping in the nonlinear damage region. The nonlinear viscoelastic material behaviour is suggested as the major cause of nonlinear attenuation and nonclassical modulation transfer. This damping model is typically used to study polycrystalline materials and to analyse mechanical properties of grain boundaries Zener (1941, 1948). Dissipation in this model arises from distortion of material structure. At the microscopic scale, structural inhomogeneities are closely related to grain boundaries, while at the meso–scales and macro–scales, inhomogeneities in elastic materials could be related to local defects such as fatigue cracks. A full explanation of this damping model is given in the following subsection. It is postulated that local nonlinear wave dissipation – not local nonlinear elasticity – is behind the investigated L–G effect. This is in line with the previous research work presented in Zaitsev et al. (2002b, 2005).

In theory, two primary mechanisms contributing to damping of elastic waves – i.e., thermoelasticity and viscoelasticity – can act simultaneously Achenbach (1973); Landau & Lifshitz (1989). In the case of propagating elastic waves, the thermoelastic effect results in the generation of temperature gradients within a solid medium. Therefore, local heat flows arise – accompanied by irreversible heat conduction processes – as explained in Zener (1938); Zener et al. (1938). These processes lead to an increase of entropy of the system and contribute to the attenuation of propagating waves. This mechanism is responsible mainly for the thermal–conduction contribution to energy dissipation. The second viscoelastic mechanism of damping is associated with irreversible processes arising from the finite velocity of individual particles in media, as discussed in Achenbach (1973); Landau & Lifshitz (1989). As a result, mechanical energy is ultimately converted into heat.

It is well known that shear horizontal guided waves cannot be attenuated by the thermoelastic effect, as explained in Achenbach (1973); Landau & Lifshitz (1989). This is due to the structure of physical and mathematical model behind the thermoelastic phenomenon. Therefore, the viscoelastic effect can only lead to the attenuation of shear horizontal guided waves. There is no reason why this effect could not be applied to model the attenuation of other types of waves propagating in solid media.

4.2.3 Shear horizontal guided waves in elastic medium with the local nonlinear inhomogeneity

The research presented investigates the acoustic equivalent of the L–G effect due to local material defects. Thus, a local nonlinear inhomogeneity of arbitrary shape is introduced into the considered mechanical system. This nonlinear region in solid medium is analogous to the significantly heated plasma that exhibit nonlinear properties, as described in Section 4.1. An introduced local nonlinearity in the mechanical medium can be interpreted as a small damage or

imperfection (e.g., fatigue crack, micro–cracks, delamination). Mathematical representation of this nonlinear region in the considered medium – described by two Lagrangian coordinates – can be given by

$$D = \{(x, y)|F(x, y) \geq 0\}. \tag{4.11}$$

The boundary of the introduced nonlinear region is defined as

$$\partial D = \{(x, y)|F(x, y) = 0\}, \tag{4.12}$$

where $F(x, y)$ is an arbitrary function that is positive in the nonlinear region of the analysed solid medium. One can see that Eq. (4.12) represents a nonparametric definition of the contour of the nonlinear region in the 2–D domain. Only finite damage is considered, so the area and the perimeter of the nonlinear region are bounded.

Nonclassical nonlinear attenuation characterises the inhomogeneity introduced into the solid medium. This assumption is consistent with the fundamental nature of the L–G effect for radio waves, where modulation transfer results from the nonlinear dissipation and the interaction of radio waves, as highlighted in Section 4.1. The mathematical model governing the propagation of shear horizontal guided waves incorporates local nonlinear damping through the Heaviside step function Θ with the arbitrarily selected function $F(x, y)$ as its parameter. Therefore, it becomes possible to decompose the stress as

$$\boldsymbol{\sigma} = \boldsymbol{\sigma}^E + \varepsilon\Theta(F(x, y))\boldsymbol{\sigma}^D, \tag{4.13}$$

where the first term (superscript E) in this equation is the linear elastic part and the second term (superscript D) is the local nonlinear part responsible for local dissipation. Here, a small parameter ε enables to identify which of the introduced terms is more significant.

Under the previously discussed assumptions Eq. (2.34) can be rewritten as

$$\rho\frac{\partial^2\mathbf{W}}{\partial t^2} = \nabla\boldsymbol{\sigma}^E + \varepsilon\nabla(\Theta(F(x, y))\boldsymbol{\sigma}^D) + \tilde{\mathbf{F}} \tag{4.14}$$

and the traction free boundary conditions become

$$\mathbf{t} = (\boldsymbol{\sigma}^E + \varepsilon\Theta(F(x, y))\boldsymbol{\sigma}^D)\mathbf{n} = 0, \text{ at } y = \pm h. \tag{4.15}$$

Hence, the mathematical model governing the propagation phenomenon and interaction of guided waves with a local nonlinearity is given by Eqs. (4.14) and (4.15). If the boundary of introduced nonlinear inhomogenity does not coincide with the surfaces of the plate, the boundary conditions remain linear and involve only the $\boldsymbol{\sigma}^E$ term.

Invariance along the z–axis is a key assumption made in this dissertation. In the case of linear elastic materials, the equations for the w displacement component are decoupled from those for the displacement u and v components. The first mentioned governing equation and its associated

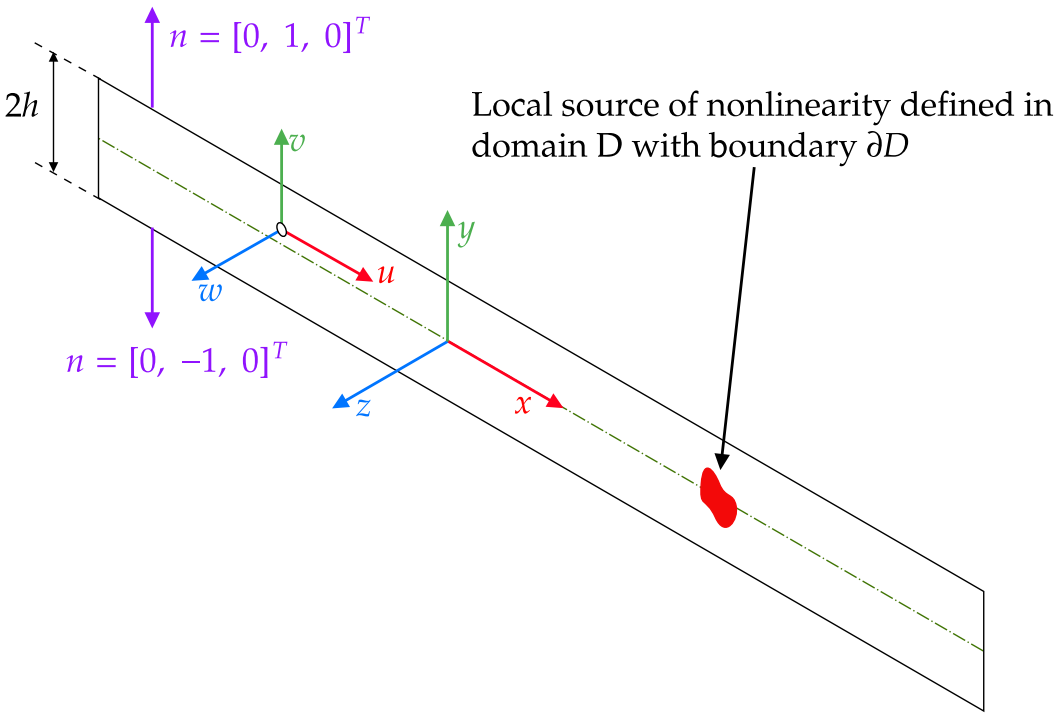

Figure 4.2: Geometrical representation of a cross–section of an elastic plate with a marked local nonlinear inhomogeneity (nonlinear damping).

boundary conditions – corresponding to the w displacement component – represent the mathematical model of shear horizontal guided waves propagation. The phenomenon of Lamb wave propagation is governed by the remaining two partial differential equations and boundary conditions corresponding to the u and v displacement components, as described in Giurgiutiu (2008). The current work focuses on the analysis of nonlinear phenomena for shear horizontal guided waves, which requires the assumption that $\mathbf{W} = [0, 0, w]^T$ and $\tilde{\mathbf{F}} = [0, 0, \tilde{F}_z]^T$. This implies that the displacement and mass forces components associated with the x and y directions have negligible magnitudes. Therefore, the general mathematical model of guided waves given by Eq. (4.14) becomes a scalar partial differential equation. In the absence of body forces, this equation can be reformulated as

$$\rho\frac{\partial^2 w}{\partial t^2} = \frac{\partial \sigma^E_{xz}}{\partial x} + \frac{\partial \sigma^E_{yz}}{\partial y} + \varepsilon\left(\Theta(F(x,y))\left(\frac{\partial \sigma^D_{xz}}{\partial x} + \frac{\partial \sigma^D_{yz}}{\partial y}\right)\right. \\ \left. + \delta(F(x,y))\left(\frac{\partial F}{\partial x}\sigma^D_{xz} + \frac{\partial F}{\partial y}\sigma^D_{yz}\right)\right). \tag{4.16}$$

In this equation, δ represents the Dirac delta function obtained by differentiating the Θ Heaviside step function. Only the t_z component of the traction vector is considered, according to the assumption adopted. Therefore, the necessary traction–free boundary conditions for the

propagation of shear horizontal guided waves are given by

$$t_z = \pm\sigma_{yz}^{E} \pm \varepsilon\Theta(F(x,y))\sigma_{yz}^{D} = 0, \text{ for } y = \pm h. \tag{4.17}$$

The following subsection provides an in–depth consideration of the nonlinear components in Eqs. (4.16) and (4.17)

4.2.4 Nonclassical nonlinear ultrasonic wave dissipation model

To incorporate the nonlinear viscoelastic effect in the assumed isotropic vicinity of the crack (the nonlinear region shown in Figure 4.2), a nonlinear dissipation function $\Psi(\dot{\varepsilon}_{GL})$ – that extends the linear dissipation model employed in Landau & Lifshitz (1989) – is proposed. This function can be given as the appropriate expansion to the fourth order i.e.,

$$\Psi(\dot{\boldsymbol{\varepsilon}}_{\boldsymbol{GL}}) = \frac{\zeta}{2}J_1^2 + \eta J_2 + \frac{\mathcal{I}}{3}J_3 + \mathcal{J}J_1J_2 + \frac{\mathcal{K}}{3}J_1^3 + \mathcal{M}J_1J_3 + \mathcal{N}J_1^2J_2 + \mathcal{O}J_2^2 + \mathcal{P}J_1^4. \tag{4.18}$$

The arguments of this function are the first–time derivatives of the assumed strain tensor components i.e., the components of the strain rate tensor. The scalars J_1, J_2 and J_3 in Eq. (4.18) represent the first, second and third invariants of the first time derivative of the assumed strain tensor (i.e., the Green–Lagrange strain tensor), respectively. These invariants are defined as follows

$$\begin{aligned} J_1 &= \operatorname{tr}(\dot{\boldsymbol{\varepsilon}}_{\boldsymbol{GL}}), \\ J_2 &= \operatorname{tr}(\dot{\boldsymbol{\varepsilon}}_{\boldsymbol{GL}}^2), \\ J_3 &= \operatorname{tr}(\dot{\boldsymbol{\varepsilon}}_{\boldsymbol{GL}}^3). \end{aligned} \tag{4.19}$$

The values of the $\Psi(\dot{\varepsilon}_{GL})$ damping function represent the total mechanical energy dissipated per unit volume. This $\Psi(\dot{\varepsilon}_{GL})$ function is in analogous to the strain energy function $\dot{\varepsilon}_{GL}$, which characterises the properties of elastic medium, as described in Landau & Lifshitz (1989); Norris (1998). The proposed model, containing the third– and fourth–order nonlinear terms, enables a comprehensive investigation of the interaction of horizontal shear waves within a region characterised by nonlinear attenuation.

The stress components corresponding to the viscous effects $\boldsymbol{\sigma}^D$ are defined by the adopted stress measure as

$$\sigma_{ij}^{D} = \frac{\partial\Psi(\dot{\boldsymbol{\varepsilon}}_{\boldsymbol{GL}})}{\partial(\dot{\varepsilon}_{GL})_{ij}}. \tag{4.20}$$

Therefore, the stress tensor representing the nonlinear viscous effect can be expressed as follows

$$\begin{aligned} \boldsymbol{\sigma}^D = {} & \zeta J_1\mathbf{I} + 2\eta\dot{\boldsymbol{\varepsilon}}_{\boldsymbol{GL}} + \mathcal{I}\dot{\boldsymbol{\varepsilon}}_{\boldsymbol{GL}}^2 + \mathcal{J}J_2\mathbf{I} + 2\mathcal{J}J_1\dot{\boldsymbol{\varepsilon}}_{\boldsymbol{GL}} + \mathcal{K}J_1^2\mathbf{I} + \mathcal{M}J_3\mathbf{I} \\ & + 3\mathcal{M}J_1\dot{\boldsymbol{\varepsilon}}_{\boldsymbol{GL}}^2 + 2\mathcal{N}J_1J_2\mathbf{I} + 2\mathcal{N}J_1^2\dot{\boldsymbol{\varepsilon}}_{\boldsymbol{GL}} + 4\mathcal{O}J_2\dot{\boldsymbol{\varepsilon}}_{\boldsymbol{GL}} + 4\mathcal{P}J_1^3\mathbf{I}, \end{aligned} \tag{4.21}$$

where $\mathbf{I}$ is the identity tensor. The elastic part of the stress tensor is linear – as mentioned earlier – and can be express as

$$\boldsymbol{\sigma}^E = \lambda\operatorname{tr}(\boldsymbol{\varepsilon}_{\boldsymbol{GL}})\mathbf{I} + 2\mu\boldsymbol{\varepsilon}_{\boldsymbol{GL}}. \tag{4.22}$$

Here, λ and μ are the Lamé constants.

It is crucial to emphasise that the definition of the stress tensor, given in differential form by the sum of Eqs. (4.21) and (4.22), can be expressed in an integral form as well. Then this definition can be related to the hereditary effects used to explain the original L–G effect for electromagnetic waves. A more detailed discussion of this topic can be found in Appendix B.

In summary, the components of the stress tensor within the introduced nonlinear region are equal to the sum of the linear elastic and nonlinear viscous terms (Eq. (4.13)). Hence, the local nonlinear imperfection is modelled by the Kelvin–Voigt model with the nonlinear viscous component fully defined by the nonlinear damping function $\Psi(\dot{\boldsymbol{\varepsilon}}_{GL})$.

The stress components associated with the damping phenomenon involved in Eqs. (4.16) and (4.17) can be expressed as

$$\begin{aligned}\sigma_{xz}^{D} &= 2\eta\dot{\varepsilon}_{xz} + \mathcal{I}(\dot{\varepsilon}_{xx}\dot{\varepsilon}_{xz} + \dot{\varepsilon}_{xy}\dot{\varepsilon}_{yz} + \dot{\varepsilon}_{xz}\dot{\varepsilon}_{zz}) + 2\mathcal{J}\dot{\varepsilon}_{xz}(\dot{\varepsilon}_{xx} + \dot{\varepsilon}_{yy} + \dot{\varepsilon}_{zz}) \\ &\quad + 3\mathcal{M}(\dot{\varepsilon}_{xx} + \dot{\varepsilon}_{yy} + \dot{\varepsilon}_{zz})(\dot{\varepsilon}_{xx}\dot{\varepsilon}_{xz} + \dot{\varepsilon}_{xy}\dot{\varepsilon}_{yz} + \dot{\varepsilon}_{xz}\dot{\varepsilon}_{zz}) + 2\mathcal{N}\dot{\varepsilon}_{xz}(\dot{\varepsilon}_{xx} \\ &\quad + \dot{\varepsilon}_{yy} + \dot{\varepsilon}_{zz})^2 + 4\mathcal{O}\dot{\varepsilon}_{xz}(\dot{\varepsilon}_{xx}^2 + 2\dot{\varepsilon}_{xy}^2 + 2\dot{\varepsilon}_{xz}^2 + \dot{\varepsilon}_{yy}^2 + 2\dot{\varepsilon}_{yz}^2 + \dot{\varepsilon}_{zz}^2),\end{aligned} \tag{4.23}$$

$$\begin{aligned}\sigma_{yz}^{D} &= 2\eta\dot{\varepsilon}_{yz} + \mathcal{I}(\dot{\varepsilon}_{xy}\dot{\varepsilon}_{xz} + \dot{\varepsilon}_{yy}\dot{\varepsilon}_{yz} + \dot{\varepsilon}_{yz}\dot{\varepsilon}_{zz}) + 2\mathcal{J}\dot{\varepsilon}_{yz}(\dot{\varepsilon}_{xx} + \dot{\varepsilon}_{yy} + \dot{\varepsilon}_{zz}) \\ &\quad + 3\mathcal{M}(\dot{\varepsilon}_{xx} + \dot{\varepsilon}_{yy} + \dot{\varepsilon}_{zz})(\dot{\varepsilon}_{xy}\dot{\varepsilon}_{xz} + \dot{\varepsilon}_{yy}\dot{\varepsilon}_{yz} + \dot{\varepsilon}_{yz}\dot{\varepsilon}_{zz}) + 2\mathcal{N}\dot{\varepsilon}_{yz}(\dot{\varepsilon}_{xx} \\ &\quad + \dot{\varepsilon}_{yy} + \dot{\varepsilon}_{zz})^2 + 4\mathcal{O}\dot{\varepsilon}_{yz}(\dot{\varepsilon}_{xx}^2 + 2\dot{\varepsilon}_{xy}^2 + 2\dot{\varepsilon}_{xz}^2 + \dot{\varepsilon}_{yy}^2 + 2\dot{\varepsilon}_{yz}^2 + \dot{\varepsilon}_{zz}^2).\end{aligned} \tag{4.24}$$

Upon substitution of the adopted mathematical definitions of the strain and strain rate tensors in Eqs. (4.23) and (4.24), the definition of the considered stress tensor components can be rewritten as

$$\begin{aligned}\sigma_{xz}^{D} &= \eta\frac{\partial\dot{w}}{\partial x} + \frac{\mathcal{I}}{4}\left(2\frac{\partial w}{\partial x}\left(\frac{\partial\dot{w}}{\partial x}\right)^2 + \frac{\partial\dot{w}}{\partial y}\left(\frac{\partial w}{\partial x}\frac{\partial\dot{w}}{\partial y} + \frac{\partial\dot{w}}{\partial x}\frac{\partial w}{\partial y}\right)\right) + \mathcal{J}\frac{\partial\dot{w}}{\partial x}\left(\frac{\partial w}{\partial x}\frac{\partial\dot{w}}{\partial x}\right. \\ &\quad \left.+\frac{\partial w}{\partial y}\frac{\partial\dot{w}}{\partial y}\right) + \frac{3\mathcal{M}}{4}\left(\frac{\partial w}{\partial x}\frac{\partial\dot{w}}{\partial x} + \frac{\partial w}{\partial y}\frac{\partial\dot{w}}{\partial y}\right)\left(2\frac{\partial w}{\partial x}\left(\frac{\partial\dot{w}}{\partial x}\right)^2 + \frac{\partial\dot{w}}{\partial y}\left(\frac{\partial w}{\partial x}\frac{\partial\dot{w}}{\partial y}\right.\right. \\ &\quad \left.\left.+\frac{\partial\dot{w}}{\partial x}\frac{\partial w}{\partial y}\right)\right) + \mathcal{N}\frac{\partial\dot{w}}{\partial x}\left(\frac{\partial w}{\partial x}\frac{\partial\dot{w}}{\partial x} + \frac{\partial w}{\partial y}\frac{\partial\dot{w}}{\partial y}\right)^2 + \mathcal{O}\frac{\partial\dot{w}}{\partial x}\left(2\left(\frac{\partial w}{\partial x}\frac{\partial\dot{w}}{\partial x}\right)^2 + \right. \\ &\quad \left. 2\left(\frac{\partial w}{\partial y}\frac{\partial\dot{w}}{\partial y}\right)^2 + \left(\frac{\partial w}{\partial x}\frac{\partial\dot{w}}{\partial y} + \frac{\partial\dot{w}}{\partial x}\frac{\partial w}{\partial y}\right)^2 + \left(\frac{\partial\dot{w}}{\partial x}\right)^2 + \left(\frac{\partial\dot{w}}{\partial y}\right)^2\right),\end{aligned} \tag{4.25}$$

$$\sigma_{yz}^{D} = \eta\frac{\partial\dot{w}}{\partial y} + \frac{\mathcal{I}}{4}\left(2\frac{\partial w}{\partial y}\left(\frac{\partial\dot{w}}{\partial y}\right)^{2} + \frac{\partial\dot{w}}{\partial x}\left(\frac{\partial w}{\partial x}\frac{\partial\dot{w}}{\partial y} + \frac{\partial\dot{w}}{\partial x}\frac{\partial w}{\partial y}\right)\right) + \mathcal{J}\frac{\partial\dot{w}}{\partial y}\left(\frac{\partial w}{\partial x}\frac{\partial\dot{w}}{\partial x} + \frac{\partial w}{\partial y}\frac{\partial\dot{w}}{\partial y}\right) + \frac{3\mathcal{M}}{4}\left(\frac{\partial w}{\partial x}\frac{\partial\dot{w}}{\partial x} + \frac{\partial w}{\partial y}\frac{\partial\dot{w}}{\partial y}\right)\left(2\frac{\partial w}{\partial y}\left(\frac{\partial\dot{w}}{\partial y}\right)^{2} + \frac{\partial\dot{w}}{\partial x}\left(\frac{\partial w}{\partial x}\frac{\partial\dot{w}}{\partial y} + \frac{\partial\dot{w}}{\partial x}\frac{\partial w}{\partial y}\right)\right) + \mathcal{N}\frac{\partial\dot{w}}{\partial y}\left(\frac{\partial w}{\partial x}\frac{\partial\dot{w}}{\partial x} + \frac{\partial w}{\partial y}\frac{\partial\dot{w}}{\partial y}\right)^{2} + \mathcal{O}\frac{\partial\dot{w}}{\partial y}\left(2\left(\frac{\partial w}{\partial x}\frac{\partial\dot{w}}{\partial x}\right)^{2} + 2\left(\frac{\partial w}{\partial y}\frac{\partial\dot{w}}{\partial y}\right)^{2} + \left(\frac{\partial w}{\partial x}\frac{\partial\dot{w}}{\partial y} + \frac{\partial\dot{w}}{\partial x}\frac{\partial w}{\partial y}\right)^{2} + \left(\frac{\partial\dot{w}}{\partial x}\right)^{2} + \left(\frac{\partial\dot{w}}{\partial y}\right)^{2}\right). \tag{4.26}$$

The elastic part of the stress components from Eqs. (4.16) and (4.17) can be rewritten as

$$\sigma_{xz}^{E} = \mu\varepsilon_{xz} = \mu\frac{\partial w}{\partial x}, \tag{4.27}$$

$$\sigma_{yz}^{E} = \mu\varepsilon_{yz} = \mu\frac{\partial w}{\partial y}. \tag{4.28}$$

Following the derived stress tensor components, this study investigates an odd nonlinear function of the w displacement component associated with shear horizontal waves. Thus, the present work focuses on the local odd nonlinearity, which has a significant consequence on the analytical calculations based on the applied perturbation method.

4.3 Interaction of shear horizontal guided waves with the local nonlinearity – perturbation analysis

4.3.1 Formulation of the problem

After substituting Eqs. (4.27) – (4.28) into the governing Eq. (4.16) and its associated boundary conditions from Eq. (4.17), the originally stated problem can be reformulated as

$$\frac{\partial^2 w}{\partial x^2} + \frac{\partial^2 w}{\partial y^2} - \frac{1}{c_s^2}\frac{\partial^2 w}{\partial t^2} = -\frac{\varepsilon}{\mu}\left(\Theta(F(x,y))\left(\frac{\partial\sigma_{xz}^{D}}{\partial x} + \frac{\partial\sigma_{yz}^{D}}{\partial y}\right) + \delta(F(x,y))\left(\frac{\partial F}{\partial x}\sigma_{xz}^{D} + \frac{\partial F}{\partial y}\sigma_{yz}^{D}\right)\right) \tag{4.29}$$

and

$$\sigma_{yz} = \sigma_{yz}^{E} + \varepsilon\Theta(F(x,y))\sigma_{yz}^{D} = 0, \text{ for } y = \pm h, \tag{4.30}$$

where $c_s = \sqrt{\frac{\mu}{\rho}}$ is the shear wave velocity in elastic solid. The nonlinear homogeneous problem given by Eqs. (4.29) and (4.30) is a complete mathematical formulation of the interaction of shear horizontal guided waves with a local nonlinear region.

Eqs. (4.29) – (4.30) define the nonlinear boundary value problem for the considered nonlinear autonomous mechanical system. Solving this problem analytically is complex and challenging

due to the nonlinearity involved. However, the perturbation techniques can be used, leading to an asymptotic approximation of the exact solution. In view of the local nature of the nonlinearity analysed, the application of the fundamental perturbation technique is adequate. This is due to the observation that the local nonlinearity does not lead to secular terms in the approximate solution, as explain in Nayfeh (2008, 2011); Holmes (2012).

The formulated problem is a model of the nonlinear scattering phenomenon involving shear horizontal waves interacting with an inclusion characterised by nonlinear attenuation properties. The approach employed to obtain the approximate solution is closely related to the technique used to derive the Born approximation, as presented in Gubernatis et al. (1977a,b); Nayfeh (2008); Achenbach (2003). It is appropriate to acknowledge that this particular approach is widely used in the analysis of scattering phenomena in the fields of electrodynamics and quantum mechanics, as discussed in Griffiths (2017a,b).

In order to determine the asymptotic expansion of the solution of the considered nonlinear scattering problem using the perturbation method, a small parameter denoted as ε is introduced into Eqs. (4.29) and (4.30). Thus, the linear elastic effects predominate the model considered and the parameter ε assures a low level of damping. The approximate solution can be expressed as

$$w(x,y,t) = w_0(x,y,t) + \varepsilon w_1(x,y,t) + \varepsilon^2 w_2(x,y,t) + \cdots , \tag{4.31}$$

where the subscripts indicate the order of approximation. Substituting Eq. (4.31) into Eqs. (4.29) and (4.30), and equating terms proportional to powers of the small parameter ε to zero, yields the system of governing equations and associated boundary conditions for the zeroth–order and first–order approximations given by

$$O(\varepsilon^0): \frac{\partial^2 w_0}{\partial x^2} + \frac{\partial^2 w_0}{\partial y^2} - \frac{1}{c_s^2}\frac{\partial^2 w_0}{\partial t^2} = 0, \tag{4.32}$$

$$O(\varepsilon^0): \pm\frac{\partial w_0}{\partial y} = 0, \text{ for } y = \pm h, \tag{4.33}$$

$$O(\varepsilon^1): \frac{\partial^2 w_1}{\partial x^2} + \frac{\partial^2 w_1}{\partial y^2} - \frac{1}{c_s^2}\frac{\partial^2 w_1}{\partial t^2} = -\frac{1}{\mu} f_1^{NL}(w_0(x,y,t)), \tag{4.34}$$

$$O(\varepsilon^1): \pm\frac{\partial w_1}{\partial y} = \mp\frac{1}{\mu}\Theta(F(x,y))\left(\sigma_{yz}^D\right)_0, \text{ for } y = \pm h, \tag{4.35}$$

respectively. The $f_1^{NL}(w_0(x,y,t))$ right–hand side term in Eq. (4.34) represents the excitation of the w_1 first–order approximate solution and is defined as

$$\begin{aligned} f_1^{NL}(w_0(x,y,t)) = \Theta(F(x,y))&\left(\frac{\partial(\sigma_{xz}^D)_0}{\partial x} + \frac{\partial(\sigma_{yz}^D)_0}{\partial y}\right) \\ &+ \delta(F(x,y))\left(\frac{\partial F}{\partial x}\left(\sigma_{xz}^D\right)_0 + \frac{\partial F}{\partial y}\left(\sigma_{yz}^D\right)_0\right). \end{aligned} \tag{4.36}$$

The $(\sigma_{xz}^{D})_0$ and $(\sigma_{yz}^{D})_0$ stress components in this term are calculated using the definitions provided in Eqs. (4.25) and (4.26), for the w_0 zeroth–order solution (i.e., after substitution $w = w_0$).

The linear differential operators on the left–hand side are identical for both i.e., the w_0 and w_1 approximate solutions. This also holds for higher order approximations. Moreover, the analysed linear differential operator is the same as the operator for the linear problem of shear horizontal guided wave propagation. In addition, the nonlinear forcing terms on the right–hand side can be interpreted as the excitation of higher–order approximate wavefields by the lower–order approximate wavefields and depend on the form of the nonlinearity assumed. Hence, the system of boundary value problems analysed – defined by Eqs. (4.32) – (4.35) – requires the iterative solution procedure.

4.3.2 Zeroth–order approximation solution

The homogeneous governing Eq. (4.32), combined with the associated boundary conditions specified in Eq. (4.33), restores the classical problem of linear shear horizontal guided wave propagation. For the investigation of the L–G effect for shear horizontal guided waves presented in this dissertation, the w_0 zeroth–order approximate solution is intentionally assumed in the following form

$$w_0 = \frac{1}{2}\vartheta \left(A_1 Y^{(m_1)}(y) e^{i(\xi_1 x - \omega_1 t)} + A_2 Y^{(m_2)}(y) \left(e^{i(\xi_2 x - \omega_2 t)} + \frac{R_{\omega_2 \pm \Omega}}{2} e^{i(\xi_3 x - \omega_3 t)} + \frac{R_{\omega_2 \pm \Omega}}{2} e^{i(\xi_4 x - \omega_4 t)} \right) \right) + c.c. \tag{4.37}$$

Therefore, for the considered $2h$–thick elastic plate, a two distinct shear horizontal guided waves corresponding to two modes denoted as m_1 and m_2 are primarily excited. The first wave, with the m_1 modeshape, is a monoharmonic "wanted" wave characterised by an angular frequency denoted as ω_1. The second wave, with the m_1 modeshape, is an amplitude–modulated "disturbing" wave with an angular carrier frequency denoted as ω_2. Additional angular frequencies are introduced as $\omega_3 = \omega_2 - \Omega$ and $\omega_4 = \omega_2 + \Omega$. The modulating angular frequency and modulation index are defined as Ω and $R_{\omega_2 \pm \Omega}$, respectively. Each pair of angular frequency and wavenumber (ω_i, ξ_i) satisfies the dispersion relation defined in Eq. (2.88). The A_1 and A_2 are the amplitudes of the "wanted" and "disturbing" waves, respectively. Furthermore, the small parameter $\vartheta \ll 1$ is employed to order the terms in the analytical expressions for the excitations for higher–order approximations that depend on the form of the introduced nonlinearity. The assumed solution corresponds to waves propagating in the positive direction of the x–axis.

The assumed zeroth–order approximation solution (Eq. (4.37)) can be reformulated as

$$w_0 = \frac{1}{2}\vartheta \left(A_1 Y^{(m_2)}(y) e^{i(\xi_1 x - \omega_1 t)} + \tilde{A}_2(x,t) Y^{(m_2)}(y) e^{i(\xi_2 x - \omega_2 t)} \right) + c.c., \tag{4.38}$$

where the $\tilde{A}_2(x,t)$ complex amplitude – that depends on the x spatial coordinate and t time – is defined as

$$\tilde{A}_2(x,t) = A_2\left(1 + \frac{R_{\omega_2\pm\Omega}}{2}e^{i((\xi_3-\xi_2)x+\Omega t)} + \frac{R_{\omega_2\pm\Omega}}{2}e^{i((\xi_4-\xi_2)x-\Omega t)}\right). \tag{4.39}$$

This expression describes the amplitude modulation of the "disturbing" wave in space and time domains.

Following the research work presented in Ginzburg (1970), this study assumes a quasi–stationary condition for the w_0 zeroth–order solution. Therefore, the following inequalities are satisfied for angular frequencies $\omega_1 \gg \Omega$, $\omega_2 \gg \Omega$ and wavenumbers $\xi_1 \gg |\xi_3 - \xi_2|$, $\xi_1 \gg |\xi_4 - \xi_2|$, $\xi_2 \gg |\xi_3 - \xi_2|$, $\xi_2 \gg |\xi_4 - \xi_2|$. This assumption simplifies further calculations. Hence, the partial derivatives of the w_0 zeroth–order solution with respect to t time and x spatial coordinate are approximately equal to

$$\frac{\partial w_0}{\partial x} \simeq \frac{1}{2}\vartheta\left(i\xi_1 A_1 Y^{(m_1)}(y)e^{i(\xi_1 x-\omega_1 t)} + i\xi_2\tilde{A}_2(x,t)Y^{(m_2)}(y)e^{i(\xi_2 x-\omega_2 t)}\right) + c.c., \tag{4.40}$$

$$\frac{\partial \dot{w}_0}{\partial x} \simeq \frac{1}{2}\vartheta\left(\xi_1\omega_1 A_1 Y^{(m_1)}(y)e^{i(\xi_1 x-\omega_1 t)} + \xi_2\omega_2\tilde{A}_2(x,t)Y^{(m_2)}(y)e^{i(\xi_2 x-\omega_2 t)}\right) + c.c., \tag{4.41}$$

$$\frac{\partial \dot{w}_0}{\partial y} \simeq -\frac{1}{2}\vartheta\left(i\omega_1 A_1 Y^{(m_1)\prime}(y)e^{i(\xi_1 x-\omega_1 t)} + i\omega_2\tilde{A}_2(x,t)Y^{(m_2)\prime}(y)e^{i(\xi_2 x-\omega_2 t)}\right) + c.c. \tag{4.42}$$

The assumptions made indicate that the $(\sigma^D_{xz})_0$ and $(\sigma^D_{yz})_0$ stress tensor components – appearing in the definition of the excitation term in the first–order approximation problem (Eq. (4.36)) – are a sum of space–time harmonic functions. The angular frequencies and wavenumbers corresponding to these harmonic functions are equal to the combinations of the (ω_1,ξ_1) and (ω_2,ξ_2) pairs of angular frequencies and wavenumbers. Substituting Eqs. (4.40) – (4.42) into Eqs. (4.25) and (4.26) yields

$$\begin{aligned}(\sigma^D_{xz})_0 = &\sum_{r=0}^{2}\sum_{s=-2+r}^{2-r}\left((\sigma^D_{xz})_0\right)_{|(2r+1)\omega_1+2s\omega_2|} + \left((\sigma^D_{xz})_0\right)_{|2s\omega_1+(2r+1)\omega_2|} = \\ &\sum_{r=0}^{2}\sum_{s=-2+r}^{2-r}\left((\alpha_{xz})_{|(2r+1)\omega_1+2s\omega_2|}e^{i\left(\left|(2r+1)\xi_1+2s\xi_2\right|x-\left|(2r+1)\omega_1+2s\omega_2\right|t\right)} + \right. \\ &\left.(\alpha_{xz})_{|2s\omega_1+(2r+1)\omega_2|}e^{i\left(\left|2s\xi_1+(2r+1)\xi_2\right|x-\left|2s\omega_1+(2r+1)\omega_2\right|t\right)}\right) + c.c.,\end{aligned} \tag{4.43}$$

$$\begin{aligned}(\sigma^D_{yz})_0 = &\sum_{r=0}^{2}\sum_{s=-2+r}^{2-r}\left((\sigma^D_{yz})_0\right)_{|(2r+1)\omega_1+2s\omega_2|} + \left((\sigma^D_{yz})_0\right)_{|2s\omega_1+(2r+1)\omega_2|} = \\ &\sum_{r=0}^{2}\sum_{s=-2+r}^{2-r}\left((\alpha_{yz})_{|(2r+1)\omega_1+2s\omega_2|}e^{i\left(\left|(2r+1)\xi_1+2s\xi_2\right|x-\left|(2r+1)\omega_1+2s\omega_2\right|t\right)} + \right. \\ &\left.(\alpha_{yz})_{|2s\omega_1+(2r+1)\omega_2|}e^{i\left(\left|2s\xi_1+(2r+1)\xi_2\right|x-\left|2s\omega_1+(2r+1)\omega_2\right|t\right)}\right) + c.c.\end{aligned} \tag{4.44}$$

The $(\alpha_{xz})_{|(2r+1)\omega_1+2s\omega_2|}$, $(\alpha_{xz})_{|2s\omega_1+(2r+1)\omega_2|}$, $(\alpha_{yz})_{|(2r+1)\omega_1+2s\omega_2|}$ and $(\alpha_{yz})_{|2s\omega_1+(2r+1)\omega_2|}$ amplitudes are functions that depend on the y spatial coordinate. Each of these amplitudes corresponds to the space–time harmonic terms in the sums provided in Eqs. (4.43) and (4.44). Moreover, these amplitudes depend on a number of quantities, including the ω_1 and ω_2 angular frequencies, the ξ_1 and ξ_2 wavenumbers, the $Y^{(m_0)}(y)$ mode shape function , the η_{m_0} square root of its eigenvalue and the A_1 and $\tilde{A}_2(x,t)$ amplitudes . It is noteworthy that the amplitude $\tilde{A}_2(x,t)$ is a slowly varying harmonic function in both spatial and time domains. Thus, the modulation transfer and the corresponding carrier angular frequencies can be identified by a detailed study of the relationship between the amplitudes of the harmonic excitation terms from Eqs. (4.43)–(4.44) and the $\tilde{A}_2(x,t)$ function.

The subscript in the above notation refers to the angular frequency and the wavenumber is omitted for simplicity. Since a local nonlinearity is investigated, the forcing term for the first–order approximation is also concentrated in a finite region. Furthermore, this excitation is polyharmonic and the set of angular frequencies is sufficient to characterise it. The adopted notation remains appropriate for the analysis of nonlocal (i.e., spread) nonlinearities based on derived equations. This is because the wavenumbers are calculated in an analogous way to the angular frequencies.

It is important to note that when the pairs (ω_1,ξ_1) and (ω_2,ξ_2) are combined in investigated problem, the resulting sums always include a combination of its even and odd multiplications. This property is caused by the presence of the odd nonlinearity in the mechanical system under consideration. One can deduce from Eqs. (4.43) and (4.44) that for the assumed definition of stress tensor the absolute sum of $2r$+1 and $2s$ factors cannot be greater than 5. This is related to the stress definitions adopted for the investigated model of mechanical system.

As evident from the established relationship, the interaction between two waves within the nonlinear region results in the generation of waves characterised by odd higher harmonics, specifically associated with the (ω_1,ξ_1) and (ω_2,ξ_2) pairs. Furthermore, the system exhibits an intermodulation phenomenon. It is manifested by generation of harmonic waves with angular frequency and wave number pairs being combinations of (ω_1,ξ_1) and (ω_2,ξ_2) pairs. These waves are known as "subsidiary" waves, as explained in Ginzburg (1970).

The nonlinear region under consideration is significantly smaller than the wavelengths of the propagating waves (i.e., $\lambda \gg d_x$, $\frac{1}{\eta} \gg d_y$), as illustrated in Figure 4.3. Therefore, the $w_0(x,y,t)$ zeroth–order solution can be approximated by linear terms of the Taylor series expansion with respect to the x and y variables Bronshtein et al. (2015). As a result, the zeroth–order approximation in the introduced nonlinear region is given by

$$\begin{aligned} w_0(x,y,t) \cong \frac{1}{2}\vartheta \Big(& A_1 e^{-i\omega_1 t}\Big(Y^{(m_1)}(y_c)e^{i\xi_1 x_c} + Y^{(m_1)}(y_c)i\xi_1 e^{i\xi_1 x_c}(x-x_c) \\ & + Y^{(m_1)\prime}(y_c)e^{i\xi_1 x_c}(y-y_c)\Big) + \tilde{A}_2(x,t)e^{-i\omega_2 t}\Big(Y^{(m_2)}(y_c)e^{i\xi_2 x_c} \\ & + Y^{(m_2)}(y_c)i\xi_2 e^{i\xi_2 x_c}(x-x_c) + Y^{(m_2)\prime}(y_c)e^{i\xi_2 x_c}(y-y_c)\Big)\Big) + c.c., \end{aligned} \tag{4.45}$$

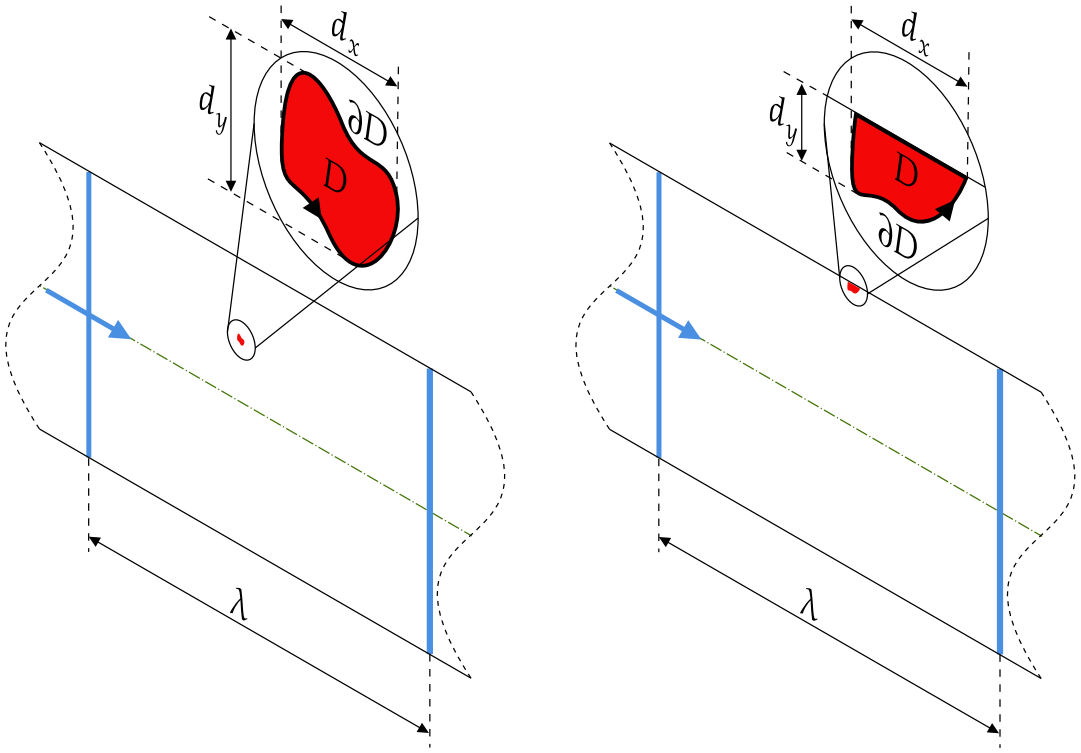

(a) (b)

Figure 4.3: Nonlinear region vs. wavelength of the propagating shear horizontal guided wave – graphical representation. Two cases are presented: (a) nonlinear region has no intersection points with the plate boundary and (b) nonlinear region has a segment of its boundary with the plate.

where x_c and y_c represent the coordinates of the geometric centre of the D region. This implies that the components of the strain and strain rate tensors are constant in the considered region. Hence, the components of the stress tensor are also constant in this domain. The components defined in Eqs. (4.43) – (4.44) can be rewritten as

$$\begin{aligned}(\sigma_{xz}^{D})_0 &= \sum_{r=0}^{2}\sum_{s=-2+r}^{2-r}\left((\sigma_{xz}^{D})_0\right)_{|(2r+1)\omega_1+2s\omega_2|} + \left((\sigma_{xz}^{D})_0\right)_{|2s\omega_1+(2r+1)\omega_2|} \\ &= \sum_{r=0}^{2}\sum_{s=-2+r}^{2-r}\Big((\Lambda_{xz})_{|(2r+1)\omega_1+2s\omega_2|}e^{-i\left|(2r+1)\omega_1+2s\omega_2\right|t} + \\ &\quad (\Lambda_{xz})_{|2s\omega_1+(2r+1)\omega_2|}e^{-i\left|2s\omega_1+(2r+1)\omega_2\right|t}\Big) + c.c.,\end{aligned} \tag{4.46}$$

$$
\begin{aligned}
(\sigma_{yz}^{D})_0 &= \sum_{r=0}^{2}\sum_{s=-2+r}^{2-r}\left((\sigma_{yz}^{D})_0\right)_{|(2r+1)\omega_1+2s\omega_2|} + \left((\sigma_{yz}^{D})_0\right)_{|2s\omega_1+(2r+1)\omega_2|} \\
&= \sum_{r=0}^{2}\sum_{s=-2+r}^{2-r}\Bigg((\Lambda_{yz})_{|(2r+1)\omega_1+2s\omega_2|}e^{-i\left|(2r+1)\omega_1+2s\omega_2\right|t} + \\
&\quad (\Lambda_{yz})_{|2s\omega_1+(2r+1)\omega_2|}e^{-i\left|2s\omega_1+(2r+1)\omega_2\right|t}\Bigg) + c.c.,
\end{aligned}
\tag{4.47}
$$

where $(\Lambda_{xz})_{|(2r+1)\omega_1+2s\omega_2|}$, $(\Lambda_{xz})_{|2s\omega_1+(2r+1)\omega_2|}$, $(\Lambda_{yz})_{|(2r+1)\omega_1+2s\omega_2|}$ and $(\Lambda_{yz})_{|2s\omega_1+(2r+1)\omega_2|}$ denote the constants characterising the stress tensor components related to nonlinear viscous phenomenon in the introduced nonlinear region. For a comprehensive overview of the angular frequencies corresponding to individual terms within the series given by Eqs. (4.43) – (4.44) and (4.46) – (4.47), please refer to Table 4.1.

Table 4.1: Summary of angular frequencies corresponding to individual components in series from Eqs. (4.43) and (4.44).

	$r=0$		$r=1$		$r=2$	
$s=\pm 0$	ω_1	ω_2	$3\omega_1$	$3\omega_2$	$5\omega_1$	$5\omega_2$
$s=\pm 1$	$\lvert\omega_1 \pm 2\omega_2\rvert$	$\lvert\omega_2 \pm 2\omega_1\rvert$	$\lvert 3\omega_1 \pm 2\omega_2\rvert$	$\lvert 3\omega_2 \pm 2\omega_1\rvert$	–	–
$s=\pm 2$	$\lvert\omega_1 \pm 4\omega_2\rvert$	$\lvert\omega_2 \pm 4\omega_1\rvert$	–	–	–	–

4.3.3 First–order approximation solution

The technique described in Meirovitch (2003); Osika et al. (2022, 2023b) can be used to modify the forcing term in the inhomogeneous governing equation and boundary conditions of a linear problem, thus transforming it into a linear problem with inhomogeneous governing equation and homogeneous boundary conditions. Therefore, the Dirac delta function was used and the following equivalent mathematical model was formulated

$$
\begin{aligned}
\frac{\partial^2 w_1}{\partial x^2} + \frac{\partial^2 w_1}{\partial y^2} - \frac{1}{c_s^2}\frac{\partial^2 w_1}{\partial t^2} &= -\frac{1}{\mu}f_1^{NL}(w_0(x,y,t)) - \delta(y-h)\frac{1}{\mu}\Theta(F(x,y))\left(\sigma_{yz}^{D}\right)_0 \\
&\quad + \delta(y+h)\frac{1}{\mu}\Theta(F(x,y))\left(\sigma_{yz}^{D}\right)_0,
\end{aligned}
\tag{4.48}
$$

$$
\pm\frac{\partial w_1}{\partial y} = 0, \text{ for } y = \pm h. \tag{4.49}
$$

However, the boundary–related forcing terms for the considered mechanical system are equal to zero due to the properties of the Dirac delta function Lighthill (1958) and the homogeneous boundary conditions defined in Eq. (4.33) for the zeroth–order solution. Therefore, further calculations do not take them into account.

The first–order approximation represents a solution of the inhomogeneous linear partial differential equation with associated homogeneous boundary conditions as defined in Eqs. (4.48) and (4.49). The inhomogeneous term in the formulated model is associated with a finite nonlinear region within the considered mechanical system. A related problem, characterised by a spatially distributed forcing term, has been investigated in Section 3.2.2. Its solution is based on the modal decomposition technique. Nevertheless, to investigate the L–G effect for shear horizontal waves – caused by the interaction of waves in the nonlinear region – the use of the Green's function is necessary. Therefore, it is essential to analyse the forcing terms in detail and to introduce the Green's function for the problem considered.

This investigation focuses on waves with wavelengths $\left(\lambda = \frac{2\pi}{\xi}\right)$ that are significantly larger than the assumed dimensions of the nonlinear region (i.e., $\lambda \gg d_x$, $\frac{1}{\eta} \gg d_y$), as illustrated in Figure 4.3. Hence, the formulation of the forcing term in Eq. (4.36) can be simplified as

$$f_1^{NL}(w_0(x,y,t)) \simeq \delta(F(x,y)) \left(\frac{\partial F}{\partial x} \left(\sigma_{xz}^D\right)_0 + \frac{\partial F}{\partial y} \left(\sigma_{yz}^D\right)_0 \right). \tag{4.50}$$

This simplification arises from the observation that the stress tensor components associated with shear horizontal waves are approximately constant in the nonlinear region investigated for long wavelengths. Therefore, the corresponding first spatial derivatives of these stress tensor components are approximately equal to zero and can be omitted in calculations. Hence, the boundary of the nonlinear region acts as the source of nonlinear waves.

An alternative perturbation method is required to perform calculations to investigate waves with wavelengths smaller than the damage size. The multiplescale technique – as described in works Nayfeh (2008); Holmes (2012) – is a suitable approach to investigate the evolution of the amplitudes of interacting waves in time and space within the region where nonlinear attenuation occurs.

The assumed zeroth–order approximation solution (Eq.(4.38)) and assumption made determine the mathematical form of the forcing term in Eq. (4.50). This local excitation is the sum of the harmonic functions and is given by

$$\begin{aligned} f_1^{NL}(w_0(x,y,t)) &= \sum_{r=0}^{2} \sum_{s=-2+r}^{2-r} \left(f_1^{NL}\right)_{|(2r+1)\omega_1+2s\omega_2|} + \left(f_1^{NL}\right)_{|2s\omega_1+(2r+1)\omega_2|} \\ &= \sum_{r=0}^{2} \sum_{s=-2+r}^{2-r} \left(F_1^{NL}\right)_{|(2r+1)\omega_1+2s\omega_2|} e^{-i|(2r+1)\omega_1+2s\omega_2|t} \\ &+ \left(F_1^{NL}\right)_{|2s\omega_1+(2r+1)\omega_2|} e^{-i|2s\omega_1+(2r+1)\omega_2|t}. \end{aligned} \tag{4.51}$$

The $\left(F_1^{NL}\right)_{|(2r+1)\omega_1+2s\omega_2|}$ and $\left(F_1^{NL}\right)_{|2s\omega_1+(2r+1)\omega_2|}$ introduced terms represent the spatial distribution of the individual harmonic excitation in space and depend on the x and y spatial

coordinates. Substituting Eqs. (4.43) and (4.44) into Eq. (4.50) yields their definition

$$\begin{aligned}\left(F_1^{NL}\right)_{|(2r+1)\omega_1+2s\omega_2|} = \delta(F(x,y))\Bigg(&\frac{\partial F(x,y)}{\partial x}\left(\Lambda_{xz}\right)_{|(2r+1)\omega_1+2s\omega_2|} \\ &+\frac{\partial F(x,y)}{\partial y}\left(\Lambda_{yz}\right)_{|(2r+1)\omega_1,+2s\omega_2|}\Bigg) e^{i\left|(2r+1)\xi_1+2s\xi_2\right|x}.\end{aligned} \tag{4.52}$$

$$\begin{aligned}\left(F_1^{NL}\right)_{|2s\omega_1+(2r+1)\omega_2|} = \delta(F(x,y))\Bigg(&\frac{\partial F(x,y)}{\partial x}\left(\Lambda_{xz}\right)_{|2s\omega_1+(2r+1)\omega_2|} \\ &+\frac{\partial F(x,y)}{\partial y}\left(\Lambda_{yz}\right)_{|2s\omega_1+(2r+1)\omega_2|}\Bigg) e^{i\left|2s\xi_1+(2r+1)\xi_2\right|x}.\end{aligned} \tag{4.53}$$

To solve the first–order approximation problem one can observe that the response of a linear system to a time–harmonic excitation is also harmonic in the time domain. Moreover, the principle of superposition can be applied due to the linear nature of the considered problem. This implies that the total response of the system is a sum of independent solutions corresponding to each harmonic component of the forcing term (Eq.(4.51)). Therefore, the first–order approximation problem has a polyharmonic solution given as

$$\begin{aligned}w_1(x,y,t) &= \sum_{r=0}^{2}\sum_{s=-2+r}^{2-r}\left(w_1\right)_{|(2r+1)\omega_1+2s\omega_2|}(x,y,t) + \left(w_1\right)_{|2s\omega_1+(2r+1)\omega_2|}(x,y,t) \\ &= \sum_{r=0}^{2}\sum_{s=-2+r}^{2-r}\left(W_1\right)_{|(2r+1)\omega_1+2s\omega_2|}(x,y)e^{-i|(2r+1)\omega_1+2s\omega_2|t} \\ &+ \left(W_1\right)_{|2s\omega_1+(2r+1)\omega_2|}(x,y)e^{-i|2s\omega_1+(2r+1)\omega_2|t}.\end{aligned} \tag{4.54}$$

Upon substitution of Eqs. (4.51) and (4.54) into Eqs. (4.48) – (4.49) and separation of variables, the governing partial differential equation and boundary conditions for each of the $(W_1)_\omega$ function can be written. To facilitate notation, the ω angular frequency is introduced to represent any value of the angular frequency that occurs in Eqs. (4.52) – (4.53). Finally, the resulting boundary value problems for each $(W_1)_\omega$ function can be expressed as

$$\frac{\partial^2(W_1)_\omega}{\partial x^2} + \frac{\partial^2(W_1)_\omega}{\partial y^2} + \frac{\omega^2}{c_s^2}(W_1)_\omega = -\frac{1}{\mu}(F_1^{NL})_\omega, \tag{4.55}$$

$$\pm\frac{\partial(W_1)_\omega}{\partial y} = 0, \text{ for } y = \pm h. \tag{4.56}$$

The Green's functions were employed to solve the boundary value problems defined in Eqs. (4.55) – (4.56). According to the definition provided in Duffy (2001); Aki & Richards (2002); Haberman (2013), the Green's functions of the investigated problem is the solution to the problem defined by

$$\frac{\partial^2 G_\omega}{\partial x^2} + \frac{\partial^2 G_\omega}{\partial y^2} + \frac{\omega^2}{c_s^2}G_\omega = -\delta(x-x_0, y-y_0), \tag{4.57}$$

$$\pm\frac{\partial G_\omega}{\partial y} = 0, \text{ for } y = \pm h, \tag{4.58}$$

where x_0 and y_0 correspond to the coordinates of the point–like excitation. Detailed investigation of this problem is given in Appendix C, where the analysis presented involves the modal decomposition with the orthogonal function base resulting from the eigenvalue problem defined by Eqs.(2.77) – (2.78) and the Fourier transform. The Green's function of the analysed problem – expanded using eigenfunctions – can be expressed as

$$\begin{aligned} G_\omega(x,y;x_0,y_0) &= \sum_{m=0}^{\infty} Y^{(m)}(y) G_\omega^{(m)}(x;x_0,y_0) = \sum_{m=0}^{\infty} \frac{Y^{(m)}(y)Y^{(m)}(y_0)}{\int_{-h}^{h} \left(Y^{(m)}(y)\right)^2 dy} \frac{i}{2\xi_m} e^{i\xi_m|x-x_0|} \\ &= \sum_{m=0}^{\infty} \frac{Y^{(m)}(y)Y^{(m)}(y_0)}{\int_{-h}^{h} \left(Y^{(m)}(y)\right)^2 dy} \frac{i}{2\xi_m} \left(\Theta(-(x-x_0))e^{-i\xi_m(x-x_0)} + \Theta(x-x_0)e^{i\xi_m(x-x_0)}\right), \end{aligned} \tag{4.59}$$

where Θ denote the Heaviside step function.

This equation demonstrates that a point–like excitation on the right–hand side of Eq. (4.57) results in the generation of all propagating and evanescent modes for shear horizontal guided waves in an elastic plate. The ξ wavenumber is a real number for propagating modes and purely imaginary for evanescent modes. Every possible pair of ω angular frequency and ξ_m wavenumber satisfies the dispersion relation given in Eq. (2.88).

The linear approximation of the Green's function in the region of local nonlinearity can be introduced analogously as for the zeroth–order solution in Eq. (4.45). Using the definition of the Taylor series expansion Bronshtein et al. (2015), properties of the Heaviside unit step and the Dirac delta functions Lighthill (1958) one can obtain the relevant approximation as

$$\begin{aligned} G_\omega(x,y;x_0,y_0) \cong \sum_{m=0}^{\infty} \frac{Y^{(m)}(y)}{\int_{-h}^{h} \left(Y^{(m)}(y)\right)^2 dy} \frac{i}{2\xi_m} e^{i\xi_m|x-x_c|} \left(Y^{(m)}(y_c) + Y^{(m)\prime}(y_c)(y_0-y_c)\right. \\ \left. + Y^{(m)}(y_c) i\xi_m |x_0 - x_c|\right). \end{aligned} \tag{4.60}$$

Appendix C provides a detailed derivation of Eqs. (4.59) – (4.60).

The definition and properties of the Green's function presented and analysed in Duffy (2001); Aki & Richards (2002); Haberman (2013); Żur (2016), shows that the solution of the investigated problems is equal to the convolution of this function with the forcing term. Therefore, for the assumed form of excitation (Eq. (4.51)), the complete solution for the first–order problem (Eqs. (4.48)–(4.49)) can be formulated as

$$\begin{aligned} w_1(x,y,t) = \sum_{r=0}^{2} \sum_{s=-2+r}^{2-r} \sum_{m=0}^{\infty} Y^{(m)}(y) \iint_D \left(G^{(m)}_{|(2r+1)\omega_1+2s\omega_2|}(x,y;x_0,y_0) \right. \\ \times \left(f_1^{NL}\right)_{|(2r+1)\omega_1+2s\omega_2|}(x_0,y_0,t) + G^{(m)}_{|2s\omega_1+(2r+1)\omega_2|}(x,y;x_0,y_0) \\ \left. \times \left(f_1^{NL}\right)_{|2s\omega_1+(2r+1)\omega_2|}(x_0,y_0,t) \right) dx_0 dy_0 + c.c. \end{aligned} \tag{4.61}$$

The above formula demonstrates that higher harmonics are generated when a time–space harmonic wave propagates through a source of local nonlinearity. Furthermore, the determined

solution incorporates the "subsidiary" waves discussed earlier that result from intermodulation. Upon substituting of Eq. (4.51) into Eq. (4.61), the double integral over the D region (for which the Dirac delta occur under the sign of the integral) can be written as a line integral over the ∂D closed contour, as explained in Gubernatis et al. (1977a,b); Achenbach (2003). This integral can be converted to a double integral using the Green's theorem McQuarrie (2003).

The study of the transfer of modulation phenomenon from the ω_2 carrier angular frequency to the ω_1 angular frequency is a crucial aspect of the research work presented. Hence, it is essential to conduct a detailed analysis of the $(w_1)_{\omega_1}$ component characterised by the ω_1 carrier angular frequency, which can be written as

$$\begin{aligned}(w_1)_{\omega_1}(x,y,t) = \sum_{m=0}^{\infty} Y^{(m)}(y) e^{-i\omega_1 t} \oint_{\partial D} \Big((\Lambda_{yz})_{\omega_1} G^{(m)}_{\omega_1}(x,y;x_0,y_0) dx_0 \\ + (\Lambda_{xz})_{\omega_1} G^{(m)}_{\omega_1}(x,y;x_0,y_0) dy_0 \Big) + c.c.\end{aligned} \tag{4.62}$$

By applying the Green's theorem to the line integral around the ∂D contour McQuarrie (2003), the $(w_1)_{\omega_1}$ term can be represented as a double integral over the area of the D region, as explain above. Since stress components are approximately constant within this domain, the analysed term can be written as

$$\begin{aligned}(w_1)_{\omega_1}(x,y,t) = \sum_{m=0}^{\infty} Y^{(m)}(y) e^{-i\omega_1 t} \iint_D \Bigg((\Lambda_{xz})_{\omega_1} \frac{\partial G^{(m)}_{\omega_1}(x,y;x_0,y_0)}{\partial x_0} \\ - (\Lambda_{yz})_{\omega_1} \frac{\partial G^{(m)}_{\omega_1}(x,y;x_0,y_0)}{\partial y_0} \Bigg) dx_0 dy_0 + c.c.\end{aligned} \tag{4.63}$$

Upon substitution of Eq. (4.60) into Eq. (4.63), the definition of the $(w)_{\omega_1}$ term can be rewritten as

$$(w_1)_{\omega_1}(x,y,t) = \sum_{m=0}^{\infty} Y^{(m)}(y) \Gamma^{(m)}_{\omega_1} e^{i(\xi_1 |x-x_c| - \omega_1 t)} \iint_D dx_0 dy_0 + c.c., \tag{4.64}$$

where $\Gamma^{(m)}_{\omega_1}$ is the amplitude of each m–th mode. For the assumed zeroth–order problem solution and introduced definition of the stress tensor, this amplitude can be expressed as

$$\begin{aligned}\Gamma^{(m)}_{\omega_1} =& \vartheta^3 A_1^3 \omega_1^3 \left(\gamma^{(m)}_{\omega_1}\right)_1 + \vartheta^3 A_1 \tilde{A}_2(x,t) \overline{\tilde{A}_2(x,t)} \left(\omega_2^2 \left(\gamma^{(m)}_{\omega_1}\right)_2 + \omega_2 \omega_1 \left(\gamma^{(m)}_{\omega_1}\right)_3\right) \\ &+ \vartheta^5 A_1 \tilde{A}_2^2(x,t) \overline{\tilde{A}_2(x,t)}^2 \left(\omega_2^3 \left(\gamma^{(m)}_{\omega_1}\right)_4 + \omega_1 \omega_2^2 \left(\gamma^{(m)}_{\omega_1}\right)_5\right) + \vartheta^5 A_1^5 \omega_1^3 \left(\gamma^{(m)}_{\omega_1}\right)_6 \\ &+ \vartheta^5 A_1^3 \tilde{A}_2(x,t) \overline{\tilde{A}_2(x,t)} \left(\omega_1^3 \left(\gamma^{(m)}_{\omega_1}\right)_7 + \omega_1^2 \omega_2 \left(\gamma^{(m)}_{\omega_1}\right)_8\right),\end{aligned} \tag{4.65}$$

where $\left(\gamma^{(m)}_{\omega_1}\right)_i$ are the additional coefficients utilised to simplify the above relationship. These coefficients can be derived through an in–depth analysis of the $\left(f_1^{NL}\right)_{\omega_1}$ forcing term in Eq. (4.51). The over–lined terms represent the complex conjugates.

Eq. (4.63) indicates that waves in the first–order approximate solution propagate in positive and negative directions along the x–axis. Furthermore, this relationship implies that all shear horizontal

modes are generated. However, it is essential to note that modes with critical frequencies exceeding the angular frequency ω_1 are evanescent. Therefore, the acoustic equivalent of the L–G effect is expected to exhibit greater prominence in the vicinity of the nonlinear region. Moreover, the amplitude of the $(w_1)_{\omega_1}$ component is proportional to the area of the nonlinear region.

Eq. (4.65) demonstrates that the $\left(\gamma_{\omega_1}^{(m)}\right)_i$ amplitudes depend on the $\tilde{A}_2(x,t)$ slowly varying in space and time amplitude and its complex conjugate. This implicates that the modulation amplitude needs special attention, to study the modulation transfer. The $\tilde{A}_2(x,t)\overline{\tilde{A}_2(x,t)}$ expression in this term states that the ω_1 carrier angular frequency can be modulated by the angular frequencies Ω and 2Ω. Moreover, it reveals that the intensity of the transferred modulation is a nonlinear function of the ω_2 and ω_1 angular frequencies. This nonlinear relationship is quadratic for ω_2 and linear for ω_1. Therefore, the transfer of modulation from higher to lower angular frequencies is more effective (when $\omega_2 > \omega_1$). The other components on the right–hand side of Eq. (4.65) also affect the modulation intensity. However, their influence is less significant. Nonetheless, these components should not be neglected, as the presence of the $\tilde{A}_2^2(x,t)\overline{\tilde{A}_2(x,t)}^2$ expression indicates the possibility of modulation the ω_1 angular carrier frequency by the Ω, 2Ω, 3Ω, and 4Ω angular frequencies.

4.4 Discussion for the analytical analysis of L–G phenomenon for shear horizontal guided waves

The presented perturbation–based analytical calculation procedure is a general technique for deriving quantitative and qualitative results for various nonlinear phenomena related to propagation and interaction of elastic guided waves in plate–like structures. However, this approach requires tedious calculations for complicated mathematical expressions. The problem investigated – that involves the proposed nonlinear viscoelastic material model – is a good example.

The nonlinear viscoelastic model proposed in the current study aligns with dissipation models previously introduced for the electromagnetic waves propagating in ionospheric plasma Bailey & Martyn (1934); Graffi (1936); Bailey (1965); Ginzburg & Gurevich (1960); Gurevich (1978). Moreover, the analytical calculations presented are consistent with the well–established Born approximation commonly used in electrodynamics and quantum mechanics Griffiths (2017a,b). The Born approximation has previously been utilised in mechanics to analyse wave scattering induced by linear elastic inclusions Gubernatis et al. (1977a,b); Achenbach (2003). Therefore, the research presented extends the applicability of the aforementioned approach to nonlinear wavefields.

The analytical results demonstrate that the intensity of the L–G effect depends not only on the level of nonlinearity (or material damage severity) but also on the angular carrier frequencies and

amplitudes of the propagating waves. As nonlinearity (or size of damage) increases, the enhancement of the nonlinear effect is observed in the wave propagating wave response. Furthermore, the intensity of the L–G effect is also more pronounced when both – i.e., the "wanted" and the "disturbing" – waves exhibit higher amplitudes. The results also reveal that modulation transfer is more effective from higher to lower angular frequency than vice versa.

Chapter 5

Numerical modelling of nonlinear shear wave propagation phenomena using Local Interaction Simulation Approach

The Local Interaction Simulation Approach (LISA) technique has been employed to simulate the interaction of shear horizontal guided waves with a hyperelastic material and a local nonlinearity of a dissipative nature. The implementation of LISA is described in this chapter. Furthermore, the results of numerical simulations – conducted to verify the approximated analytical solutions presented in Chapters 3 and 4 – are also presented.

5.1 Local Interaction Simulation Approach for the nonlinear shear horizontal wavefield

The LISA method was initially proposed in the field of physics to model wave propagation in heterogeneous media containing sharp interfaces and material inclusions with different properties Delsanto et al. (1992, 1994, 1997). This modelling technique has also been used in numerous studies on damage detection based on Lamb waves Lee & Staszewski (2003a,b); Packo et al. (2012); Kijanka et al. (2013); Stepinski et al. (2013). In addition, the work presented in Packo et al. (2019) demonstrates the application of LISA to modelling of Lamb waves propagation phenomenon in hyperelastic media. Numerous works demonstrate the application of LISA for modelling of nonlinear media e.g., Scalerandi & Agostini (2002); Scalerandi et al. (2003); Obenchain & Cesnik (2014) and anisotropic materials e.g., Sundararaman & Adams (2008); Nadella & Cesnik (2013); Obenchain et al. (2015).

The LISA is based on the Finite Difference (FD) formulas that can be used for approximating the spatial derivatives in the elastodynamics governing differential Eq. (2.45). The explicit central

difference formula is used for the time domain discretisation. Therefore, the method is highly suitable for parallel computation, as demonstrated in Packo et al. (2012, 2019); Kijanka et al. (2013).

In this dissertation, the LISA method is applied to investigate nonlinear phenomena associated with shear horizontal waves in a medium described by two Lagrangian coordinates. The geometric model of the simulated system is discretised into a regular grid of rectangular cells. Material properties are assumed to be uniform within each cell, although these properties may vary between them. Therefore, LISA is particularly suited to investigate wave propagation in complex media with heterogeneous properties and sharp material boundaries in linear and nonlinear solid materials.

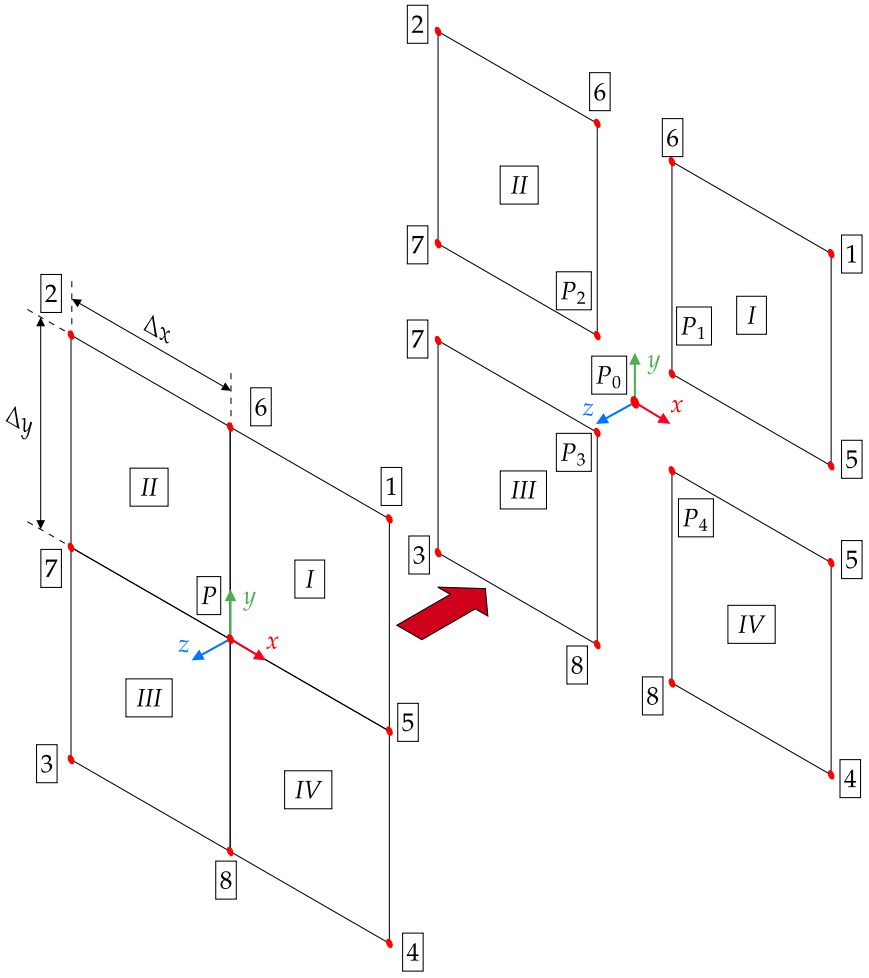

Figure 5.1: Discretisation of the geometrical model for the LISA technique.

The method is used to model two scenarios of shear horizontal guided wave propagation. The distributed nonlinearity is considered in the first case. A hyperelastic material – defined for the entire material model in Section 3.1 – is considered. A local nonlinearity representing structural damage (e.g., fatigue crack) is modelled in the second scenario. Nonlinear viscoelastic damping

– introduced in Section 4.2.4 – is implemented for this type of nonlinearity. The implementation of the LISA method for both nonlinearities follows the general approach presented in Packo et al. (2019).

In order to derive iterative equations for the nonlinear LISA implemented for shear horizontal waves, differential formulas are used to replace the spatial derivatives in Eq. (2.45). These iterative equations are formulated for the nodal point P (shown in Fig. 5.1) at the intersections of four adjacent grid cells. Since the cells involved are considered to be discontinuous, the P point is replaced by four separate P_1, P_2, P_3 and P_4 points, as shown in Fig. 5.2. The elastodynamic equations describing shear horizontal displacements of material particles are then evaluated at the introduced separate points. These equations can be expressed as

$$\frac{\sigma_{xz}^{(I)} - \sigma_{xz}^{(P_1)}}{\frac{\Delta x}{2}} + \frac{\sigma_{yz}^{(I)} - \sigma_{yz}^{(P_1)}}{\frac{\Delta y}{2}} \simeq \rho^{(I)} \ddot{w}, \tag{5.1}$$

$$\frac{\sigma_{xz}^{(P_2)} - \sigma_{xz}^{(II)}}{\frac{\Delta x}{2}} + \frac{\sigma_{yz}^{(II)} - \sigma_{yz}^{(P_2)}}{\frac{\Delta y}{2}} \simeq \rho^{(II)} \ddot{w}, \tag{5.2}$$

$$\frac{\sigma_{xz}^{(P_3)} - \sigma_{xz}^{(III)}}{\frac{\Delta x}{2}} + \frac{\sigma_{yz}^{(P_3)} - \sigma_{yz}^{(III)}}{\frac{\Delta y}{2}} \simeq \rho^{(III)} \ddot{w}, \tag{5.3}$$

$$\frac{\sigma_{xz}^{(IV)} - \sigma_{xz}^{(P_4)}}{\frac{\Delta x}{2}} + \frac{\sigma_{yz}^{(P_4)} - \sigma_{yz}^{(IV)}}{\frac{\Delta y}{2}} \simeq \rho^{(IV)} \ddot{w}, \tag{5.4}$$

where $\rho^{(i)}$ is the material density for the i–th cell and $i \in \{I, II, II, IV\}$.

The assumed stress localisation for each cell can be seen in Fig. 5.2. To ensure stress continuity between adjacent cells, Eqs. (5.1) – (5.4) must be supplemented by the stress–continuity conditions i.e., $\sigma_{xz}^{(P_1)} = \sigma_{xz}^{(P_2)}$,$\sigma_{xz}^{(P_3)} = \sigma_{xz}^{(P_4)}$, $\sigma_{yz}^{(P_1)} = \sigma_{yz}^{(P_4)}$ and $\sigma_{yz}^{(P_2)} = \sigma_{yz}^{(P_4)}$. These assumptions lead to the reduction of the stress tensor components in the considered relations. The stress–based iterative equation for the P node is obtained by summing the equations for each cell, enforcing stress continuity and assuming that the displacements of each additional node are equal i.e., $w = w_{P_1} = w_{P_2} = w_{P_3} = w_{P_4}$. The resultant relation is thus given as

$$\frac{\sigma_{xz}^{(I)} - \sigma_{xz}^{(II)} - \sigma_{xz}^{(III)} + \sigma_{xz}^{(IV)}}{\frac{\Delta x}{2}} + \frac{\sigma_{yz}^{(I)} + \sigma_{yz}^{(II)} - \sigma_{yz}^{(III)} - \sigma_{yz}^{(IV)}}{\frac{\Delta y}{2}} \simeq \sum_i \rho^{(i)} \ddot{w}. \tag{5.5}$$

Upon time discretisation and utilisation of the second–order central differential scheme for the time derivative, the final iterative equation is given as

$$\begin{aligned} w_{k+1} = 2w_k - w_{k-1} + \frac{\Delta t}{\sum_i \rho^{(i)}} \Bigg(& \frac{\left(\sigma_{xz}^{(I)}\right)_k - \left(\sigma_{xz}^{(II)}\right)_k - \left(\sigma_{xz}^{(III)}\right)_k + \left(\sigma_{xz}^{(IV)}\right)_k}{\frac{\Delta x}{2}} \\ & + \frac{\left(\sigma_{yz}^{(I)}\right)_k + \left(\sigma_{yz}^{(II)}\right)_k - \left(\sigma_{yz}^{(III)}\right)_k - \left(\sigma_{yz}^{(IV)}\right)_k}{\frac{\Delta y}{2}} \Bigg), \end{aligned} \tag{5.6}$$

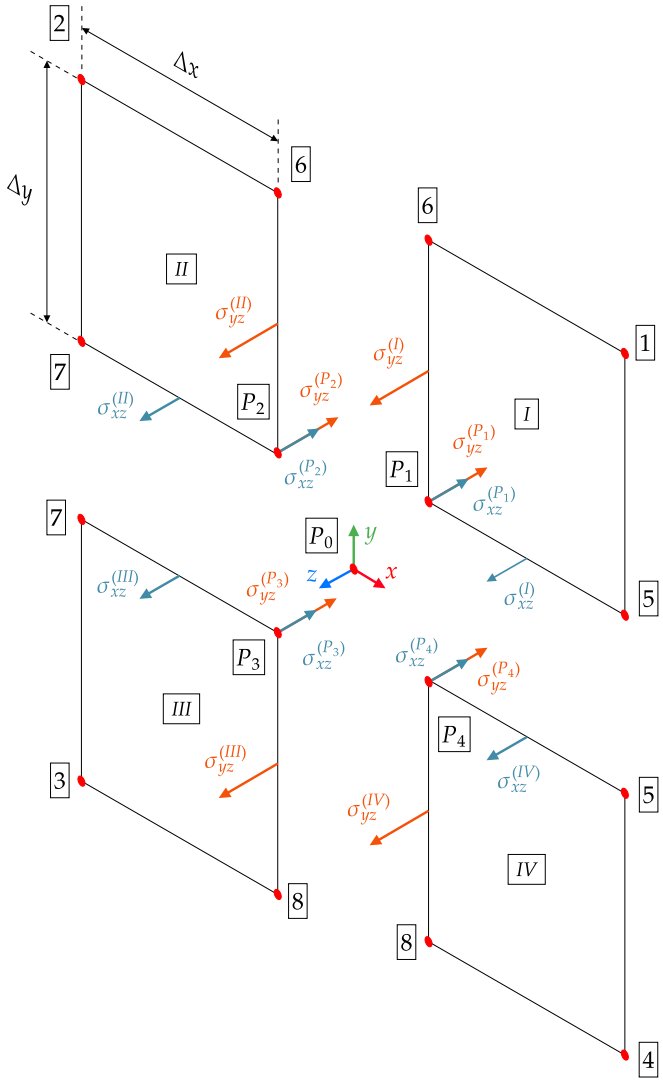

Figure 5.2: The discretisation scheme for the LISA for shear horizontal waves. Stress tensor components used to obtain iterative equations are illustrated.

where the k subscript indicates the time step number.

The derivation of the LISA iterative equation presented in this study is based on evaluating the elastodynamic equation and ensuring the continuity of specific stress tensor components at cell interfaces. This approach can be applied to the assumed forms of elastic and viscoelastic constitutive relationships between stress and strain tensors, as well as the geometric definition of strain and corresponding strain rate.

In this work, the second Piola–Kirchhoff stress and the Green–Lagrange strain tensors – described and analysed in Sections 2.3 and 2.4 – are adapted. The components of the stress tensor used in Eq. (5.5) are functions of spatial derivatives of the w displacement wavefield. These components need to be approximated by finite differences in order to develop the numerical model based on the LISA. The finite differences used to approximate the relevant partial

derivatives of the w displacement wavefield – with respect to the x and y spatial coordinates that were used to calculate the individual stress components – are given in Table 5.1. The substitution of these equations into the general constitutive relations between the stress tensor components and the w wavefield allows one to determine the final iterative equation. These equations can be used for numerical modelling of shear wave propagation.

As previously mentioned, mechanical systems in which guided waves can propagate are considered only in this work. To implement the traction–free boundary conditions, the geometrical model – i.e., the cross section of $2h$–thick plate – was assumed to be surrounded by an additional layer of material cells. Material parameters of this layer were set to zero. Therefore, propagation of the group of guided waves considered in this study could be modelled since the required boundary conditions were satisfied.

Table 5.1: The finite difference approximations of the partial derivatives of the w wavefield with respect to the x and y spatial coordinates for stress tensor components from Eq. (5.5)

Stress component	Finite difference approximation of first spatial partial derivative of w	
	$\frac{\partial w}{\partial x} \simeq$	$\frac{\partial w}{\partial y} \simeq$
$\sigma_{xz}^{(I)}$	$\frac{w_5 - w_0}{\Delta x}$	$\frac{1}{2}\left(\frac{w_1 - w_5}{\Delta y} + \frac{w_6 - w_0}{\Delta y}\right)$
$\sigma_{yz}^{(I)}$	$\frac{1}{2}\left(\frac{w_5 - w_0}{\Delta x} + \frac{w_1 - w_6}{\Delta x}\right)$	$\frac{w_6 - w_0}{\Delta y}$
$\sigma_{xz}^{(II)}$	$\frac{w_0 - w_7}{\Delta x}$	$\frac{1}{2}\left(\frac{w_6 - w_0}{\Delta y} + \frac{w_2 - w_7}{\Delta y}\right)$
$\sigma_{yz}^{(II)}$	$\frac{1}{2}\left(\frac{w_0 - w_7}{\Delta x} + \frac{w_6 - w_2}{\Delta x}\right)$	$\frac{w_6 - w_0}{\Delta y}$
$\sigma_{xz}^{(III)}$	$\frac{w_0 - w_7}{\Delta x}$	$\frac{1}{2}\left(\frac{w_0 - w_8}{\Delta y} + \frac{w_7 - w_3}{\Delta y}\right)$
$\sigma_{yz}^{(III)}$	$\frac{1}{2}\left(\frac{w_0 - w_7}{\Delta x} + \frac{w_8 - w_3}{\Delta x}\right)$	$\frac{w_0 - w_8}{\Delta y}$
$\sigma_{xz}^{(IV)}$	$\frac{w_5 - w_0}{\Delta x}$	$\frac{1}{2}\left(\frac{w_5 - w_4}{\Delta y} + \frac{w_0 - w_8}{\Delta y}\right)$
$\sigma_{yz}^{(IV)}$	$\frac{1}{2}\left(\frac{w_5 - w_0}{\Delta x} + \frac{w_4 - w_8}{\Delta x}\right)$	$\frac{w_0 - w_8}{\Delta y}$

The LISA is a numerical technique based on the FD method and therefore requires numerical stability for efficient calculations. For linear homogeneous media and the adopted explicit time scheme the numerical stability condition – based on the spectral analysis – can be provided by the Courant–Friedrichs–Lewy (CFL) number given as Virieux (1984b,a); Sundararaman & Adams (2009)

$$CFL = c_{max}\Delta t\sqrt{\frac{1}{\Delta x^2} + \frac{1}{\Delta y^2}} \leq 1, \tag{5.7}$$

where Δt and Δx, Δy represent the time step and size of the numerical grid, respectively; c_{max} denotes the maximum velocity of the wave propagating in the modelled solid medium. The CFL

number ensures that for a given grid spacing, the appropriate time step is selected to guarantee numerical stability. In addition, when numerical modelling of wave propagation is performed, dispersion resulting from simulations need to be compared with analytical dispersion to ensure adequate model accuracy. Nevertheless, it is important to note that Eq. (5.7) is valid only for linear models. Numerical modelling of nonlinear wave propagation demands a case–by–case approach to the stability problem.

5.2 Numerical modelling of nonlinear shear horizontal wave propagation in hyperelastic material

This section presents numerical simulation results for the problem of shear horizontal guided waves propagation in the Landau–Lifshitz hyperelastic material. The results validate the approximated analytical solution - based on the multiplescale perturbation method – presented in Chapter 3. The simulated wavefield is analysed in the wavenumber–frequency domain, using the modal decomposition and the two–dimensional Fourier transform. Numerical implementation of the modal decomposition is described, before the results are presented.

5.2.1 Numerical implementation of modal decomposition

The simulated shear horizontal guided wavefield was analysed using the modal decomposition, to assess the analytical results given in Eqs. (3.51) and (3.53). The amplitude distribution in the space–time domain corresponding to the m–th shear horizontal eigenmode was calculated as

$$A^{(m)}(x,t) = \frac{\int_{-h}^{h} Y^{(m)}(y) w(x,y,t) dy}{\int_{-h}^{h} (Y^{(m)}(y))^2 dy}. \tag{5.8}$$

In this relationship, $w(x,y,t)$ denotes the total wavefield in the modelled nonlinear system whereas $Y^{(m)}(y)$ indicates the modeshape of the particular m–th shear horizontal mode.

The integrals in Eq. (5.8) were computed numerically using the trapezoidal integration method Dahlquist & Bjorck (2008). This approach enables one to determine the distributions of the chosen shear horizontal modeshapes, along the direction of propagation, for modelled guided waves, for each simulation time step. Fig. 5.3 schematically presents the implementation of the calculation of the amplitude corresponding to the SH0 and SH1 modes, for the arbitrarily assumed spatial coordinate $x = x_0$.

5.2.2 Numerical results for developed numerical models

A 2–D model of a semi–infinite 500 mm plate with a 2 mm thickness was considered. Material characteristics that correspond to aluminium were assumed to be uniform in each cell building the

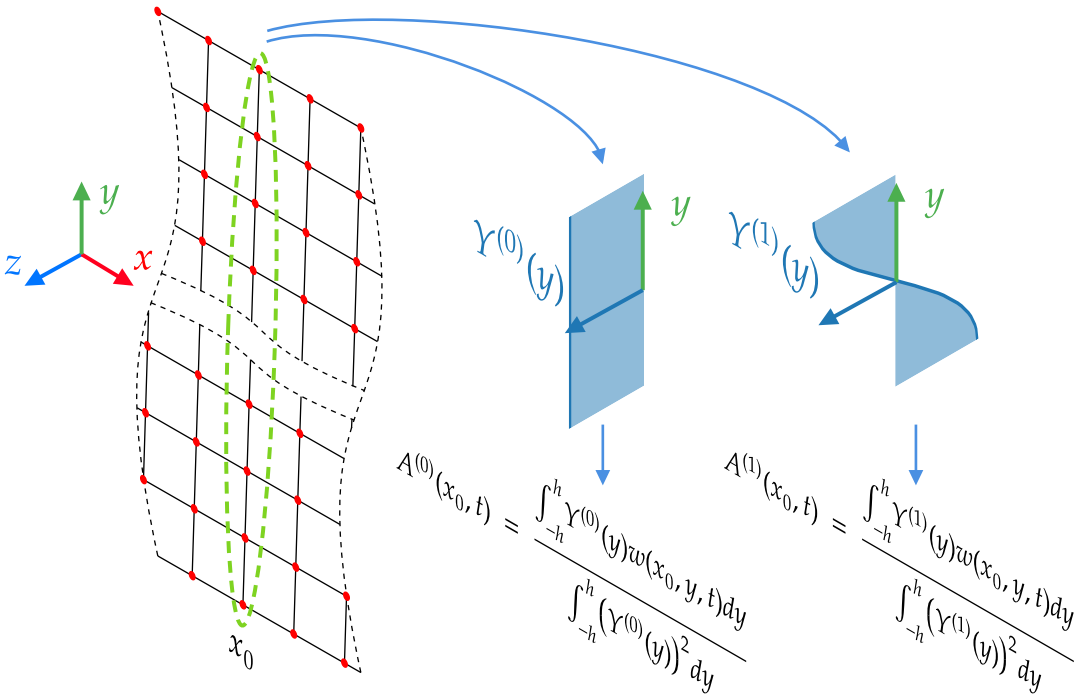

Figure 5.3: Schematic representation of the mode decomposition, implemented for the developed numerical model for $x = x_0$.

model. The assumed linear and nonlinear material parameters utilised in the developed simulation model are summarised in Table 5.2. The Landau's TOECs and FOECs have been obtained based on the data reported in Wang & Li (2009). Appendix A demonstrates the technique used to determine all parameters of the Landau–Lifshitz model, based on the data corresponding to the selected material model. The density $\rho = 2700$ kg/m^3 was assumed.

The dispersion characteristics of the developed linear numerical models with the given material parameters were first validated against the analytical dispersion relations. The mesh size was set to $\Delta x = \Delta y = 0.05$ mm, resulting in 40 elements through the thickness of the modelled cross–section of the plate. The grid size adopted in the defined numerical model guaranteed sufficient convergence to the theoretical characteristics. The time step for the simulations was set to $\Delta t = 0.01$ μs, in order to guarantee the stability of the numerical model.

Table 5.2: Material properties (in GPa) of aluminium used in numerical simulations of nonlinear shear horizontal guided wave propagation.

λ	μ	$\mathcal{A}$	$\mathcal{B}$	$\mathcal{C}$	$\mathcal{E}$	$\mathcal{F}$	$\mathcal{G}$	$\mathcal{H}$
51.08	26.32	-195.90	-118.31	-3.46	81.74	165.23	228.40	-25.12

The 35– and 50–cycle Hanning–windowed harmonic burst signals – with frequencies equal to 0.7 and 1.3 MHz – were utilised to excite the SH0 and SH1 modes, respectively. The number of

cycles in the excitation signals were selected to guarantee the effective generation of the modes investigated. The excitation was imposed as a displacement through the thickness of the modelled cross–section of the plate. and assigned to the left–hand side of the plate, as shown in

The 35– and 50–cycle Hanning–windowed harmonic burst signals – with frequencies equal to 0.7 and 1.3 MHz – were utilised to excite the SH0 and SH1 modes, respectively. The number of cycles in the excitation signals were selected to guarantee the effective generation of the modes investigated. The excitation was imposed as a displacement through the thickness of the modelled cross–section of the plate and assigned to the left–hand side of the plate, as shown in Figs. 5.4 and 5.5. The distribution of the displacement excitation in the y–axis direction corresponds to the SH0 and SH1 modeshapes. The maximum amplitudes of the excitation signals were assumed to be equal to 1 μm.

In order to verify the theoretical results presented in Chapter 3 – and obtained using the perturbation technique in its multiplescale variant – amplitude spectra in the wavenumber–frequency domain were investigated numerically. Response signals from top nodes on the modelled plate were analysed for each time step using the 2–D Fourier transform. Amplitudes of resulting spectra were expressed in decibels (dB) and normalised to the maximum values.

5.2.2.1 Numerical simulation results for the dispersive SH1 mode

Numerical simulation results for the dispersive SH1 mode were firstly investigated. The results were compared with the analytical solution given in Section 3.2.

The theoretical analysis in Chapter 3 (Eq. (3.51)) demonstrates that the first and higher harmonics of odd order are generated due to the interaction of the SH1 mode with the nonlinear material. The simulated characteristics in the wavenumber–frequency domain presented in Fig. 5.4 confirm the presence of this effect. The results in Fig. 5.4a give the total solution. The contributions of the first four eigenfunctions of the shear horizontal guided waves (i.e., SH0, SH1, SH2 and SH3) to the total solution is given in Fig. 5.4b–e. The modal decomposition, as defined by Eq. (5.8), was employed to compute these analytical contributions.

The results of numerical simulations demonstrate that the amplitude spectra in the wavenumber–frequency domain that corresponds to the SH0 (Fig. 5.4b) and SH2 (Fig. 5.4d) mode shapes do not exhibit higher harmonics of the excited wave in the modelled system. This observation is consistent with the derived theory. However, some background noise and numerical discrepancies can be observed in the analysed characteristics, due to very small amplitude levels analysed.

The odd higher harmonics are exhibited in the calculated amplitude spectra corresponding to the SH1 and SH3 modeshapes (Fig. 5.4c,e). Interestingly, the first harmonic is dominant when the characteristic for the SH1 eigenfunction is analysed in Fig. 5.4c, whereas the third harmonic

prevails in the characteristic for the SH3 mode shape in Fig. 5.4e. This result also aligns well with the analytical solution presented in Chapter 3.

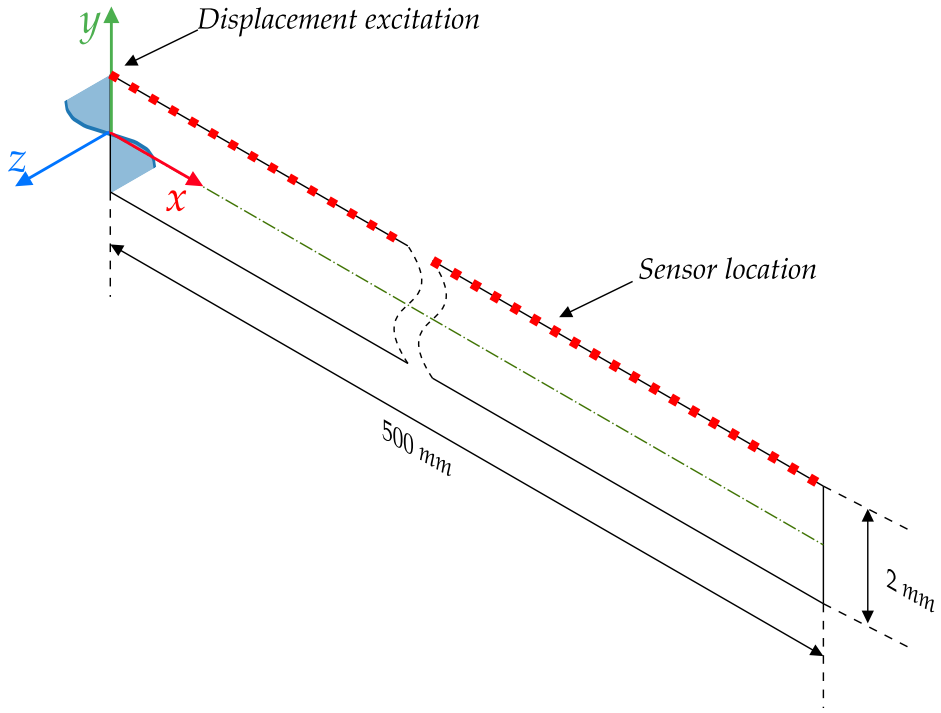

Figure 5.4: The two–dimensional numerical model of a 2 mm thick semi–infinite aluminium plate developed for nonlinear wave propagation modelling, based on the LISA technique. The model considers the SH1 mode propagation.

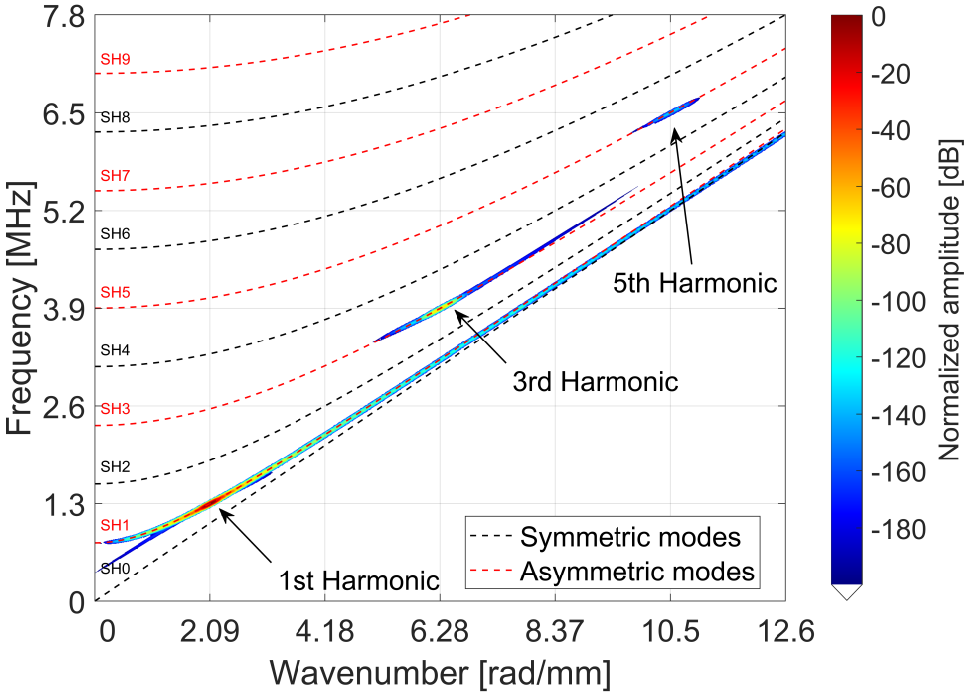

(a) The amplitude spectrum characteristic for signals collected at the nodes on the surface of the modelled plate.

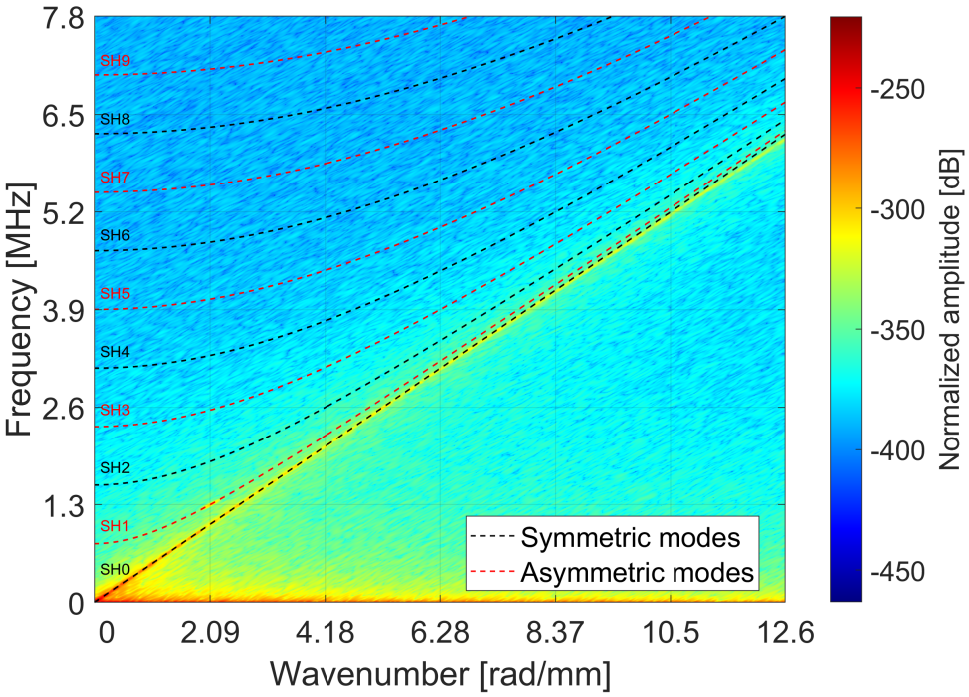

(b) The amplitude spectrum characteristic corresponding to the SH0 modeshape.

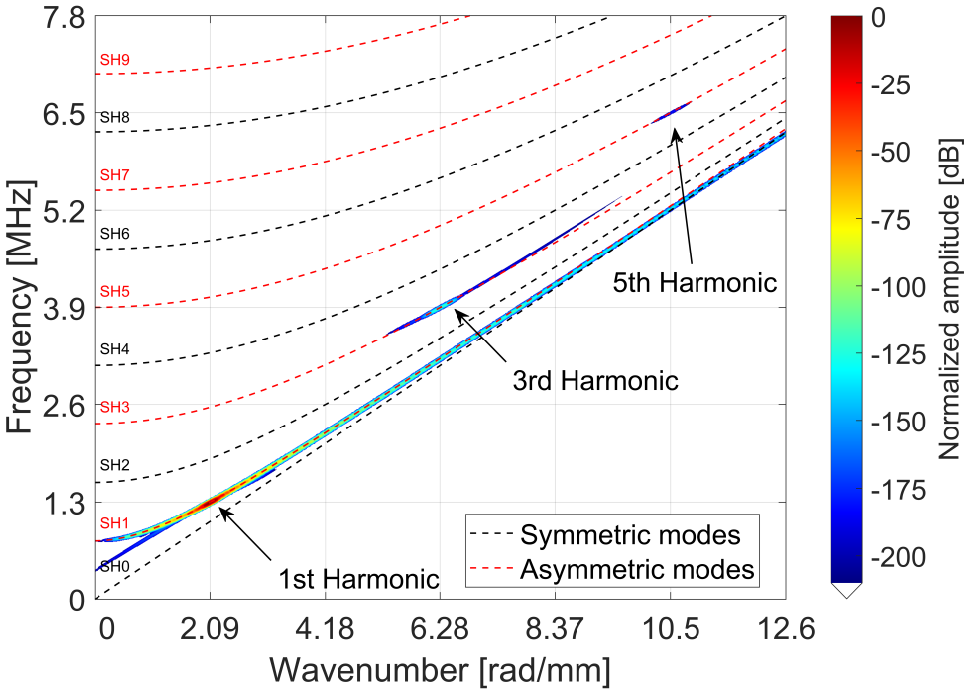

(c) The amplitude spectrum characteristic corresponding to the SH1 modeshape.

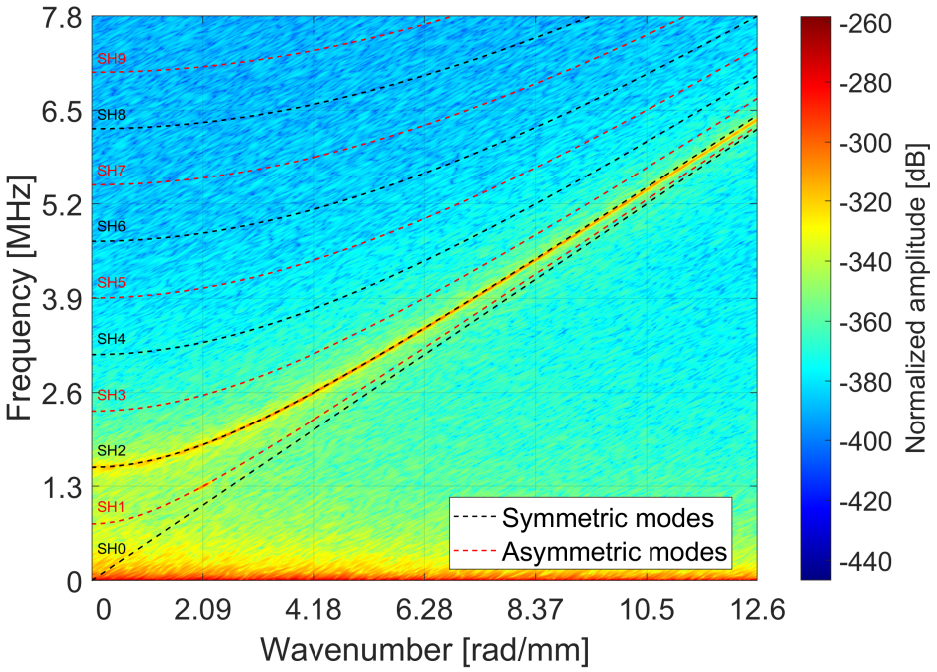

(d) The amplitude spectrum characteristic corresponding to the SH2 modeshape.

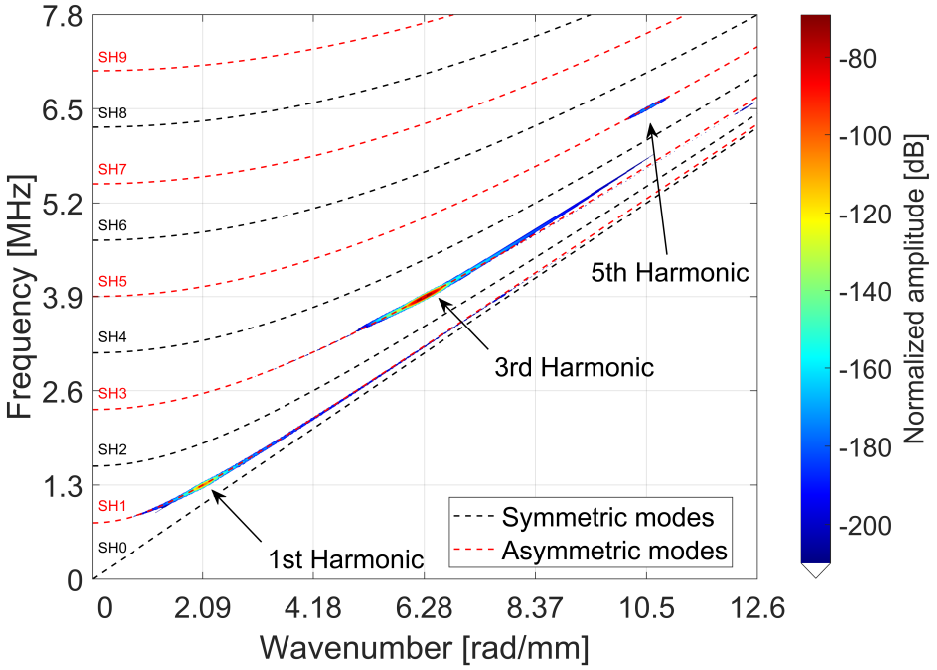

(e) The amplitude spectrum characteristic corresponding to the SH3 modeshape.

Figure 5.4: The amplitude spectrum characteristics in the wavenumber–frequency domain corresponding to the signals collected for the numerical model with selectively excited SH1 mode at a frequency of 1.3 MHz. The dashed lines correspond to the theoretical dispersion curves. Please note that the white background in figures (a), (c) and (e) correspond to numerical amplitudes smaller than -200 dB.

5.2.2.2 Numerical simulation results for the nondispersive SH0 mode

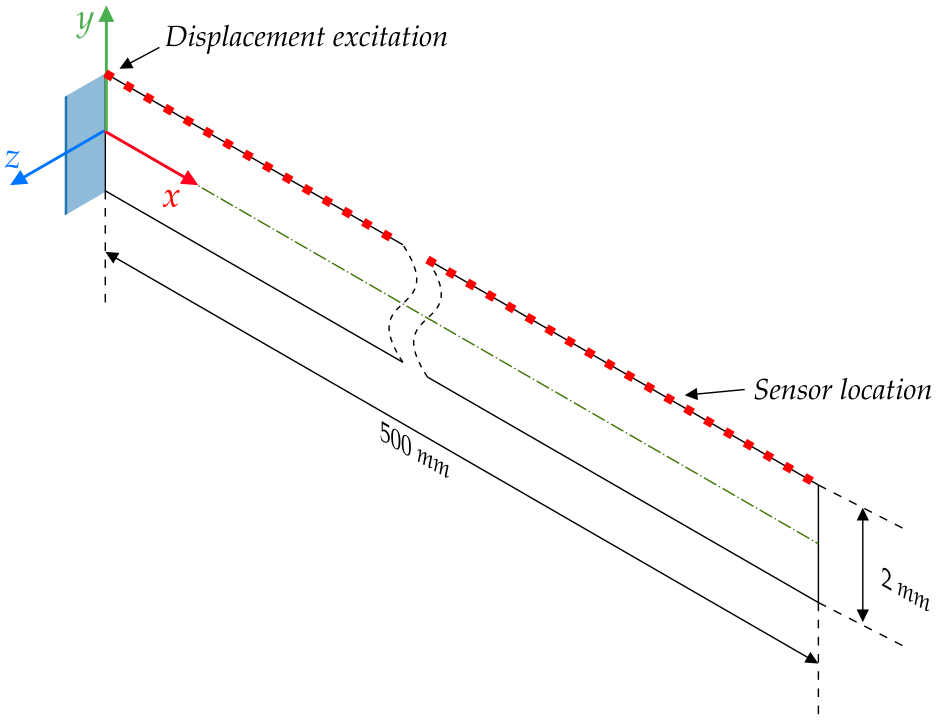

Figure 5.5: The two-dimensional numerical model of a 2 mm thick semi-infinite aluminium plate was developed for nonlinear wave propagation modelling based on the LISA technique. This investigation considered the SH1 mode.

The following section presents the simulation results for the numerical case with the selectively excited SH0 mode. In this case, the analysis presented in Section 3.2 demonstrates that when the SH0 mode interacts with the nonlinear material, the response amplitude spectrum should include the first harmonic and higher odd harmonics. Moreover, the developed theory predicts that only the SH0 modeshape contribution is expected in the amplitude spectrum characteristics. Fig. 5.6 presents the simulated results. These results align well with the developed theory. The characteristic in the wavenumber–frequency domain of the total response of the system measured on the surface of the plate is presented in Fig. 5.6a. The contributions related to the SH0, SH1, SH2, and SH3 modeshapes are illustrated in Figs. 5.6b–e. Here, only the contribution related to the SH0 mode shape can be observed, as expected. The remaining contributions correspond to the dispersion curves of linear mode shapes. Some background noise and numerical discrepancies can be also observed in the analysed characteristics. However, these effects do not prevail the major findings of the presented results.

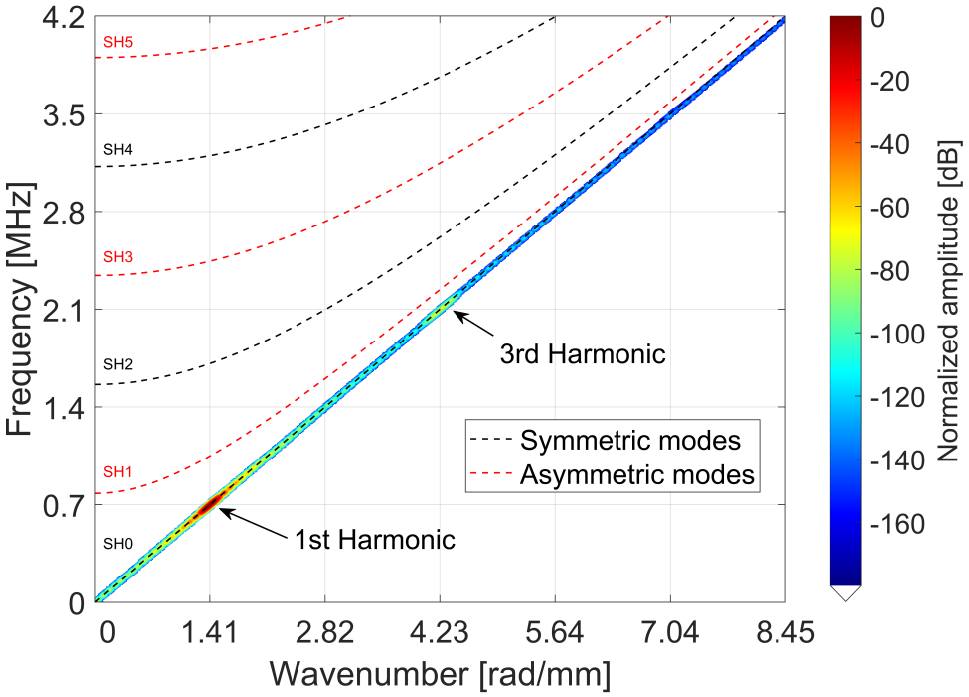

(a) The amplitude spectrum characteristic for signals collected at the nodes on the surface of the modelled plate.

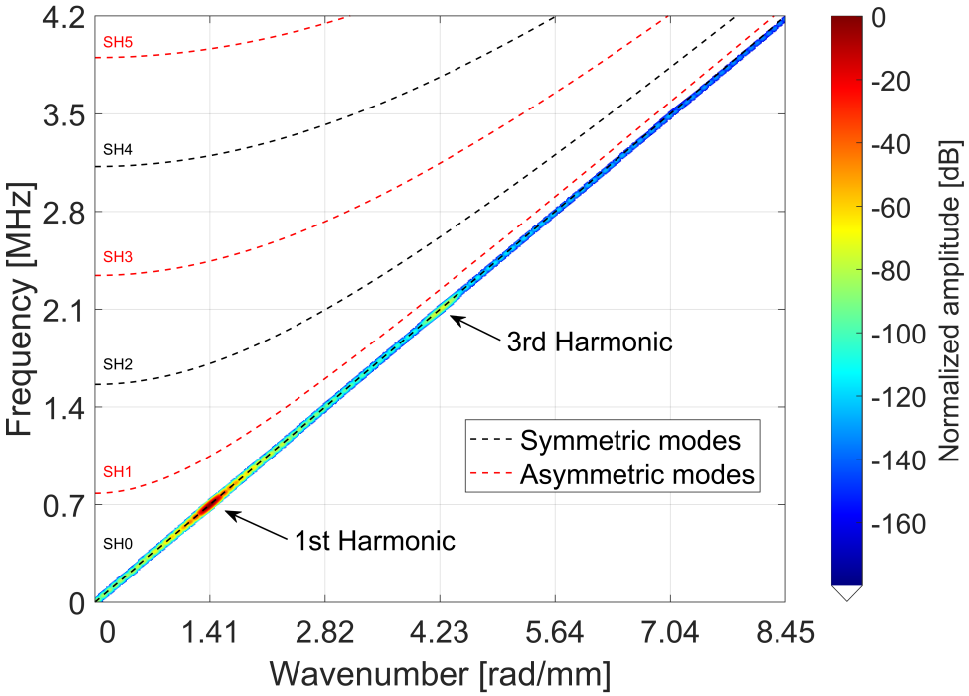

(b) The amplitude spectrum characteristic corresponding to the SH0 mode shape.

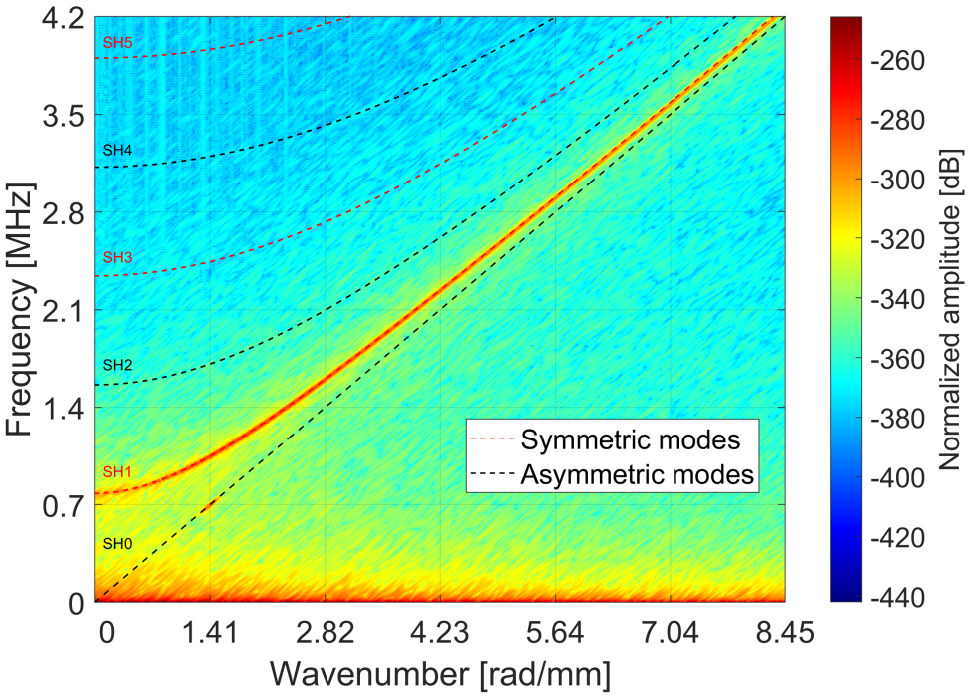

(c) The amplitude spectrum characteristic corresponding to the SH1 mode shape.

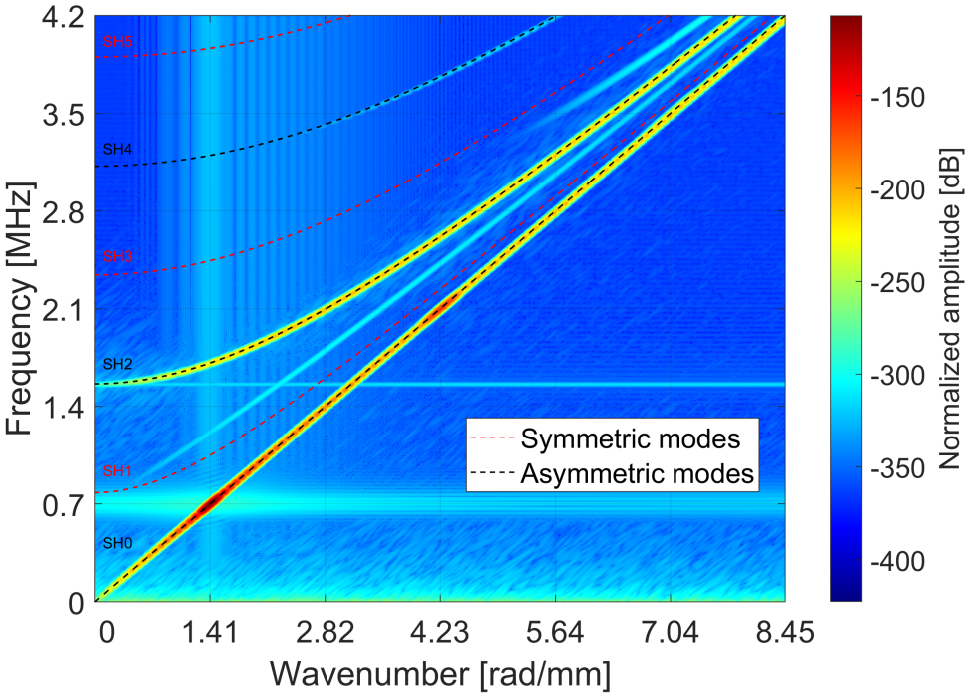

(d) The amplitude spectrum characteristic corresponding to the SH2 mode shape.

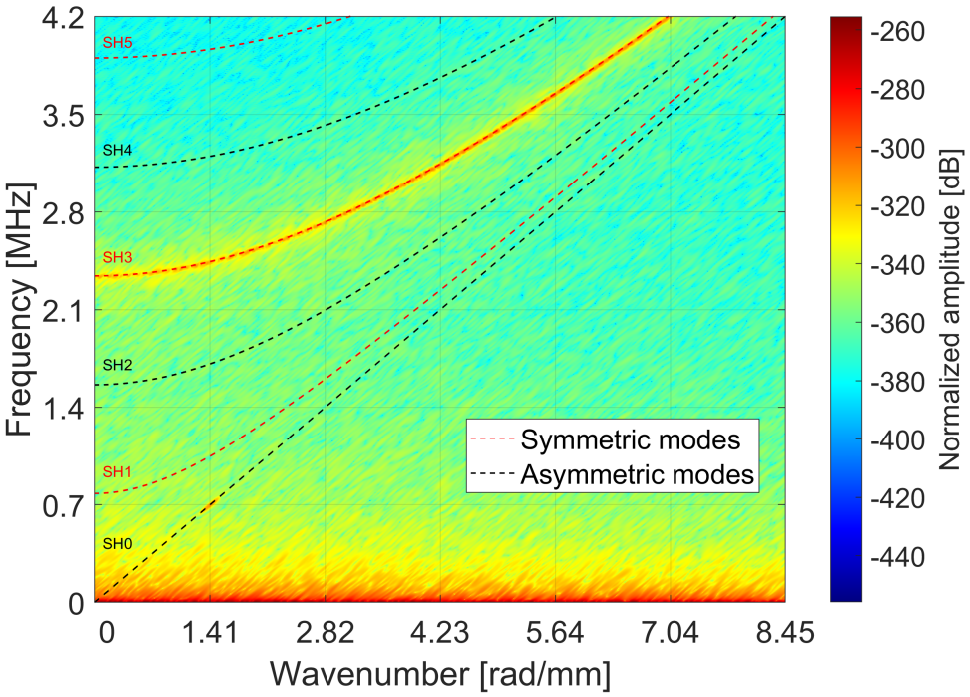

(e) The amplitude spectrum characteristic corresponding to the SH3 mode shape.

Figure 5.6: The amplitude spectrum characteristics in the wavenumber–frequency domain corresponding to the signals collected for the numerical model with selectively excited SH0 mode at a frequency of 0.7 MHz. The dashed lines correspond to the theoretical dispersion curves. Please note that the white background in figures (a), (c) and (e) correspond to numerical amplitudes smaller than -180 dB.

5.2.3 Summary

The presented results of numerical simulations demonstrate that the interaction of an excited dominant mode of shear horizontal guided waves – which is harmonic in space and time – with a hyperelastic material leads to the generation of higher harmonic components. The displacement field is notably distorted, and the calculated amplitude spectra in the wavenumber–frequency domain confirm this fact. The amplitudes of higher harmonics corresponding to individual mode shapes (i.e., eigenfunctions) can be used as a measure of this distortion. Both numerical examples conducted for SH1 and SH0 dominant modes demonstrate agreement with the analytical investigations developed in Chapter 3.

The generated higher harmonic waves are characterised by circular frequencies and wavenumbers that are odd multiplications of the angular frequency and wavenumber corresponding to the dominant mode propagating in an analysed mechanical system. The wavefield associated with these nonlinear waves is nonorthogonal with eigenfunctions

corresponding to modeshapes of shear horizontal guided waves with numbers that are odd multiplications of the number of excited driving mode. The wavefield resulting from the interaction between excited wave with nonlinear material, along with the wavefield corresponding dominant mode, can be interpreted as a nonlinear mode of shear horizontal guided waves in accordance with the theory related to vibrations of discrete and continuous mechanical systems presented in Rosenberg (1966); Vakakis & Rand (1992a,b); Nayfeh & Nayfeh (1994, 1995); Kerschen (2014).

The distortion of the dispersion curves for the excited SH1 and SH0 modes is insignificant for the model parameters considered in this case. This prediction results from the analytical solution given by Eqs. (3.43) and (3.49) and is also illustrated in Fig. 3.1.

5.3 Numerical modelling of the acoustic equivalent of the Luxembourg–Gorky effect for shear horizontal guided waves

This section describes numerical simulation undertaken to validate the acoustic equivalent of the L–G effect for shear horizontal guided waves, analysed analytically in Chapter 4. The results are presented in the frequency and combined wavenumber–frequency domains.

5.3.1 Numerical model

Numerical simulations were performed to verify the introduced nonlinear viscoelastic damping used to explain the acoustic equivalent of the L–G effect. The LISA was used to model wave propagation in a semi–infinite plate of 1000 mm length and 2 mm thickness. The cross–section of the plate was discretised into a regular grid of square cells. Elastic material properties corresponding to aluminium were assumed to be uniform within each cell. The nonlinear region was modelled using only one cell, as illustrated in Fig. 5.7. This cell represents a small local nonlinear viscoelasticity (i.e., locally reinforced damping representing small damage e.g., microcrack or short crack) for which the analytical calculations were conducted in Chapter 4.

In the region where the investigated material exhibits nonlinear behaviour, parameters of the proposed nonlinear viscoelastic damping model were selected arbitrarily. The values of these nonlinear parameters were chosen to ensure numerical stability and consistency between the numerical model and the presented analytical calculations, which were based on the perturbation method.

The linear elastic parameters i.e., the Lamé constants, were assumed as λ = 51.08 GPa and μ = 26.32 GPa, while the material density was taken to be ρ = 2700 $\frac{kg}{m^3}$. The enhanced nonlinear

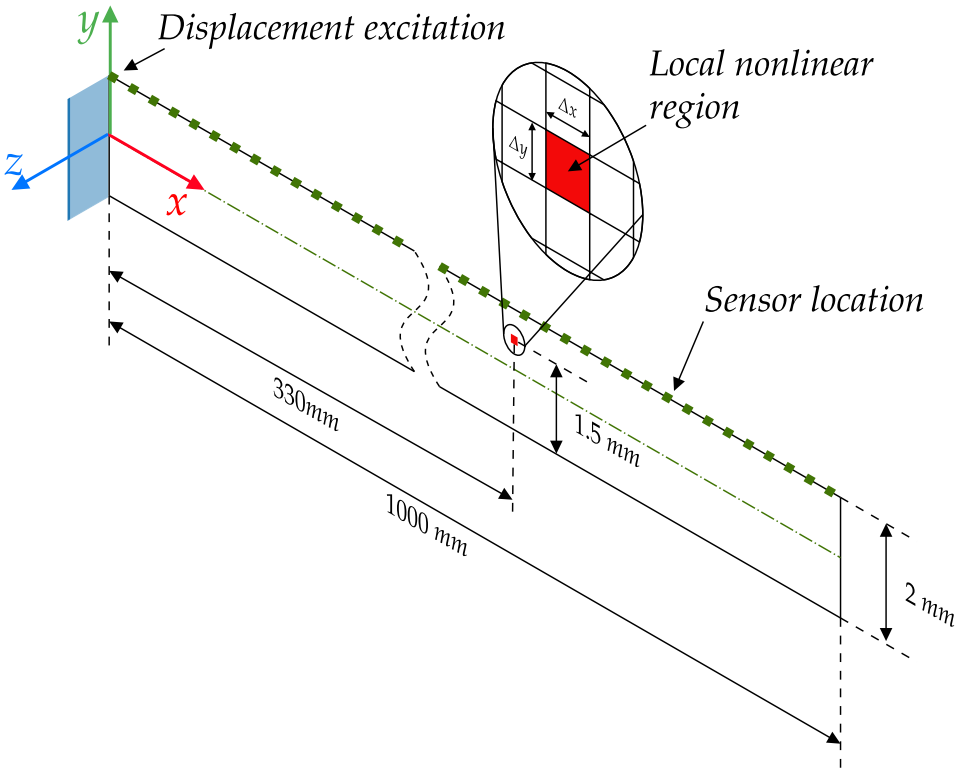

Figure 5.7: Two–dimensional 2 mm thick semi–infinite plate model utilised for the nonlinear wave propagation modelling based on the LISA technique. The SH0 mode is evaluated in this investigation. Nonlinear local viscous damping is assumed and modelled using only one cell.

damping in the material region – that modelled a local defect – was achieved by defining the nonlinear parameters used in Eq. (4.18). The values assigned to these parameters, namely $\mathcal{I}$, $\mathcal{J}$, $\mathcal{K}$, $\mathcal{M}$, $\mathcal{N}$, $\mathcal{O}$ and $\mathcal{P}$ were chosen arbitrarily and were all equal to 10^{-11} Pa·s.

To accurately simulate the dynamics of an elastic aluminium plate, the dimensions of the grid were set to $\Delta x = \Delta y = 0.1$ mm. As a result, the cross–section of the plate was divided into 20 elements across its thickness. For numerical stability, the time step for simulations was set as $\Delta t = 0.01$ μs. The final numerical model used a space and time discretisation that ensured sufficient convergence of the analytical and numerical dispersion characteristics. This approach was adequate for the accurate analysis and modelling of shear horizontal guided waves propagating in the modelled aluminium plate.

The shear horizontal guided waves were generated in the investigated system through displacement excitation. This excitation was applied across the thickness of the plate and assigned to the left–hand side of the system, as shown in Fig. 5.7. In order to excite a specific mode of the shear horizontal guided wave, it is important to match the excitation profile in the y–axis direction

with the corresponding modeshape. Therefore, the excitation signal was defined to ensure this matching. Thus, the excitation signal was given as

$$w(x,y,t)\Big|_{x=0} = \frac{1}{2}Y^{(0)}(y)\left(A_1 e^{-i\omega_1 t} + A_2\left(1 + R_{\omega_2\pm\Omega}\cos(\Omega t)\right)e^{-i\omega_2 t}\right) + c.c., \tag{5.9}$$

where A_1 and A_2 are the carrier amplitudes for the monoharmonic and amplitude modulated waves, respectively and $R_{\omega_2\pm\Omega}$ denote the modulation index. Such excitation guaranteed that only the SH0 mode was excited in the modelled plate.

5.3.2 Numerical simulation results

The work presented in this section investigates the acoustic equivalent of the L–G effect for shear horizontal guided waves. Two numerical case studies were conducted. In both cases two waves were excited simultaneously using the displacement excitation defined in Eq. (5.9). In all simulations performed, the carrier amplitudes of these were set to A_1 = 1 μm and A_2 = 0.75 μm, whereas the modulation index of one wave was equal to $R_{\omega_2\pm\Omega}$ = 1/3. Hence, the maximum displacement of the material particle was equal to 2 μm. In the first case investigated, the angular frequency of the "wanted" wave was higher than that of the "disturbing" wave (i.e., $\omega_1 > \omega_2$). Subsequently, the opposite angular frequency condition (i.e., $\omega_2 > \omega_1$) was analysed. Furthermore, both scenarios investigated the effect of the ω_1, ω_2 angular frequencies on the modulation transfer. The first scenario involved a constant value of ω_1 and an increasing value of ω_2. In contrast, the second scenario relied on a constant value of ω_2 and a rising value of ω_1. The modulation intensity associated with the nonlinear modulation transfer was evaluated utilising the modulation index defined as

$$R_{\omega_1\pm\Omega} = \frac{A_{\omega_1-\Omega} + A_{\omega_1+\Omega}}{A_{\omega_1}}, \tag{5.10}$$

where $A_{\omega_1-\Omega}$ and $A_{\omega_1+\Omega}$ denote the amplitudes of the first left and right sidebands of the ω_1 carrier angular frequency, respectively. The A_{ω_1} coefficient denotes the amplitude of the shear horizontal guided wave to which the modulation is transferred.

5.3.2.1 Nonlinear nonclassical modulation transfer

This section provides a demonstration of the nonlinear modulation transfer through two distinct examples. In the first case, the transfer of modulation is studied from lower to higher frequencies. This scenario involves two waves, the "wanted" and "disturbing" waves, with the carrier frequencies of f_1 = 750 kHz and f_2 = 185 kHz, respectively. The "disturbing" wave was subjected to amplitude modulation described by Eq. (5.9), with the modulating frequency of 41 kHz.

Fig. 5.8 illustrates two response spectra for wave responses representing the linear system and the system with the local nonlinear viscoelasticity. Both responses were acquired 340 mm, from the

excitation point i.e., 10 mm behind the modelled defect in the nonlinear system. This measurement point was located in the vicinity of the modelled nonlinear region, to maximise the observation of the L–G effect. This is consistent with earlier conclusions from the analytical investigations that all propagating and evanescent modes of shear horizontal guided waves are generated due to the interaction of the shear horizontal waves and the nonlinear region. Therefore, the L–G effect will be more pronounced in the vicinity of damage rather than long distance away from the damage, where amplitudes corresponding to the evanescent modes will decay. The response of the modelled mechanical system was measured under continuous displacement excitation. In order to calculate the amplitude spectra, simulated responses were windowed using the Chebyshev window with the side lobe level of -130 dB.

Fig. 5.8 shows that the response spectrum of the simulated linear system, only exhibits the frequency components corresponding to the applied excitation, as expected. In contrast, the response spectrum of the simulated plate with the local nonlinearity exhibits the third harmonic of the fundamental f_1 frequency. In addition, frequency components associated with the "subsidiary" waves, which are waves of frequencies that are combinations of f_1 and f_2 frequencies, can be also observed in this response spectrum. However, the nonlinear modulation transfer from the "disturbing" wave to the "wanted" wave – which corresponds to the L–G effect – cannot be observed for the assumed parameters and applied excitation.

In order to better understand the behaviour of the simulated systems, both linear and nonlinear responses were acquired for all surface nodes of the simulated plate cross–section. These responses were then analysed in the wavenumber–frequency domain using the Fourier transform. The analysis was performed to identify which shear horizontal guided wave modes were generated due to the wave interaction with the local nonlinearity simulating a defect.

Fig. 5.9a and Fig. 5.9b give the results for the linear and nonlinear simulated plates. These results are plotted together with the theoretical dispersion curves. The results for the linear system in Fig. 5.9 exhibit only frequency components corresponding to the excitation, as expected. When the system with the local nonlinearity is analysed in Fig. 5.9b additional components related to the "subsidiary" waves – with frequencies equal to the combinations of f_1 and f_2 – can be identified. However, the modulation is not transferred from the "disturbing" to the "wanted" wave for assumed parameters and excitation. These results also show that the excitation of the SH0 mode in the nonlinear system, results in the generation of the SH1 and SH2 modes. It is evident that the local damping nonlinearity serves as a source of generation of higher shear horizontal guided wave modes. This nonlinear phenomenon has been anticipated by the analytical calculations presented in Chapter 4.

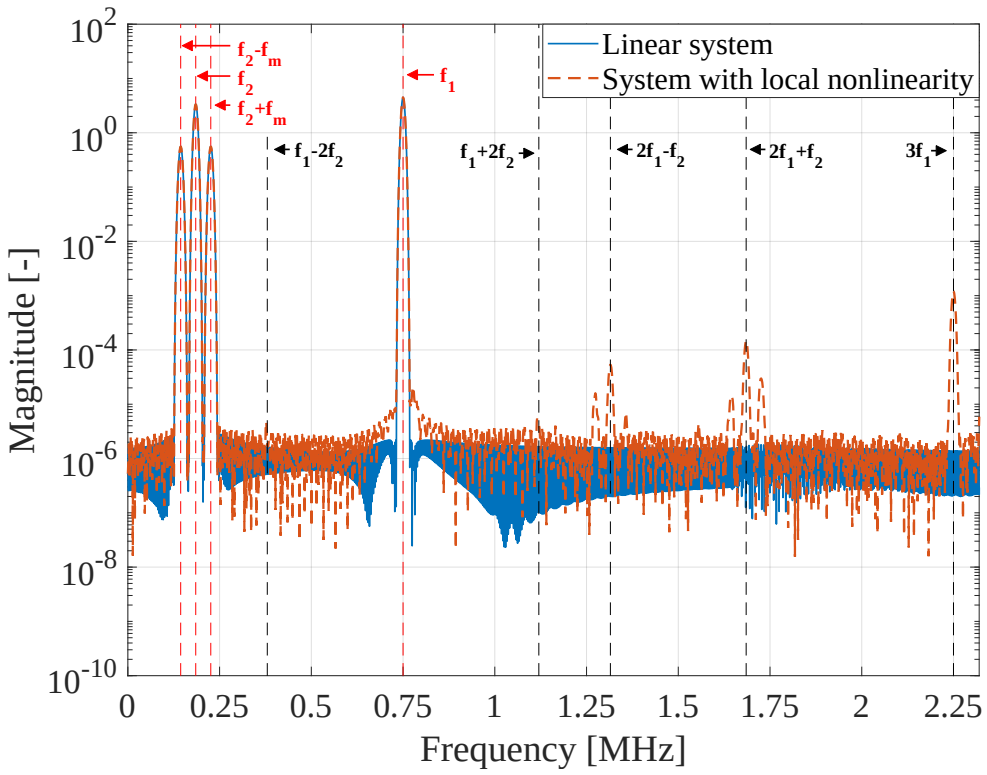

Figure 5.8: Simulated wave response amplitude spectra for the case when the excitation frequency $\omega_1 > \omega_2$. The response was acquired 10 mm behind the simulated damage. The response for the linear system (i.e., without damage) was captured in the same position.

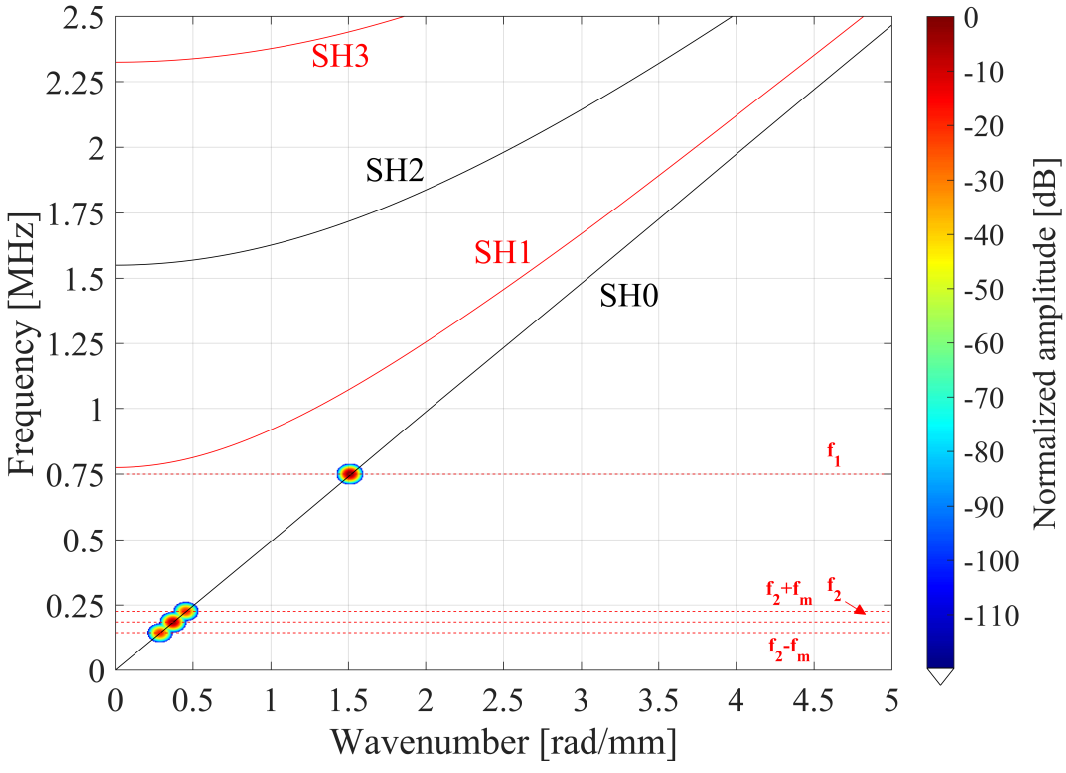

(a)

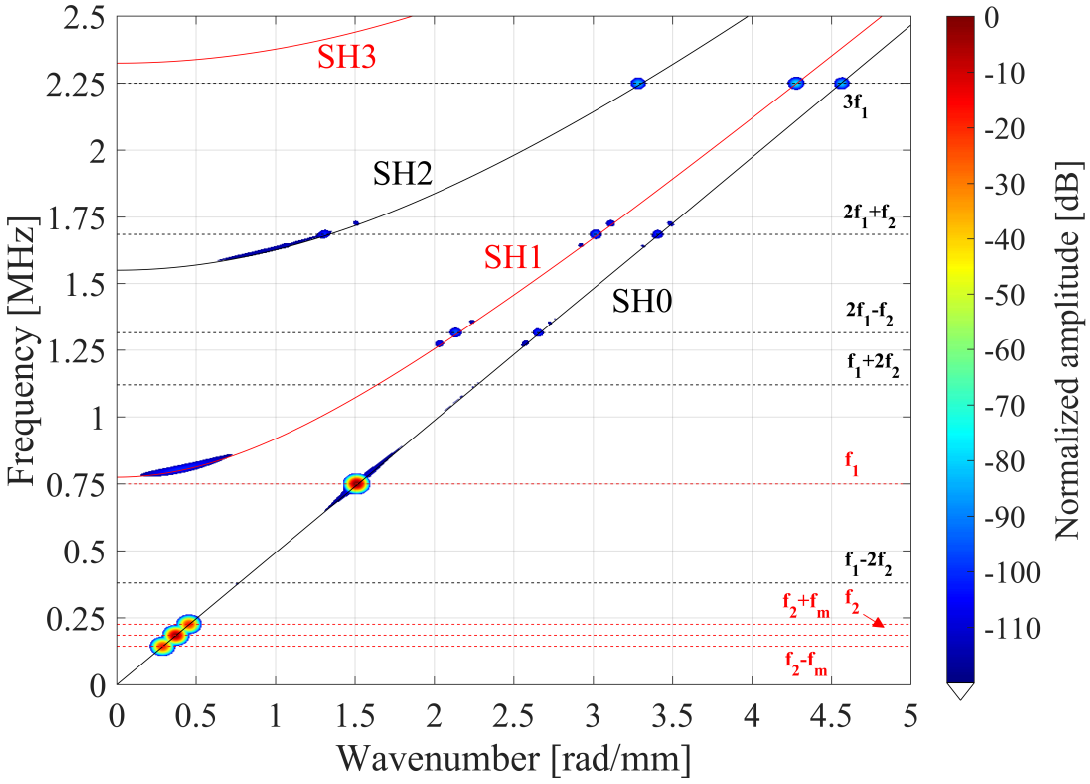

(b)

Figure 5.9: Amplitude spectra in the wavenumber–frequency domain for simulated responses acquired on the surface of the plates for the excitation frequency $\omega_1 > \omega_2$: (a) linear system; (b) nonlinear system. Simulated results are imposed on the solid lines corresponding to the theoretical dispersion curves. Note that the white background represents numerical amplitudes smaller than -120 dB.

In the second numerical case investigated, the carrier frequencies of the "wanted" and "disturbing" waves were equal to f_1 = 185 kHz and f_2 = 750 kHz, respectively. All other parameters were identical to those used in the first example. The results are presented in Fig. 5.10. Again, for the linear system considered, no transfer of modulation, generation of higher harmonics or frequency components – corresponding to the combinations of f_1 and f_2 frequencies – were observed, as anticipated. However, the system with local nonlinearity exhibits the third harmonic of the f_2 fundamental frequency in response spectrum. Furthermore, frequency components related to the "subsidiary" waves – i.e., waves whose carrier frequencies are combinations of f_1 and f_2 frequencies – can be also observed in the spectrum for the nonlinear system.

More importantly, the modulation transfer from the "wanted" wave to "disturbing" wave can be observed in Fig. 5.10 for the analysed nonlinear system in the second case investigated. This

effect is also noticeable for carrier frequencies corresponding to the "subsidiary" waves and the third harmonic of the f_2 fundamental frequency. Fig. 5.11 displays a zoomed spectrum around the f_1 carrier frequency, confirming the existence of the L–G effect for the simulated system with the local damping nonlinearity, predicted by the approximated analytical solution given in Chapter 4.

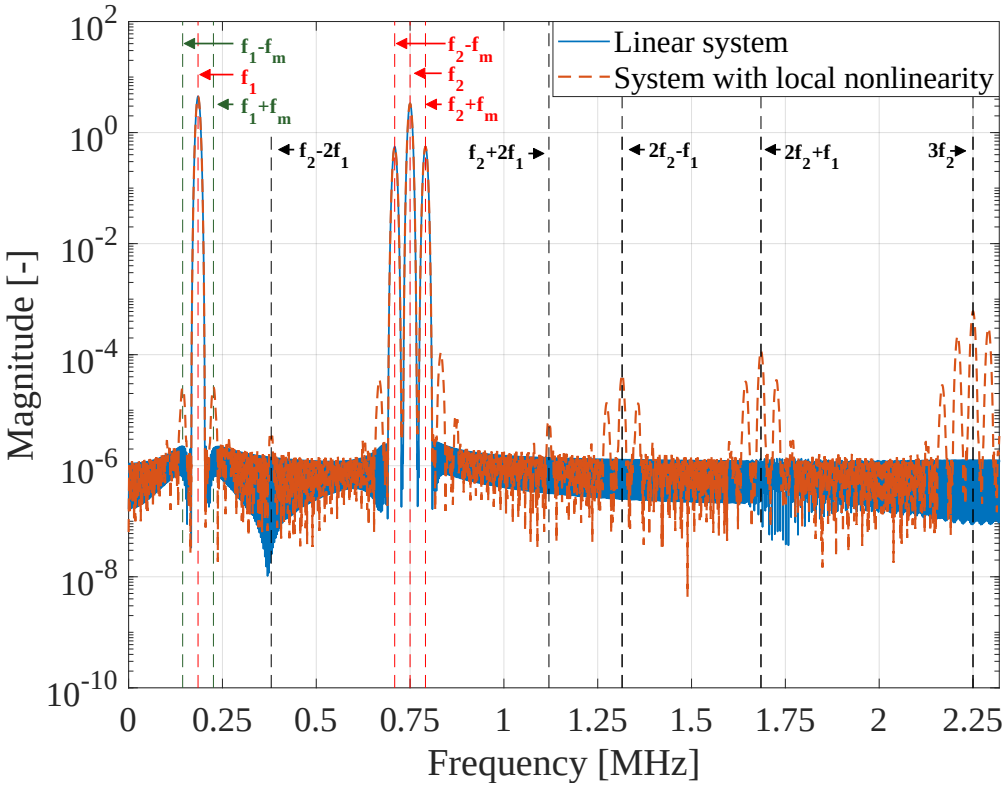

Figure 5.10: Simulated wave response amplitude spectra for the case when the excitation frequency $\omega_2 > \omega_1$. The response was acquired 10 mm behind the simulated damage. The response for the linear system (i.e., without damage) was captured in the same position.

By analogy to the first case investigated, the simulations for the $\omega_1 < \omega_2$ excitation condition were also analysed in the wavenumber–frequency domain. The results are presented in Fig. 5.12a and Fig. 5.12b. The linear system exhibits in Fig. 5.12a only frequency components in the response spectrum that correspond to the excitation frequencies. In contrast, the results for the nonlinear system in Fig. 5.12b confirms that when $\omega_1 < \omega_2$, the modulation is transferred from the "disturbing" to the "wanted" wave. In addition, similarly to the results presented in Fig. 5.9b, higher shear horizontal guided wave modes are also generated. The amplitude spectra for the nonlinear system indicate the existence of the SH0, SH1, and SH2 modes for the frequency range investigated. Clearly, when the first fundamental mode was initially excited, the interaction of this mode with the local nonlinearity leads to higher mode generation. Therefore, the simulated results

confirm the predictions given by the analytical solution in Chapter 4 and demonstrate the effectiveness of LISA for nonlinear wave propagation and interaction simulations.

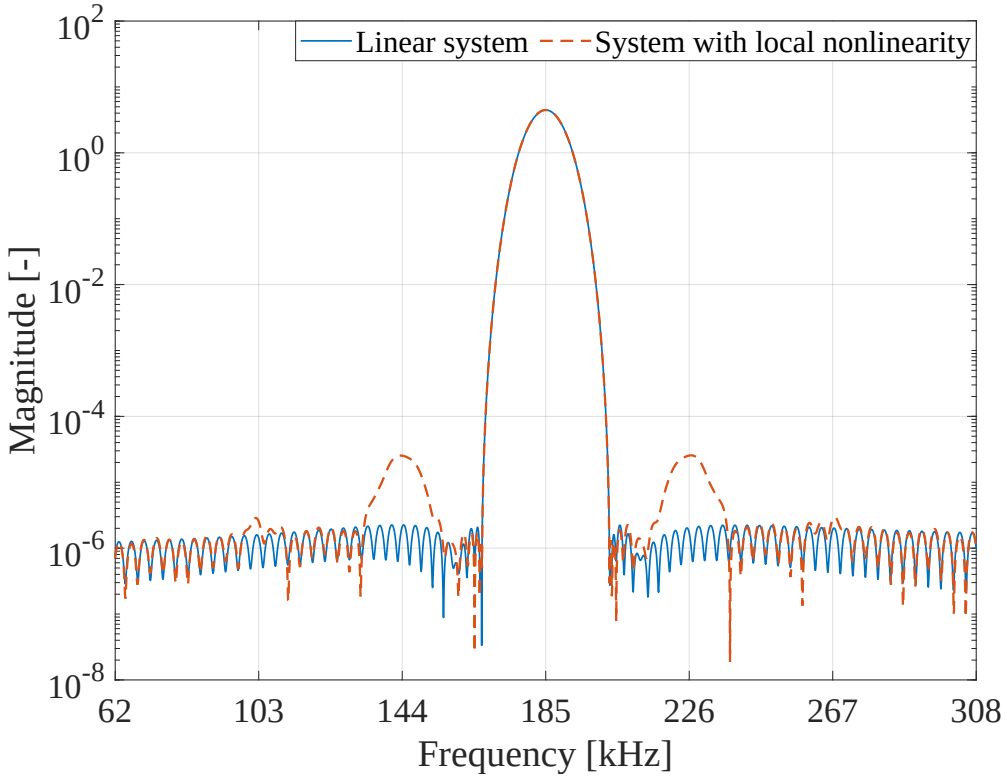

Figure 5.11: The amplitude spectra from Fig. 5.10 zoomed around the f_1 carrier frequency.

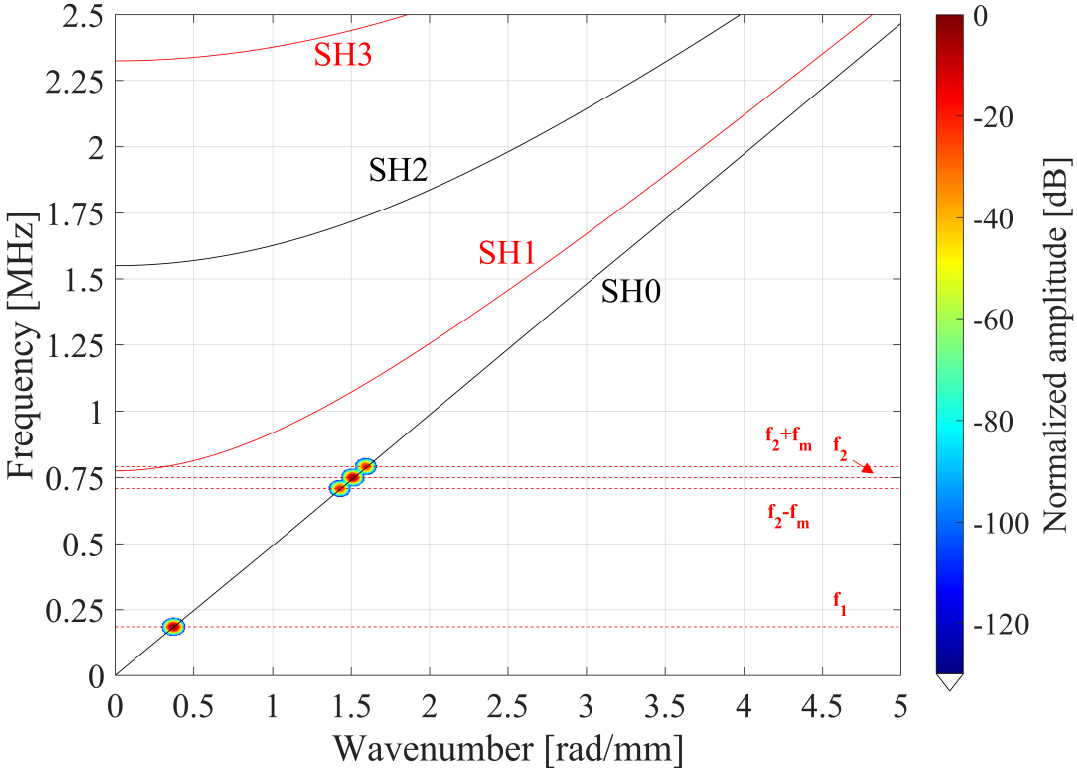

(a)

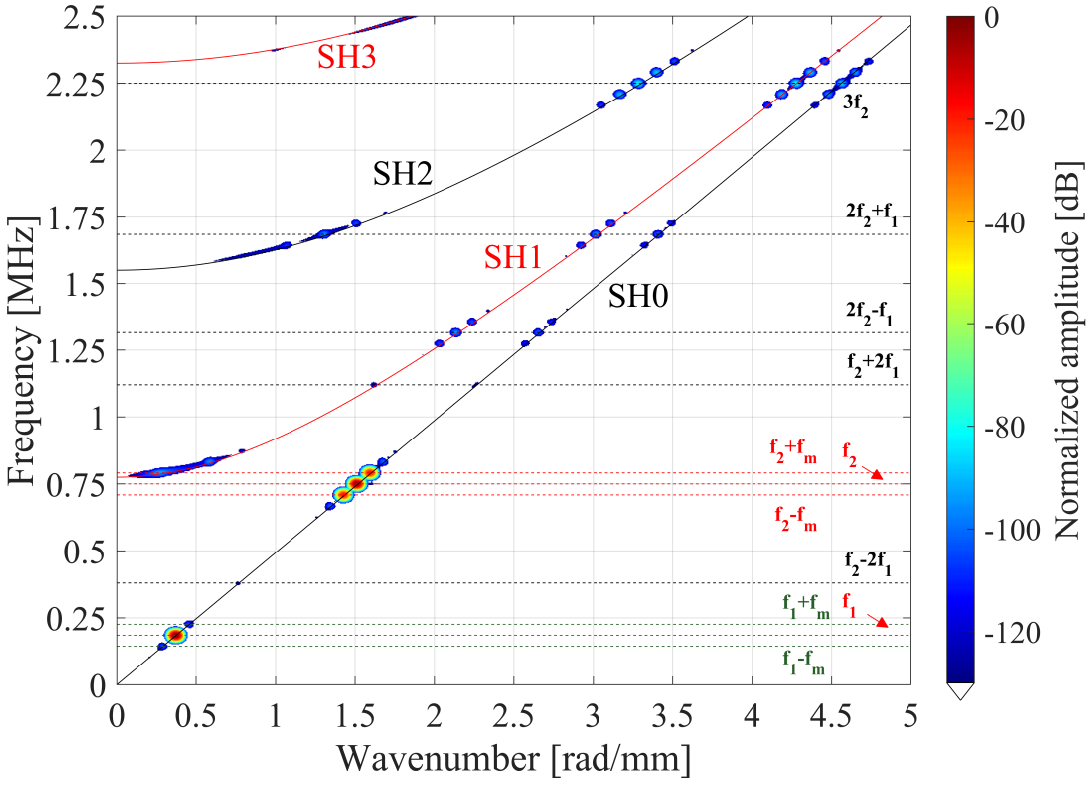

(b)

Figure 5.12: Amplitude spectra in the wavenumber–frequency domain for simulated responses acquired on the surface of the plates for the excitation frequency $\omega_1 < \omega_2$: (a) linear system; (b) nonlinear system. Simulated results are imposed on the solid lines corresponding to the theoretical dispersion curves. Note that the white background represents numerical amplitudes smaller than -120 dB.

5.3.2.2 Analysis of modulation intensity of the Luxembourg–Gorky effect

The simulation results reported in the previous section illustrate the acoustic equivalent of the L–G phenomenon for shear horizontal guided waves. This section investigates the intensity of the transferred modulation with respect to the frequencies of the excited waves. Firstly, the frequency f_1 = 185 kHz of the "wanted" wave was kept constant and the modulation intensity was calculated for various f_2 frequencies of the "disturbing" wave. Fig. 5.13 illustrates that in this case the modulation intensity grows monotonically with the increasing frequency of the "wanted" wave. This relationship is nonlinear and can be approximated by a quadratic function.

Similar simulations were performed for the constant f_2 = 750 kHz frequency of the "disturbing" wave and different f_1 frequencies of the "wanted" wave. The results presented in Fig. 5.14 demonstrate that the modulation intensity also grows monotonically with increasing

frequencies of the "disturbing" wave. However, in contrast to Fig. 5.13, the relationship between the modulation intensity and the frequency of the "wanted" wave is a relatively weak nonlinear function that could be linearised. The nonlinear distortion is associated with the assumed order of the adopted nonlinear viscous damping model and its parameters. Both characteristics are consistent with the analytical solution given by Eq. (4.65) in Chapter 4.

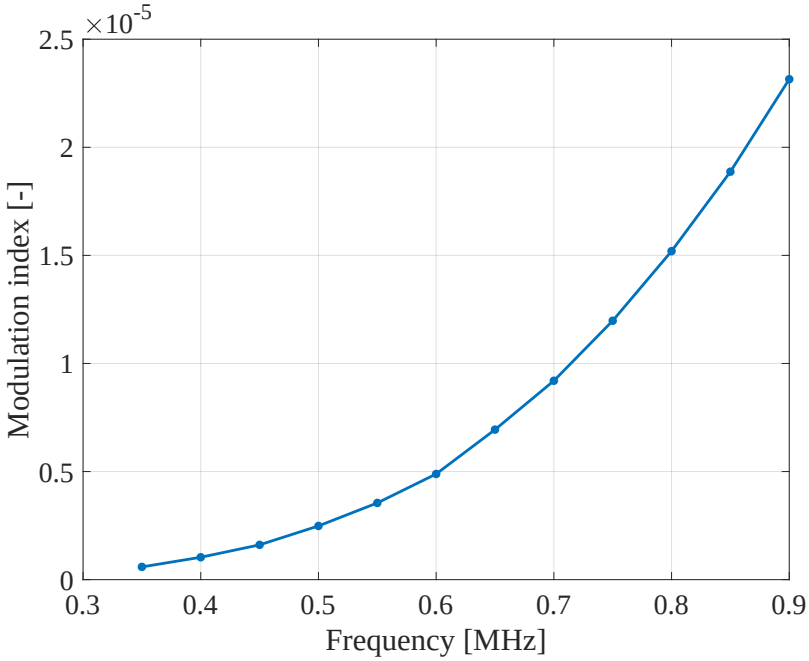

Figure 5.13: The dependence between the modulation index (Eq. (5.10)) of the nonlinear modulation transfer and the f_2 carrier frequency of the "disturbing" wave.

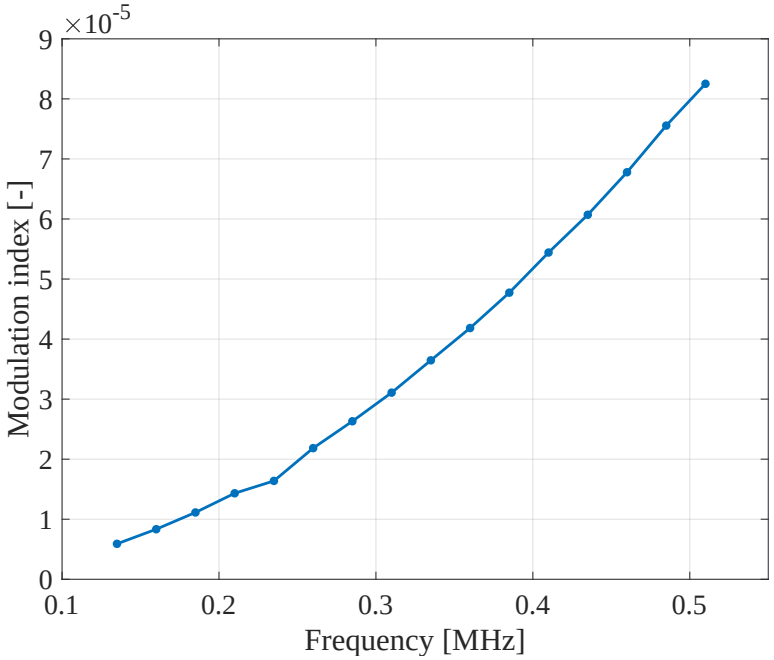

Figure 5.14: The dependence between the modulation index (Eq. (5.10)) of the nonlinear modulation transfer and the f_1 carrier frequency of the "wanted" wave.

5.3.3 Summary

The objective of the presented study was to investigate the acoustic equivalent of the L–G effect for shear horizontal guided waves. This was achieved through numerical simulations, which enabled a deeper understanding of the nonlinear modulation transfer that occurs in the presence of local damage. A new model of nonclassical nonlinear damping – based on the Kelvin–Voigt viscoelastic model proposed in Chapter 4 – was implemented in numerical simulations. These simulations were conducted using the LISA technique implemented for the shear horizontal wavefield.

The simulation results confirm that the proposed theoretical model of a local damage can be used to explain the analysed nonlinear L–G effect. Furthermore, the results indicate that the nonlinear modulation transfer in the presence of local damage is more effective from higher to lower frequencies than in the opposite direction. The results also show that the transferred modulation intensity depends on the frequencies of the "disturbing" and "wanted" waves. However, this dependence is more nonlinear for the frequency of the "disturbing" wave. The results also show that the local damage (or nonlinearity) leads to the generation of higher-–order modes of shear horizontal guided waves. These numerical simulation results fully agree with the analytical approximated solutions given in Chapter 4.

Chapter 6

Experimental studies on the L–G effect for shear horizontal waves

This chapter presents the experimental part of the research work performed. The laboratory tests were conducted to observe the nonclassical nonlinear phenomenon investigated i.e., the L–G effect. A beam specimen with a fatigue crack was used to facilitate these investigations. An intact beam specimen was also studied as a reference. The experimental tests aimed to observe the L–G effect in the case of shear movement of material particles. The specimens were excited using piezoelectric transducers. Data acquisition was performed using laser vibrometry.

Theoretical studies investigating the interaction of shear horizontal guided waves with hyperelastic material, as detailed in Chapters 3 and 5, have identified significant challenges in the experimental decomposition of the wavefield within material and verification of dispersion curve distortion. While the measurement limitations have imposed constraints on wavefield analysis within specimens, the analytical and numerical calculations presented in Chapters 3 and 5, incorporating nonlinear parameters given in Bhalla et al. (1983); Wang & Li (2009); Packo et al. (2012, 2019), indicated a minor distortion of the dispersion curve. In addition, experimental limitations in frequency and wavenumber resolution, depending on measurement time and geometrical dimensions of the investigated components, as well as unavoidable measurement noise, would further complicate data interpretation. Given these aspects and considering the limited relevance of replication of previous experimental studies on higher harmonic generation presented in Liu et al. (2013b,a); Shengbo & Cheng (2019); Fuzhen Wen (2021); Lissenden (2021) to the current research objectives, the experimental focus shifted to the L–G effect. This nonlinear phenomenon could be effectively studied using available measurement techniques and equipment.

6.1 Experimental arrangements

The experimental tests were performed to observe and analyse the nonlinear L–G effect investigated analytically and numerically in Chapters 4 and 5. Two 10 × 10 × 600 mm beam specimens made of PA38 (AW–6060) aluminium were used in these tests. Small notches were introduced 230 mm from one edge of the beams in both tested specimens for fatigue crack initiation. One of the investigated beams was fatigue–loaded. A three–point bending test was conducted to initiate and propagate a crack. The specimen was fatigued to obtain a 5 mm crack (see Fig. 6.1). The depth of the crack was measured from the top of the beam. Furthermore, the crack was generated to the specified depth throughout the entire width of the beam. The second notched beam was left intact and served as an undamaged referenced sample.

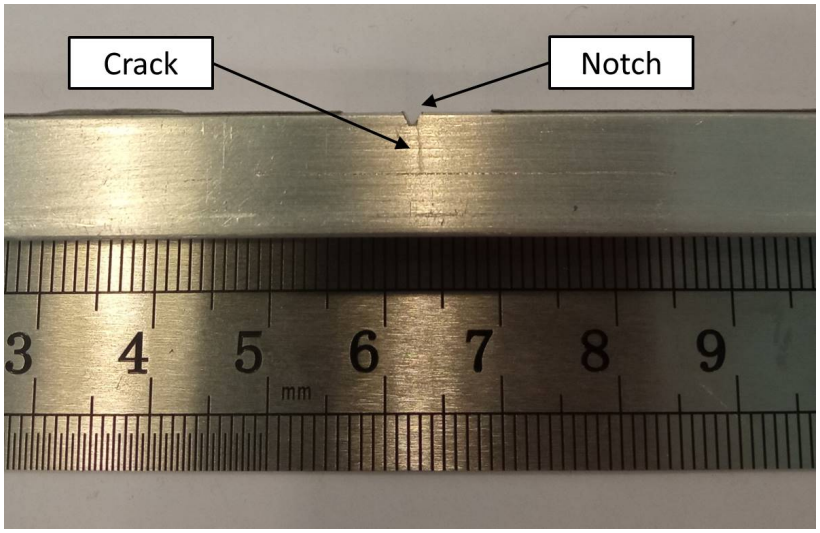

(a)

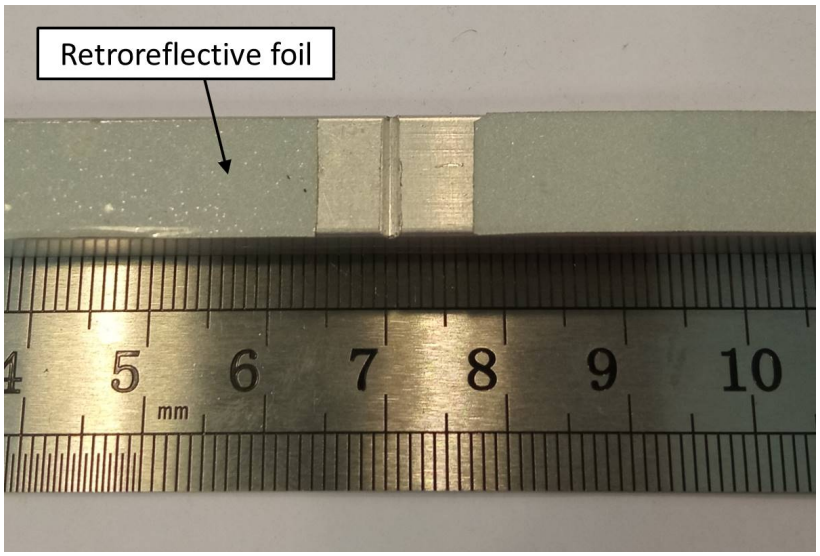

(b)

Figure 6.1: Generated 5 mm fatigue crack in a beam specimen: (a) side and (b) top views.

Both beam specimens were instrumented with two low–profile Noliac CSAP03 (10 × 10 × 0.5 mm) shear plate actuators made of NCE51 piezoceramic material. These shear plates of 3.321 pF capacitance provided a maximum free stroke of 1.5 μm. The actuators used to excite the specimens were bonded to the top and bottom surfaces of the tested beams, 25 mm from one edge of the beam. A cyanoacrylate adhesive was used for bonding. Since both electrodes of the piezoceramic plates were located on the top and bottom surfaces, a copper tape was used to wire (see Fig. 6.2) and power the actuators. The soldering temperature was controlled in order not to exceed the 368°C Curie temperature of the NCE51 material.

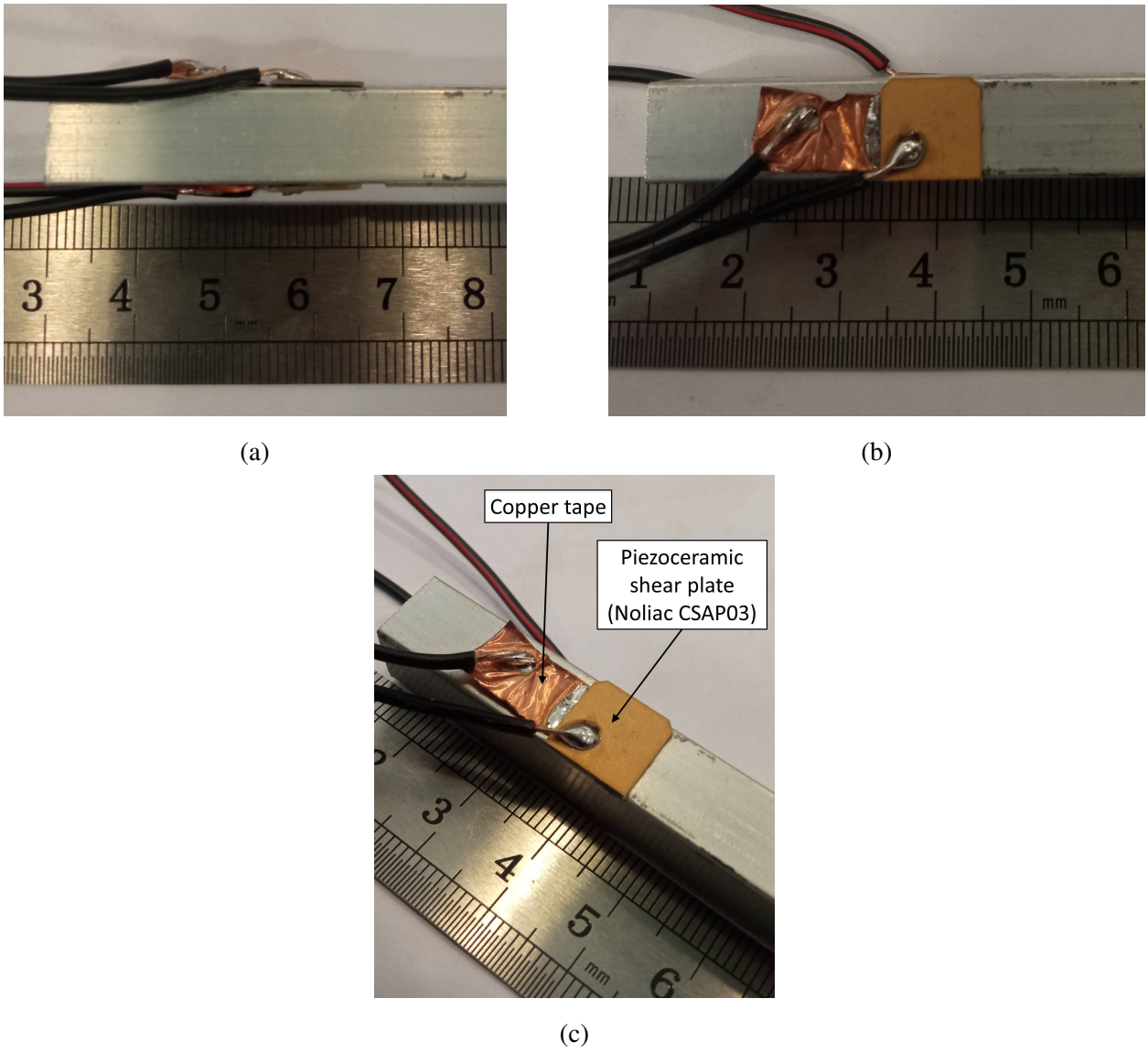

(a) (b)

(c)

Figure 6.2: Surface–bonded and wired Noliac CSAP03 shear plate piezoceramic actuators used in experimental tests: (a) side, (b) top and (c) perspective views.

The actuators, located on the top and bottom surfaces of each aluminium beam, were used to generate “wanted” and “disturbing” ultrasonic excitations (see the description of the nomenclature

used in Chapter 4). The "wanted" and "disturbing" excitations corresponded to monoharmonic and amplitude–modulated signals, respectively. The excitation signals for both piezoelectric actuators were generated using the two–channel *Keysight Agilent 33522A* arbitrary waveform generator. The data sequences of excitation signals were generated using Matlab and sent via Ethernet to the generator. The excitation signals were enveloped using a Hanning window. The excitation signals powering the shear plate actuators were amplified individually using the *E&I 1020L RF* and *Trek 2100HF* amplifiers to guarantee enough power and adequate Signal–to–Noise Ratio (SNR) for acquired responses. A two–channel *Keysight EDUX1002G* digital oscilloscope was used to control the excitation signals and avoid possible intrinsic nonlinearities related to excitation and measurement experimental chains. For both actuators, the voltage signals used to excite the shear movement of material particles for each measurement had a maximum amplitude of 150 V. In addition, the modulation index of the "disturbing" wave was kept constant at 0.5.

Small rubber tube elements were used to support the beam specimens when the laboratory tests were conducted, as shown in Fig. 6.3. The contact area between the rubber elements and the tested components measured approximately 5 × 10 mm. The intention was to provide boundary conditions that minimally influence acquired responses.

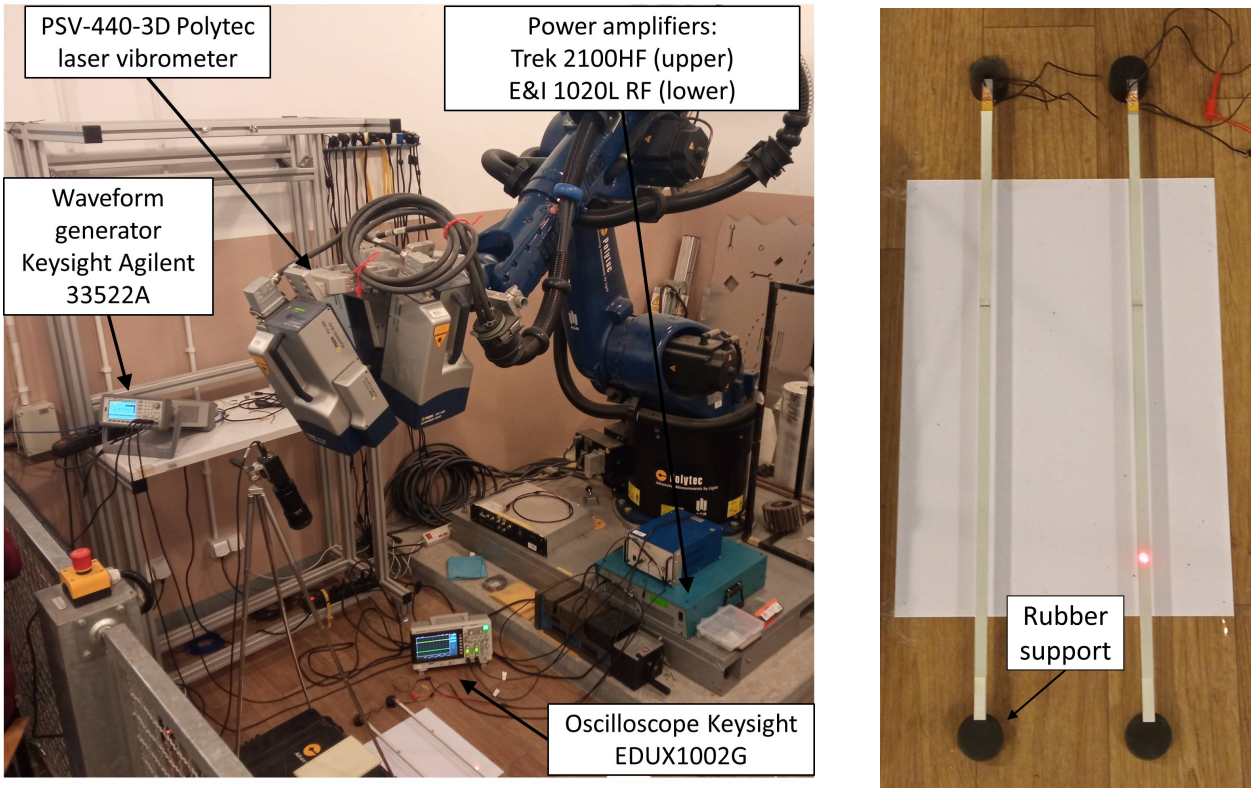

(a) (b)

Figure 6.3: Views of the (a) experimental setup and (b) beam specimens used to investigate the L–G effect for shear elastic waves.

A *PSV–400–3D Polytec* scanning laser vibrometer and a Kuka robot were used to gather responses at measurement points located on the upper surfaces of the beams. Non–contact measurements minimise potential nonlinearities that could arise from piezoceramic–based sensors Mallet et al. (2004); Staszewski et al. (2004); Spytek et al. (2023).

When responses of considered systems were acquired, the sampling frequency was equal to 2.56 MHz, which corresponded to the maximum setting of the acquisition system used. In order to enhance the SNR of the collected velocity signals, retroreflective foil strips were bonded to the upper surfaces of the beams. The retroreflective foil was not used in the vicinity of the crack to avoid disturbances to crack–wave interactions. The laser beams from three independent vibrometer heads were focused on a single point, allowing for velocity measurements in the x, y and z directions. Altogether, 15 measurement points alongside the 310 mm beam path were used, as shown in Fig. 6.4.

A trigger signal from the utilised arbitrary waveform generator was used to initiate measurements. In order to guarantee consistent initial and wave propagation conditions for the subsequent measurements taken, the period of the signal triggering of the measurement was much longer than the duration of the excitation signal. The total time of collected signals was equal to 0.2 s, which corresponded to the duration of the excitation signals. For each measurement point, 30 time–domain responses were collected and subsequently averaged in order to reduce the level of measurement noise. The modulation index corresponding to the transferred nonlinear modulation – defined in Eq. (5.10) – was used to analyse the L–G effect. Since multiple wave reflections were possible for the analysed time signals, the average value of modulation indices for all individual measuring points was used as a quantitative measure of modulation transfer.

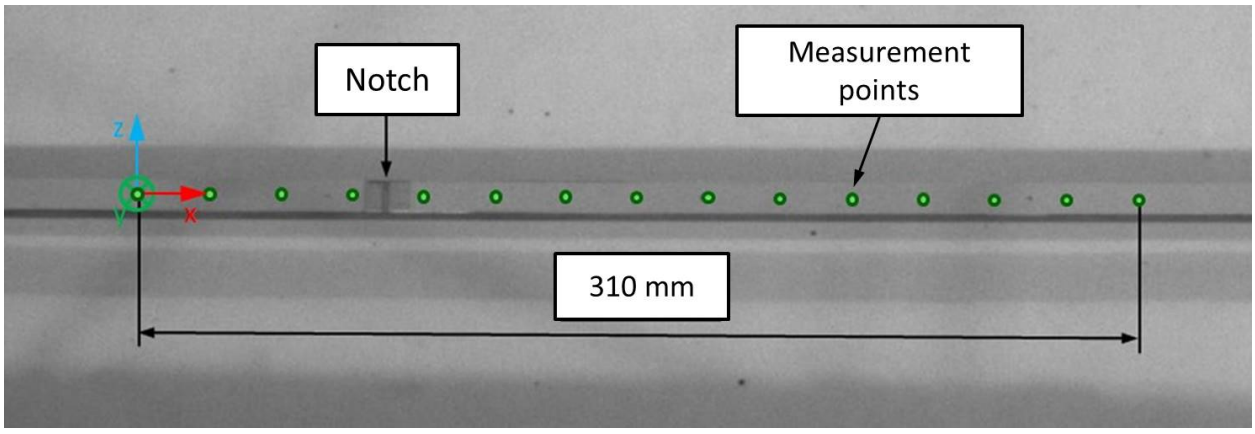

Figure 6.4: An example of a top view screenshot from a *PSV–400–3D Polytec* system showing the beam specimen, v–notch position, defined measurement points and assumed coordinate system.

6.2 Experimental results

6.2.1 Observation of the L–G effect for shear horizontal waves

The primary objective of the measurement tests was to verify the existence of the L–G effect for a cracked beam subjected to shear motion. Measurements were conducted using constant amplitude values and varying "wanted" and "disturbing" carrier frequencies of the excitation signals. Measurements were performed using both i.e., damaged and undamaged samples.

This section presents two experimental cases demonstrating nonlinear modulation transfer. The first case involved a nonlinear modulation transfer from lower to higher frequencies. The carrier frequencies for the "wanted" and "disturbing" waves were f_1 = 700 kHz and f_2 = 347 kHz, respectively. The "disturbing" wave was amplitude modulated, and the modulation frequency was f_m = 18.7 kHz. The excitation frequencies were chosen so that the relevant higher harmonics and combinations of these frequencies did not coincide, thus avoiding any potential ambiguity in measurement results.

Since the analytical and simulation works on the L–G effect presented in Chapters 4 and 5 corresponded to the displacement filed, the Fourier transform of the acquired velocity responses in time domain were divided by $i2\pi f$ term, where f is frequency, to avoid inconsistencies between results of numerical simulations and experimental measurements. This operation corresponds to integrating the velocity signal in the time domain Lighthill (1958); Duffy (2004).

Figs. 6.5a and 6.5b give the results in the frequency domain for the undamaged and cracked beams, respectively. The relevant responses were gathered for the arbitrarily selected fourth measurement point located in the crack vicinity (see Fig. 6.4). The results show that the frequency components associated with the excitation can be identified for the measurements corresponding to both investigated beams. The vertical dashed red lines indicate the carrier frequencies excited in the beams.

For the undamaged beam, the higher harmonics of the f_1 and f_2 frequencies cannot be seen in the amplitude spectrum presented in Fig. 6.5a. One "subsidiary" component with a frequency equal to $9f_2 - 3f_1$ can be observed for this specimen and is indicated by a black dashed line. Furthermore, frequency components associated with modulation transfer from "disturbing" to "wanted" frequencies can be identified. The relevant sidebands are indicated using vertical dashed green lines. It is worth noting that the values of amplitude spectra corresponding to these frequencies are noticeably different. One is very close to the measurement noise level for the considered measurement point.

For the sample with generated crack also higher harmonics of the f_1 and f_2 frequencies are not visible in the amplitude spectrum shown in Fig. 6.5b. However, the "subsidiary" component corresponding to $f_1 - f_2$, $3f_1 - 4f_2$ and $2f_1 - f_2$ frequencies can be identified. Moreover,

frequency components associated with modulation transfer from “disturbing” to “wanted” frequencies can be observed in the calculated amplitude spectrum. The relevant sidebands are indicated using vertical dashed green lines. For this sample, the values of amplitude spectra corresponding to these sideband frequencies are almost identical.

The averaged modulation index value for all individual measuring points was employed as a comprehensive measure of the modulation transfer for both specimens. Regarding the frequency pair under consideration, the average modulation indices – after removing results that were identified as outliers – were equal to $4.39 \cdot 10^{-3}$ and $4.22 \cdot 10^{-3}$ for the damaged and undamaged tested beam components, respectively. This means that the results obtained for the investigated carrier frequency pair do not unambiguously indicate that the presence of the crack is the source of the L–G effect for the frequency pair considered in this measurement case. This phenomenon should be manifested by the higher values of the amplitude spectrum for the damaged sample than for the undamaged sample at frequencies corresponding to the transferred modulation.

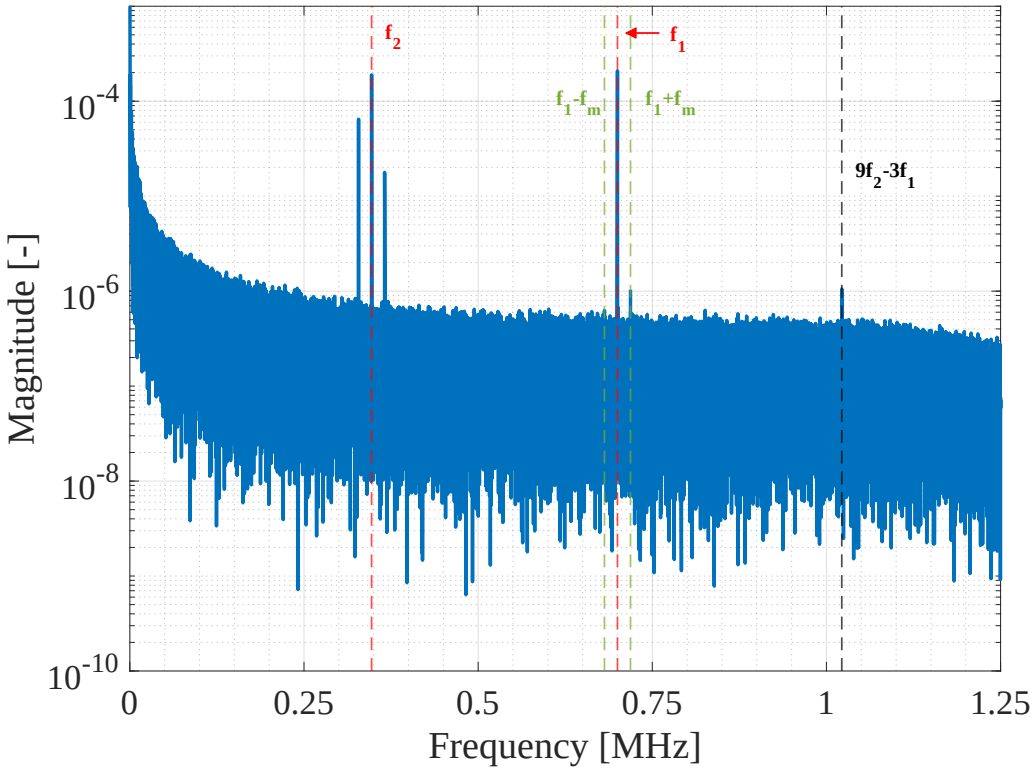

(a)

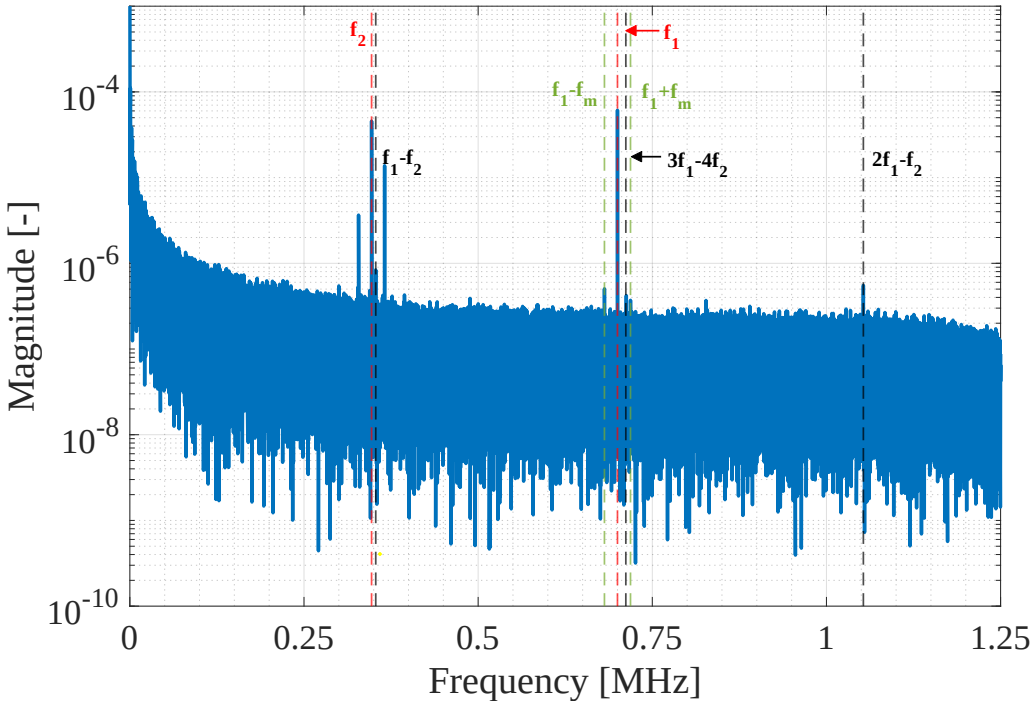

(b)

Figure 6.5: Amplitude response spectra corresponding to particle motion in assumed y–axis direction for "wanted" and "disturbing" frequencies equal to f_1 = 700 kHz and f_2 = 347 kHz, respectively for (a) undamaged beam specimen and (b) cracked beam.

The frequency components other than those resulting from the adopted excitation that can be observed in the amplitude spectrum corresponding to beam without crack and presented in Fig. 6.5a are possibly related to nonlinear intrinsic effects (e.g. transducer bonding, rubber support) and propagating waves of different polarity than shear waves. The latter effect is an inherent consequence of the experimental setup. Previous research shows that the transducers used for excitation generate also non–shear wave components Aleksiewicz-Drab et al. (2024). Even if the amplitude of these waves is relatively small, their interaction with damage leads inevitably to the generation of nonlinear components in the investigated shear direction. In addition, phenomena related to the interaction of the waves with the material – in which non–local elastic nonlinearities are present – can also be a source of nonlinear effects Shan et al. (2024).

For the results shown in Fig. 6.5b, which correspond to the sample with generated crack, localised damage must be considered as another source of nonlinear effects. However, its influence cannot be unambiguously identified and distinguished from the above–mentioned intrinsic sources of nonlinearities present in the system under investigation. This observation is in agreement with the analytical and numerical results, according to which the modulation transfer is less effective when $f_1 > f_2$ than in the opposite condition. Thus, measurements were made for

the second case, and the modulation transfer was studied when $f_2 > f_1$ was used to completely confirm the analytical and numerical calculations.

The second measurement case involved a nonlinear modulation transfer from higher to lower frequencies. The carrier frequencies for the "wanted" and "disturbing" waves were f_1 = 250 kHz and f_2 = 797 kHz, respectively. The "disturbing" wave was amplitude modulated, and the modulation frequency was f_m = 18.7 kHz. The excitation frequencies were selected so that the relevant higher harmonics and combinations of these frequencies did not coincide, thus avoiding any potential ambiguity in the measurement results. Fig. 6.5a and Fig. 6.5b give the results in the frequency domain for an undamaged specimen and specimen with generated crack, respectively. For consistency with the previously described measurement case, the presented calculated amplitude spectra correspond to measurement point number four (see Fig. 6.4).

The frequency components related to the excitation can be identified for the result corresponding to undamaged and damaged beams. The vertical dashed red lines indicate the carrier frequencies excited in the investigated specimens. Higher harmonics of the f_1 carrier frequency can be observed in the amplitude spectrum presented in Fig. 6.5a that correspond to the undamaged beam. In addition, "subsidiary" components with carrier frequencies equal to $4f_1 - f_2$ and $f_2 - 2f_1$ can be noticed and are marked by a black dashed line. Moreover, the modulation transfer from the f_2 to f_1 frequency can be observed, and the vertical dashed green lines indicate the relevant sidebands.

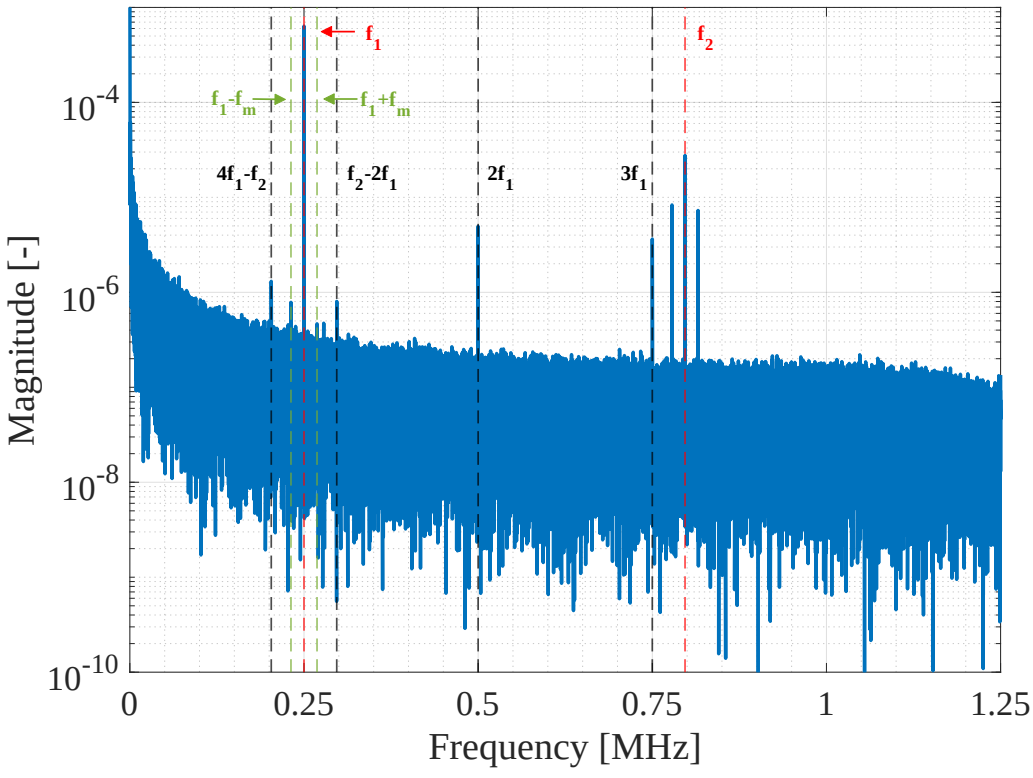

(a)

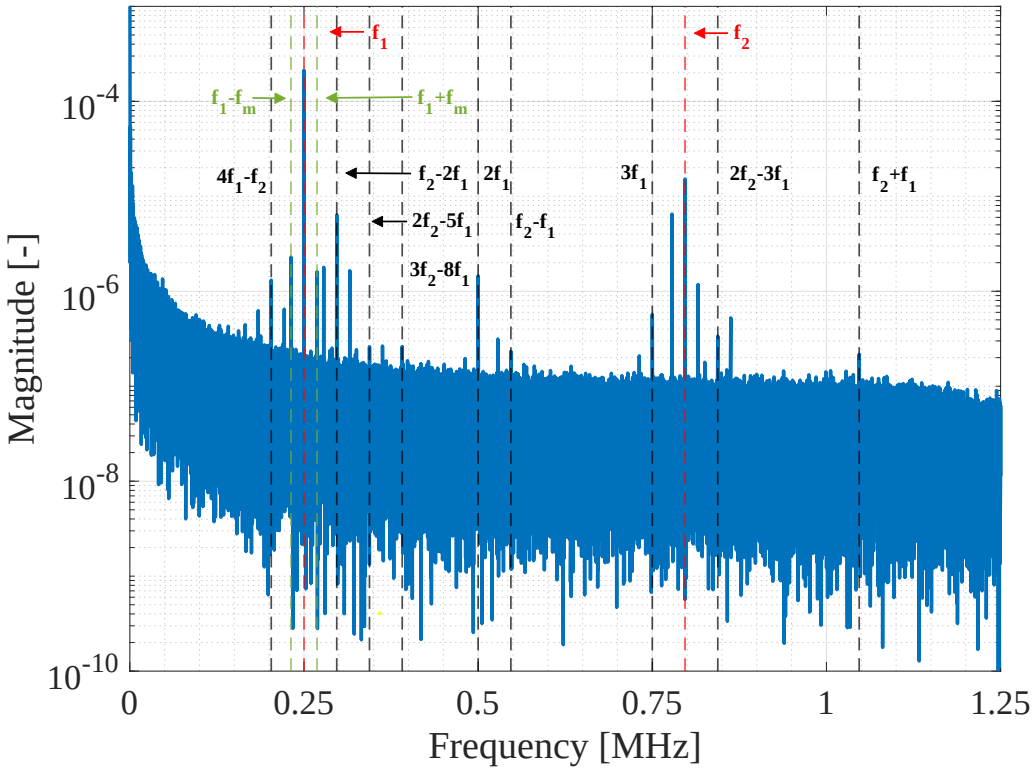

(b)

Figure 6.6: Amplitude response spectra corresponding to particle motion in assumed y–axis direction for "wanted" and "disturbing" frequencies equal to f_1 = 250 kHz and f_2 = 797 kHz, respectively for (a) undamaged beam specimen and (b) cracked beam.

When the beam is cracked, in the amplitude spectrum presented in Fig. 6.5b, the frequencies excited can be identified in the analysed response of the investigated system. In addition, "subsidiary" waves are also visible, and a number of these components are larger than those of the undamaged beam, as are the amplitudes corresponding to them. Moreover, the frequency components associated with the modulation transfer to these frequency components are also noticeable. Furthermore, modulation transfer components from "disturbing" to "wanted" frequency are noticeable, with amplitudes higher than those observed in the undamaged beam.

The averaged modulation index value for the measurement points was employed as a comprehensive measure of the modulation transfer from carrier frequency f_2 to f_1. Regarding the frequency pair under consideration, the average modulation indices after removing outliers were equal to $7.70{\cdot}10^{-3}$ and $5.35{\cdot}10^{-3}$ for the damaged and undamaged tested beam specimens, respectively. It means that the results obtained for the investigated carrier frequency pair reveal that the presence of the crack is the source of the L–G effect for the frequency pair considered in this measurement case. This phenomenon is manifested by the significant higher values of the

amplitude spectrum for the damaged sample than for the undamaged sample at frequencies corresponding to the transferred modulation.

Additional frequency components observed for this measurement case in the amplitude spectrum of the intact beam (Figure 6.6a) that do not correspond to excitation are likely to be caused by inherent nonlinear effects. These effects may include nonlinearities of the investigated system, such as transducer bonding or rubber support, as well as wave interactions within the nonlinear material Aleksiewicz-Drab et al. (2024); Shan et al. (2024).

A local crack in the sample significantly contributes to nonlinear frequency components present in the amplitude spectra given in Fig. 6.6b. Unlike other inherent nonlinear sources within the system, the influence resulting from the presence of the crack can be clearly observed. These findings support previous analytical and numerical calculations, which demonstrate that the modulation transfer is significantly enhanced when $f_2 > f_1$.

6.2.2 Experimental analysis of modulation intensity of the L–G effect

The intensity of the nonlinear modulation transfer was also investigated for varying carrier frequencies of "wanted" and "disturbing" waves. The results presented correspond to the mean modulation intensity index i.e., for the f_1 and f_2 frequency pair calculated for all measurement points.

Firstly, the f_1 = 700 kHz carrier frequency of the "wanted" wave was maintained constant and the modulation index was investigated for various values of f_2 carrier frequencies of the "disturbing" wave, ranging from 197 kHz to 797 kHz with a 150 kHz increment. Fig. 6.7 shows the results demonstrating that the modulation intensity for the cracked beam grows monotonically with the increase of the "disturbing" wave carrier frequency. The relationship presented is nonlinear and can be approximated by a second–order polynomial. This observation confirms the conclusions obtained from theoretical calculations and numerical simulations (see Chapters 4 and 5). In contrast, when the beam is undamaged, the modulation intensity remained approximately constant with increasing values of the f_2 frequency.

Secondly, the f_2 = 497 kHz frequency of the "disturbing" wave was kept constant. The modulation index was calculated for varying values of the f_1 frequency of the "wanted" wave. The f_1 frequencies varied from 100 kHz to 700 kHz with an increment of 150 kHz.

Fig. 6.8 presents the results indicating that the modulation intensity for the cracked beam grows monotonically with the increase of the "wanted" wave frequency. This relationship can be more accurately approximated by a first–order polynomial rather than a second–order polynomial. This observation is consistent with the theoretical calculations and numerical simulations (see Chapters 4 and 5). In contrast, when the beam is undamaged,the modulation intensity remained approximately constant with increasing values of the f_1 frequency.

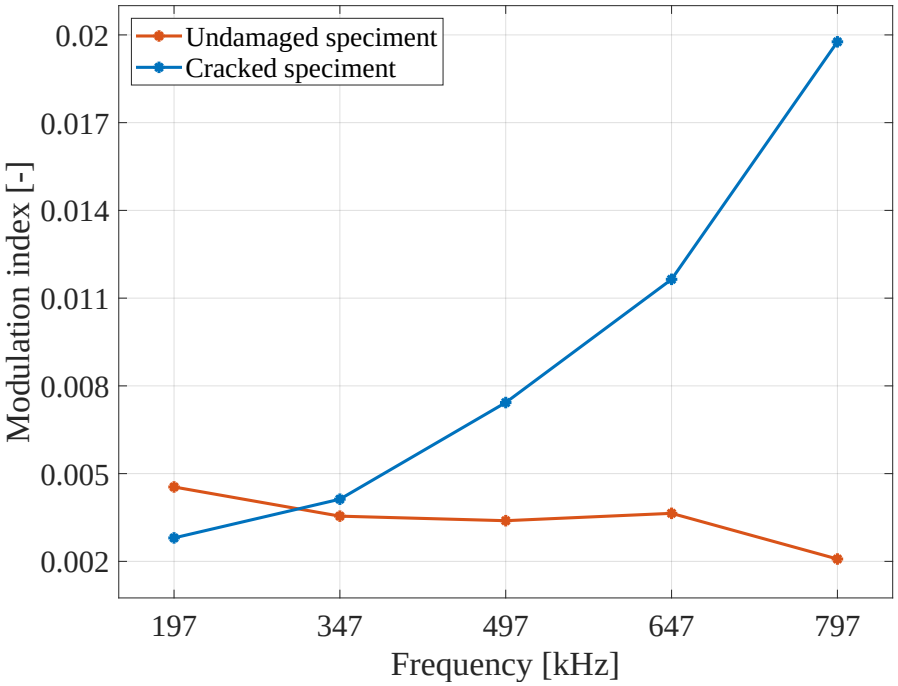

Figure 6.7: The mean modulation index for the investigated nonlinear modulation transfer phenomenon, calculated for varying values of the f_2 carrier frequency of the "disturbing" wave excited in the analysed specimens.

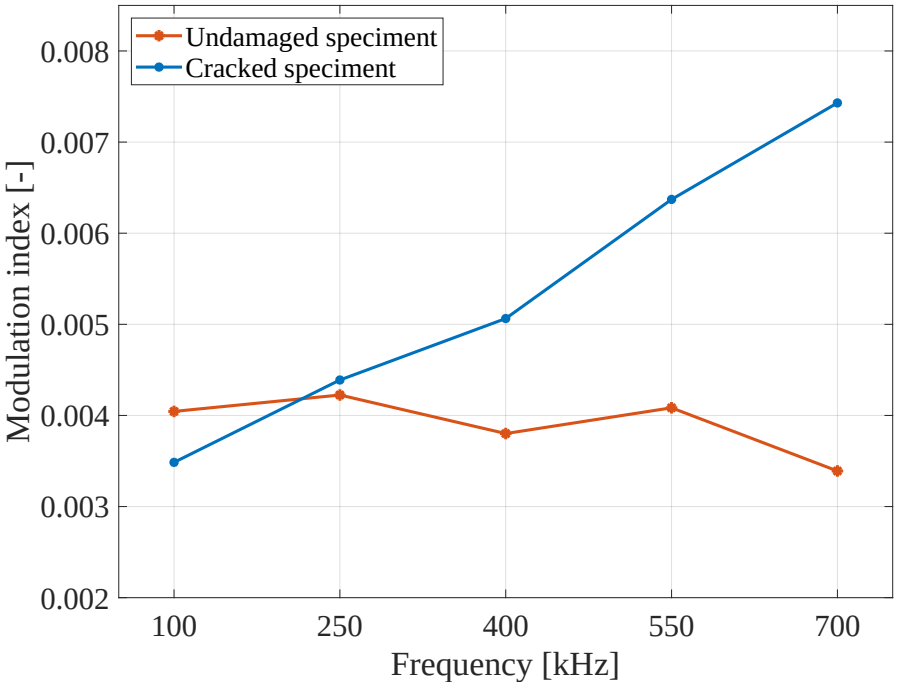

Figure 6.8: The mean modulation index for the investigated nonlinear modulation transfer. The relevant experiment was conducted for the constant value of f_2 "disturbing" wave frequency and different f_1 frequencies of the "wanted" wave.

6.3 Summary and conclusions

The presented experimental results demonstrate unambiguously the observation of the L–G effect for the ultrasonic shear wavefield. Although the modulation transfer has been observed for both i.e., undamaged and damaged beams, the results show that the presence of damage significantly enhances the nonlinear modulation transfer when the frequency of "disturbing" waves was bigger than the "wanted" wave. The results align with one of the conclusions indicated by the analytical calculations and confirmed by the simulation studies, showing that the transfer of modulations from higher frequencies to lower frequencies is more efficient and increases the amplitudes of the frequency components resulting from nonlinear modulation transfer. In addition, the relationship between the modulation intensity and the excitation frequency is more nonlinear for the increasing frequency of the "disturbing" wave than for the increasing frequency of the "wanted" wave.

The experimental research also shows that various nonlinearities inherent to the investigated system (e.g., intrinsic nonlinearities related to the material and/or measurement chains) could not be eliminated and influenced the measurement results. Therefore, potential applications of detection methods based on the nonlinear phenomenon studied should not only consider the specific frequency pair used in one experimental case but also how the modulation index varies with changes in the "disturbing" and "wanted" carrier frequencies.

Chapter 7

Conclusions and future work

This dissertation has investigated two nonlinear phenomena associated with shear horizontal guided waves. The first phenomenon is a higher harmonic generation, which occurs when propagating waves interact with nonlinear material described by the hyperelastic model. The second phenomenon is the acoustic equivalent of L–G effect, which relies on a nonclassical nonlinear modulation transfer between carrier frequencies of propagating waves. The analytical studies of these two nonlinear effects – based on the perturbation technique – have been performed. This analytical work was validated by numerical simulations based on a unique implementation of the LISA technique for nonlinear shear horizontal waves. The experimental work undertaken has focused on the L–G effect, validating the results of analytical calculations and numerical simulations. This chapter summarises the research work performed and major research findings. Finally, some ideas for future research work are proposed.

7.1 Summary of the dissertation

The research involved four main tasks. First, a comprehensive literature review was carried out to identify knowledge gaps related to the interactions of shear horizontal guided waves with hyperelastic material and the acoustic equivalent of L–G effects. This review allowed the identification of the research areas to be investigated, enabling formulation of the overall objectives and the scope of the research work undertaken. The second task was the analytical analysis of the nonlinear phenomena investigated. These analytical calculations were based on two variants of the perturbation method. The third task was the development of numerical tool for modelling of the mentioned phenomena and verification of the analytical calculations. This task was based on the LISA implementations for a nonlinear shear wavefield. The final task involved the experimental work related to the nonlinear L–G effect. In what follows, all these tasks are described in more details using the chapter structure of the thesis.

Chapter 1 of the thesis provides a literature review divided into two main parts. The first part is a general overview of nonlinear phenomena observed and studied in the field of wave propagation in solids. This overview has identified knowledge gaps related to shear horizontal guided waves. Two general groups of wave propagation nonlinearities were identified i.e., classical and nonclassical nonlinear effects. One nonlinear phenomenon from each group – not thoroughly investigated and explained – have been selected for research investigations. These are the shear horizontal guided wave interaction with a nonlinear material characterised by hyperelastic models (classical nonlinear effect) and the acoustic equivalent of the L–G effect (nonclassical nonlinear effect). In the second part of the literature review, studies on analytical modelling, numerical simulations and experimental tests related to these two nonlinear phenomena were discussed. Based on the literature review, the general aims of the work and the resulting objectives were specified.

Chapter 2 of the thesis provides a theoretical introduction to the fundamentals of wave propagation in solids. The chapter begins with an outline of the assumptions underlying the calculations. The Lagrange's description of the deformable medium has been used. The coordinate systems adopted in the analytical calculations has been presented. In addition, various measures of the stress and strain fields used in the mechanics of deformable bodies have been described. Finally, the equations governing the dynamics of a continuous solid medium have been derived. Furthermore, this chapter presents the general relationship between the strain and stress tensors in the case of a linear solid medium. A general analysis of bulk wave propagation in solids has been given, leading to the identification of the main types of waves propagating in linear elastic media. Due to the main subject of the thesis, the material presented part focuses only on the propagation of linear shear horizontal guided waves.

Chapter 3 presents the analysis of interaction between small–amplitude shear horizontal guided waves and a nonlinear elastic material described by the Landau–Lifshitz model of hyperelasticity. In order to address the interresonance between individual modes - resulting from secular terms in the approximate solution – the multiplescale perturbation method was employed. This approach has led to the investigation of some previously unexplored areas in the theoretical mechanics. The analytical calculations performed have demonstrated the possibility of extending the well–known concept of nonlinear vibration modes in discrete and continuous mechanical systems Rosenberg (1966); Vakakis & Rand (1992a,b); Nayfeh & Nayfeh (1994); Nayfeh (1995); Nayfeh & Nayfeh (1995); Kerschen (2014) to nonlinear shear horizontal guided wave propagation. Furthermore, analytical calculations have revealed how the wavefield is distorted due to the interaction with the hyperelastic material and the associated distortion of the dispersion relations for each mode. Separate calculations have been performed for the nondispersive SH0 mode and other dispersive modes. For the former, the shear horizontal wavefield remains undistorted across the plate thickness. This is described solely by the eigenfunction corresponding

to the SH0 mode, whereas higher harmonics are generated and can be identified in the wavenumber–angular frequency domain. The wavefield exhibits distortion across the plate thickness for dispersive modes and can be decomposed using eigenfunctions derived from the linear shear horizontal guided wave propagation analysis.

In Chapter 4, an acoustic equivalent of the L–G effect was investigated for shear horizontal guided waves. For the sake of completeness, the initial part of the chapter presents a fundamental background of electrodynamics and explains the original L–G effect for radio waves. This important background is followed by the introduction of a new model that allows for modelling of local damage in solids. This model has been motivated by the idea suggesting that small local material defects could be modelled using the theory of polycrystalline materials Zaitsev et al. (2002a,b). The model proposed in this chapter is based on nonlinear viscoelasticity Zener (1941, 1948). The L–G effect retooled for shear horizontal wave propagation has been explained using this new physical model. Analytical calculations performed have been in line with the explanation of the original L–G effect for electromagnetic waves. The proposed nonlinear model of viscoelasticity is compatible with dissipation models introduced for ionospheric plasma Bailey & Martyn (1934); Graffi (1936); Bailey (1965); Ginzburg & Gurevich (1960); Gurevich (1978). In addition, the proposed analytical calculation approach is in line with the well–established Born approximation in electrodynamics and quantum mechanics Griffiths (2017a,b). The Born–approximation has been previously used in mechanics to investigate wave scattering caused by linear inclusions Gubernatis et al. (1977a,b); Achenbach (2003). Hence, the research presented in this work extends the applicability of the aforementioned approaches to nonlinear wavefields. Moreover, the problem investigated demonstrates the relevance of the proposed model for modelling various nonlinear interactions of waves propagating in solids with structural defects, e.g., fatigue cracks. It is anticipated that well–known material viscoelastic models, such as the Maxwell, Zener and other models described in Christensen (2012); Carcione (2022), could be adopted and extended to incorporate nonlinear characteristics, by applying the multiple integral representation Findley et al. (1989) or fractional derivatives Podlubny (1998); Holm (2019)

Chapter 5 consists of three main parts. The first part provides a general scheme for the implementation of the LISA method for modelling nonlinear phenomena associated with shear horizontal wave propagation. The second part presents simulation results that validate the theory developed for the nonlinear interaction between shear horizontal guided waves and Landau–Lifshitz material. The simulations involved the excitation of either the nondispersive SH0 or the dispersive SH1 mode in a numerical model of nonlinear plate. The results gathered on the surface of the modelled plate confirm the generation of higher harmonics, which have been observed in the wavenumber–frequency domain. Moreover, a wavefield decomposition based on individual eigenfunctions of shear horizontal guided wave modes was performed. Calculated amplitude spectra from the simulation data confirm the analytical results, indicating that the

amplitude spectrum corresponding to a particular eigenfunction of shear horizontal guided wave mode contains regions that do not correspond to the dispersion curves for that mode in the case of linear systems. In addition, no significant distortion of the dispersion curve was observed, which results from the values of the nonlinear material coefficients, amplitudes of excited waves and resolutions of wavenumber and frequency imposed by model dimensions and simulation time. The third part of the chapter presents the numerical modelling of the L–G efect for shear horizontal guided waves using the local defect model originally proposed. Continuous excitation leading to the propagation of SH0 mode was performed in a numerical model of a linear plate with a local nonlinear region representing the defect. The results are in agreement with analytical calculations and show a more effective modulation transfer from higher to lower frequencies. The dependence of the modulation index on carrier frequencies of “disturbing” and “wanted” waves has been determined. Computed amplitude spectra in the wavenumber–frequency domain demonstrate that all shear horizontal guided wave modes are generated due to interactions between excited waves within the local nonlinear viscoelastic material region. Overall, the numerical simulation results proved the analytical investigations.

Chapter 6 presents laboratory experiments on the L–G effect for shear horizontal waves. Aluminium beams, one damaged and the other undamaged, have been tested. The results corresponding to the undamaged sample serve as a reference. Shear horizontal waves have been generated in investigated systems using piezoelectric transducers. Laser vibrometry has been used to measure velocity responses of the investigated systems at 15 specified points. Calculated amplitude spectra in the frequency domain – based on gathered response signals – exhibit the acoustic equivalent of the L–G effect for the considered motion of solid particles. The experimental results confirm the analytical and simulation results and demonstrate the more efficient modulation transfer from higher to lower frequency. The dependence of the modulation index on the carrier frequencies of the “disturbing” and “wanted” waves has been also determined experimentally and is consistent with the presented analytical and numerical results.

7.2 Main conclusions and contributions

Following the research investigation on enthralling nonlinear phenomena associated with shear horizontal guided wave propagation – namely the classical higher harmonic generation and the nonclassical modulation transfer known as the acoustic equivalent of the L–G effect – both main research hypotheses formulated in Section 1.3 have been proven. Based on the studies that were conducted, two major conclusions can be drawn. These conclusions also form major contributions to the research field investigated.

The first main conclusion is that the concept of nonlinear modes – previously formulated in mechanics for nonlinear vibrations of discrete and continuous mechanical systems – can be

extended to the propagation of multi–modal and dispersive shear horizontal guided waves in solids, which can be described by a hyperelastic material model. This conclusion is particularly significant as the physical mechanism of the interaction of considered waves and nonlinear material has not been thoroughly investigated in mechanics due to the fact that previous research has focused on higher harmonics generation. Furthermore, the problem of distortion of the wavefield and dispersion relations and their description have been addressed for the first time in this study, and it provides a deeper understanding of the physical fundamentals of this classical, nonlinear phenomenon.

The second main conclusion is that the local nonclassical, nonlinear dissipation model for material damage can be formulated to explain the L–G effect for shear horizontal guided waves. It is shown that the proposed local damage can be interpreted as a locally distorted structure of the medium. Furthermore, this local nonlinear material region can be treated as a source of enhanced nonlinear dissipation. Similar but linear mechanism has previously been defined for polycrystalline materials, where the grain boundaries can be treated as a source of dissipation Zener (1937, 1938); Zener et al. (1938). The analytical calculations performed show that the interaction of monochromatic "wanted" and amplitude–modulated "disturbing" waves in the region characterised by nonlinear viscoelasticity leads to modulation transfer and allows a deeper understanding of its physical fundamentals. In particular, it is worth highlighting that the provided explanation of the L–G phenomenon for shear horizontal guided waves is consistent with the physical mechanism of the original phenomenon first observed for radio waves, which is based on the nonlinear dissipation of radio waves in the ionosphere.

7.2.1 Analytical research work

More specifically the following additional conclusions and contributions can be drawn from the conducted analytical work. When the interaction between shear horizontal guided waves and the plate modelled using Landau–Lifshitz hyperelasticity description is analysed these conclusions are as follows:

- The analytical results show that the interaction between the considered group of waves and the nonlinear material results not only in the generation of odd higher harmonics, observed in the wavenumber–frequency domain, but also in a distortion of the wavefield across the plate thickness. However, it was found that when the driving mode is SH0, the wavefield is not distorted through the thickness of the plate, but only higher wave harmonics are generated. The amplitude distribution of these higher harmonics along the thickness of the plate corresponds to the eigenfunction for the SH0 mode.

- The decomposition of the approximate solution with respect to the orthogonal function base – resulting from the problem of the linear propagation of the shear horizontal guided wave in

plates – indicate which harmonics are present in the amplitude spectra in the wavenumber–frequency domain for individual eigenfunctions. Only odd harmonics of the wavenumber–frequency pair corresponding to the driving mode can be present, and only the amplitudes corresponding to modes with a number equal to the odd multiplication of the number of driving modes are nonzero.

- The analytical results show that the propagation of shear horizontal guided waves leads to distortions of the dispersion curves for each driving mode. However, for the typical values of the parameters describing the nonlinear elasticity of metallic materials and the displacement amplitudes considered, these distortions are small and could be difficult to detect in practice due to the limited resolution of frequency and wavenumber.

- The distortion of the wavefield, characterised by the amplitudes of the higher harmonic waves and the distortion of the dispersion curves, depends on the nonlinear material parameters and the amplitudes of the excited waves.

More detailed conclusions related to the analytical study of the L–G effect for shear horizontal guided waves can be given as follows:

- The results show that that the intensity of the studied nonlinear effect is proportional to the values of the parameters describing the local nonlinear region, which is modelled as damage. Furthermore, it has been shown that the modulation intensity depends on amplitudes and carrier frequencies of the propagating waves and the size of damage.

- Analytical calculations predict that the interaction of “disturbing” and “wanted” shear horizontal guided waves – which may be different or identical modes – within the nonlinear region of the considered system will generate all shear horizontal guided modes, both propagating and evanescent.

- Results of analytical calculation reveals that the intensity of the transferred modulation is a nonlinear function of the f_1 and f_2 frequencies of “wanted” and “disturbing” waves, respectively. This nonlinear relationship is approximately quadratic for f_2 and linear for f_1. Therefore, the transfer of modulation from higher to lower angular frequencies is more effective (when $f_2 > f_1$).

7.2.2 Numerical simulations

The application of the LISA method confirms the analytical results obtained. More detailed conclusions related to numerical simulations of the shear horizontal wave interaction with the distributed nonlinearity can be drawn as follows:

- The results for the SH0 mode show that the wavefield remains undistorted through the plate thickness, aligning with the eigenfunction corresponding to SH0 mode. Amplitude spectra for other modes represent numerical noise.

- The simulation results in which the SH1 mode was excited as a driving mode, the wavefield exhibits distortion alongside the plate thickness. The wavefield distortion measure is the amplitudes of the harmonics of the wavenumber and frequency pair corresponding to the driving mode.

- Numerical simulation results indicate that the distortion of dispersion curves is negligible for the excited SH1 and SH0 modes.

When the numerical simulation results related to the horizontal shear wave interaction with the local nonlinearity (the L–G effect) are analysed, the following conclusions can be made:

- The simulation results for the L–G effect confirmed that transferring modulation from the f_2 carrier frequency of "disturbing" wave to the f1 carrier frequency of "wanted" waves is more efficient when $f_2 > f_1$.

- The results show that when the f_2 frequency increases, while the f_1 frequency remains constant, the modulation index that relates to the modulation transfer also increases. A second–order polynomial could be used to approximate this relationship.

- When the f_1 frequency increases, and the f_2 wave frequency remains constant, the relevant modulation index also increases. However, this time a first–order polynomial approximates this relationship.

- Amplitude spectra in the wavenumber–frequency domain have been calculated based on results collected from the surface of the modelled plate, which included a local nonlinear region that was a model of local damage. These confirm that as a result of the interaction between "disturbing" and "wanted" waves in the nonlinear region of the modelled system, other modes than those excited and propagating in the plate are generated.

- The results of the conducted numerical simulations confirm that the interaction of "disturbing" and "wanted" waves within the nonlinear region leads to the generation of higher harmonics and "subsidiary" waves.

The implementation of the LISA numerical tool for shear wavefiled and nonlinear interactions with investigated distributed and local nonlinearities is a new development that contributes to computational mechanics.

7.2.3 Experimental results

The experimental results not only demonstrate that the L–G effect can be observed for the shear motion of solid particles but also confirm all previous findings from the theoretical analysis and numerical simulations. More details conclusions can be summarised as follows:

- The experimental results also show that transferring modulation from higher to lower frequencies is more efficient than vice versa.
- The presence of higher harmonics and "subsidiary" waves can be observed in amplitude spectra of wave responses, as predicted by the analytical and numerical calculations.
- The measurements show that when the carrier frequency of "disturbing" wave increases, the index of transferred modulation also increase and this relationship can be approximated by a second–order polynomial. In contrast, similar characteristic for the frequency of the "wanted" wave can be approximated by a first–order polynomial. Similar characteristics obtained for the undamaged beam remain relatively unchanged.

7.3 Potential future work

The research work presented in this thesis has provided better understanding of the two nonlinear phenomena investigated. In addition, the results obtained indicate promising research directions for investigation. Potential future research areas are described below.

The classical nonlinear wave interaction with materials investigated in the thesis brings some immediate potential ideas for future research. The distortion of dispersion curves of shear horizontal guided waves – resulting from the wave interaction with a hyperelastic material – could be further studied. Different nonlinear parameters (or nonlinear materials) and wave amplitudes should be investigated to establish significant levels of distortion that could be observed in practice and measured experimentally, if possible. A broader theoretical and numerical analysis to investigate the interaction of shear horizontal guided and Lamb waves in a hyperelastic material should also be a further research step. Analytical approaches and numerical tools developed in the thesis could be used to facilitate this research. In addition, another area of research that needs to be investigated is the use of the analytical and numerical calculations to identify nonlinear parameters that characterise various materials and relevant microstructure.

The nonclassical nonlinear crack–wave interaction L–G effect investigated also sparks some potential directions for research investigations. The effect of modulation frequency and modulation index of the "disturbing" wave on the transferred modulation needs to be further investigated. The role of the thermoelastic effects – often mention in conjunction with the L–G effect – should be

also investigated. A topic for potential research is the application of other viscoelastic models for damage modelling.

More experimental work is needed to establish crack detection parameters that could be used in practical damage detection applications. One important question is how microstructural distributed changes affect the nonlinear shear wavefield. Another important problem is to determine how the modulation index depends on the carrier frequency of the "disturbing" and "wanted" waves in experimental studies that involve different contact–type structural damage.

The work presented involves two independent nonlinear phenomena. However, these phenomena could be studied together to mimic combined distributed (e.g., microcracks) and local (fatigue cracks) damage. Such investigations could lead to various nonlinear interactions, attractive for potential damage detection applications.

Appendix A

The Landau's TOECs and FOECs calculation

The macro–scale behaviour of nonlinear material can be described using the Landau–Lifshitz model. The Landau's nonlinear coefficients are often tabulated for various e.g., Bhalla et al. (1983). The relations between hyperelastic constants for different models can be found in Norris (1998). For example, the relation between the third order Landau's elastic constants $\mathcal{A}$, $\mathcal{B}$, $\mathcal{C}$ and the c_{ijk} constants is a system of linear equations and can be written in a matrix form as

$$\begin{bmatrix} c_{111} \\ c_{112} \\ c_{123} \\ c_{144} \\ c_{155} \\ c_{456} \end{bmatrix} = \begin{bmatrix} 2 & 6 & 2 \\ 0 & 2 & 2 \\ 0 & 0 & 2 \\ 0 & 1 & 0 \\ \frac{1}{2} & 1 & 0 \\ \frac{1}{4} & 0 & 0 \end{bmatrix} \begin{bmatrix} \mathcal{A} \\ \mathcal{B} \\ \mathcal{C} \end{bmatrix} \tag{A.1}$$

or in a shorter version as

$$\mathbf{C}_{TOEC} = \mathbf{A}_{TOEC}\mathbf{L}_{TOEC}. \tag{A.2}$$

When solving Eq. (A.1), the number of solutions needs to be checked and then the Kronecker–Capelli theorem is of great importance. Given the rank of the $[\mathbf{A}_{TOEC}|\mathbf{C}_{TOEC}]$ augmented matrix and the $\mathbf{A}_{TOEC}$ coefficient matrix, the number of solutions for a linear system can be established. The augmented matrix is defined as

$$[\mathbf{A}_{TOEC}|\mathbf{C}_{TOEC}] = \left[\begin{array}{ccc|c} 2 & 6 & 2 & c_{111} \\ 0 & 2 & 2 & c_{112} \\ 0 & 0 & 2 & c_{123} \\ 0 & 1 & 0 & c_{144} \\ \frac{1}{2} & 1 & 0 & c_{155} \\ \frac{1}{4} & 0 & 0 & c_{456} \end{array}\right] \tag{A.3}$$

One can observe that the rank of the $\mathbf{A}_{TOEC}$ is equal to three, and the rank of the $[\mathbf{A}_{TOEC}|\mathbf{C}_{TOEC}]$ augmented matrix may be equal to three or four. Since, the exact and unique solution of Eq. (A.1) exists if the rank of the augmented matrix is equal to three (number of unknowns). Otherwise, the exact solution does not exist, and only an approximated solution can be found. In this case, the definition of the Moon–Penrose matrix inversion (even for rectangle matrices) can be useful, allowing for the minimisation of the value of the $\|\mathbf{C}_{TOEC} - \mathbf{A}_{TOEC}\mathbf{L}_{TOEC}\|$ expression Penrose (1955). To calculate the best approximation of $\mathbf{L}_{TOEC}$, the $\mathbf{C}_{TOEC}$ matrix must be multiplied by the Moon–Penrose inversion $\mathbf{A}^{+}_{TOEC}$ from the left–hand side, i.e.,

$$\mathbf{L}_{TOEC} = \mathbf{A}^{+}_{TOEC}\mathbf{C}_{TOEC}. \tag{A.4}$$

The fourth–order Landau's (i.e. $\mathcal{E}$, $\mathcal{F}$, $\mathcal{G}$, $\mathcal{H}$) can be determined in the same way.

Appendix B

Analogy between hereditary effect for mechanical and electromagnetic systems

The sum of Eqs. (4.21) and (4.22) describes anelastic effects in the damage area of the considered mechanical system. These equations express the relationship between stress and strain tensors in a differential form. Following the work in Findley et al. (1989); Osika et al. (2023b), the definition of stresses can be also presented in the integral form given as

$$\begin{aligned}\boldsymbol{\sigma} = &\int_0^t \left(\varsigma_1 J_1(\tau_1)\mathbf{I} + \varsigma_2 \dot{\boldsymbol{\varepsilon}}_{\boldsymbol{GL}}(\tau_1)\right) d\tau_1 + \int_0^t \int_0^t \left(\varsigma_3 \dot{\boldsymbol{\varepsilon}}_{\boldsymbol{GL}}(\tau_1)\dot{\boldsymbol{\varepsilon}}_{\boldsymbol{GL}}(\tau_2) + \varsigma_4 J_2(\tau_1,\tau_2)\mathbf{I}\right.\\ &\left.+\varsigma_5 J_1(\tau_1)\dot{\boldsymbol{\varepsilon}}_{\boldsymbol{GL}}(\tau_2) + \varsigma_6 J_1(\tau_1)J_1(\tau_2)\mathbf{I}\right) d\tau_1 d\tau_2 + \int_0^t \int_0^t \int_0^t \left(\varsigma_7 J_3(\tau_1,\tau_2,\tau_3)\mathbf{I}\right.\\ &+\varsigma_8 J_1(\tau_1)\dot{\boldsymbol{\varepsilon}}_{\boldsymbol{GL}}(\tau_2)\dot{\boldsymbol{\varepsilon}}_{\boldsymbol{GL}}(\tau_2) + \varsigma_9 J_1(\tau_1)J_2(\tau_2,\tau_3)\mathbf{I} + \varsigma_{10} J_1(\tau_1)J_1(\tau_2)\dot{\boldsymbol{\varepsilon}}_{\boldsymbol{GL}}(\tau_2)\\ &\left.+\varsigma_{11} J_2(\tau_1,\tau_2)\dot{\boldsymbol{\varepsilon}}_{\boldsymbol{GL}}(\tau_2) + \varsigma_{12} J_1(\tau_1)J_1(\tau_2)J_1(\tau_3)\mathbf{I}\right) d\tau_1 d\tau_2 d\tau_3,\end{aligned} \tag{B.1}$$

where the relaxation kernel functions: ς_1, ς_2 are functions of $(t-\tau_1)$; ς_3, ..., ς_6 are functions of $(t-\tau_1, t-\tau_2)$; ς_7, ..., ς_{12} are functions of $(t-\tau_1, t-\tau_2, t-\tau_3)$.

It is well known that hereditary effects define dynamic systems for which the present states depend on the current external and internal forces due to the history of past motion. Eq. (B.1) is a classical relation that describes the nonlinear hereditary effect between the stress and strain tensors. If the forms of the relaxation functions are chosen appropriately, the stress definitions given in a differential form in Eqs. (4.21) – (4.22) and the definition given in an integral form in Eq. (B.1) are identical. Thus, the proposed Kelvin–Voigt model with a nonlinear viscous term describes nonlinear hereditary effects.

An analogous mathematical model has been used in Graffi (1936); Fabrizio & Morro (2003) to describe the current in the ionosphere and to model radio wave propagation (see Eq. (4.10)).

Therefore, the proposed model of nonlinear attenuation in shear horizontal wave propagation is analogous to the attenuation model used to explain the original L–G effect in radio waves.

Appendix C

Green's function for the time–independent problem in shear horizontal guided wave propagation

The Green's function is a mathematical tool that can be used to solve linear inhomogeneous differential equations and boundary value problems Duffy (2001); Haberman (2013); Aki & Richards (2002). This appendix presents the derivation of the $G_\omega(x, y; x_0, y_0)$ Green's function that is the solution to the following time–independent linear problem defined by an inhomogeneous partial differential governing equation and homogeneous boundary conditions given by

$$\frac{\partial^2 G_\omega}{\partial x^2} + \frac{\partial^2 G_\omega}{\partial y^2} + \frac{\omega^2}{c_s^2} G_\omega = -\delta(x - x_0, y - y_0), \tag{C.1}$$

$$\pm \frac{\partial G_\omega}{\partial y} = 0, \text{ for } y = \pm h, \tag{C.2}$$

where the x_0 and y_0 coordinates defines localisation of inhomogeneous term that is the δ Dirac delta function. The subscript has been intentionally introduced into the notation to indicate that the $G_\omega(x, y)$ Green's function corresponding to an assumed value of the ω parameter is under consideration.

In order to solve the inhomogeneous problem defined by Eqs. (C.1) and (C.2), one can first solve a homogeneous problem using the separation of variables method Moon & Spencer (1961); Meirovitch (1980, 2003); Rao (2006). Calculations resulting from this technique lead to a self–adjoint boundary problem with respect to the y independent variable Osika et al. (2022). Solving this boundary value problem yields an infinite set of distinctive eigenvalues and corresponding orthogonal eigenfunctions. Moreover, each eigenvalue corresponds to a single partial differential equation (i.e., the Klein–Gordon equation), which describes the distribution of the solution of the homogenous problem along the x–direction. A detailed analysis of these

calculations is presented in Section 2.8. Based on these investigations and knowing that the resulting function basis is a complete set of functions – due to the fact that the considered problem is self–adjoint Meirovitch (1980, 2003); Rao (2006) – the solution of the investigated problem can be written as

$$G_\omega(x,y;x_0,y_0)=\sum_{m=0}^{\infty}Y^{(m)}(y)G_\omega^{(m)}(x;x_0,y_0). \tag{C.3}$$

Substituting Eq. (C.3) to Eq. (C.1) yields

$$\sum_{m=0}^{\infty}Y^{(m)}\frac{\partial^2 G_\omega^{(m)}}{\partial x^2}+\sum_{m=0}^{\infty}Y^{(m)\prime\prime}G_\omega^{(m)}+\frac{\omega^2}{c_s^2}\sum_{m=0}^{\infty}Y^{(m)}G_\omega^{(m)}=-\delta(x-x_0,y-y_0). \tag{C.4}$$

By grouping the terms and using the properties of eigenfunctions resulting from the problem under consideration (i.e., $Y^{(m)\prime\prime}(y)=-\eta_m^2Y^{(m)}(y)$), Eq. (C.4) can be rewritten as

$$\sum_{m=0}^{\infty}Y^{(m)}\left(\frac{\partial^2 G_\omega^{(m)}}{\partial x^2}-\eta_m^2G_\omega^{(m)}+\frac{\omega^2}{c_s^2}G_\omega^{(m)}\right)=-\delta(x-x_0,y-y_0) \tag{C.5}$$

Multiplying Eq. (C.5) by $Y^{(m)}(y)$ and then integrating over the variable y in the interval $\langle -h,h\rangle$ and applying orthogonality conditions, leads to an infinite number of uncoupled partial differential equations with respect to the $G_\omega^{(m)}(x;x_0,y_0)$ functions, i.e.

$$\frac{\partial^2 G_\omega^{(m)}}{\partial x^2}-\eta_m^2G_\omega^{(m)}+\frac{\omega^2}{c_s^2}G_\omega^{(m)}=-\frac{\int_{-h}^{h}Y^{(m)}(y)\delta(x-x_0,y-y_0)dy}{\int_{-h}^{h}(Y^{(m)}(y))^2dy}=-\frac{Y^{(m)}(y_0)\delta(x-x_0)}{\int_{-h}^{h}(Y^{(m)}(y))^2dy}. \tag{C.6}$$

The above formula results from the following property of the Dirac delta function in 2–D space $\delta(x-x_0,y-y_0)=\delta(x-x_0)\delta(y-y_0)$ and its filtering property Morse & Feshbach (1953); Lighthill (1958); Duffy (2004). In order to solve Eq. (C.6), the Fourier transform can be calculated with respect to the x variable as

$$\hat{G}_\omega^{(m)}(\xi;x_0,y_0)=\int_{-\infty}^{\infty}G_\omega^{(m)}(x;x_0,y_0)e^{-i\xi x}dx. \tag{C.7}$$

Applying the Fourier transform and its properties yields Duffy (2004)

$$-\xi^2\hat{G}_\omega^{(m)}-\eta_m^2\hat{G}_\omega^{(m)}+\frac{\omega^2}{c_s^2}\hat{G}_\omega^{(m)}=-\frac{Y^{(m)}(y_0)e^{-i\xi x_0}}{\int_{-h}^{h}(Y^{(m)}(y))^2dy} \tag{C.8}$$

Eventually, the $\hat{G}_\omega^{(m)}(\xi;x_0;y_0)$ Fourier transform of the $G_\omega^{(m)}(x;x_0,y_0)$ function can be determined as

$$\hat{G}_\omega^{(m)}(\xi;x_0,y_0)=\frac{1}{\xi^2-\frac{\omega^2}{c_s^2}+\eta_m^2}\frac{Y^{(m)}(y_0)e^{-i\xi x_0}}{\int_{-h}^{h}(Y^{(m)}(y))^2dy}=\frac{1}{\xi^2-\xi_m^2}\frac{Y^{(m)}(y_0)e^{-i\xi x_0}}{\int_{-h}^{h}(Y^{(m)}(y))^2dy} \tag{C.9}$$

Following this relation and the definition of the inverse Fourier transform, the $G_{\omega}^{(m)}(x;x_0,y_0)$ Green's function corresponding to m–th eigenfunction can be given

$$G_{\omega}^{(m)}(x,y;x_0,y_0)=\frac{1}{2\pi}\int_{-\infty}^{\infty}\hat{G}_{\omega}^{(m)}(x)e^{i\xi x}d\xi=\frac{Y^{(m)}(y_0)}{\int_{-h}^{h}\left(Y^{(m)}(y)\right)^2dy}\frac{i}{2\xi_m}e^{i\xi_m|x-x_0|} \tag{C.10}$$

Inserting Eq. (C.10) into Eq. (C.3) yields the relationship that defines the solution of the problem defined by Eqs. (C.1) and (C.2)

$$G_{\omega}(x,y;x_0,y_0)=\sum_{m=0}^{\infty}Y^{(m)}(y)G_{\omega}^{(m)}(x;x_0,y_0)=\sum_{m=0}^{\infty}\frac{Y^{(m)}(y)Y^{(m)}(y_0)}{\int_{-h}^{h}\left(Y^{(m)}(y)\right)^2dy}\frac{i}{2\xi_m}e^{i\xi_m|x-x_0|}. \tag{C.11}$$

When the derived Green's function is applied to solve the problem for which the inhomogeneous term is localised in a finite, small region, it is convenient to determine a linear approximation of this function. Thus, simplified calculations can be performed, as demonstrated in Osika et al. (2023b). In order to determine the linear approximation for the function defined in Eq. (C.12), one can rewrite this equation as

$$\begin{aligned}G_{\omega}(x,y;x_0,y_0)&=\sum_{m=0}^{\infty}\frac{Y^{(m)}(y)Y^{(m)}(y_0)}{\int_{-h}^{h}\left(Y^{(m)}(y)\right)^2dy}\frac{i}{2\xi_m}e^{i\xi_m|x-x_0|}\\&=\sum_{m=0}^{\infty}\frac{Y^{(m)}(y)Y^{(m)}(y_0)}{\int_{-h}^{h}\left(Y^{(m)}(y)\right)^2dy}\frac{i}{2\xi_m}\left(\Theta(-(x-x_0))e^{-i\xi_m(x-x_0)}+\Theta(x-x_0)e^{i\xi_m(x-x_0)}\right),\end{aligned} \tag{C.12}$$

where Θ denotes the Heaviside step function. Using the definition of the Taylor series expansion of Bronshtein et al. (2015) linear approximation of the investigated function can be formulated in a general form

$$\begin{aligned}G_{\omega}(x,y;x_0,y_0)=G_{\omega}(x,y;x_c,y_c)&+\left.\frac{\partial G_{\omega}(x,y;x_0,y_0)}{\partial x_0}\right|_{\substack{x_0=x_c\\y_0=y_c}}\\&+\left.\frac{\partial G_{\omega}(x,y;x_0,y_0)}{\partial y_0}\right|_{\substack{x_0=x_c\\y_0=y_c}}+\cdots,\end{aligned} \tag{C.13}$$

which is correct for the x_0 and y_0 arguments close to the values of x_c and y_c. Using the properties of the Heaviside unit step and the Dirac delta functions – given in Morse & Feshbach (1953); Lighthill (1958); Duffy (2001, 2004) – one can obtain the relevant approximation as

$$\begin{aligned}G_{\omega}(x,y;x_0,y_0)\cong\sum_{m=0}^{\infty}&\frac{Y^{(m)}(y)}{\int_{-h}^{h}\left(Y^{(m)}(y)\right)^2dy}\frac{i}{2\xi_m}e^{i\xi_m|x-x_c|}\left(Y^{(m)}(y_c)+Y^{(m)\prime}(y_c)(y_0-y_c)\right.\\&\left.+Y^{(m)}(y_c)i\xi_m|x_0-x_c|\right).\end{aligned} \tag{C.14}$$

Bibliography

Achenbach, J. (1973). *Wave Propagation in Elastic Solids*. Elsevier. https://doi.org/10.1016/c2013-0-04485-4

Achenbach, J. (2003). *Reciprocity in Elastodynamics*. Cambridge Monographs on Mechanics. Cambridge University Press. https://doi.org/10.1017/CBO9780511550485

Akgün, G. & Demiray, H. (2001). Interactions of nonlinear acoustic waves in a fluid-filled elastic tube. *International Journal of Engineering Science*, 39(5), 563–581. https://doi.org/10.1016/s0020-7225(00)00057-4

Aki, K. & Richards, P. (2002). *Quantitative Seismology*. University Science Books. https://books.google.pl/books?id=sRhawFG5_EcC

Aleksiewicz-Drab, E., Ziaja-Sujdak, A., Radecki, R., & Staszewski, W. J. (2024). Directivity and excitability of ultrasonic shear waves using piezoceramic transducers—numerical modeling and experimental investigations. *Sensors*, 24(11), 3462. https://doi.org/10.3390/s24113462

Auld, B. (1973). *Acoustic fields and waves in solids*. A Wiley-Interscience publication. Wiley. https://books.google.pl/books?id=_2MWAwAAQBAJ

Aymerich, F. & Staszewski, W. (2010a). Experimental study of impact-damage detection in composite laminates using a cross-modulation vibro-acoustic technique. *Structural Health Monitoring*, 9(6), 541–553. https://doi.org/10.1177/1475921710365433

Aymerich, F. & Staszewski, W. (2010b). Impact damage detection in composite laminates using nonlinear acoustics. *Composites Part A: Applied Science and Manufacturing*, 41(9), 1084–1092. https://doi.org/10.1016/j.compositesa.2009.09.004

Bailey, V. (1965). Some nonlinear phenomena in the ionosphere. *Journal of Research of the National Bureau of Standards, Section D: Radio Science*, 69D(1), 9. https://doi.org/10.6028/jres.069d.013

Bailey, V. & Martyn, D. (1934). XXXII. The influence of electric waves on the ionosphere. *The London, Edinburgh, and Dublin Philosophical Magazine and Journal of Science*, 18(118), 369–386. https://doi.org/10.1080/14786443409462506

Baranov, V. B. (2006). Kinetic and hydrodynamic approaches in space plasma. *The physics of the heliospheric boundaries*, 5, 1–26. https://www.researchgate.net/publication/253686280_Kinetic_and_Hydrodynamic_Approaches_in_Space_Plasma

Bassanini, P. (1974). Numerical results for a cross-modulation problem in a rarefied nonlinear plasma. *Radio Science*, 9(10), 857–865. https://doi.org/10.1029/RS009i010p00857

Bhalla, A., Hellwege, K., Cook, W., Hellwege, A., Hearmon, R., Jerphagnon, J., Kurtz, S., Liu, S., Nelson, D., & Oudar, J. (1983). *Elastic, Piezoelectric, Pyroelectric, Piezooptic, Electrooptic Constants, and Nonlinear Dielectric Susceptibilities of Crystals*. Landolt-Börnstein: Numerical Data and Functional Relationships in Science and Technology - New Series. Springer Berlin Heidelberg. https://books.google.pl/books?id=r1vTvwEACAAJ

Boller, C., Chang, F.-K., & Fujino, Y. (2009). *Encyclopedia of Structural Health Monitoring*. https://doi.org/10.1002/9780470061626

Breazeale, M. A. & Ford, J. (1965). Ultrasonic studies of the nonlinear behavior of solids. *Journal of Applied Physics*, 36(11), 3486–3490. https://doi.org/10.1063/1.1703023

Breazeale, M. A. & Thompson, D. O. (1963). Finite-amplitude ultrasonic waves in aluminum. *Applied Physics Letters*, 3(5), 77–78. https://doi.org/10.1063/1.1753876

Broda, D., Pieczonka, L., Hiwarkar, V., Staszewski, W., & Silberschmidt, V. (2016). Generation of higher harmonics in longitudinal vibration of beams with breathing cracks. *Journal of Sound and Vibration*, 381, 206–219. https://doi.org/10.1016/j.jsv.2016.06.025

Broda, D., Staszewski, W., Martowicz, A., Uhl, T., & Silberschmidt, V. (2014). Modelling of nonlinear crack–wave interactions for damage detection based on ultrasound—a review. *Journal of Sound and Vibration*, 333(4), 1097–1118. https://doi.org/10.1016/j.jsv.2013.09.033

Bronshtein, I. N., Semendyayev, K. A., Musiol, G., & Mühlig, H. (2015). *Differentiation*, 432–456. Springer Berlin Heidelberg. https://doi.org/10.1007/978-3-662-46221-8_6

Cantrell, J. H. & Yost, W. T. (2001). Nonlinear ultrasonic characterization of fatigue microstructures. *International Journal of Fatigue*, 23, 487–490. https://doi.org/10.1016/S0142-1123(01)00162-1

Carcione, J. M. (2022). *Wave Fields in Real Media - Wave Propagation in Anisotropic, Anelastic, Porous and Electromagnetic Media* (fourth edition ed.). Elsevier. https://doi.org/10.1016/C2021-0-00938-X

Chadwick, P. (1999). *Continuum Mechanics: Concise Theory and Problems*. Dover books on physics. Dover Publications. https://books.google.pl/books?id=QSXIHQsus6UC

Chillara, V. K. & Lissenden, C. (2014). Nonlinear guided waves in plates: A numerical perspective. *Ultrasonics*, 54. https://doi.org/10.1016/j.ultras.2014.04.009

Christensen, R. (2012). *Theory of Viscoelasticity: An Introduction*. Elsevier Science. https://books.google.pl/books?id=-k2-WE7QIkYC

Croxford, A. J., Wilcox, P. D., Drinkwater, B. W., & Nagy, P. B. (2009). The use of non-collinear mixing for nonlinear ultrasonic detection of plasticity and fatigue. *The Journal of the Acoustical Society of America*, 126(5), EL117–EL122. https://doi.org/10.1121/1.3231451

Dahlquist, G. & Bjorck, A. (2008). *Numerical Methods in Scientific Computing: Volume 1*. Other Titles in Applied Mathematics. Society for Industrial and Applied Mathematics (SIAM, 3600 Market Street, Floor 6, Philadelphia, PA 19104). https://books.google.pl/books?id=qy83gXoRps8C

de Boer, P. T. & Vester, M. (2018). Sideband asymmetry in ionospheric cross modulation. *Radio Science*, 53(5), 640–655. https://doi.org/10.1002/2017rs006525

de Lima, W. & Hamilton, M. (2003). Finite-amplitude waves in isotropic elastic plates. *Journal of Sound and Vibration*, 265(4), 819–839. https://doi.org/10.1016/S0022-460X(02)01260-9

Delsanto, P., Schechter, R., Chaskelis, H., Mignogna, R., & Kline, R. (1994). Connection machine simulation of ultrasonic wave propagation in materials. ii: The two-dimensional case. *Wave Motion*, 20(4), 295 – 314. https://doi.org/10.1016/0165-2125(94)90016-7

Delsanto, P., Schechter, R., & Mignogna, R. (1997). Connection machine simulation of ultrasonic wave propagation in materials iii: The three-dimensional case. *Wave Motion*, 26(4), 329–339. https://doi.org/10.1016/S0165-2125(97)00013-9

Delsanto, P., Whitcombe, T., Chaskelis, H., & Mignogna, R. (1992). Connection machine simulation of ultrasonic wave propagation in materials. i: the one-dimensional case. *Wave Motion*, 16(1), 65–80. https://doi.org/10.1016/0165-2125(92)90047-6

Deng, M. (1999). Cumulative second-harmonic generation of lamb-mode propagation in a solid plate. *Journal of Applied Physics*, 85(6), 3051–3058. https://doi.org/10.1063/1.369642

Deng, M., Wang, P., & Lv, X. (2005). Experimental verification of cumulative growth effect of second harmonics of lamb wave propagation in an elastic plate. *Applied Physics Letters*, 86(12), 124104. https://doi.org/10.1063/1.1891295

Donskoy, D. M. & Sutin, A. M. (1998). Vibro-acoustic modulation nondestructive evaluation technique. *Journal of Intelligent Material Systems and Structures*, 9(9), 765–771. https://doi.org/10.1177/1045389x9800900909

Duffy, D. (2004). *Transform Methods for Solving Partial Differential Equations* (second edition ed.). Chapman and Hall/CRC. https://doi.org/10.1201/9781420035148

Duffy, D. G. (2001). *Green's Functions with Applications* (1st ed.). Chapman and Hall/CRC. https://doi.org/10.1201/9781420034790

Eringen, A. (1974). *Elastodynamics*. Number t. 1 in Elastodynamics. Academic Press. https://books.google.pl/books?id=XF4WAwAAQBAJ

Fabrizio, M. & Morro, A. (2003). *Electromagnetism of Continuous Media: Mathematical Modelling and Applications*. Oxford University Press. https://doi.org/10.1093/acprof:oso/9780198527008.001.0001

Fillinger, L., Zaitsev, V., Gusev, V., & Castagnède, B. (2006). Wave self-modulation in an acoustic resonator due to self-induced transparency. *Europhysics Letters (EPL)*, 76(2), 229–235. https://doi.org/10.1209/epl/i2006-10267-5

Findley, W., Lai, J., & Onaran, K. (1989). *Creep and Relaxation of Nonlinear Viscoelastic Materials: With an Introduction to Linear Viscoelasticity*. Dover Civil and Mechanical Engineering. Dover. https://books.google.pl/books?id=NN73kxl0mjIC

Fuzhen Wen, Shengbo Shan, L. C. (2021). Third harmonic shear horizontal waves for material degradation monitoring. *Structural Health Monitoring*, 20(2), 475–483. https://doi.org/10.1177/1475921720936983

Ginzburg, V. (1970). *The Propagation of Electromagnetic Waves in Plasmas*. Commonwealth and International Library. Pergamon Press. https://books.google.pl/books?id=vF55AAAAIAAJ

Ginzburg, V. L. (1948). The theory of luxemburg–gorky effect. *Izvestiya Akademii Nauk SSR, Seriya Fizicheskaya*, 12, 253.

Ginzburg, V. L. & Gurevich, A. V. (1960). Nonlinear phenomena in a plasma located in an alternating electromagnetic field. *Soviet Physics Uspekhi*, 3(1), 115–146. https://doi.org/10.1070/pu1960v003n01abeh003261

Giurgiutiu, V. (2008). *Structural Health Monitoring Structural Health Monitoring with Piezoelectric Wafer Active Sensors*. Academic Press. https://doi.org/10.1016/B978-0-12-088760-6.X5001-6

Graff, K. (2012). *Wave Motion in Elastic Solids*. Dover Books on Physics. Dover Publications. https://books.google.pl/books?id=jorRAgAAQBAJ

Graffi, D. (1936). Una teoria ereditaria dell'effetto lussemburgo. *Rendiconti del Seminario Matematico della Università di Padova*, 7, 36–54. https://api.semanticscholar.org/CorpusID:125700255

Griffiths, D. (2017a). *Introduction to Quantum Mechanics*. Cambridge University Press. https://doi.org/10.1017/9781316995433

Griffiths, D. J. (2017b). *Introduction to Electrodynamics*. Cambridge University Press. https://doi.org/10.1017/9781108333511

Gubernatis, J. E., Domany, E., & Krumhansl, J. A. (1977a). Formal aspects of the theory of the scattering of ultrasound by flaws in elastic materials. *Journal of Applied Physics*, 48(7), 2804–2811. https://doi.org/10.1063/1.324141

Gubernatis, J. E., Domany, E., Krumhansl, J. A., & Huberman, M. (1977b). The Born approximation in the theory of the scattering of elastic waves by flaws. *Journal of Applied Physics*, 48(7), 2812–2819. https://doi.org/10.1063/1.324142

Gurevich, A. V. (1976). Nonlinear phenomena in the ionosphere. *Radiophysics and Quantum Electronics*, 19(5), 595–597. https://doi.org/10.1007/BF01043546

Gurevich, A. V. (1978). *Nonlinear Phenomena in the Ionosphere*. Springer Berlin Heidelberg. https://doi.org/10.1007/978-3-642-87649-3

Gusev, V., Tournat, V., & Castagnède, B. (2009). *Nonlinear Acoustic Phenomena in Micro-inhomogenous Media*, (Chapter 17, 431–471). John Wiley & Sons, Ltd. https://doi.org/10.1002/9780470611609.ch17

Guyer, R. A. & Johnson, P. A. (1999). Nonlinear mesoscopic elasticity: Evidence for a new class of materials. *Physics Today*, 52(4), 30–36. https://doi.org/10.1063/1.882648

Haberman, R. (2013). *Applied Partial Differential Equations: With Fourier Series and Boundary Value Problems*. Featured Titles for Partial Differential Equations. Pearson. https://books.google.pl/books?id=hGNwLgEACAAJ

Hackett, R. M. (2016). *Finite Elasticity*. Springer International Publishing. https://doi.org/10.1007/978-3-319-23273-7

Hamilton, M. F., Ilinskii, Y. A., & Zabolotskaya, E. A. (2004). Separation of compressibility and shear deformation in the elastic energy density (l). *The Journal of the Acoustical Society of America*, 116(1), 41–44. https://doi.org/10.1121/1.1736652

Herrmann, J., Kim, J.-Y., Jacobs, L. J., Qu, J., Littles, J. W., & Savage, M. F. (2006). Assessment of material damage in a nickel-base superalloy using nonlinear rayleigh surface waves. *Journal of Applied Physics*, 99(12), 124913. https://doi.org/10.1063/1.2204807

Herzer, H.-R., Becker, M. M., & Schneider, E. (2019). *The Acousto-elastic Effect and Its Use in NDE*, 235–250. Springer International Publishing. https://doi.org/10.1007/978-3-319-26553-7_56

Hikata, A., Chick, B. B., & Elbaum, C. (1965). Dislocation contribution to the second harmonic generation of ultrasonic waves. *Journal of Applied Physics*, 36(1), 229–236. https://doi.org/10.1063/1.1713881

Holm, S. (2019). *Waves with Power-Law Attenuation*. Springer International Publishing. https://doi.org/10.1007/978-3-030-14927-7

Holmes, M. (2012). *Introduction to Perturbation Methods*. Texts in Applied Mathematics. Springer New York. https://books.google.pl/books?id=EX5iNglbqB4C

Huxley, L. & Ratcliffe, J. (1949). A survey of ionospheric cross-modulation (wave interaction or luxembourg effect). *Proceedings of the IEE - Part III: Radio and Communication Engineering*, 96(43), 433–440. https://doi.org/10.1049/pi-3.1949.0093

Jhang, K.-Y. (2009). Nonlinear ultrasonic techniques for nondestructive assessment of micro damage in material: A review. *International Journal of Precision Engineering and Manufacturing*, 10(1), 123–135. https://doi.org/10.1007/s12541-009-0019-y

Jhang, K.-Y., Lissenden, C., Solodov, I., Ohara, Y., & Gusev, V. (2020a). *Measurement of Nonlinear Ultrasonic Characteristics*. https://doi.org/10.1007/978-981-15-1461-6

Jhang, K.-Y., Lissenden, C., Solodov, I., Ohara, Y., & Gusev, V. (2020b). *Measurement of Nonlinear Ultrasonic Characteristics*. https://doi.org/10.1007/978-981-15-1461-6

Johnson, P., Zinszner, B., & Rasolofosaon, P. (1996). Resonance and elastic non-linear phenomena in rock. *Journal of Geophysical Research*, 101, 11553–11564. https://doi.org/10.1029/96JB00647

Johnson, P. A. & Shankland, T. J. (1989). Nonlinear generation of elastic waves in granite and sandstone: Continuous wave and travel time observations. *Journal of Geophysical Research: Solid Earth*, 94(B12), 17729–17733. https://doi.org/10.1029/jb094ib12p17729

Jones, G. L. & Kobett, D. R. (1963). Interaction of elastic waves in an isotropic solid. *The Journal of the Acoustical Society of America*, 35(1), 5–10. https://doi.org/10.1121/1.1918405

Ju, T., Achenbach, J. D., Jacobs, L. J., & Qu, J. (2019). Nondestructive evaluation of thermal aging of adhesive joints by using a nonlinear wave mixing technique. *NDT & E International*, 103, 62–67. https://doi.org/10.1016/j.ndteint.2019.02.006

Kanda, K. & Sugiura, T. (2021). Internally resonant guided waves arising from quadratic classical nonlinearities with damping. *International Journal of Solids and Structures*, 216, 250–257. https://doi.org/10.1016/j.ijsolstr.2020.11.033

Kerschen, G., editor (2014). *Modal Analysis of Nonlinear Mechanical Systems*. Springer Vienna. https://doi.org/10.1007/978-3-7091-1791-0

Kevorkian, J. & Cole, J. (2013). *Perturbation Methods in Applied Mathematics*. Applied Mathematical Sciences. Springer New York. https://books.google.pl/books?id=1YTSBwAAQBAJ

Kijanka, P., Radecki, R., Packo, P., Staszewski, W. J., & Uhl, T. (2013). Gpu-based local interaction simulation approach for simplified temperature effect modelling in lamb wave propagation used for damage detection. *Smart Materials and Structures*, 22(3), 035014. https://doi.org/10.1088/0964-1726/22/3/035014

Klepka, A., Staszewski, W., Jenal, R., Szwedo, M., Iwaniec, J., & Uhl, T. (2011). Nonlinear acoustics for fatigue crack detection – experimental investigations of vibro-acoustic wave modulations. *Structural Health Monitoring*, 11(2), 197–211. https://doi.org/10.1177/1475921711414236

Korneev, V., Nihei, K., & Myer, L. (1998). *Nonlinear interaction of plane elastic waves*. https://doi.org/10.2172/290877

Korneev, V. A. & Demčenko, A. (2014). Possible second-order nonlinear interactions of plane waves in an elastic solid. *The Journal of the Acoustical Society of America*, 135(2), 591–598. https://doi.org/10.1121/1.4861241

Kundu, T. (2019). *Nonlinear Ultrasonic and Vibro-Acoustical Techniques for Nondestructive Evaluation*. https://doi.org/10.1007/978-3-319-94476-0

Lai, W., Rubin, D., & Krempl, E. (2010). *Introduction to Continuum Mechanics*. Elsevier. https://doi.org/10.1016/b978-0-7506-8560-3.x0001-1

Lamb, H. (1917). On waves in an elastic plate. *Proceedings of the Royal Society of London. Series A, Containing Papers of a Mathematical and Physical Character*, 93(648), 114–128. https://doi.org/10.1098/rspa.1917.0008

Landau, L. D. & Lifshitz, E. M. (1989). *Theory of Elasticity*. Course of theoretical physics. Pergamon Press. https://books.google.pl/books?id=YjDiQwAACAAJ

Layzer, D., Menzel, D., & Hughes, C. (1965). Ionospheric cross modulation - a microscopic theory. *Journal of Research of the National Bureau of Standards, Section D: Radio Science*, 69D(1), 59. https://doi.org/10.6028/jres.069d.016

Lee, B. C. & Staszewski, W. J. (2003a). Modelling of lamb waves for damage detection in metallic structures: Part I. wave propagation. *Smart Materials and Structures*, 12(5), 804–814. https://doi.org/10.1088/0964-1726/12/5/018

Lee, B. C. & Staszewski, W. J. (2003b). Modelling of lamb waves for damage detection in metallic structures: Part II. wave interactions with damage. *Smart Materials and Structures*, 12(5), 815–824. https://doi.org/10.1088/0964-1726/12/5/019

Li, W., Choi, J., & Cho, Y. (2015). Second harmonic generation of shear horizontal guided wave propagation in plate-like structures. *Physics Procedia*, 70, 451–454. https://doi.org/10.1016/j.phpro.2015.08.283

Lighthill, M. J. (1958). *An Introduction to Fourier Analysis and Generalised Functions*. Cambridge University Press. https://doi.org/10.1017/cbo9781139171427

Lissenden, C., Liu, Y., & Rose, J. (2015). Use of non-linear ultrasonic guided waves for early damage detection. *Insight - Non-Destructive Testing and Condition Monitoring*, 57. https://doi.org/10.1784/insi.2015.57.4.206

Lissenden, C. J. (2021). Nonlinear ultrasonic guided waves—principles for nondestructive evaluation. *Journal of Applied Physics*, 129(2), 021101. https://doi.org/10.1063/5.0038340

Liu, Y., Chillara, V. K., Lissenden, C., & Rose, J. (2013a). Third harmonic shear horizontal and rayleigh lamb waves in weakly nonlinear plates. *Journal of Applied Physics*, 114, 114908–114908. https://doi.org/10.1063/1.4821252

Liu, Y., Chillara, V. K., & Lissenden, C. J. (2013b). On selection of primary modes for generation of strong internally resonant second harmonics in plate. *Journal of Sound and Vibration*, 332(19), 4517–4528. https://doi.org/10.1016/j.jsv.2013.03.021

Mallet, L., Lee, B. C., Staszewski, W. J., & Scarpa, F. (2004). Structural health monitoring using scanning laser vibrometry: Ii. lamb waves for damage detection. *Smart Materials and Structures*, 13(2), 261–269. https://doi.org/10.1088/0964-1726/13/2/003

Matlack, K. H., Kim, J.-Y., Jacobs, L. J., & Qu, J. (2011). Experimental characterization of efficient second harmonic generation of lamb wave modes in a nonlinear elastic isotropic plate. *Journal of Applied Physics*, 109(1), 014905. https://doi.org/10.1063/1.3527959

Matlack, K. H., Kim, J.-Y., Jacobs, L. J., & Qu, J. (2014). Review of second harmonic generation measurement techniques for material state determination in metals. *Journal of Nondestructive Evaluation*, 34(1). https://doi.org/10.1007/s10921-014-0273-5

Mayer, A. (1990). Thermoelastic attenuation of surface acoustic waves. *International Journal of Engineering Science*, 28(10), 1073–1082. https://doi.org/10.1016/0020-7225(90)90135-6

McQuarrie, D. (2003). *Mathematical Methods for Scientists and Engineers*. University Science Books. https://books.google.pl/books?id=FmAAwE8MSwoC

Meirovitch, L. (1980). *Computational Methods in Structural Dynamics*. Mechanics: Dynamical Systems. Springer Netherlands. https://books.google.pl/books?id=MrcYngyZD6cC

Meirovitch, L. (2003). *Fundamentals of Vibration*. Mcgraw-Hill Publ.Comp. https://books.google.pl/books?id=WJnpPAAACAAJ

Meo, M. & Zumpano, G. (2005). Nonlinear elastic wave spectroscopy identification of impact damage on a sandwich plate. *Composite Structures*, 71(3–4), 469–474. https://doi.org/10.1016/j.compstruct.2005.09.027

Miklowitz, J. (1978). *The Theory of Elastic Waves and Waveguides*. North-Holland Series in Applied Mathematics and Mechanics. Elsevier Science. https://books.google.pl/books?id=YiAbAQAAIAAJ

Min, T.-K. & Vo-Dai, N. (2008). Kelvin-voigt model for dynamics of crack opening in shrinkage cracking. *KSCE Journal of Civil Engineering*, 12(3), 149–154. https://doi.org/10.1007/s12205-008-0149-2

Mindlin, R. & Yang, J. (2006). *An Introduction to the Mathematical Theory of Vibrations of Elastic Plates*. G - Reference,Information and Interdisciplinary Subjects Series. World Scientific. https://books.google.pl/books?id=gOFoDQAAQBAJ

Mingxi, D. (1998). Cumulative second-harmonic generation accompanying nonlinear shear horizontal mode propagation in a solid plate. *Journal of Applied Physics*, 84(7), 3500–3505. https://doi.org/10.1063/1.368525

Moon, P. & Spencer, D. E. (1961). *Field Theory Handbook*. Springer Berlin Heidelberg. https://doi.org/10.1007/978-3-642-53060-9

Morse, P. & Feshbach, H. (1953). *Methods of Theoretical Physics*. International series in pure and applied physics. McGraw-Hill. https://books.google.pl/books?id=l8ENAQAAIAAJ

Morse, P. & Ingard, K. (1986). *Theoretical Acoustics*. International series in pure and applied physics. Princeton University Press. https://books.google.pl/books?id=KIL4MV9IE5kC

Moussatov, A., Gusev, V., & Castagnède, B. (2003). Self-induced hysteresis for nonlinear acoustic waves in cracked material. *Physical Review Letters*, 90(12). https://doi.org/10.1103/physrevlett.90.124301

Müller, M. F., Kim, J.-Y., Qu, J., & Jacobs, L. J. (2010). Characteristics of second harmonic generation of lamb waves in nonlinear elastic plates. *The Journal of the Acoustical Society of America*, 127(4), 2141–2152. https://doi.org/10.1121/1.3294714

Nadella, K. S. & Cesnik, C. E. S. (2013). Local interaction simulation approach for modeling wave propagation in composite structures. *CEAS Aeronautical Journal*, 4(1), 35–48. https://doi.org/10.1007/s13272-012-0061-9

Nagy, P. B. (1998). Fatigue damage assessment by nonlinear ultrasonic materials characterization. *Ultrasonics*, 36(1–5), 375–381. https://doi.org/10.1016/s0041-624x(97)00040-1

Narasimhan, M. (1993). *Principles of Continuum Mechanics*. A Wiley Interscience publication. Wiley. https://books.google.pl/books?id=MqweAQAAIAAJ

Nayfeh, A. (2008). *Perturbation Methods*. Physics textbook. Wiley. https://books.google.pl/books?id=eh6RmWZ51NIC

Nayfeh, A. (2011). *Introduction to Perturbation Techniques*. Wiley Classics Library. Wiley. https://books.google.pl/books?id=EX5iNglbqB4C

Nayfeh, A. & Mook, D. (1979). *Nonlinear Oscillations*. Pure and Applied Mathematics: A Wiley Series of Texts, Monographs and Tracts. Wiley. https://books.google.pl/books?id=SQq0QgAACAAJ

Nayfeh, A. & Pai, P. (2004). *Linear and Nonlinear Structural Mechanics*. John Wiley & Sons, Ltd. https://doi.org/10.1002/9783527617562

Nayfeh, A. H. (1995). On direct methods for constructing nonlinear normal modes of continuous systems. *Journal of Vibration and Control*, 1(4), 389–430. https://doi.org/10.1177/107754639500100402

Nayfeh, A. H. & Nayfeh, S. A. (1994). On Nonlinear Modes of Continuous Systems. *Journal of Vibration and Acoustics*, 116(1), 129–136. https://doi.org/10.1115/1.2930388

Nayfeh, A. H. & Nayfeh, S. A. (1995). Nonlinear Normal Modes of a Continuous System With Quadratic Nonlinearities. *Journal of Vibration and Acoustics*, 117(2), 199–205. https://doi.org/10.1115/1.2873898

Norris, A. N. (1998). Finite-amplitude waves in solids. *Nonlinear Acoustics*, 263–277. Academic press San Diego. https://books.google.pl/books?id=k-kWozCE0jIC

Nowacki, W. (1986). *Thermoelasticity*. III: Comparative Literature; 15. Elsevier Science & Technology Books. https://books.google.pl/books?id=0fxQAAAAMAAJ

Obenchain, M. B. & Cesnik, C. E. S. (2014). Guided wave interaction with hole damage using the local interaction simulation approach. *Smart Materials and Structures*, 23(12). https://doi.org/10.1088/0964-1726/23/12/125010

Obenchain, M. B., Nadella, K. S., & Cesnik, C. E. S. (2015). Hybrid global matrix/local interaction simulation approach for wave propagation in composites. *AIAA Journal*, 53(2), 379–393. https://doi.org/10.2514/1.j053101

Ogden, R. (1997). *Non-linear Elastic Deformations*. Dover Civil and Mechanical Engineering. Dover Publications. https://books.google.pl/books?id=2u7wCaojfbEC

Ong, W., Chiu, W., & Rose, L. (2017). Numerical simulation of cumulative nonlinear symmetric lamb waves in an aluminium plate. *Procedia Engineering*, 188, 217–224. https://doi.org/10.1016/j.proeng.2017.04.477

Osika, M. & Kijanka, P. (2024). Ultrasound shear wave propagation modeling in general tissue–like viscoelastic materials. *Ultrasound in Medicine & Biology*, 50(4), 627–638. https://doi.org/10.1016/j.ultrasmedbio.2024.01.008

Osika, M., Radecki, R., Ziaja-Sujdak, A., & Staszewski, W. J. (2021). Modelling of the shear horizontal waves high-order harmonics generation using local interaction simulation approach. *European Workshop on Structural Health Monitoring*, 200–209. https://doi.org/10.1007/978-3-030-64594-6_21

Osika, M., Ziaja-Sujdak, A., Radecki, R., Cheng, L., & Staszewski, W. (2022). Nonlinear modes in shear horizontal wave propagation–analytical and numerical analysis. *Journal of Sound and Vibration*, 540, 117247. https://doi.org/10.1016/j.jsv.2022.117247

Osika, M., Ziaja-Sujdak, A., Radecki, R., & Staszewski, W. J. (2023a). Experimental investigation of modulation transfer phenomenon due to shear horizontal ultrasonic wave interaction with local nonlinearity. *European Workshop on Structural Health Monitoring*, 203–209. https://doi.org/10.1007/978-3-031-07254-3_20

Osika, M., Ziaja–Sujdak, A., Radecki, R., & Staszewski, W. (2023b). The luxembourg–gorky effect for elastic shear horizontal guided waves — analytical and numerical modelling. *International Journal of Engineering Science*, 193, 103933. https://doi.org/10.1016/j.ijengsci.2023.103933

Packo, P., Bielak, T., Spencer, A., Staszewski, W., Uhl, T., & Worden, K. (2012). Lamb wave propagation modelling and simulation using parallel processing architecture and graphical cards. *Smart Materials & Structures*, 21. https://doi.org/10.1088/0964-1726/21/7/075001

Packo, P., Radecki, R., Leamy, M. J., Uhl, T., & Staszewski, W. J. (2019). Modeling and numerical simulations in nonlinear acoustics used for damage detection. *Nonlinear Ultrasonic and Vibro-Acoustical Techniques for Nondestructive Evaluation*, 103–137. https://doi.org/10.1007/978-3-319-94476-0_3

Packo, P., Uhl, T., Staszewski, W. J., & Leamy, M. J. (2016). Amplitude-dependent lamb wave dispersion in nonlinear plates. *The Journal of the Acoustical Society of America*, 140(2), 1319–1331. https://doi.org/10.1121/1.4961489

Penrose, R. (1955). A generalized inverse for matrices. *Mathematical Proceedings of the Cambridge Philosophical Society*, 51(3), 406–413. https://doi.org/10.1017/S0305004100030401

Perzyna, P. (1998). *Localization and Fracture Phenomena in Inelastic Solids*. Springer Vienna. https://doi.org/10.1007/978-3-7091-2528-1

Pieczonka, L., Klepka, A., Martowicz, A., & Staszewski, W. (2015). Nonlinear vibroacoustic wave modulations for structural damage detection: An overview. *Optical Engineering*, 55, 011005. https://doi.org/10.1117/1.OE.55.1.011005

Plotkin, V. V. (1977). Nonlinear energy transfer between radio waves in a collisional plasma. *Radiophysics and Quantum Electronics*, 20(2), 115–119. https://doi.org/10.1007/bf01034195

Podlubny, I. (1998). *Fractional Differential Equations: An Introduction to Fractional Derivatives, Fractional Differential Equations, to Methods of Their Solution and Some of Their Applications*. ISSN. Elsevier Science. https://books.google.pl/books?id=K5FdXohLto0C

Rao, S. (2006). *Vibration of Continuous Systems*. John Wiley & Sons, Ltd. https://doi.org/10.1002/9780470117866

Rao, S. S. (2011). *The Finite Element Method in Engineering* (fifth edition ed.). Butterworth-Heinemann. https://www.sciencedirect.com/book/9781856176613/the-finite-element-method-in-engineering

Reismann, H. (1968). On the forced motion of elastic solids. *Flow Turbulence and Combustion*, 18, 156–165. https://doi.org/10.1007/BF00382343

Renaud, G., Bosch, J. G., van der Steen, A. F. W., & de Jong, N. (2010). The luxembourg-gorky effect for in vitro characterization of lipid-coated microbubbles. *2010 IEEE International Ultrasonics Symposium*, 786–789. https://doi.org/10.1109/ultsym.2010.5935699

Rose, J. (2014). *Ultrasonic Guided Waves in Solid Media*. Cambridge University Press. https://doi.org/10.1017/CBO9781107273610

Rosenberg, R. M. (1966). On Nonlinear Vibrations of Systems with Many Degrees of Freedom. *Advances in Applied Mechanics*, 9(C), 155–242. https://doi.org/10.1016/S0065-2156(08)70008-5

Savage, J. C. (1966). Thermoelastic attenuation of elastic waves by cracks. *Journal of Geophysical Research*, 71(16), 3929–3938. https://doi.org/10.1029/jz071i016p03929

Scalerandi, M. & Agostini, V. (2002). Simulation of the propagation of ultrasonic pulses in nonlinear and/or attenuative media. *Journal of Computational Acoustics*, 10(03), 275–294. https://doi.org/10.1142/s0218396x02001693

Scalerandi, M., Agostini, V., Delsanto, P. P., Van Den Abeele, K., & Johnson, P. A. (2003). Local interaction simulation approach to modelling nonclassical, nonlinear elastic behavior in solids. *The Journal of the Acoustical Society of America*, 113(6), 3049–3059. https://doi.org/10.1121/1.1570440

Shan, S., Zhang, Y., Liu, Z., Wen, F., Cheng, L., & Staszewski, W. J. (2024). Cross-modulation in guided wave propagation: how does it relate to the luxemburg-gorky effect? *Journal of Sound and Vibration*, 568, 117961. https://doi.org/10.1016/j.jsv.2023.117961

Shengbo, S. & Cheng, L. (2019). Mixed third harmonic shear horizontal wave generation: interaction between primary shear horizontal wave and second harmonic lamb wave. *Smart Materials and Structures*, 28. https://doi.org/10.1088/1361-665X/ab1fce

Skalmierski, B. (1991). *Mechanics*. Elsevier. https://doi.org/10.1016/b978-0-444-98730-3.50004-0

Sokolnikoff, I. (1956). *Mathematical Theory of Elasticity*. McGraw-Hill. https://books.google.pl/books?id=yxMIAQAAIAAJ

Solodov, I., Krohn, N., & Busse, G. (2002). Can: an example of nonclassical acoustic nonlinearity in solids. *Ultrasonics*, 40(1–8), 621–625. https://doi.org/10.1016/s0041-624x(02)00186-5

Solodov, I. Y. (1998). Ultrasonics of non-linear contacts: propagation, reflection and nde-applications. *Ultrasonics*, 36(1), 383–390. Ultrasonics International 1997. https://doi.org/10.1016/S0041-624X(97)00041-3

Spytek, J., Ambrozinski, L., & Pelivanov, I. (2023). Non-contact detection of ultrasound with light – review of recent progress. *Photoacoustics*, 29, 100440. https://doi.org/https://doi.org/10.1016/j.pacs.2022.100440

Srivastava, A. & Lanza di Scalea, F. (2009). On the existence of antisymmetric or symmetric lamb waves at nonlinear higher harmonics. *Journal of Sound and Vibration*, 323(3), 932–943. https://doi.org/10.1016/j.jsv.2009.01.027

Staszewski, W. J., Boller, C., & Tomlinson, G. R. (2003). *Health Monitoring of Aerospace Structures: Smart Sensor Technologies and Signal Processing*. Wiley. https://doi.org/10.1002/0470092866

Staszewski, W. J., Lee, B. C., Mallet, L., & Scarpa, F. (2004). Structural health monitoring using scanning laser vibrometry: I. lamb wave sensing. *Smart Materials and Structures*, 13(2), 251–260. https://doi.org/10.1088/0964-1726/13/2/002

Stepinski, T., Uhl, T., & Staszewski, W. (2013). *Advanced Structural Damage Detection: From Theory to Engineering Applications*. Wiley. https://doi.org/10.1002/9781118536148

Sun, M., Li, X., & Kube, C. M. (2023). Interaction of elastic waves in solids with quadratic and cubic nonlinearity. *The Journal of the Acoustical Society of America*, 154(5), 3285–3309. https://doi.org/10.1121/10.0022381

Sundararaman, S. & Adams, D. (2009). Accuracy and convergence using a local interaction simulation approach in one, two, and three dimensions. *Journal of Applied Mechanics-transactions of The Asme - J APPL MECH*, 76. https://doi.org/10.1115/1.2871105

Sundararaman, S. & Adams, D. E. (2008). Modeling guided waves for damage identification in isotropic and orthotropic plates using a local interaction simulation approach. *Journal of Vibration and Acoustics*, 130(4). https://doi.org/10.1115/1.2890389

Tellegen, B. D. H. (1933). Interaction between radio-waves? *Nature*, 131(3319), 840–840. https://doi.org/10.1038/131840a0

Truesdell, C. & Noll, W. (2004). *The Non-Linear Field Theories of Mechanics*. Springer Berlin Heidelberg. https://doi.org/10.1007/978-3-662-10388-3_1

Vakakis, A. & Rand, R. (1992a). Normal modes and global dynamics of a two-degree-of-freedom non-linear system-i. low energies. *International Journal of Non-Linear Mechanics*, 27(5), 861–874. https://doi.org/10.1016/0020-7462(92)90040-E

Vakakis, A. & Rand, R. (1992b). Normal modes and global dynamics of a two-degree-of-freedom non-linear system—ii. high energies. *International Journal of Non-Linear Mechanics*, 27(5), 875–888. https://doi.org/10.1016/0020-7462(92)90041-5

Van Den Abeele, K., Johnson, P., & Sutin, A. (2000). Nonlinear elastic wave spectroscopy (news) techniques to discern material damage, part i: Nonlinear wave modulation spectroscopy (nwms). *Research in Nondestructive Evaluation*, 12, 17–30. https://doi.org/10.1080/09349840009409646

Viktorov, I. A. (1967). Rayleigh and lamb waves. *Rayleigh and Lamb Waves*, 33. https://api.semanticscholar.org/CorpusID:117743928

Virieux, J. (1984a). P-sv wave propagation in heterogeneous media: Velocity-stress finite-difference method. *Geophysics*, 51, 889–901. https://doi.org/10.1190/1.1442147

Virieux, J. (1984b). Sh -wave propagation in heterogeneous media: Velocity-stress finite-difference method. *Geophysics*, 49, 1933–1942. https://doi.org/10.1190/1.1441605

Wang, H. & Li, M. (2009). Ab initio calculations of second-, third-, and fourth-order elastic constants for single crystals. *Phys. Rev. B*, 79, 224102. https://doi.org/10.1103/PhysRevB.79.224102

Whitham, G. (1999). John Wiley and Sons, Ltd. https://doi.org/10.1002/9781118032954

Wochner, M. S., Hamilton, M. F., Ilinskii, Y. A., & Zabolotskaya, E. A. (2008). Nonlinear torsional wave beams. *AIP Conference Proceedings*, 1022(1), 335–338. https://doi.org/10.1063/1.2956224

Yang, Y., Ng, C.-T., & Kotousov, A. (2019). Second-order harmonic generation of lamb wave in prestressed plates. *Journal of Sound and Vibration*, 460, 114903. https://doi.org/10.1016/j.jsv.2019.114903

Zabolotskaya, E. A., Hamilton, M. F., Ilinskii, Y. A., & Meegan, G. D. (2004). Modeling of nonlinear shear waves in soft solids. *The Journal of the Acoustical Society of America*, 116(5), 2807–2813. https://doi.org/10.1121/1.1802533

Zaitsev, V., Gusev, V., & Castagnede, B. (2002a). Luxemburg-gorky effect retooled for elastic waves: A mechanism and experimental evidence. *Physical Review Letters*, 89(10). https://doi.org/10.1103/physrevlett.89.105502

Zaitsev, V., Gusev, V., & Castagnède, B. (2002b). Observation of the "luxemburg–gorky effect" for elastic waves. *Ultrasonics*, 40(1-8), 627–631. https://doi.org/10.1016/s0041-624x(02)00187-7

Zaitsev, V., Nazarov, V., Gusev, V., & Castagnede, B. (2006). Novel nonlinear-modulation acoustic technique for crack detection. *NDT & E International*, 39(3), 184–194. Emerging Technologies in NDT - Third International Conference. https://doi.org/10.1016/j.ndteint.2005.07.007

Zaitsev, V. Y., Nazarov, V. E., Tournat, V., Gusev, V. E., & Castagnède, B. (2005). Luxemburg-gorky effect in a granular medium: Probing perturbations of the material state via cross-modulation of elastic waves. *Europhysics Letters (EPL)*, 70(5), 607–613. https://doi.org/10.1209/epl/i2005-10023-5

Zarembo, L. K. & Krasil'nikov, V. A. (1971). Nonlinear phenomena in the propagation of elastic waves in solids. *Soviet Physics Uspekhi*, 13(6), 778–797. https://doi.org/10.1070/pu1971v013n06abeh004281

Zener, C. (1937). Internal friction in solids. i. theory of internal friction in reeds. *Physical Review*, 52(3), 230–235. https://doi.org/10.1103/physrev.52.230

Zener, C. (1938). Internal friction in solids II. general theory of thermoelastic internal friction. *Physical Review*, 53(1), 90–99. https://doi.org/10.1103/physrev.53.90

Zener, C. (1941). Theory of the elasticity of polycrystals with viscous grain boundaries. *Physical Review*, 60(12), 906. https://doi.org/10.1103/PhysRev.60.906

Zener, C. (1948). *Elasticity and Anelasticity of Metals*. Chicago University Committee on Publications in the Physical Sciences. University of Chicago Press. https://books.google.pl/books?id=FKcZAAAAIAAJ

Zener, C., Otis, W., & Nuckolls, R. (1938). Internal friction in solids III. experimental demonstration of thermoelastic internal friction. *Physical Review*, 53(1), 100–101. https://doi.org/10.1103/physrev.53.100

Zienkiewicz, O. & Taylor, R. (2013). *The Finite Element Method for Solid and Structural Mechanics*. The Finite Element Method. Elsevier Science. https://doi.org/10.1016/C2009-0-26332-X

Żur, K. K. (2016). Green's function for frequency analysis of thin annular plates with nonlinear variable thickness. *Applied Mathematical Modelling*, 40(5), 3601–3619. https://doi.org/10.1016/j.apm.2015.10.014

Żur, K. K., Firouzi, N., Rabczuk, T., & Zhuang, X. (2023). Large deformation of hyperelastic modified timoshenko–ehrenfest beams under different types of loads. *Computer Methods in Applied Mechanics and Engineering*, 416, 116368. https://doi.org/10.1016/j.cma.2023.116368

Żak, A. (2024). *A Finite Element Approach for Wave Propagation in Elastic Solids*. Springer Nature Switzerland. https://doi.org/10.1007/978-3-031-56836-7